THÈSE

Pour obtenir le grade de

DOCTEUR DE L'UNIVERSITÉ GRENOBLE ALPES

École doctorale : EEATS - Electronique, Electrotechnique, Automatique, Traitement du Signal
Spécialité : Optique et Radiofréquences
Unité de recherche : CEA LETI - Laboratoire d'électronique et de technologie de l'information

Interaction guides d'onde/hologrammes pour la mise au point d'émetteurs directifs dans les dispositifs de Réalité Augmentée

Evaluation of the interaction between waveguides and holograms for the development of directional emitters for Augmented Reality applications

Présentée par :

Salaheddine TOUBI

Direction de thèse :

Elise GHIBAUDO PROFESSEURE DES UNIVERSITES, UNIVERSITE GRENOBLE ALPES	Directrice de thèse
Christophe MARTINEZ Université Grenoble Alpes	Co-directeur de thèse

Rapporteurs :

Jean-Louis DE BOUGRENET DE LA TOCNAYE
PROFESSEUR, IMT Atlantique
Bernard KRESS
SENIOR SCIENTIST, Google

Thèse soutenue publiquement le **5 février 2026**, devant le jury composé de :

Jean-Emmanuel BROQUIN, PROFESSEUR DES UNIVERSITES, Grenoble INP - UGA	Président
Elise GHIBAUDO, PROFESSEURE DES UNIVERSITES, Grenoble INP - UGA	Directrice de thèse
Christophe MARTINEZ, DIRECTEUR DE RECHERCHE, CEA Centre de Grenoble	Co-directeur de thèse
Jean-Louis DE BOUGRENET DE LA TOCNAYE, PROFESSEUR, IMT Atlantique	Rapporteur
Bernard KRESS, SENIOR SCIENTIST, Google	Rapporteur
Olivier HAEBERLÉ, PROFESSEUR DES UNIVERSITES, Université de Haute-Alsace	Examinateur
Pascal PICART, PROFESSEUR DES UNIVERSITES, Le Mans Université	Examinateur
Christophe PEROZ, SCIENTIST, Google	Examinateur

Remerciements

Je tiens à adresser mes sincères remerciements aux membres du jury de cette thèse. Je remercie tout particulièrement M. Jean-Emmanuel Broquin pour l'honneur qu'il m'a fait en acceptant de présider ce jury. Mes remerciements vont également à M. Jean-Louis de Bougrenet de La Tocnaye ainsi qu'à M. Bernard Kress pour avoir accepté d'être les rapporteurs de ce travail. Je leur suis profondément reconnaissant pour l'intérêt qu'ils ont porté à cette thèse, ainsi que pour leurs remarques pertinentes, constructives et encourageantes, qui ont contribué à enrichir ce travail.

À mes encadrants, je voudrais exprimer toute ma reconnaissance, car j'ai eu la chance d'être accompagné par deux personnes exceptionnelles, aussi bien sur le plan scientifique qu'humain. J'exprime toute ma gratitude envers ma directrice de thèse, Mme Elise Ghibaudo, pour son accompagnement attentionné, sa pédagogie, ainsi que son soutien humain et scientifique tout au long de cette aventure. J'adresse également mes plus sincères remerciements à M. Christophe Martinez ; sans lui, ce travail n'aurait pas été possible. Grâce à son encadrement quotidien, j'ai énormément appris : comment être rigoureux scientifiquement, mais aussi patient et persévérant. Le futur chercheur que je serai conservera sans aucun doute toutes les compétences et les valeurs acquises à vos côtés. S'il y a une chose que je retiens pour les futurs doctorants, c'est que l'encadrement est plus important que le sujet. J'ai eu la chance précieuse d'avoir les deux.

Je tiens à remercier l'ensemble des membres de mon équipe durant cette thèse. Yann Lee, sans toi, une grande partie de ce travail n'aurait pas pu aboutir. Merci pour ton implication dans la fabrication des lots photoniques, pour ton soutien expérimental précieux, mais aussi pour ton sens de l'humour unique qui va beaucoup me manquer. Sylvia, grâce à ta persévérance et à ton optimisme, nous avons finalement réussi à obtenir les bons échantillons. Je garderai en mémoire ta gentillesse ainsi que tous ces petits moments de bureau partagés (« michoko », « chocolat », « comme ci comme ça »...). J'ai également eu l'opportunité d'encadrer Sophia Blanco-Rincon, étudiante en dernière année du cycle ingénieur à l'INSA Rennes, dans le cadre de son stage. Ton soutien, aussi bien en simulation qu'en expérimentation, a été très important pour mon travail. Je tiens à te remercier pour ton implication, ta gentillesse et la qualité de ton travail. À ton tour maintenant de vivre l'aventure de la thèse : je te souhaite une très belle continuation à Nantes. Je souhaite également remercier les anciens doctorants et postdoctorants de l'équipe : Matthias, Fabian, Kyllian et Paul.

Je tiens à remercier Stéphanie Le Calvez (cheffe du Laboratoire Architectures et Systèmes Photoniques - LASP), ainsi que Stéphane Fanget (chef du Service Intégration Systèmes Photoniques – SISP), en premier lieu pour m'avoir donné le feu vert pour réaliser ma thèse. Tout au long de ces trois années, ils ont montré beaucoup d'intérêt pour mes travaux et ont constamment

été à l'écoute des différents besoins et difficultés rencontrées.

Je suis reconnaissant envers la collaboration établie entre les départements DOPT et DPFT, qui m'a permis d'obtenir les échantillons nécessaires à la réalisation de ce travail. Je remercie, à ce titre, les différents laboratoires et services impliqués : le LASP, le LAIP, le DPFT/SSURF ainsi que le DPFT/SPAT. Je tiens tout particulièrement à remercier Api Warsono, Laurence Gabette et Chafik Mhamdi pour leur soutien précieux et leur aide tout au long de cette collaboration.

Je tiens à remercier chaleureusement l'ensemble des membres du LASP pour leur accueil, leur bienveillance et les nombreux moments partagés tout au long de ces années de thèse. Je pense notamment à Anis, Nathalie, Laurent, Pierre, Florence, Fred, Michel, Kim, Andrea, Loïck, Oriane, Éric, Guillaume, Seliman, Alexis, Clarisse, Jonathan, ainsi qu'à toutes les personnes que j'oublie malheureusement de citer ici. Qu'elles me pardonnent, elles ont malgré tout toute leur place dans ces remerciements. Ces trois années passées au LASP ont été pour moi une expérience humaine et scientifique particulièrement enrichissante, remplie de rencontres, d'échanges et de souvenirs précieux. Merci sincèrement à chacune et à chacun d'avoir contribué à rendre cette aventure si agréable.

Je tiens également à remercier et à souhaiter beaucoup de courage à mes amis doctorants du LASP : Paul, Matthis, Cyrielle, Gabriel, Guilhem et Mouad. Je vous souhaite à tous une très belle continuation et beaucoup de réussite dans vos parcours scientifiques et personnels.

Je tiens également à remercier mon ami de trail, Matthieu Finet. Partager avec toi ces courses dans les montagnes grenobloises a été un véritable plaisir, en particulier dans les moments les plus difficiles de cette thèse. Le sport et la nature ont souvent représenté pour moi un refuge et un équilibre précieux, et ces instants passés à courir ensemble resteront parmi mes beaux souvenirs.

Enfin, je souhaite dédier cette thèse à ma chère famille : mes parents, mes frères et ma sœur. En tant que premier docteur de la famille, j'espère que ce travail pourra encourager et inspirer les générations futures à poursuivre des études ambitieuses et, pourquoi pas, à voir naître encore de nombreux docteurs dans notre famille. Vous avez toujours été ma principale source de motivation et d'inspiration, et je vous dédie ce travail avec énormément d'amour et de reconnaissance. J'espère vous rendre fiers. À mes parents, Rahal et Zohra, à mes frères Mohamed, Hajjaj, Omar, Mustapha, Said, Lkbir, Abdelatif et Jawad, ainsi qu'à ma sœur Milouda : recevez toute ma gratitude, mon affection et mon profond respect.

Titre en français :

Interaction guides d'onde/hologrammes pour la mise au point d'émetteurs directifs dans les dispositifs de Réalité Augmentée

Résumé de la thèse en français :

La thèse traite de l'enjeu de l'efficacité énergétique dans les dispositifs optiques proches de l'œil. Il s'agit de dispositifs sous forme de lunettes intelligentes ou de casques intégrant un écran. Une image virtuelle est projetée dans l'œil en superposition avec le champ visuel réel.

Pour des lunettes, il est nécessaire que l'image projetée soit suffisamment visible en conditions extérieures lumineuses, sans pour autant entraîner une forte consommation électrique ni augmenter la taille de la batterie. Pour une solution conventionnelle utilisant un micro écran LCOS (Liquid Crystal on Silicon), on calcule des pertes optiques d'environ 40 dB : un photon atteint la rétine pour 10 000 photons émis à la surface de l'écran.

Il apparait que ces versions miniaturisées d'écran, dérivées d'écrans classiques, présentent des propriétés d'émission mal adaptées à ces dispositifs, car un système optique se trouve entre l'œil et le micro-écran. Il faut donc raisonner à l'inverse : selon l'application, quel nouveau type d'écran doit être développé ?

La thèse évalue ainsi une approche de micro-écran non conventionnel, basé sur un circuit photonique intégré dans le visible et sur des éléments holographiques. Les propriétés d'émission de chaque pixel sont adaptées à l'application considérée ; elles incluent notamment le contrôle de la direction d'émission et de la divergence. On utilise une diode laser, dont l'étendue géométrique est minimale. La lumière est distribuée sur la surface de l'écran via une division en guides d'onde. Le signal est ensuite extrait vers l'espace libre à travers un composant actif, élément clé de cette thèse. Après extraction, un élément holographique micrométrique, codant une fonction optique, permet de rediriger le signal. L'enregistrement de ces fonctions optiques constitue le second sujet clé de mon travail.

Nous estimons pour cette approche innovante une efficacité optique d'environ 20 dB, soit un gain en nombre de photons 100 fois supérieur à l'approche conventionnelle. Pour l'extraction, la thèse propose et évalue une solution innovante brevetée. Elle remplace la solution basée sur un réseau de diffraction par un couplage évanescent entre le guide d'onde et une couche à haut indice, suivi d'une réflexion totale interne vers l'espace libre par une structure prismatique. La couche à haut indice est modulée par un cristal liquide ferroélectrique, permettant une commutation sur une durée théoriquement inférieure à 100 μs.

La thèse analyse ce composant en détail : longueur d'extraction, divergence, dispersion spectrale, polarisation du signal extrait, et autres paramètres. Elle fournit des éléments théoriques, une démonstration passive du principe, ainsi que des perspectives intéressantes à poursuivre.

Un prototype passif a été développé dans cette thèse pour démontrer l'intérêt de l'approche d'écran directif. Il met en œuvre une imprimante holographique dont le principe de fonctionnement est décrit dans le manuscrit. Ce travail a valu l'obtention du premier prix du Student Optical Design Challenge à SPIE AR|VR|MR 2025.

Mots-clefs en français :

Photonique intégrée, holographie, micro-écran, réalité augmentée, affichage proche de l'œil.

Résumé vulgarisé en français :

Notre laboratoire conduit des recherches sur une source d'image innovante et énergétiquement efficace pour les lunettes intelligentes dédiées aux applications de réalité augmentée. Le principe consiste à afficher une image virtuelle flottant dans l'espace réel. Ce type d'application est très intéressant : par exemple, afficher un sous-titrage dans une langue étrangère sous le visage de l'interlocuteur pendant une discussion, tout en maintenant le contact visuel, ainsi que bien d'autres usages.

Les lunettes doivent rester légères, avec un facteur de forme comparable à celui de lunettes de vue classiques, tout en intégrant une source d'image (un micro-écran). L'autonomie doit atteindre au moins une journée, et l'image doit rester visible même en extérieur lorsque la luminosité ambiante est élevée.

Dans les solutions conventionnelles, un photon seulement atteint la rétine parmi 10 000 émis. Améliorer significativement ce rendement permet soit d'augmenter l'autonomie, soit d'accroître la brillance de l'image. Notre recherche vise à innover en proposant une solution d'écran proche de l'œil nouvelle, basée sur un circuit photonique intégré et des éléments holographiques jouant un rôle similaire à des micromiroirs : ils dirigent la lumière là où est le besoin.

Avec notre approche, le rendement estimé est d'un photon sur 100. C'est une efficacité 100 fois supérieure à celle des approches conventionnelles.

Ce développement nécessite de valider plusieurs blocs technologiques avant d'obtenir un écran complet. La thèse traite du fonctionnement de ces éléments holographiques, en enregistrant à l'échelle micrométrique des fonctions optiques de type miroir incliné permettant de réfléchir le signal dans des directions précises. La thèse aborde également la question de l'extraction de la lumière, celle-ci étant initialement confinée dans le circuit photonique. Pour la déconfiner vers l'espace libre en direction de l'œil, nous proposons une solution innovante, brevetée, basée sur un effet tunnel puis une redirection du signal depuis le substrat de verre vers l'espace libre. Je développe les bases du principe physique de fonctionnement et en donne une validation expérimentale.

Title in English:

Evaluation of the interaction between waveguides and holograms for the development of directional emitters for Augmented Reality applications

Summary of the thesis in English:

The thesis addresses the challenge of power efficiency in near-eye displays (NEDs). These devices take the form of smart eyewear or headsets with a display. A virtual image is projected into the eye and superimposed onto the real visual field.

For smart eyewear, the projected image must remain visible in bright outdoor conditions, without excessive power consumption or increasing battery size. For a conventional solution using an LCoS (Liquid Crystal on Silicon) with an LED as a primarily source, the optical losses (transmission to the eye) reach about 40 dB: only one photon reaches the retina for every 10 000 photons emitted at the surface of the display.

The miniaturized versions of displays (micro-display), derived from classical screen technologies, exhibit emission properties that are poorly suited to the architecture of near-eye displays. This is because an optical system lies between the eye and the micro-display. It is necessary to think other way around: depending on this application, what new type of display should be developed?

The thesis evaluates a non-conventional micro-display approach based on an integrated photonic circuit (PIC) operating in the visible range, combined with holographic elements (HOE). The emission properties of each pixel are designed to the targeted application; they include control of both emission direction and beam divergence. A laser diode is used as the source, due to its low étendue. Light is distributed across the display surface via a distribution of waveguides. The signal is then extracted into the free space through an active component. After extraction, a micrometer-scale holographic element encoding a reflection function, redirects the beam. The extraction component constitutes the first central topic of my thesis, while the recording of the optical functions in the hologram forms the second.

For this innovative approach, the estimated optical efficiency is around 20 dB, corresponding to a photon gain 100 times higher than that of the conventional approach. For light extraction, the thesis proposes and evaluates an innovative, patented solution. It replaces the diffraction grating approach with an evanescent coupling mechanism between the waveguide and a high-index layer, followed by total internal reflection (TIR) toward free space using a micrometric prismatic structure. The high-index layer is modulated by a ferroelectric liquid crystal, allowing a theoretically achievable switching time below 100 μs.

The thesis analyzes this component in terms of: extraction length, angular divergence, spectral dispersion, polarization of the extracted signal, and other key parameters. Theoretical foundations and a passive demonstration of the principle are provided.

In holography, pixelated holograms are recorded using a holographic printer. A passive NED prototype was developed to demonstrate the relevance of this directional display. This work was awarded the first prize in the Student Optical Design Challenge at SPIE AR|VR|MR 2025.

Keywords in English:

Integrated photonic circuits, holography, micro-displays, near-eye displays

Public-readable summary in English:

Our laboratory conducts research on an innovative and energy efficient image source for smart eyewear and headsets designed for augmented reality (AR) applications. The principle is to project a virtual image that appears to float in the real world. This type of application is particularly interesting: for example, showing subtitles in a foreign language just below the speaker's face during a conversation, while still maintaining eye contact, among many other possible uses.

The glasses must remain lightweight, with a form factor comparable to that of conventional eyeglasses, while integrating an image source (a micro-display). The battery life must last at least a full day, and the image must remain visible even outdoors in bright ambient conditions.

In conventional solutions, only one photon reaches the retina out of 10 000 emitted. Improving this efficiency increases battery life and improves image brightness. Our research aims to innovate by proposing a new micro-display solution based on an integrated photonic circuit combined with holographic elements that act like micromirrors, directing light exactly where it is needed. With our approach, the estimated efficiency is one photon out of 100. This is 100 times higher than the conventional approaches.

This development requires validating several technological building blocks before achieving a complete micro-display. The thesis studies the operating principles of these holographic elements, which record micrometer-scale optical functions acting as tilted mirrors to reflect light in precise directions. The thesis also addresses the challenge of light extraction: the light is initially confined within the photonic circuit, and to extract it into free space toward the eye, we propose an innovative patented solution based on an tunneling mechanism followed by redirection through the glass substrate into free space. I discuss the physical principal of this concept and provide experimental validation.

List of Abbreviations

AR Augmented Reality.

BC Boundary Condition.

CFF Critical Flicker Fusion.

CMOS Complementary Metal-Oxide Semiconductor.

EB EyeBox.

EPE Exit Pupil Expansion.

EQE External Quantum Efficiency.

ER EyeRelief.

FDE Finite Difference Eigen-Mode.

FDTD Finite Difference Time Domain.

FEM Finite Element Method.

FLC Ferroelectric Liquid Crystal.

FoV Field of View.

FWHM Full Width at Half Maximum.

HMD Head-Mounted Display.

HOE Holographic Optical Element.

IPD Interpupillary Distance.

ITO Indium Tin Oxide.

LC Liquid Crystal.

LBS Laser Beam Scanning.

LCoS Liquid Crystal on Silicon.

LD Laser Diode.

LED Light Emitting Diode.

LPCVD Low-Pressure Chemical Vapour Deposition.

MEMS Micro-Electro-Mechanical System.

MLA Microlens Array.

MMI Multi-Mode Interference.

MR Mixed Reality.

MTF Modulation Transfer Function.

NED Near-Eye Display.

NIL Nanoimprint Lithography.

OLED Organic Light Emitting Diode.

OPE Orthogonal Pupil Expander.

PBS Polarizing Beam Splitter.

PECVD Plasma-Enhanced Chemical Vapour Deposition.

PIC Photonic Integrated Circuit.

PPD Pixels Per Degree.

PSM Parallel Stacked Mirror.

RCWA Rigorous Coupled-Wave Analysis.

RI Refractive Index.

Rx Prescription Glasses.

SEM Scanning Electron Microscope.

SiN Silicon Nitride.

SLM Spatial Light Modulator.

SLED Superluminescent LED.

SmC Smectic C Phase.

SSFLC Surface-Stabilized Ferroelectric Liquid Crystal.

TE Transverse Electric.

TIR Total Internal Reflection.

TM Transverse Magnetic.

VBG Volume Bragg Grating.

VR Virtual Reality.

WPE Wall Plug Efficiency.

XR Extended Reality.

n_{eff} Effective refractive index.

Contents

General Introduction **1**

1 Introduction and Context **4**
1.1 Motivation of this Work . . . 5
1.2 Near-Eye Displays: Past, Present and Future . . . 6
1.3 NED Optical Architectures . . . 10
1.4 NED Efficiency: Motivation, Alternatives, and Our Solution . . . 24
1.5 System Design and Requirements . . . 31
1.6 Scope and Purpose of this Research . . . 36
1.7 Conclusion . . . 37

2 Active Component for Light Extraction I **38**
2.1 Total Internal Reflection . . . 39
2.2 Waveguide Mode . . . 41
2.3 Extraction Requirements and Specifications . . . 47
2.4 Diffraction Grating: Conventional Extraction Approach . . . 48
2.5 Evanescent Coupling: Innovative Extraction Approach . . . 58
2.6 Conclusion . . . 74

3 Active Component for Light Extraction II **76**
3.1 Motivation for Liquid Crystal Integration . . . 77
3.2 Active Component for Light Extraction . . . 87
3.3 Results: Passive Extraction Demonstration . . . 102
3.4 Conclusion . . . 113

4 Holographic Pixelization **114**
4.1 Preliminary Physics . . . 115
4.2 Simulations: PSM and Kogelnik . . . 120
4.3 Recording Materials . . . 130
4.4 Holographic Printer . . . 134
4.5 Characterization and Results . . . 138
4.6 Conclusion . . . 143

5 Prototype: Passive Demonstration of Efficiency **144**
5.1 Introduction and Motivation . . . 145
5.2 Preliminary Physics: Radiometric/Photometric Notions . . . 148
5.3 Building Blocks . . . 151
5.4 Characterization and Performance . . . 154

5.5 Conclusion 170

General Conclusion **171**

References **173**

Appendix **190**

A Asymetric coupling **190**

Résumé en français **196**

General Introduction

Our interpretation of the world relies mainly on vision, hearing, and touch. Among these senses, vision plays a central role. Our wide field of view allows us to perceive our surroundings, anticipate potential dangers through peripheral vision, and appreciate the beauty of nature and its colors.

The close relationship between human vision and the field of optics has made optics one of the earliest scientific disciplines. Human beings have long sought to understand optical phenomena, whether in producing fire, interpreting vision, or observing the stars. Inventions such as the telescope and the microscope profoundly expanded our understanding of the world. Over time, light itself became a captivating subject of study, revealing a dual nature that is both wave and particle. Throughout history, optics has been and continues to be a field that inspires curiosity and drives scientific research.

Technological advancements, particularly in display technologies, have significantly transformed our daily lives. Whether it is a computer monitor at work, a television at home, or a smartphone in our pocket, we interact with these visible optical technologies every day. The next major evolution in this field may be near-eye displays (NEDs), which bring the screen close to the eye and integrate virtual information into the real world. This is the principle behind Augmented Reality (AR). Regardless of the commercial trajectory of this technology, from a scientific and engineering perspectives, it presents a fascinating set of challenges. These challenges drive progress in optics field, and the solutions developed can be beneficial for many other applications.

Although older than electronics, optics has progressed more slowly because it faces fundamental physical limits such as diffraction, dispersion, étendue conservation, phase and polarization control, and source integration. These constraints slow down scalability and make efficiency, size, and integration major challenges for NEDs

Current challenges in NEDs include clearly defined use cases, achieving a small form factor, and improving power efficiency. For the use cases, advances in optical hardware, software, and multimodal AI suggest that this technology may become the next major human–machine interface.

Regarding optical hardware, the common approach is to miniaturize existing displays into devices of a size less than a square centimeter and assume that they can directly serve as NEDs sources. In reality, we need to work that backward: we should begin by defining the application and then design a new display technology that best fits its requirements.

This thesis proposes a new display concept based on a photonic integrated circuit (PIC). In the early 1970s, the field of integrated photonics leveraged advances in CMOS microcircuit fabrication to integrate multiple optical functions onto a single chip. The development of optical fiber for data transmission established near-infrared wavelengths as the standard operating domain. This thesis aims to apply integrated photonics within the visible spectrum and combine

it with holography, which enables the encoding of optical functions. This combination forms the central focus of the thesis.

Our display concept is directional; we focus on energy efficiency by considering the path of a photon from its emission at the source to its arrival at the eye pupil. Efficiency is essential for wearable NEDs, enabling lighter devices with smaller batteries while still providing sufficient autonomy for a full day of use and delivering bright images that remain visible outdoors.

This thesis follows the context of a previous project at CEA-Leti. The project brought together several key building blocks: integrated photonics, holography, and liquid crystals. My work investigates how these elements can be combined to meet the requirements of a directional display.

The first chapter recalls the general context. I provide key concepts and definitions related to NED optical architectures, such as microdisplays and combiners. I present a comparison of the main display technologies, with a primary focus on optical efficiency from the display surface to the eye pupil. Emerging technologies are discussed. Our concept of a direction display is introduced along with its main building blocks.

The second chapter discusses light extraction from a waveguide into free space. I briefly recall the definition of waveguide modes and the effective index. I compare a classical solution for light extraction based on a diffraction grating with our innovative approach, which we patented during this work. The extraction requirements and specifications are outlined. The comparison covers the extraction rate, divergence, polarization, wavelength dependence, and other relevant parameters.

The third chapter continues this analysis with a deeper focus on the extraction component considered as an active element. Theoretical elements are presented for ferroelectric liquid crystals. I describe the implementation of the extraction component and the operation of a prismatic structure used for total internal reflection. A passive demonstration using a high-index resin fabricated through nanoimprint lithography is also presented, offering an interesting perspective for future work.

The fourth chapter is dedicated to holography. I present holography and volume Bragg gratings, along with their angular and spectral selectivity. This chapter describes the holographic printer and demonstrate the recording of a reflective optical function inside hologram elements at the micrometer scale.

The fifth chapter presents a NED prototype. It demonstrates an example an example of a passive near-eye display with a static image to illustrate the benefits of a directional display, particularly its impact on the luminance of the virtual image. Some photometric quantities are introduced, including étendue, intensity, and luminance.

Chapter 1

Introduction and Context

Contents

1.1 Motivation of this Work **5**
1.2 Near-Eye Displays: Past, Present and Future **6**
1.2.1 What is a NED/HMD? 6
1.2.2 Historical Evolution of NEDs 7
1.2.3 Reality-Virtuality Continuum 9
1.3 NED Optical Architectures **10**
1.3.1 Human-Centric Design: The Visual System 10
1.3.2 Virtual Image 13
1.3.3 Combiner 14
1.3.4 Micro-displays 16
1.3.5 Micro-LED 17
1.3.6 LCoS 18
1.3.7 LBS 20
1.3.8 Power Consumption 22
1.4 NED Efficiency: Motivation, Alternatives, and Our Solution **24**
1.4.1 Optical Losses in Conventional NEDs 24
1.4.2 Recent Advances: Laser Displays 26
1.4.3 Our Directional Display Concept 28
1.5 System Design and Requirements **31**
1.5.1 Control of the EyeBox 31
1.5.2 Pixel Design and RGB 32
1.5.3 Dimensioning and Process 34
1.6 Scope and Purpose of this Research **36**
1.7 Conclusion **37**

1.1 Motivation of this Work

The context of my PhD research project concerns the development of a *Near-Eye Display* (NED); a type of display system designed to be placed close to the eyes. They are usually mounted on the head in the form of smart glasses or headsets. There are numerous terminologies and taxonomies in this field [1].

An example of a NED is *smart eyewear*, as illustrated in Figure 1.1(a). The role of such devices is to enhance interaction with reality, for instance, through navigation or translation. This type of application is called *Augmented Reality* (AR).

Smart eyewear is closer in *form factor* to prescription glasses than to conventional consumer-electronics headsets. Power consumption and size are key hardware challenges. The path to mass adoption is, for the moment, limited by the use cases. However, advances in optical hardware, software, and multimodal AI are likely to make NEDs the next major human–machine interface.

This thesis focuses on the efficiency of the optical hardware aspect, mainly on the image source (the *micro-display*). Figure 1.1(b) illustrates the optical losses in a conventional NED solution. Out of 10 000 photons emitted at the display surface, only one photon reaches the retina. This corresponds to a loss of 40 dB, or an efficiency of 0.01%.

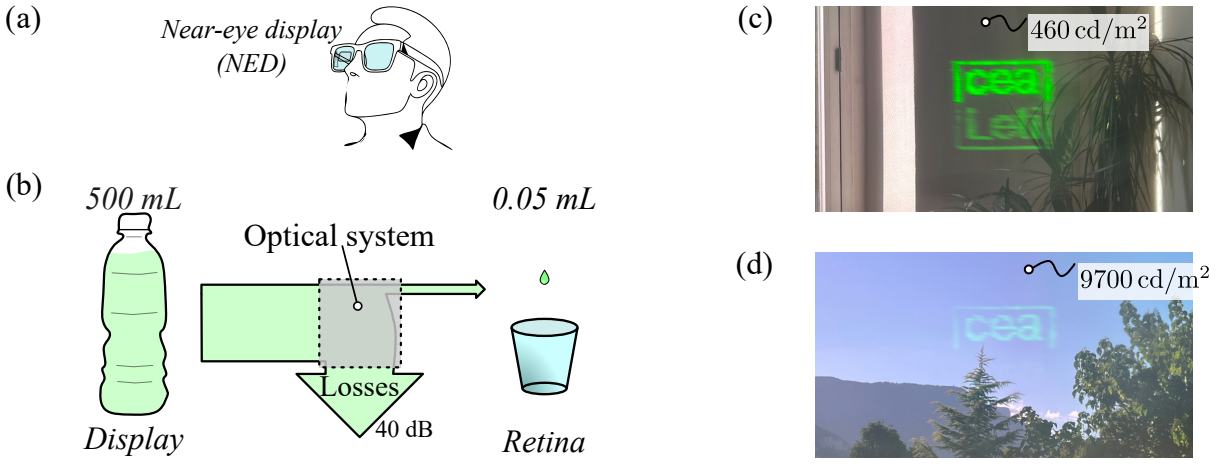

Figure 1.1: (a) NED in the form of smart eyewear; prescription-glasses form factor. (b) Illustration of optical losses in a conventional NED. (c) Photograph of a virtual image through a NED prototype developed in this thesis (see Chapter 5). (d) Same image taken under bright outdoor ambient conditions.

Efficiency is directly related to power consumption. Increasing the number of photons delivered to the retina requires an increase in electrical power input. Improving the efficiency is important for managing power consumption, reducing generated heat [2], and minimizing battery size.

In everyday large displays, such as PC monitors or home TVs, multiple users can view the screen from different angles. Micro-displays in NEDs are miniature versions of these displays, offering similar resolutions but condensed into micrometric pixels. However, they exhibit similar angular properties. In NEDs, there is only a single viewer. Also there is an optical system between the user eye and the micro-display which limits the transmitted optical power. By analogy, the optical system can be likened to a window in a house: the smaller the window, the less light that enters, and consequently, the dimmer the interior becomes.

In Figure 1.1(c), I show a photograph of a NED virtual image developed in this thesis. The

image displays the words “cea” and “Leti”. These two patterns have different angular properties on the display side. In fact, the “cea” pattern is coupled 6–7 times more efficiently than the “Leti” pattern. Under bright ambient conditions, such as outdoors (see Figure 1.1(d)), only the more efficient part remains visible.

In AR applications, the high luminance/brightness (units of *nit* or candela per square meter cd/m^2) of the virtual image is essential for everyday use. However, this must not come at the cost of excessive power consumption. It is important to note that both patterns in Figure 1.1(c) consume the same amount of power, but the upper one is more efficient.

In this chapter, I present the current state of NEDs. The optical principles will be described, and I will review the main types of microdisplays currently in use. Since efficiency is the focus of this thesis, related aspects will be discussed alongside the state of the art. Finally, our proposed solution will be described, including key design elements.

1.2 Near-Eye Displays: Past, Present and Future

1.2.1 What is a NED/HMD?

The purpose of a NED is to form an image on the retina. A NED consists of an image source, such as a display panel, and an optical system that magnifies and projects the virtual image of the display to a distance ranging from a few tens of centimeters to infinity. These elements are mounted on the head. A head-mounted display (HMD) is another term commonly for NED.

Figure 1.2(a) shows a NED architecture in its simplest form [3]. The on-axis schematic corresponds more to virtual headsets. In the case of smart eyewear, the optical hardware can be mounted on the temple of the glasses, and the virtual image is combined with reality using a transparent *combiner* [4, 5], similar to the beam splitter function.

The hardware of a NED can be made more complex by including drive electronics, head and eye tracking, gesture sensing, and other components [1]. The more immersive the NED, the further it diverges from the form factor of prescription glasses.

Figure 1.2(b1) shows the Meta Ray-Ban display. This is a *monocular* NED, meaning that the virtual image is projected onto one eye only. The intended use case is information “snacking”, such as GPS navigation, as illustrated in Figure 1.2(b2). The field of view (FoV) of the virtual image is approximately 20°.

Figure 1.2(c1) shows the other end of the immersion spectrum. This type of device is more like a computer attached to the head, where the digital experience is the more emphasized than the form factor. The FoV is around 100°. Figure 1.2(c2) illustrates a use-case example involving multiple virtual monitors. These monitors are world-locked, meaning the virtual images remain fixed in space. Depending on the use case, either oriented toward information snacking or toward more digital and immersive experience, different form factors can be adopted.

The typical luminance of a PC monitor is around 250 cd/m^2. For smart eyewear, where *see-through* option is important, the virtual image must compete with ambient luminance; otherwise, the image will appear washed out. The required output luminance at the eye, depending on the transmission of the glasses, typically ranges from 1 000 cd/m^2 to 10 000 cd/m^2.

The use case determines the choice of the microdisplay technology. For example, the Apple Vision Pro uses a micro-OLED panel, where the “O” stands for *organic*. This technology is well suited for immersive Virtual Reality (VR), as it provides high contrast, excellent color quality, and fast response time. However, micro-OLEDs have relatively low peak luminance,

and because they are organic, they suffer from burn-in and lifetime degradation under high-luminance operation [6, 7]. For VR, which is a *video see-through* NED (where the outside world is viewed through cameras), the low luminance of OLEDs is not critical.

In contrast, the Meta display uses a microdisplay based on LCoS (Liquid Crystal on Silicon). This type of display is a valve-like solution that requires a primary illumination source. By using an *inorganic* LED for illumination, the display can achieve high luminance, making it suitable for outdoor applications.

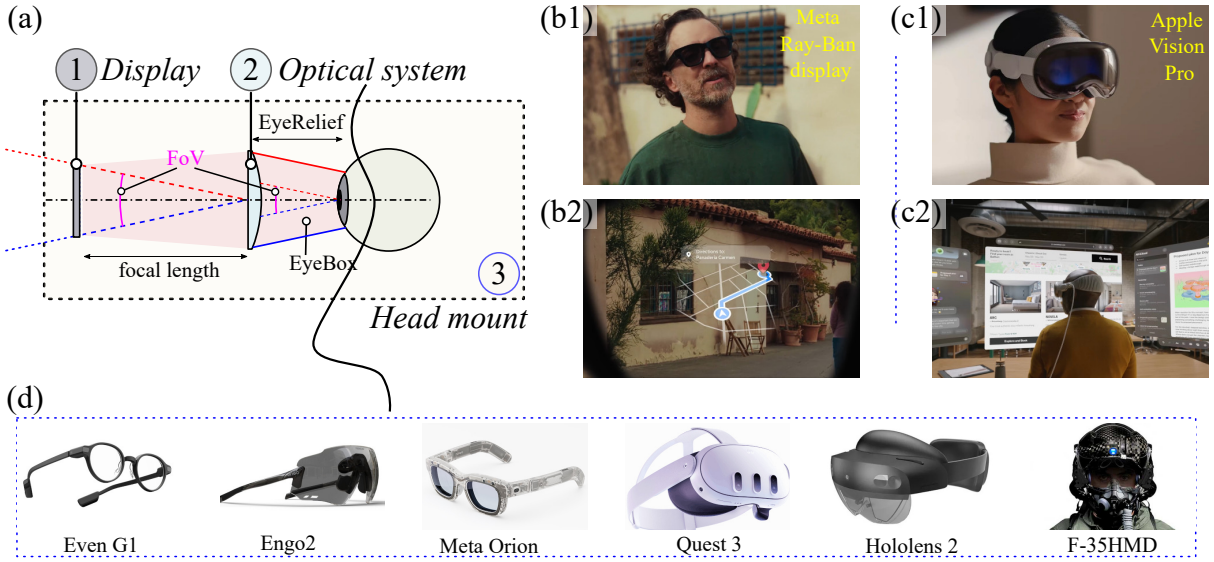

Figure 1.2: (a) Constituent elements of a NED: μdisplay, relay optics, and head mount. (b) Meta Ray-Ban display smart eyewear for information "snacking", such as GPS navigation, versus Apple's Vision Pro headset for mixed reality applications, such as world-locked monitors. (c) Examples of NEDs products. Form factors dictated by the intended application. (Photos courtesy of online sources.)

Figure 1.2(d) shows several consumer, industrial, and military NEDs. The range of use cases is broad, from simple textual information to immersive entertainment, professional training, medical visualization, and military assistance.

The takeaway is that the use case, through parameters such as FoV, resolution, luminance, and combiner efficiency, defines the requirements and determines the choice of microdisplay technology. In this thesis, I investigate an efficient microdisplay capable of delivering high luminance, suitable for smart eyewear and *optical see-through* headsets.

1.2.2 Historical Evolution of NEDs

The invention of the stereoscope by Charles Wheatstone in 1838 [8], using mirrors, and later in 1849 by David Brewster [9], using lenses, marked a breakthrough in the understanding of binocular vision and depth perception. By presenting slightly different images to each eye (binocular disparity), the stereoscope created a convincing illusion of three-dimensionality (perception of depth). Figure 1.3(a) shows illustrations from C. Wheatstone's 1838 paper on the stereoscope and binocular vision [8]. Figure 1.3(b) presents a practical and portable stereoscope developed by D. Brewster.

The invention of displays, marked a next step to make this stereoscope dynamic and interactive. In 1968 [10], Ivan Sutherland used two miniature Cathode Ray Tubes (CRTs), one for

each eye with focusing optics. Half-silvered mirrors in prism combined the images from CRTs with real world (see Figure 1.3(c)). This was the first time the concept of HMD was introduced, lying the foundation for modern AR. Sutherland used a head tracking system using mechanical arm or ultrasonic tracking system. Both were heavy and restrictive and were suspended from the ceiling to the HMD. To describe the bulkiness, the name "Sword of Damocles" was giving later to this first HMD prototype. Sutherland used this system to conduct early experiments in binocular display.

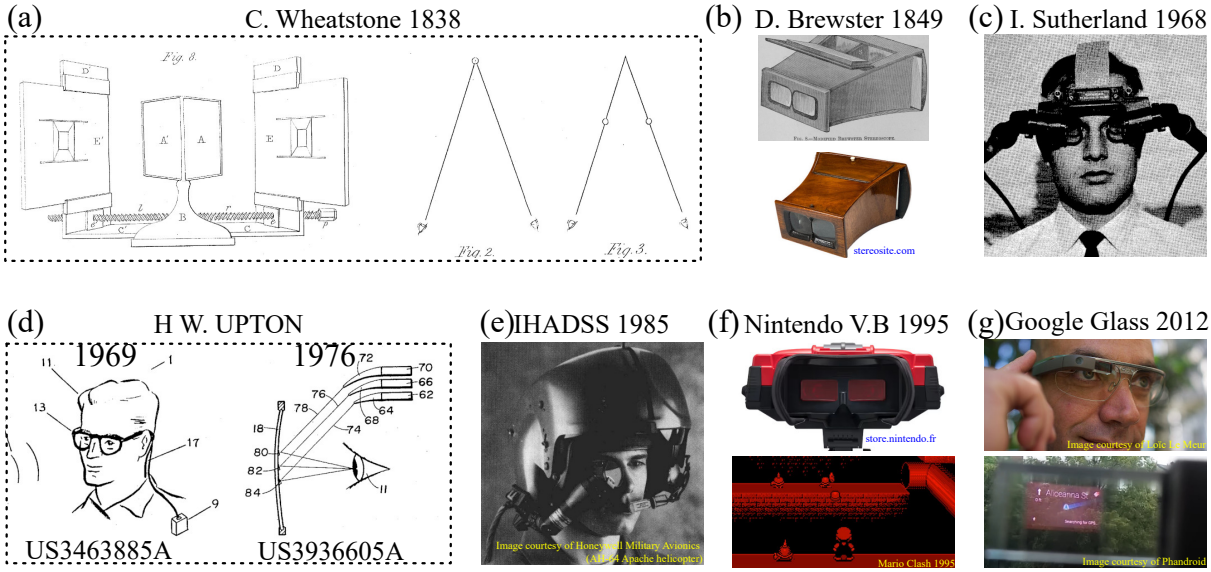

Figure 1.3: (a) Illustration by Charles Wheatstone (1838) of a stereoscope using two mirrors to create the perception of 3D, and an illustration of stereoscopic vision. (b) Brewster's lenticular stereoscope (1849). (c) Ivan Sutherland's head-mounted display (HMD), employing two miniature cathode ray tubes (CRTs). (d) Examples of patents on smart eyewear integrating audio and display functions. (e) Military application of a monocular HMD in the Apache helicopter. (f) Consumer gaming product: Nintendo's Virtual Boy, using a scanning display based on a linear red LED array and oscillating mirror. (g) Consumer smart eyewear: Google Glass monocular display using an LCoS.

Some early patents by Upton [11] describe the use of eyewear to assist people who are hard of hearing or deaf, for applications such as speech-reading (see Figure 1.3(d)). The system could be audio-only (head-mounted speech) or include a display.

Defense was the first application sector of HMD [3]. In 1970s the US military introduced VTAS (Visual Target Acquisition System) for operational flight. It used a standard flight helmet with minimal design to avoid interference with FoV of the pilot. The combiner was a small and semi-transparent visor. Targeting symbols (reticle) was projected onto the visor, allowing the pilot to see the aiming reference combined with the real-world view.

The U.S. Army deployed the first operational monocular HMD (IHADSS, see Figure 1.3(e)) for military use on the Apache helicopter. This system highlighted the importance of this technology, particularly for navigation and weapons delivery.

On early 1980s, US Air Force developed VR HMD for flight cockpit simulations. The Visually Coupled Airborne Systems Simulator (VCASS) provided an extremely large FoV. It used miniature CRTs for their ability to provide high-resolution.

Later on, in 1988, NASA introduced VIEW (Virtual Interface Environment Workstation), a VR HMD using monochromatic liquid crystal displays (LCDs) of 640x200 pixels. Optics

provided a 120-degree FoV per eye. This was an early precursor to modern VR. It was used for telerobotics to remotely control robots.

In the 1990s, VR entered the consumer space [1]. For example, Sega introduced the Sega VR in 1993, and Nintendo released the Virtual Boy in 1995 (see Figure 1.3(f)).

Google introduced AR to the public through Google Glass in 2012 (see Figure 1.3(g)). It used an LCoS microdisplay, and the FoV was about 15° diagonal [1]. This was the first attempt for smart eyewear, but it lacked public acceptance.

Between 2016 and 2019, increased attention was given to industrial use cases, with devices such as the HoloLens by Microsoft and the Magic Leap. The COVID-19 pandemic in 2020 further boosted interest in NED applications.

In late 2024, Meta introduced *Orion*, a binocular immersive smart eyewear prototype designed as a technology demonstrator. This NED integrates emerging components such as a microLED (inorganic LED) display and a diffractive lightguide combiner based on high-refractive-index silicon carbide (SiC). Rather than a commercial product, *Orion* was intended to illustrate the potential of future NEDs and to highlight the technological advances still required for practical deployment. The estimated prototype cost was approximately $10,000. One year later, Meta released the Ray-Ban monocular display to familiarize consumers with smart eyewear.

1.2.3 Reality-Virtuality Continuum

Different taxonomies are used to classify the various types of NEDs, which can lead to confusion. A unified framework helps establish clarity when comparing systems, especially across different research areas.

In 1995, Milgram [12] proposed a classification defined along a continuum, with the real world at one end and the virtual world at the other.

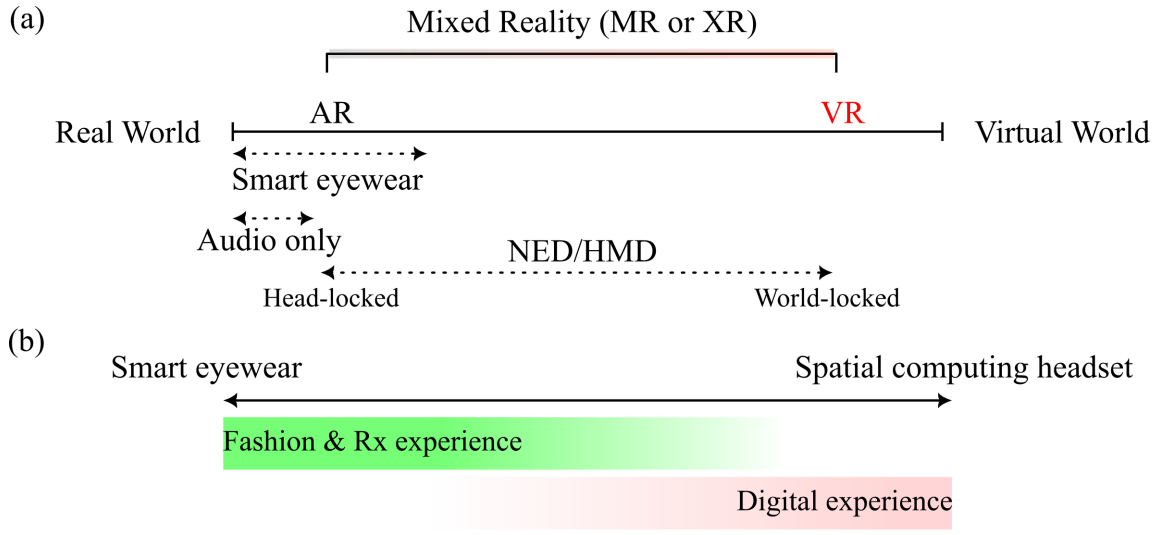

Figure 1.4: (a) Illustration of the reality–virtuality continuum, showing the transition from the real world to the virtual world through augmented reality (AR), mixed reality (MR), and virtual reality (VR), inspired by Milgram (1995). (b) Simplified representation of the spectrum from smart eyewear to spatial computing headsets, highlighting the overlap between fashion and prescription glasses (Rx) and digital experiences.

Along this continuum (see Figure 1.4(a)), we find Augmented Reality (AR) and Virtual Reality (VR). Mixed Reality (MR) represents a combination of real and virtual worlds. AR provides a direct view of the real environment with virtual elements that can be head-locked; as the user moves their head, the virtual image moves accordingly. VR, on the other hand, offers complete immersion in a fully virtual, simulated environment. In MR, the level of presence lies between AR and VR, where virtual objects can be world-locked and remain fixed relative to the real world. Access to the real world can occur through video rather than a direct optical see-through view. Video see-through is more of VR than MR.

All these classifications fall under the category of NEDs. Audio eyewear is included as a first step before NEDs, showing the gradual transition from audio to visual augmentation.

In Figure 1.4(b), a classification from B. Kress* presents a more simplified version tailored for consumers. Smart eyewear should be more aesthetic and comfortable, with a prescription-glasses form factor. In this type of NED, efficiency is crucial, as the eyewear must support a full day of use on a single charge. On the other hand, head-worn headsets prioritize the digital experience and are typically intended for indoor use.

1.3 NED Optical Architectures

1.3.1 Human-Centric Design: The Visual System

Human factors are at the center of NED design. These factors span multiple domains: the visual system at the core [13], biomechanics (including the head and neck), anthropometric variables [14, 15] (such as interpupillary distance, head width, etc.), and even social factors (such as discretion and style). Together, these factors drive the specifications and constraints that guide the design of a near-eye display.

In this section, I discuss several human factors related to the visual system [1, 16–22]. Understanding the specifics of human vision is essential and can be used as an advantage to reduce complexity and avoid overdesigning the NED beyond the limits of human visual needs [13].

Our interpretation of the world is spatial, but our visual system is based on angular characteristics. In Figure 1.5(a), we show a schematic of the eye in which the fundamental angular contributions are illustrated. The angle β represents the eye rotation. The rotation of both eyes to focus on the same object is called *vergence*. This allows binocular vision and depth perception.

The angle γ illustrates *accommodation*, where the lens changes shape to focus objects at different distances onto the retina. The human eye can focus on objects as close as 10 diopters, this ability declines with age (presbyopia).

The angle α represents the convergence of the optical signal on the retina. It determines the *resolution* (or visual acuity); the ability of the eye to resolve small features. The resolution is highest at the center of gaze, the *fovea*, where the cone density is greatest, allowing for a spatial resolution of approximately 1 arcminute (1/60 degree). This corresponds to about 60 pixels per degree (PPD), or equivalently, 30 cycles per degree. Visual acuity decreases rapidly with eccentricity; as we move away from the fovea (> 2–3°) [1].

The angle θ represents the location of image details in the *Field of View* around the fovea. The FoV describes the angular extent of the observable scene. Eye and head rotations can

*SPIE AR|VR|MR Fireside Chat

increase the FoV.

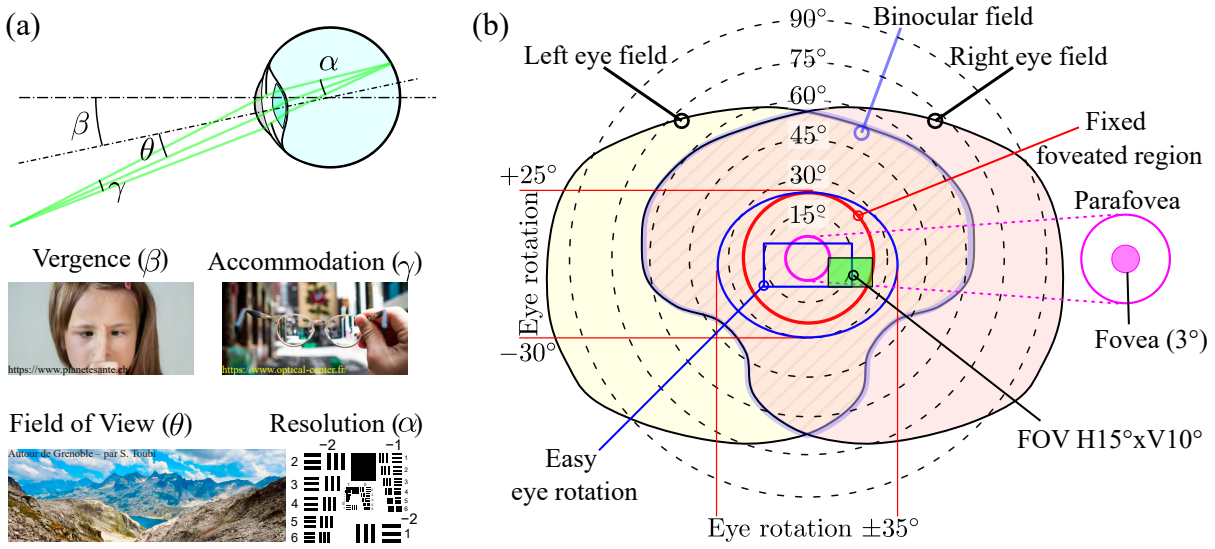

Figure 1.5: (a) Human vision is characterized by angular parameters including vergence (eye rotation), accommodation (focus), Field of View (observable extent), and resolution (smallest distinguishable angular size). (b) Human field of vision and binocular vision represented in a polar plot. The center corresponds to the direction of gaze without eye or head movement.

If you consider a standard smartphone with a screen size of 70×146 mm^2 and a resolution of 1179×2256 pixels viewed at a distance of 40 cm, it subtends an FoV of $\approx 10° \times 20°$. This corresponds to a horizontal resolution of approximately 118 PPD (i.e., 0.5 arcmin per pixel). This value is above the visual acuity of 60 PPD (20/20 vision), which is good. However, for a NED, there is no need to exceed this limit, as it would simply result in overdesign.

The resolution in a NED is determined not only by the pixel density of the microdisplay, but also by how these pixels are stretched angularly over the FoV of the virtual image. If we consider the Apple Vision pro headset with a microdisplay of 3660×3200 pixels per eye and a horizontal resulting FoV of 100°, we obtain a virtual image resolution of approximately $\approx$ 37 PPD (i.e., 1.6 arcmin per pixel). This is low but acceptable as an angular resolution.

Retinal resolution is not a single fixed number; it depends on color, contrast, eccentricity, and the observer. A recent study [23] suggests human resolution limits of up to 94 PPD for achromatic patterns, which is significantly higher than the commonly known value of 60 PPD.

Figure 1.5(b) shows the binocular FoV of the human eyes. This schematic was adapted from [16, 24]. Two regions overlap: the left-eye and right-eye monocular FoVs.

For a single eye, the monocular FoV extends about 60° toward the nose and approximately 100° toward the temple. The total horizontal (H) FoV of both eyes together is therefore around 200°. In the vertical (V) direction, the FoV extends roughly 60° upward (toward the forehead) and about 75° downward (toward the cheeks), resulting in a total vertical FoV of approximately 135°. The binocular FoV is roughly 120° horizontally (and symmetric) and around 130° vertically (and asymmetric).

At the center, a circle indicates the parafovea, with the fovea located in the middle. Note that the human FoV is dynamic, as both the eyes and head can rotate. In the illustration of this polar plot, the gaze is fixed at the center, corresponding to the position of the fovea. Horizontally, the eyes can rotate by about ±35° to change gaze [25], while vertical eye rotation ranges from

+25° (upward) to -35° (downward) [16]. The unconstrained eye rotation, without compensatory head movement, is shown by a red circle that defines the fixed foveated region. A blue rectangle indicates the range of easy eye rotation[†].

In the plot, an example of a monocular smart eyewear with a FoV of 15° × 10° is overlaid in the right-eye field. The virtual image is positioned with an offset from the center to help reduce distraction and eye strain. Eye strain from monocular NEDs can arise due to binocular rivalry, where one eye perceives the display while the other does not. Proper positioning of the monocular image, especially for daily wear, can be very important [26].

Table 1.1: Summary of some key human visual parameters relevant to NED design.

Visual acuity [1]	60 PPD (1 arcmin or 30 cycles/°)	"20/20" vision benchmark
Acuity for NED [1]	>45 PPD	Decent angular resolution starts at 45 PPD for people in their 20s–30s
Interpupillary distance (IPD) [1]	Mean 63 mm (range 50–75 mm)	NED must support population coverage Decent EyeBox ≥10 mm (H) × 8 mm (V)
Vergence–Accommodation Conflict (VAC) [1, 27]	≤0.5 diopter (comfortable limit)	Controls fatigue; core ergonomic constraint
Luminance (Brightness) [1]	Indoor: 500–1000 nit (cd/m^2); Outdoor: >3000 nit	Brightness required for outdoor visibility depend on the transmission of the NED
Equivalent of 1 W for human sensitivity	530 $nm \rightarrow$ 589 lm / 640 $nm \rightarrow$ 120 lm / 450 $nm \rightarrow$ 26 $lumen$	Values for photopic vision. Green appears much brighter for the same optical power
Color in hight ambient environment [28]	Blue performs worst	Text contrast for blue is low even at high brightness
Critical Flicker Fusion (CFF) [20]	60–90 Hz (bright) 30–50 Hz (dim)	Depends on luminance and retinal eccentricity
Laser safety for laser display eg. LBS [29]	MPE: a few μW to 10 μW entering the pupil of the eye	Depends on exposure time, wavelength, and mode (continuous or pulsed); standards: EN 60825, ANSI Z136.1
Ocular dominance [30]	70% of population are right-eye dominant	Display should be on the right eye for monocular NEDs

Table 1.1 summarizes several parameters relevant to NED design, such as visual acuity, interpupillary distance (IPD), and others. For further reading on human vision, see John E. Greivenkamp's *Visual Optics*.[‡]

Flicker is the perceived fluctuation (*papillotement*) in brightness that occurs when light intensity is modulated in time. The critical flicker fusion frequency for steady perception is typically around or above 50 Hz [31]. For continuous motion, a display should operate at least at 25 Hz. Thus, our display should operate at a minimum of 50 Hz to ensure both brightness stability (retinal) and motion continuity (cortical).

Two key takeaway elements are the angular resolution, which depends on the FoV and determines the pixel pitch, and the refresh rate of the display, which must be high enough to avoid flicker. These two elements will be relevant later on.

[†] https://lucaskazansky.com/Design-informed-by-Human-Factors

[‡] John E. Greivenkamp, *Visual Optics* — MIL-HDBK-141.

1.3.2 Virtual Image

The optical principle of NED is illustrated in the virtual image formation shown in Figure 1.6(a). Each pixel position on the display corresponds to a specific angle of parallel rays in front of the eye. The two extreme pixels and their corresponding rays define the FoV. The FoV is contained within this angular span, which determines the apparent size of the virtual image. The FoV depends on both the display size and the focal length of the optical system. In this illustration, the lens is assumed to produce parallel rays, corresponding to a virtual image at infinity.

The full EyeBox (EB) corresponds to the intersection of the fields of all pixels. Within this 3D space, the full image is visible. A large EB allows comfortable viewing. The EB is commonly defined as a surface at a fixed distance from the lens (EyeRelief). In this schematic, the lens acts as the limiting aperture. The EB decreases as the EyeRelief increases.

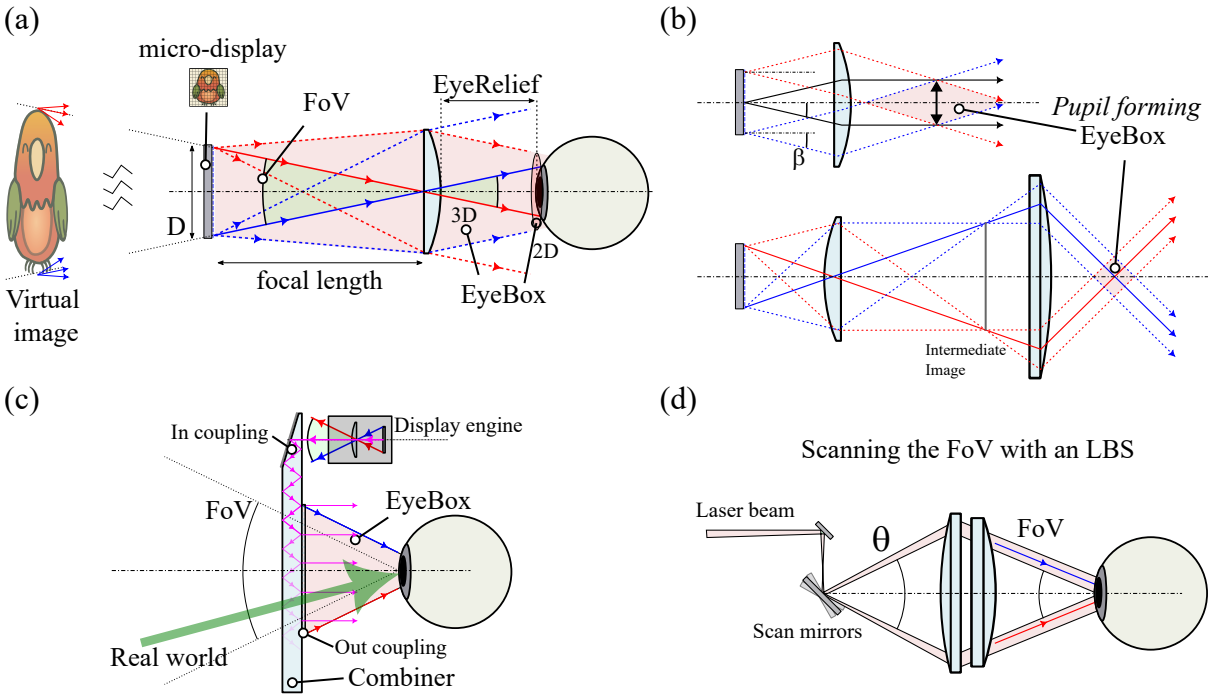

Figure 1.6: (a) Illustration of virtual image formation in a NED and related elements: FoV, EyeBox, and EyeRelief. (b) Example of a simple pupil-forming system. (c) Light-guide combiner. (d) Virtual image formation based on scanning display.

Figure 1.6(b) shows the EB in a pupil-forming system, where the output rays are confined to a minimum diameter after the lens (the shaded diamond area) [32]. In the first, the object rays have a small field angle β and are not limited by the lens aperture. As β increases, the EB expands and the minimum diameter shifts toward the lens, returning to the situation shown in (a), which corresponds to a non–pupil-forming system. By adding a second lens, it is possible to have a pupil-forming, as shown in the second schematic in (b). This is known as a compound microscope configuration; however, it increases the length of the optical system.

The EB must have a diameter larger than the eye pupil and account for IPD and potential eye rotation when scanning the FoV. The human eye pupil typically ranges from 2 mm to 7 mm in diameter, depending on the ambient light level. A minimum EB size can be around 10 mm^2.

For a non–pupil-forming system, the EB can be increased by enlarging the lens diameter,

though this trade-off increases the overall system volume. Note that as the FoV increases, the EB becomes smaller at the EyeRelief position.

For pupil-forming systems, such as in (b), the advantages include a well-defined EB, adjustability with EyeRelief, uniform brightness, and reduced vignetting. However, such systems can require additional optical elements. As will be shown later, in our *directional display*, even with a single lens, a pupil-forming configuration can be achieved by tilting the pixel emission angles.

There is a trade-off between EB size and efficiency. As the EB increases, the rays are spread over a larger area, thus reducing the luminance of the virtual image. Increasing the luminance would therefore require increasing the optical power.

Figure 1.6(c) introduces the concept of a lightguide *combiner*. The *display engine* consists of the microdisplay and the relay optics (for collimation). The virtual image is contained within the cone of rays that defines the FoV. These rays are coupled into a glass substrate through total internal reflection (TIR) and are extracted at the outcoupling zone in front of the eye. Each ray angle corresponds to a specific pixel position in the image. The lightguide is also transmissive to the real world, allowing the virtual and real wolds to be combined.

Figure 1.6(d) shows the principle of a scanning display. The virtual image is formed directly by scanning the angular rays; no matrix display is needed. A single collimated point source is angularly scanned using mirrors. The image can be scanned directly onto the retina if the beam waist is smaller than the eye pupil (Maxwellian view display [33, 34]). This type of scanning display will be referred to as laser beam scanning (LBS).

1.3.3 Combiner

The role of the combiner is to merge the real and virtual worlds. Designing a combiner is challenging, as it must manage the rays of the FoV, handle color (RGB), and remain sufficiently transparent to the real world. Combiners rely on one or a combination of reflection, refraction, and diffraction. All of these can depend on wavelength and angle through dispersion and efficiency. A combiner should not degrade the quality and color uniformity of the virtual image.

Combiners can be divided into three families: waveguides, free-space, and free-form prisms [1]. The term *waveguide* is often used in this NED field, although these structures function more accurately as lightguides through multiple TIR. The waveguides related to wave theory are discussed in Chapters 2 and 3, as our display principle is based on a photonic integrated circuit. I will refer to the multiple–TIR-based combiners as lightguides and not as waveguides [5, 35–37].

In Figure 1.7(a), we have two types of lightguide combiners: geometric (reflective) and diffractive. The in-coupling element can be a prism, a diffraction grating, or a transmission or reflection hologram. These elements redirect the FoV rays into the TIR domain. The refractive index (RI) of the lightguide sets the TIR domain through the critical angle. As the RI increases, a larger FoV can be trapped by TIR. On the extraction side, we have out-coupling elements; in the schematic, these can be partial reflectors or leaky out-coupling gratings. The rays are split, which helps to increase the EB size. Note that some leakage can occur in the opposite direction, which is not shown here. This is especially true for symmetric binary gratings, causing "eyeglow".

The display engine is very small in smart eyewear. Consequently, the exit pupil of the relay optics can be small. Figure 1.7(b) shows a schematic of exit pupil replication used to overcome

this limitation. This is also known as exit pupil expansion (EPE). After coupling in one direction, the rays are partially split, while some of them are redirected downward. The out-coupler then partially extracts the rays toward the eye. This creates multiple copies of the display engine exit pupil, resulting in a larger and more comfortable EB.

Figure 1.7(c) shows an example of a free-space combiner, known as a *birdbath* combiner. In this example, the system is monolithic; made from a single piece of plastic or glass. The architecture includes an LCoS microdisplay illuminated by an LED source. A PBS (polarizing beam splitter) polarizes the illumination by filtering out one polarization (for example, "s"). The LCoS pixels operate by rotating the linear polarization from "p" to "s". The reflected pixel rays are collimated by a curved reflector, and a second reflector (a simple beam splitter) directs the rays toward the eye, acting as the combiner.

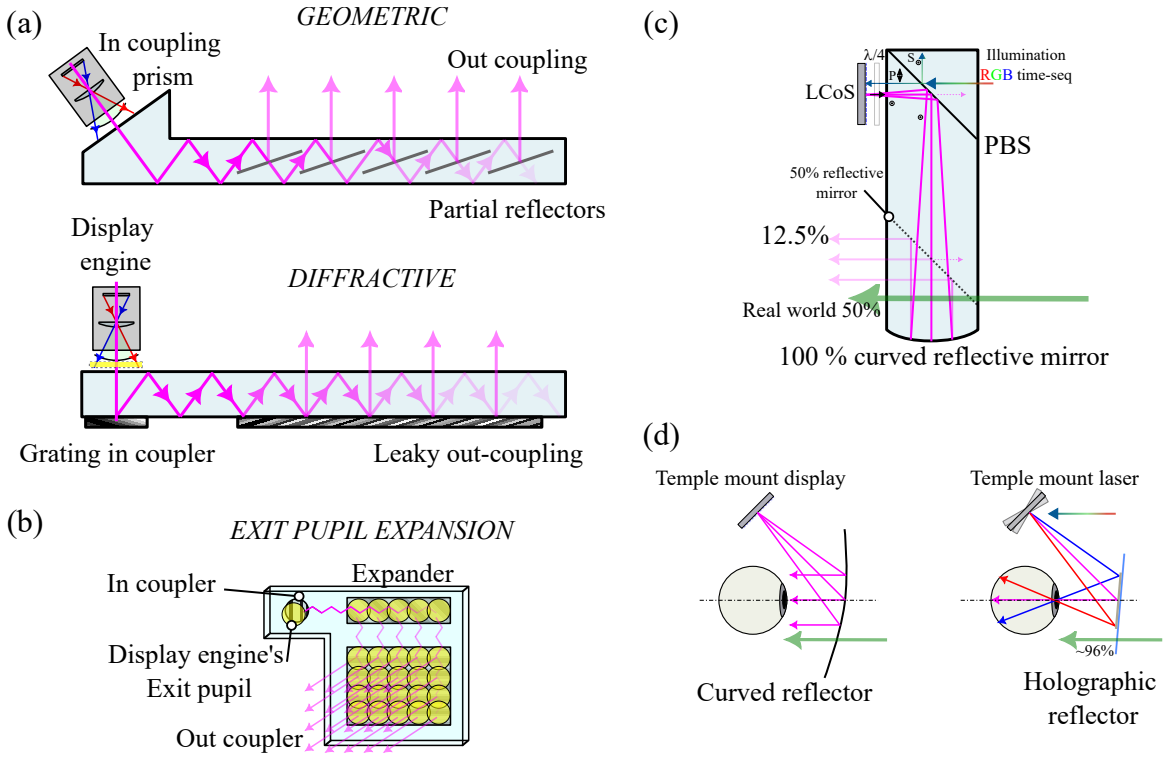

Figure 1.7: (a) Multiple TIR combiners (lightguides): geometric and diffractive types (known as "waveguides"). (b) Enlargement of the EyeBox by expanding the exit pupil through splitting (copying) the display engine's exit pupil. (c) Google Glass free-space combiner based on a beamsplitter (birdbath configuration). (d) Free-space combiners such as curved and holographic reflectors.

Figure 1.7(d) shows another example of a free-space combiner, such as a curved reflector that collimates the microdisplay rays toward the eye. The reflector can also be holographic. In this example, I show a Maxwellian-view type that scans the FoV directly onto the retina. In the chapter 5 with our passive prototype, we will use a simple holographic free-space combiner that collimates the rays toward the eye.

Free-form prism combiners are not shown here; however, in principle, they can employ one or more TIR on free-form surfaces that also provide optical power for collimation. For the transmitted (see-through) path, an additional surface can act as a compensator to correct the external rays.

1.3.4 Micro-displays

The image sources of NEDs can be divided into emissive and non-emissive types [6, 38, 39]. Emissive displays are self-emissive, meaning that each pixel emits light directly. In contrast, non-emissive displays modulate or steer the light from an external illumination source. Figure 1.8 summarizes the typical technologies used for NEDs [1].

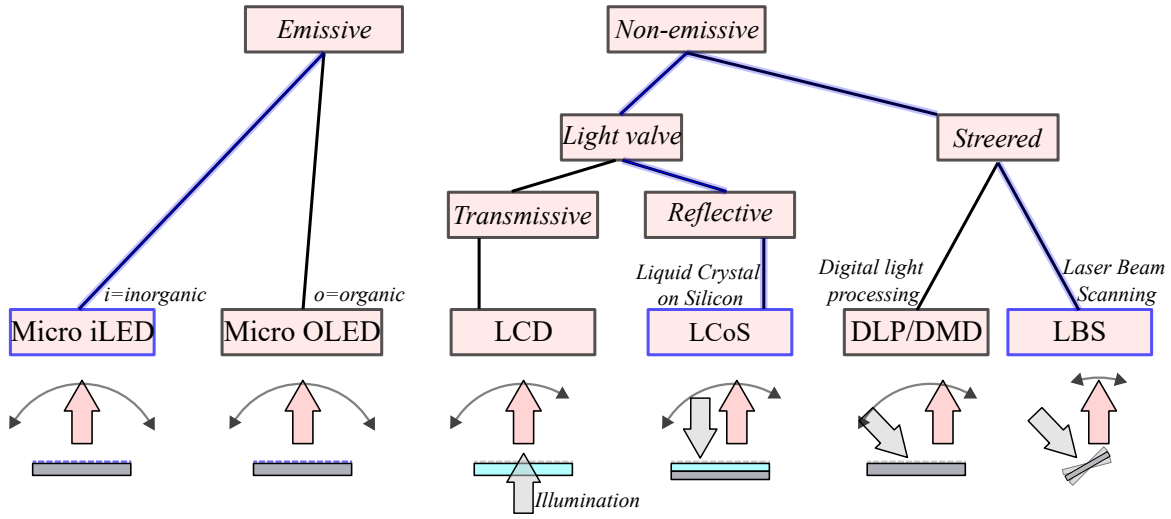

Figure 1.8: Microdisplay technologies used in near-eye displays.

For the emissive type, the main technologies are inorganic and organic light-emitting diodes, denoted as *µLED* and *µOLED*, respectively. The emission in both cases is wide, as it originates from spontaneous emission and follows a Lambertian profile after light extraction. A Lambertian source exhibits constant luminance over a wide observation angle. The µLED emission [40–42] can slightly deviate from the Lambertian intensity profile ($I(\theta) = I_0 \cos(\theta)$) due to the geometry of the emitter. µLEDs can provide high brightness without significant degradation compared to organic µOLEDs. µOLEDs are typically used in mixed-reality (MR) video see-through systems or in AR systems with highly efficient combiners and very low transmission of the real world. In this work, we consider only µLEDs as a competitor for comparison with our directional laser-based solution.

For the non-emissive type, light-valve displays modulate the intensity through polarization control using liquid crystals (LC) and polarizers that absorb light. These include transmissive microdisplays such as LCDs (liquid crystal displays) and reflective ones, such as LCoS (liquid-crystal-on-silicon). The emission properties are determined by the illumination source. Such systems can achieve high brightness when illuminated by inorganic LEDs used as backlights or frontlights. LCoS is a mature technology that continues to evolve and is currently the most suitable solution for full-color microdisplays in smart eyewear. LCD panels, on the other hand, are more commonly used in VR headsets. In this work, we keep LCoS, as it is driven by a silicon backplane that enables a small pixel pitch and therefore high resolution within a compact area.

For the steered type, we have the digital micromirror device (DMD) technology, also known as DLP (digital light processing) from Texas Instruments [43]. The DMD is a microelectromechanical system (MEMS) device consisting of a pixelated array of tilting mirrors that switch between ON and OFF states to reflect the incident light. The illumination scheme differs from that of LCoS and does not rely on polarization control; instead, it uses a combination of the

incidence angle and TIR to separate the illumination path from the reflected image signal. DLP can achieve more than twice the brightness of LCoS, as it does not require polarization filtering of the LED illumination. However, polarized light is more desirable for lightguide combiners, since certain optical elements, such as diffractive couplers, are polarization-dependent. DLP systems often require bulky illumination optics, which limit their suitability for compact smart eyewear. However, they are well suited for use in headsets, microprojectors, head-up displays, and as spatial light modulators [6].

Laser beam scanning (LBS) is a steering solution based on MEMS oscillating mirrors that rotate to change the angle of a laser beam. The mirror motion can be driven by electrostatic, piezoelectric, or electromagnetic (Lorentz force) actuation. The image is formed by sequentially scanning FoV following a principle similar to that of a traditional cathode-ray tube (CRT) display. LBS is compact, bright, and highly efficient. This type, along with μLED and LCoS, is considered one of the main display technologies to be compared with our proposed solution. In the following sections, I will discuss their advantages, operating principle, and power consumption.

1.3.5 Micro-LED

The μLED is a miniature inorganic light-emitting diode that emits light when electrons and holes recombine radiatively inside InGaN/GaN multiple quantum wells (MQWs) [44]. Figure 1.9(a) illustrates the classification of LED, miniLED, and μLED technologies. For μLEDs, the pixel pitch can be as small as a few micrometers. The color, or emitted photon energy, depends on the semiconductor bandgap. For example, InGaN can be used for blue and green emission, where the indium (In) composition helps to reduce the bandgap energy. Red emission can, in principle, be obtained by further increasing the indium content; however, the radiative recombination efficiency decreases drastically due to the formation of defects and strain in the high-indium InGaN layer. Therefore, alternative materials such as AlGaInP are preferred for red μLEDs. Achieving monolithic integration of RGB μLEDs remains one of the main challenges in μLED fabrication [45].

Figure 1.9(b) illustrates the process known as *pick-and-place* of subpixels. In this approach, RGB panels are separately fabricated, each using the most efficient materials for its corresponding color. The process begins with the epitaxial growth of InGaN/GaN (for example) on sapphire, SiC, or silicon substrates. After patterning through etching and surface passivation, the μLED pixels are picked and placed onto a CMOS backplane. For RGB panel, this step requires precise alignment, which increases process complexity and reduces yield [45].

Monolithic RGB integration, where all colors are based on InGaN, suffers from low red emission efficiency. In the other hand, transferring and aligning separate RGB μLEDs remains a complex and yield-limited process.

A single-color panel, such as green, as shown in Figure 1.9(c), can be practical for applications such as military, industrial, or even consumer use for info-snacking.

Current approaches for achieving full color are based on either using three separate RGB panels or employing color-conversion methods [38, 45–49].

Figure 1.9(d) shows the X-cube approach for combining the three colors [47]. This approach also can suffers from alignment and yield challenges, and increased optical volume. Figure 1.9(e) illustrates the principle of quantum-dot (QD) color conversion, where a blue μLED panel excites red and green QDs. However, QD-based conversion can suffer from efficiency losses, blue light

leakage, and QD aging. Figure 1.9(f) shows an alternative configuration where three panels are used in parallel, each coupled into the lightguide combiner through its own incoupler. However, this design results in a larger lateral size.

The external quantum efficiency (EQE) in μLEDs is low and is strongly size dependent [50, 51]. EQE describes the conversion efficiency of injected electrons into photons escaping from the device. The EQE decreases for smaller μLEDs due to surface non-radiative recombination. As the emitter size is reduced, the surface-to-volume ratio increases, leading to a higher density of surface defects and reduced radiative recombination.

Figure 1.9(g) shows the EQE as a function of the μLED size. The EQE drop is less pronounced for green due to the higher indium content in the InGaN [52].

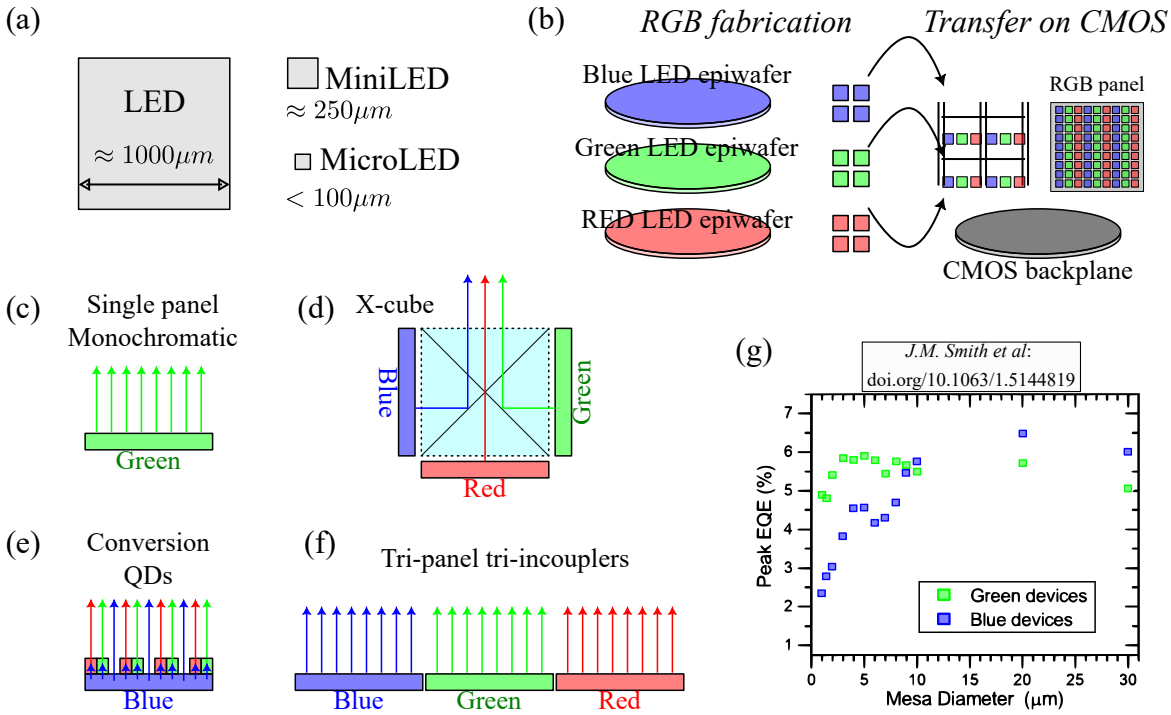

Figure 1.9: (a) LED size classifications. (b) Fabrication process of a full-color microLED display panel through pick-and-place transfer from separate panels. (c) Single-panel monochrome microLED display. (d) RGB combination using X-Cube and tri-panel approaches. (e) RGB generation through quantum dot color conversion of a blue panel. (f) Three separate panels for RGB. (g) Size dependence of microLED external quantum efficiency (EQE).

1.3.6 LCoS

Liquid Crystal (LC) on Silicon uses an active matrix liquid crystal display (LCD) on a reflective silicon backplane[§]. Figure 1.10(a) illustrates the operating principle of amplitude modulation. The incident polarized illumination is modulated in intensity: each pixel locally rotates the polarization of the reflected light, which is then either transmitted or absorbed by the output polarizer or blocked by a PBS. The modulation occurs through phase retardation caused by the LC birefringence and orientation [53–55].

[§] Avegant's White Paper LCoS vs MicroLED

Figure 1.10(b) illustrates the activation of a pixel. The incident polarized light is reflected by the polarizing beam splitter (PBS) and passes through the LC pixel, which acts as a $\lambda/4$ retarder. The linear polarization is converted into circular polarization. After reflection by the mirror, the light passes through the $\lambda/4$ layer again, converting the circular polarization back into linear polarization with an orthogonal orientation. This rotated polarization is transmitted by the PBS, resulting in a bright pixel. For a dark pixel, the LC does not introduce a $\lambda/4$ retardation. In LCoS displays, colors are usually generated using time-sequential RGB LED illumination. The color frames are merged by visual persistence to produce a full-color image. The illumination module can merge the RGB LED light using an X-cube or a homogenizer. Figure 1.10(c) shows a conventional LCoS architecture with a PBS cube, and on the right, an illustration of an illumination system.

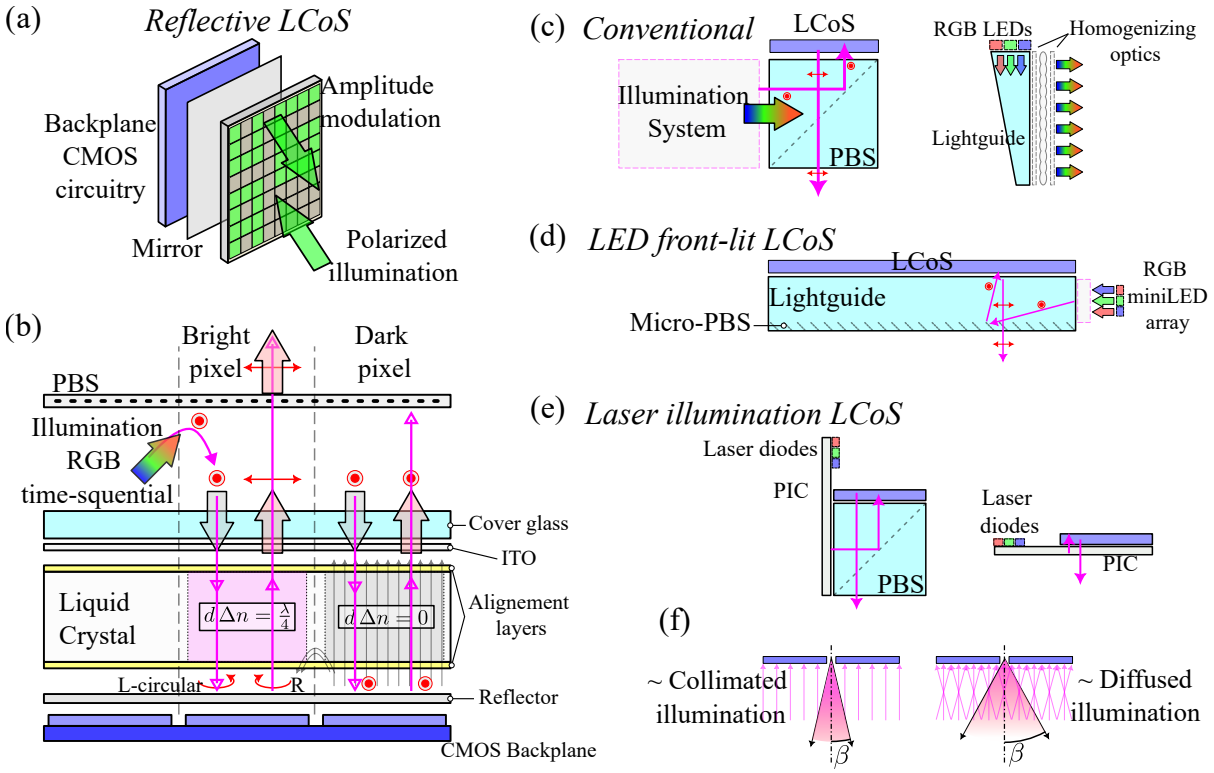

Figure 1.10: (a) Schematic of an LCoS panel (light-valve type display). (b) Operating principle of LCoS pixels based on amplitude modulation. (c) Conventional LCoS system using backlit illumination and a PBS; on the right, schematic of an illumination lightguide using RGB LEDs. (d) Front-lit LED illumination using a micro-PBS, a lightguide, and miniLEDs (Himax). (e) Laser backlit illumination (Vitrealab) and front-lit laser illumination (Meta). (f) Pixel divergence in LCoS displays depends on illumination and is diffraction-limited.

The conventional configuration in (c) will be referred to as a "*back-lit*" illumination setup. The role of the PBS here is polarization filtering, similar to the function of crossed polarizer films in LCDs. However, the PBS increases the overall volume of the display engine[¶].

Other smaller illumination exist[‖] [56]. Figure 1.10(d) shows a compact illumination system from Himax [57–59], which uses a light-guide and micro-PBSs. This configuration is a *front-lit*

[¶] Omnivision's OP03011

[‖] Avegant's AG-30L2 specifications

illumination scheme based on miniLEDs.

Figure 1.10(e) shows some emerging LCoS technologies based on *laser* illumination. PIC stands for *Photonic Integrated Circuit* [60]. The circuit, or chip, distributes visible light from laser diode sources through a network of waveguides, where the light is guided; typically in single-mode waveguides.

The example with the PBS cube is from VitreaLab[**], whose waveguides are fabricated via femtosecond direct laser writing. The guided light is outcoupled into free space using nano-imprinted micromirrors. To the right in (e) is an illustration from the aricle of Meta [61], showing a PIC-based illumination system without a PBS cube. Meta used waveguides fabricated through a CMOS-compatible process using silicon nitride (SiN) on glass (SiO_2). Light is outcoupled using diffractive gratings.

Laser-based illumination is particularly interesting because it provides intrinsically polarized light for LCoS illumination, high color purity, and high directionality from the laser sources (low étendue). In our directional display concept, we also employ a PIC-based approach.

The pixel divergence in LCoS depends on the illumination, which is an advantage. This is illustrated in Figure 1.10(f) by the divergence angle β. For example, if the illumination is perfectly collimated, the divergence is diffraction-limited by the pixel size. However, if the illumination has a large étendue, the divergence becomes wider than the diffraction limit.

LCoS pixel pitch can be as small as 3–5 μm. Another emerging technology is F-LCoS [62, 63], which is based on ferroelectric liquid crystals (FLCs). I describe FLCs more in details in the chapter 3. This type offers faster response times and helps reduce color breakup in the image caused by time-sequential illumination. Pixel sizes can reach 1.5 μm since FLCs are less sensitive to pixel crosstalk (fringe field effects) compared to nematic LCs.

Similar to local dimming in LCDs, emerging approaches are being developed to increase the efficiency and contrast of LCoS displays, such as zonal illumination by Meta [61, 64] and adaptive LED illumination by Avegant [65].

1.3.7 LBS

LBS is a laser-based display technology [66–68]. The image is formed through a scanning process, which allows a large FoV to be obtained with a small footprint.

The beam is generated using an RGB laser module [69, 70]. Figure 1.11(a) illustrates the laser module, where the individual beams from the laser diodes (LDs) are collimated and combined using dichroic mirrors, resulting in a coaxial RGB beam. This beam is then scanned using MEMS mirrors to form the image. Since the LDs can be switched in parallel to produce the colors, no time-sequential operation is required as in LCoS displays.

Figure 1.11(b) shows the scanning process. Two architectures are presented [71, 72]: the first forms the 2D image using two 1D monoaxial MEMS mirrors, while the second employs a single 2D biaxial MEMS mirror [73]. The FoV is proportional to the mirror deflection angle.

Figure 1.11(c) shows the 2D scanning operation of an LBS system. In raster scanning, one mirror operates in resonant mode (for example, along the x-axis), while the second mirror is driven out of resonance with a sawtooth deflection along the y-axis. During scanning, the image is painted through time modulation of the laser diodes (LDs); by pulsing them in synchronization with the beam position.

[**]VitreaLab LCoS-based quantum light chip

In Lissajous scanning, a single 2D MEMS mirror operates in resonance along both axes. The resonant actuation consumes less MEMS power [74]. The sampling is less uniform than in raster scanning. For constant pulsing, the pixel density is higher near the corners of the scan, which reduces brightness uniformity.

LBS is different from pixelated devices. Here, the angular resolution ("pixel") is determined by the mirror diameter. Figure 1.11(d) illustrates the angular resolution for two mirror diameters. The number of pixels, or the overall image resolution, depends on the scanning type. The resolution is related to maximum deflection angle of the mirror [67, 75].

Using laser diodes (LDs) in LBS results in speckle noise. These granular patterns reduce image quality and represent a limiting factor, in addition to the small EyeBox caused by the low divergence of the beam [76].

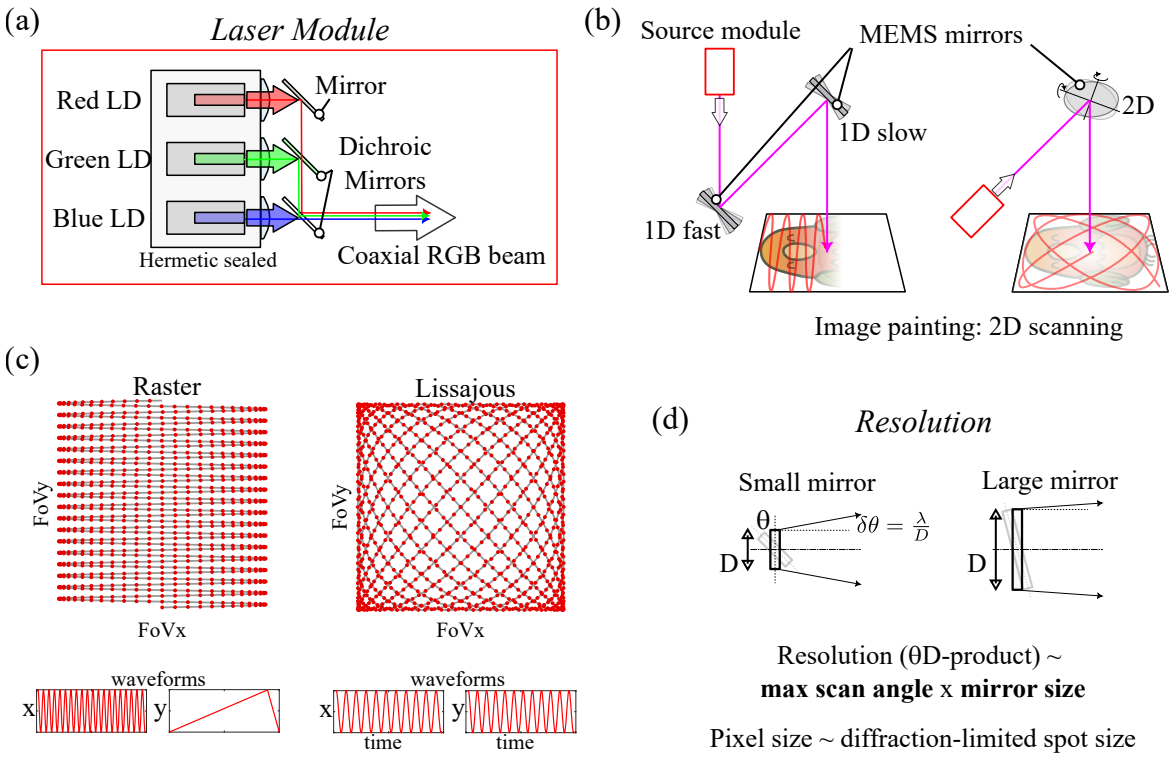

Figure 1.11: (a) Laser module: RGB lasers collimated and combined into a coaxial beam. (b) Beam scanning by angular deflection to form an image using MEMS mirrors: either two 1D mirrors or a single 2D mirror. (c) Two common 2D scanning patterns: Lissajous and raster scanning. (d) Resolution and pixel count in laser beam scanning systems.

For see-though application, the ambiant contrast can make speckle less noticeable [61, 77]. Different despeckling methods can be implemented to reduce speckle noise. Goodman [78] discusses several optical methods for suppressing speckle, such as temporal averaging through a moving screen or a vibrating diffuser [79], decorrelation by using wavelength diversity [80], and reduction of temporal and spatial coherence in the source.

For LDs, the spectral linewidth is typically below 1 *n*m. Superluminescent light-emitting diodes (SLEDs) have a moderate spectral linewidth of less than 10 *n*m [81]. SLEDs, which combine characteristics of LEDs and LDs by using single-pass gain in a waveguide [82], exhibit moderate temporal coherence and can replace LDs to reduce speckle noise. Also they are

polarized and highly directional.

However, there are still challenges to overcome, particularly regarding efficiency for the green (512 *nm*) [83]. Recent improvements have been reported by Exalos on SLED performance [83–85]. The green SLED suffers from a low wall-plug efficiency (WPE), defined as the ratio of optical to electrical power, which is typically around 1%. Pushing the emission toward pure green at 532 *n*m requires increasing the indium content, which further reduces the efficiency below 1%. In comparison, InGaN LDs exhibit a WPE roughly ten times higher, around 5-10%.

For laser safety, potential MEMS scanner failures [1] or high laser exposure [29, 86] must comply with established eye-safety regulations.

1.3.8 Power Consumption

Power consumption in NED is not a straightforward question to answer. LBS is known to be a very efficient solution, but its EB is small. Increasing the EB means spreading the rays over a larger area, which increases the étendue and reduces brightness. Similarly, green microLED panels can be very efficient, but their emission is wide, leading to optical losses at the entrance pupil of the optical system. In RGB panels using X-cubes, the limited acceptance cone angle further increases the power consumption. Likewise, for LCoS, the overall efficiency is not only affected by the reflectivity of the modulation layer, or losses in the homogenizer and polarization filters. The WPE of the display alone does not fully represent the overall efficiency of the NED.

NED efficiency is about the full system. From the rays on the display surface to the rays reaching the retina. Figure 1.12 illustrate the three main blocks where efficiency is evaluated.

First block, the image source:
How much optical power is generated for 1 W of electrical input? A more relevant quantity at this stage is not the WPE, but the luminous efficacy (lm/W), which represents the luminous power per watt of electrical input. Luminous power accounts for the spectral sensitivity of the human eye. For example, the luminous efficacy should be calculated for generating a white point (D65) in the color space, which defines the required optical power ratio among the RGB components. It should be noted that the human eye is most sensitive to green light; therefore, a single-color efficient green display will exhibit high luminous efficacy.

A review paper by Y. Qian et al. [38] discusses the power consumption of microdisplays in NED applications. The power consumption of a complete microdisplay is rarely reported. The following values are only rough estimates.

Typical luminous efficacies are as follows: μLED approximately 30 lm/W for green panel only, and around 3 lm/W for RGB using X-cube, mainly due to the low EQE of the red. Power consumption also depends on the CMOS driving backplane; If all pixels are off, the integrated circuit typically consumes 50–100 mW. JPD [47] RGB X-cube report 10–15 lm/W. For LCoS, the luminous efficacy is approximately 5 lm/W based on LED illumination (Himax [59]), and can be increased to about 10 lm/W with polarization recycling [87]. For LBS, the efficacy is typically around 15 lm/W, with MEMS driving consuming about 135 mW. OSRAM reports values up to 21 lm/W [70].

Second block, entrance pupil:
This concerns the étendue matching between the emitted rays and the acceptance cone of the optical system. Étendue is a geometrical quantity that describes how rays are spread out for an extended source (units of square-meter times steradian (m^2·sr)). For a reminder on étendue, refer to Chapter 5, Section 5.2. Here, we are interested in how much of the emitted light is actually

coupled into the optical system. In this regard, μLED exhibit the largest mismatch due to their wide emission angle, followed by LCoS and then LBS.

For μLED, integrating microlens arrays (MLAs) and other approaches can improve light extraction and beam directionality [88–90]. Reducing divergence through an MLA requires the emitter size to be small compared to the microlens diameter. The microlens can reduce the divergence but simultaneously increases the effective emitter size, this can cause overlap of the emitters (étendue conservation).

For LCoS based on LED illumination, the rays are distributed over the illumination area, resulting in a lower divergence compared to μLEDs. For LBS, the laser source by default has a very low étendue compared to LED emission.

Third block, the EyeBox:
The rays are distributed over a larger EB to improve viewing comfort, but this reduces brightness. Increasing the EB size requires higher power consumption. The EB should be carefully optimized to balance viewing comfort and power efficiency. For lightguide combiners with exit pupil expansion (EPE), the EB is on a non–pupil-forming configuration. As FoV increases, the EB size decreases, leading to a trade-off between EB size, optical efficiency, and FoV. Giving the EB size, the overall NED efficiency can thus be expressed as the luminance at the EB (in *nit* or cd/m^2) per watt of electrical power.

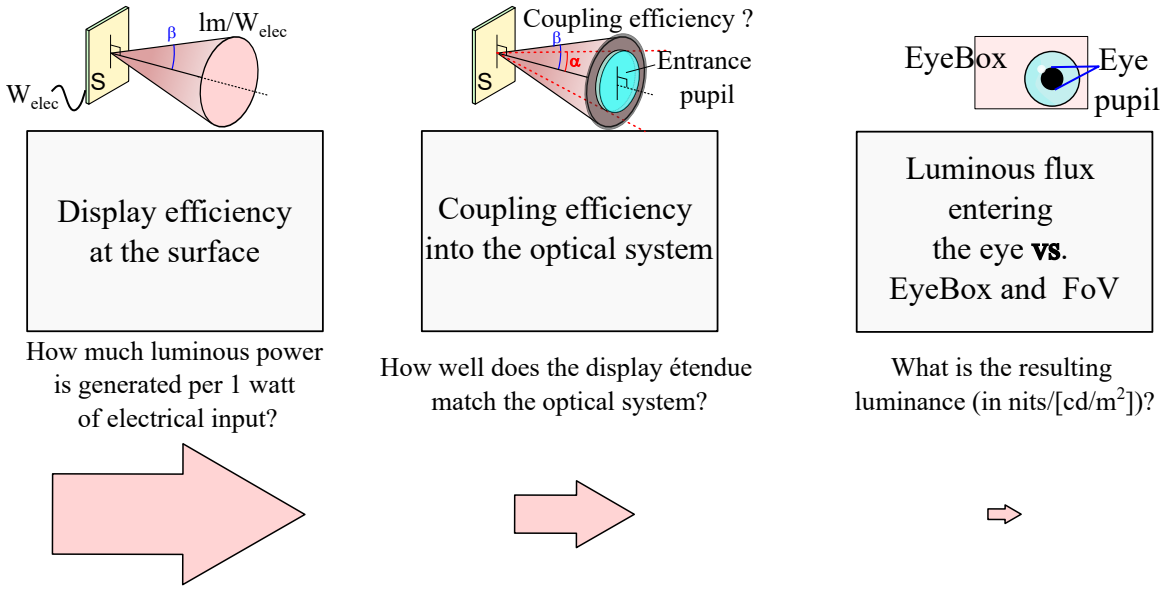

Figure 1.12: The efficiency of NED begins at the display source (lumen per electrical watt), followed by étendue matching with the optical system (coupling efficiency in %), and finally the luminance at the eye (in nit). The overall system "WPE" can be expressed in nit per electric watt.

For the first block, the power consumption of the image source depends on the addressed percentage of the full image. This is referred to as the average pixels lit (APL, in %), where APL = 0% corresponds to all pixels being off, and APL = 100% corresponds to the full FoV being addressed. Figure 1.13 provides a rough estimation of the power consumption for a 3-lm white image as a function of the APL. This figure was adapted from [38].

A horizontal line at 1 W indicates the threshold beyond which the display power consumption can be considered very high. For smart eyewear, other building blocks also demand power in addition to the display. This limit represents the maximum acceptable power budget for a smart

eyewear system. It should be noted that as power consumption increases, thermal issues and management complexity also increase [2]. Higher power consumption leads to larger batteries and weight, which affect the overall form factor.

A low APL (below 15%) is suitable for smart eyewear, as these systems are not immersive. In contrast, fully immersive experiences require an APL close to 100%.

The power consumption of μLED increases rapidly with APL. LCoS exhibit approximately constant power consumption, as they rely on an illumination system fully on. LCoS dimming can improve efficiency. Monochromatic green μLED and LBS displays are the most efficient solutions.

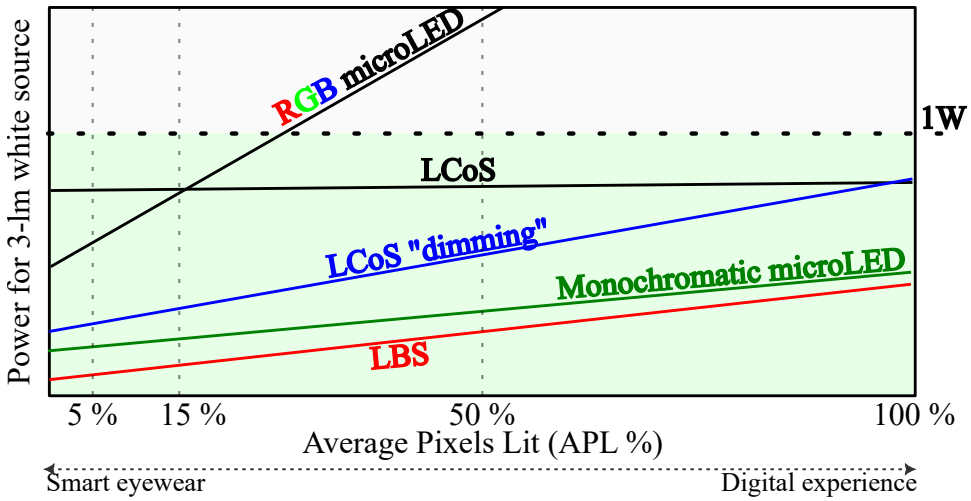

Figure 1.13: Power consumption as a function of the average pixels lit (APL). These curves are for estimation purposes only; details can be found in [38].

For LCoS systems based on laser illumination using PIC, factors such as the laser diodes, their integration, the coupling efficiency into the waveguide, waveguide splitting, propagation losses, and extraction efficiency must all be evaluated. The display power consumption will be comparable to that of conventional LCoS systems. However, proper étendue matching (as discussed in Blocks 2 and 3) can positively impact the overall system efficiency.

1.4 NED Efficiency: Motivation, Alternatives, and Our Solution

1.4.1 Optical Losses in Conventional NEDs

Blocks 2 and 3 in NED efficiency are very important. The key question is: how many photons reach the retina compared to the number of photons generated at the display surface? The goal of this section is to provide an estimated value for a conventional configuration: an LCoS display based on LED illumination with a beam splitter and a diffractive lightguide combiner with EPE and large EB.

Figure 1.14(a) shows normalized intensity patterns. For a Lambertian profile, the intensity decreases angularly as $\cos(\beta)$. Other profiles are plotted with $\cos^p(\beta)$, where $p = 3$ and $p = 10$. As p increases, the emission is more directional. An angular divergence cone of $\beta_0 = 15°$ is

indicated, a value based on a conventional architecture [91]. For a Lambertian emission, the profile is wider compared to this acceptance cone. This results in a low coupling efficiency.

Figure 1.14(b) shows the coupling efficiency into the entrance pupil of half-angle β_0. The schematic illustrates the mismatch between the emission and the acceptance cone. The plotted curve shows the coupling efficiency as a function of β_0: as β_0 increases, the collected flux also increases. At $\beta_0 = 15°$, a Lambertian profile yields a coupling efficiency of 6.7%, while a more directional profile with $p = 10$ reaches 31.7%.

Figure 1.14(c) presents a summary of the optical losses. These are separated for each element, as illustrated in Figures (d) and (e). The schematic (d) corresponds to the display engine. The schematic (e) represents a diffractive lightguide combiner. This conventional optical architecture is inspired by a MagicLeap patent [91].

For the display engine, the *transmission losses* are distributed as follows: the LED, with respect to the collimation optics and an acceptance angle of 15.5°, results in 11.46 dB (7.14%). LED polarization filtering 3 dB loss (50%). The PBS transmission, reflectivity, and $\lambda/4$ plate together contribute 1.37 dB of loss (73%). The LCoS reflectivity adds 1.87 dB (65%). The relay optics transmission accounts for 0.46 dB (90%). The overall loss is 18.16 dB (1.5%).

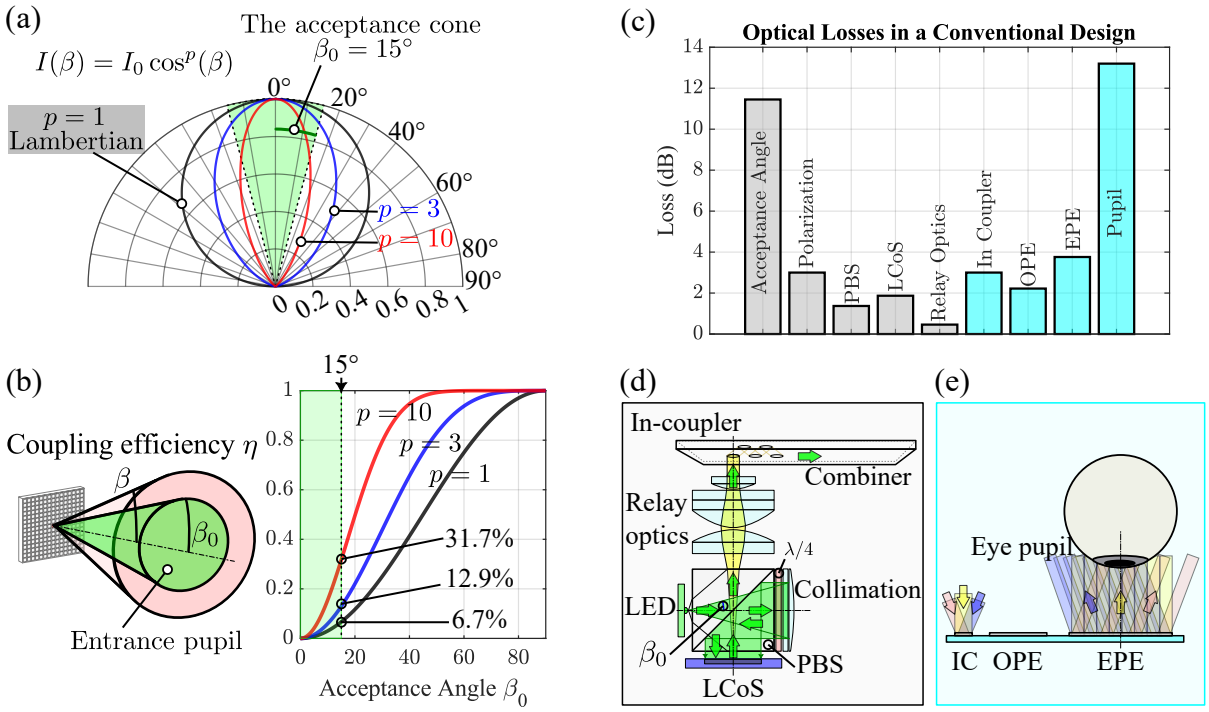

Figure 1.14: (a) Polar plot of the intensity profile for a Lambertian and other emission profiles. (b) Coupling efficiency into an entrance pupil defined by the angle β_0 for different emission profiles, including the Lambertian case ($p = 1$). (c) Optical losses in a conventional NED optical architecture. (d) Example of a conventional display engine (projector) based on MagicLeap1 [91]. (e) Schematic of a diffractive lightguide combiner and the eye.

For the diffractive lightguide combiner, the incoupler introduces a loss of 3 dB (50%), the expander (OPE, orthogonal pupil expander [92]) contributes 2.22 dB (60%), and the outcoupler (EPE) adds 3.77 dB (42%). The total loss at this stage is around 9 dB (12.6%).

The last element is the eye pupil with respect the EyeBox size. Suppose a large comfortable EB where the exit pupil expansion (EPE) is 21×28 mm^2 (estimated from [91]).

The coupling into the eye can be roughly estimated by the ratio of the eye pupil surface to the EPE surface. For a pupil diamter of the eye of 6 mm, we get 13.18 dB (4.8%). We note that a 6 mm pupil corresponds to low-brightness conditions. For a 4 mm pupil, the coupling efficiency drops to 16.70 dB (2.14%). The total loss of the combiner is estimated to be around 22 dB (0.6%).

Taking the total of Blocks 2 and 3, we have around $\approx$ **40 dB (0.01%)**. *Only one photon out of 10 000 emitted at the display surface reaches the retina.*

1.4.2 Recent Advances: Laser Displays

LCoS is a mature technology. LBS is efficient due to étendue considerations, but its eyebox is small, and the scanning process can result in lower image quality. μLED technology is improving, although full RGB is not yet mature.

Each technology has its own advantages and trade-offs. However, recent improvements in LCoS using PIC illuminator appear promising, particularly in terms of luminous efficacy (Block 1) and étendue matching (Block 2).

Recently, in mid and late 2025, LCoS displays using PIC-based illuminators, as reported in the Meta Nature article [61] and the AR Alliance laser display [93], have made this technology increasingly promising. This is particularly interesting for us, as PIC-based displays operating in the visible range are the main focus of this thesis.

According to Meta [93], and as shown in Figure 1.15(a), current conventional LCoS is a mature and ready technology, which is demonstrated in their Meta Ray-Ban display product. μLEDs are considered promising as the next-generation μdisplay technology, while laser-based displays are expected to be the end goal [61].

Figure 1.15(b) shows a schematic of the Meta front-lit PIC illuminator. The panel is flat compared to a conventional LCoS architecture based on a PBS cube. The estimated volume of the full display engine is around 0.8–0.9 cm^3 (see Supplementary 12 in [61]). This size reduction makes the projector more compact. Using an F-LCoS panel is expected to further reduce the volume to about 0.4 cm^3.

Figure 1.15(c) shows the PIC. The RGB laser diodes (LDs) are edge-coupled using a tapered waveguide (see Supplementary 5-10 in [61]). For this prototype, the alignment was active. However, in the future, they are targeting edge-coupled flip-chip bonding with passive alignment pillars. Details on the Meta laser-to-PIC coupling can be found in [94].

The reported wall plug efficiency (WPE) of the LDs are 32%, 10%, and 20% for red (635 nm), green (520 nm), and blue (450 nm), respectively. The green and blue LDs are GaN-based, while the red LD is GaAs-based. Flip-chip edge coupling is a mature technology for optical communication at a wavelength of 1.5 μm [95], typically achieving a coupling loss of 1.5 dB (70%). In the visible range, Meta ([61] Supplementary 5) reported current coupling efficiencies of 77%, 52%, and 23% for RGB, respectively. However, their target for future designs is 80% for all RGB LDs. This is, without doubt, an optimistic projection, as alignment tolerances must be carefully considered. According to [94], in the best alignment conditions, a coupling loss of 1.5 dB was achieved, which is similar to the infrared range results reported by IMEC [95]. They reported state-of-the-art propagation losses in the visible range are 0.1, 0.3, and 1.1 dB/cm for RGB respectively.

After coupling, the colors are combined into a single waveguide using a directional coupler. The light is then distributed into multiple waveguides through Y-splitters. Before entering the

emission region, the light is demultiplexed into separate RGB waveguides. In the emission region, extraction gratings are used to couple the light out. A reflective polarizer is used to recycle the light emitted in the opposite direction due to the binary grating.

The measured insertion losses of the 9-stage Y-splitter tree are 0.16, 0.11, and 0.09 dB for RGB, respectively. For the multiplexer, the measured efficiencies are 1.25, 2.6, and 0.45 dB for RGB, respectively. These values deviate from the simulated loss of 0.13 dB, due to directional coupler tolerances and critical dimension variations during fabrication.

The total measured efficiency of the PIC, from coupling to extraction, is 14%, 7%, and 5% for R, G, and B, respectively.

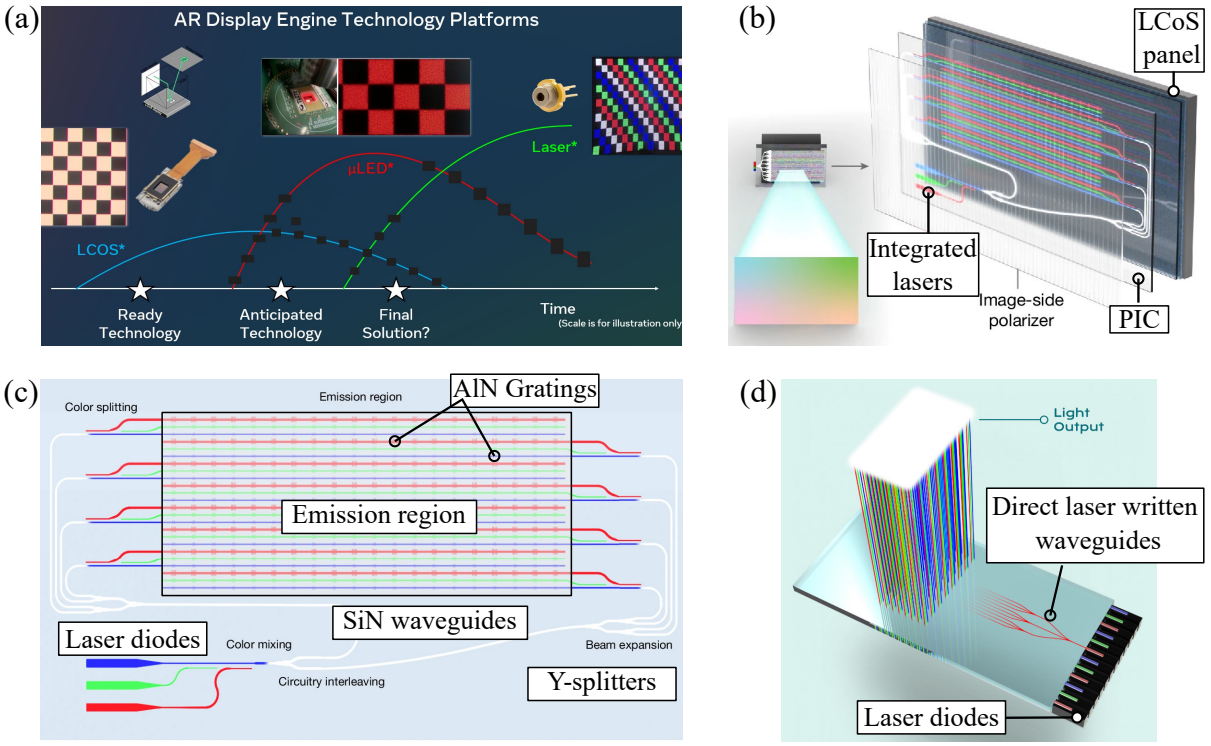

Figure 1.15: (a) AR microdisplay roadmap from Meta [93]. (b) Flat-panel LCoS front-lit PIC illuminator from Meta nature article [61]. (c) Illustration of the PIC illuminator architecture and its subcomponents [61]. (d) VitreaLab backlit LCoS PIC illuminator (vitrealab.com).

In Supplementary 5 of [61], a luminous efficacy of 13 lm/W is reported for the display engine (PIC illuminator + LCoS panel + relay optics). This value represents an estimated performance for an optimized future version.

Let us verify this value based on the reported results. The measured PIC illuminator efficiencies are 14%, 7%, and 5% for RGB, respectively. Considering the LCoS reflectivity mentioned at 70%, and estimating the relay optics and polarizer film efficiencies at 80%, we can approximate the total system efficiency.

Based on the reported wavelengths, the corresponding luminous efficacies are approximately 150, 485, and 30 lm/W for RGB, respectively. Using the reported WPE values of the LDs and assuming a white point composition with flux ratios of 25%, 70%, and 5% for RGB, and taking into account the combined losses from the PIC, LCoS reflectivity, and relay optics, the resulting luminous efficacy of the current version is about 2 lm/W.

For the optimized future version of the PIC, the expected efficiencies are 51%, 52%, and 43% for RGB, respectively. resulting in a calculated luminous efficacy of approximately 12.7 lm/W. This is consistent with the reported value 13 lm/W for the optimized future version.

Figure 1.15(d) shows an illustration from VitreaLab of their PIC illuminator for LCoS. Their waveguide technology is based on femtosecond direct laser writing [96, 97]. Based on the presentation[††], they expect luminous efficacy of the projector at 10 lm/W.

The key takeaway is that PIC in the visible is gaining attention and is promising. Several challenges remain, including the WPE and thermal management of the LDs, efficient LD-to-PIC coupling, and optical losses in the subcomponents. Ongoing industrial and academic alliances and efforts are actively addressing these challenges [93].

1.4.3 Our Directional Display Concept

Description

Our display concept is PIC-based. It is not an illumination unit for an LCoS system; however, it still relies on a liquid crystal for pixel activation.

In the NED efficiency chain, our focus is on addressing étendue matching by designing directional pixels. We aim to combine the low étendue advantage of laser beam scanning (LBS), *but* in the form of a pixelated device. This approach helps overcome the limitations associated with beam scanning.

Figure 1.16(a) shows a schematic of the proposed concept. Each pixel can have a specific direction (γ) and divergence (β).

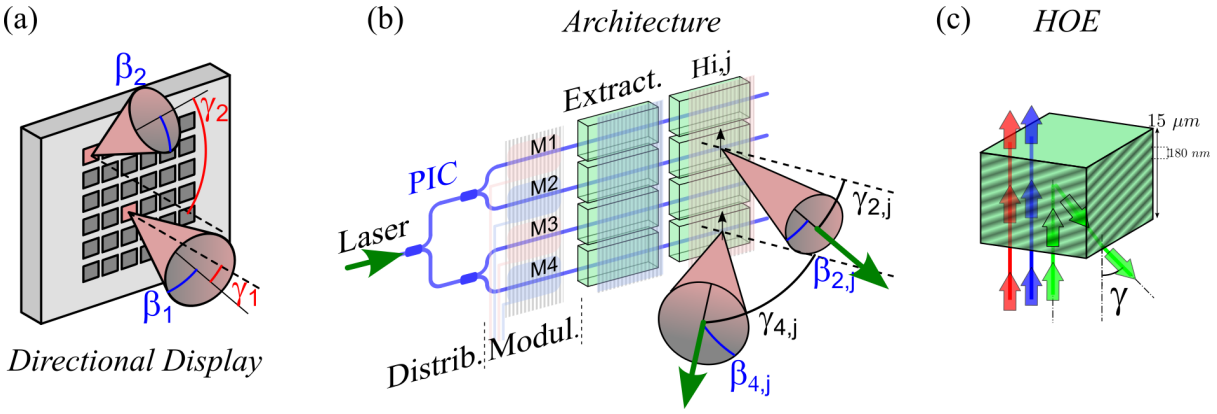

Figure 1.16: (a) Our directional microdisplay concept, where each pixel has a fixed direction angle γ and divergence β. (b) The architecture is based on a PIC with modulation stage, active extraction elements, and pixelated holograms. (c) Schematic of a holographic pixel, or holographic optical element (HOE), used to add directivity to the extracted light.

Figure 1.16(b) illustrates the subcomponents of the architecture. A laser diode is coupled into a PIC waveguide, where the light is distributed and divided into a series of waveguides. These waveguides correspond to the rows of the pixelated device. The signal level in each row is modulated in a modulation stage, and the light is locally extracted at each pixel via an *active*

[††]SPIE AR|VR|MR Fireside Chat by B. Kress — see VitreaLab presentation at 41 min

extraction component. The emission properties (direction and divergence) are controlled by a holographic optical element (HOE), represented by the green boxes. The HOE is a pixelated reflection hologram in which optical functions are encoded through interference.

The term *pixelated* does not refer to the actual emissive pixels of the display. The pixelated hologram can be positioned over several emitters (the actual pixels), giving them identical emission properties.

Figure 1.16(c) shows a schematic of a hologram pixel. This element is wavelength and angle selective, making it fully compatible with the PIC approach. In the schematic, the hologram reflects the incident green rays at an angle γ. The wavelength selectivity can be around 10 nm; this depends on other parameters (more details are provided in Chapter 4). The key takeaway is that this HOE is highly transparent, and RGB functions can also be recorded.

My thesis focuses on two key subcomponents: the *active extraction element* and the *pixelated hologram*, by the recorded reflection angles γ.

Optical Losses

Previously, for a conventional architecture, we calculated optical losses of about 40 dB. This section discusses the optical losses in our proposed approach.

Figure 1.17(a) shows an illustration of the building blocks of our directional microdisplay. The system includes a laser diodes array, PIC, modulation stage, an LC layer, a holographic layer, and the driving electronics.

Figure 1.17(b) summarizes the optical losses. The LD-to-PIC coupling loss is 1.55 dB (70%). For the splitter, we assume 0.22 dB; however, when dividing one waveguide into 1024 outputs, a tree of 10 successive divisions is required. The overall splitting losses amount to 2.23 dB (60%). Propagation losses are estimated at 3 dB (50%), MEMS modulation at 3 dB, extraction losses at 2.22 dB, the HOE at 0.46 dB (90%), and PIC transparency; since we operate in reflection at 2.22 dB. The total losses of the PIC panel are therefore about ≈ 15 dB (3%).

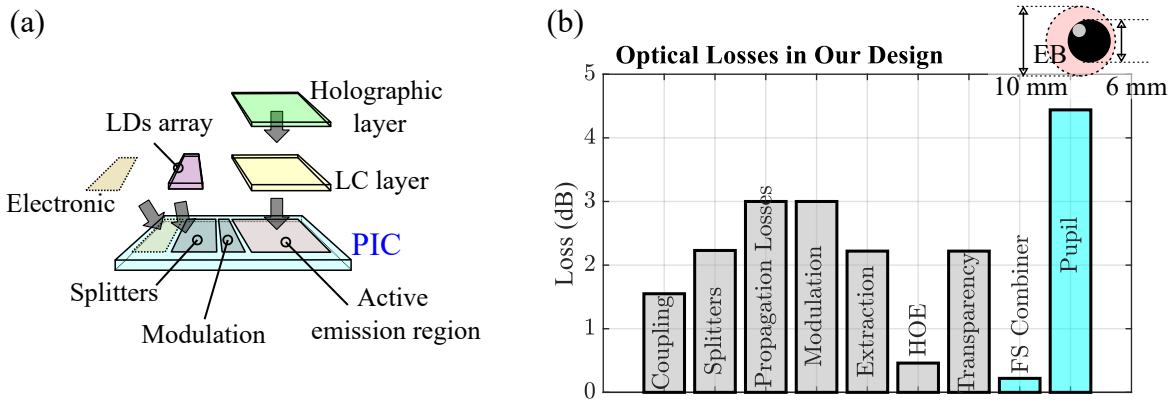

Figure 1.17: (a) Exploded view of the building blocks. (b) Estimation of the optical losses in our approach.

For the combiner, we consider an efficient free-space holographic combiner with a loss of 0.22 dB (95%). For the EyeBox losses, we assume a 10 mm diameter. As will be discussed later, with a directional display we can have an EB as pupil-forming with only one lens. For an eye pupil of 6 mm, the loss is 4.44 dB (36%). The overall combiner loss is therefore 4.66 dB,

leading to a total system loss of about ≈ 20 dB (1%). This represents an overall improvement factor of approximately ×100 compared to the 40 dB for conventional case.

Technological Challenges

As discussed with Meta PIC illuminator, PIC operating in the visible range are promising, though several technological challenges must still be addressed to bring this technology to full maturity. The efficiency of laser diodes, particularly in the green range, must be improved. Similar improvements are required for green SLEDs to achieve a pure green 532 *n*m [83–85].

LD-to-PIC coupling also needs to be addressed in terms of efficiency tolerance, integration type; such as flip-chip bonding [95], bonding speed considerations, and also thermal management [94] since heat can reduce the lasing efficiency [98].

Figure 1.18 shows other technological challenges. For propagation loss, our current value is about 3 dB/cm at 660 *n*m, which is high compared to 0.1 dB/cm at 635 *n*m reported by Meta or other state-of-the-art results [60]. Further improvement is required to reduce the absorption losses in our SiN waveguides [99].

For the modulation stage, we have some unpublished (yet) patents on this topic. MEMS technology was selected for its speed, low optical loss, low power consumption, and potential for a compact footprint [100].

Light extraction is a key element of our concept. I addressed this point in Chapters 2 and 3 using an innovative method based on evanescent coupling and total internal reflection. This solution satisfies our specified design requirements when compared to diffraction-based outcoupling gratings. One of the challenges is the switching speed, for which I identified ferroelectric liquid crystals as a potential solution.

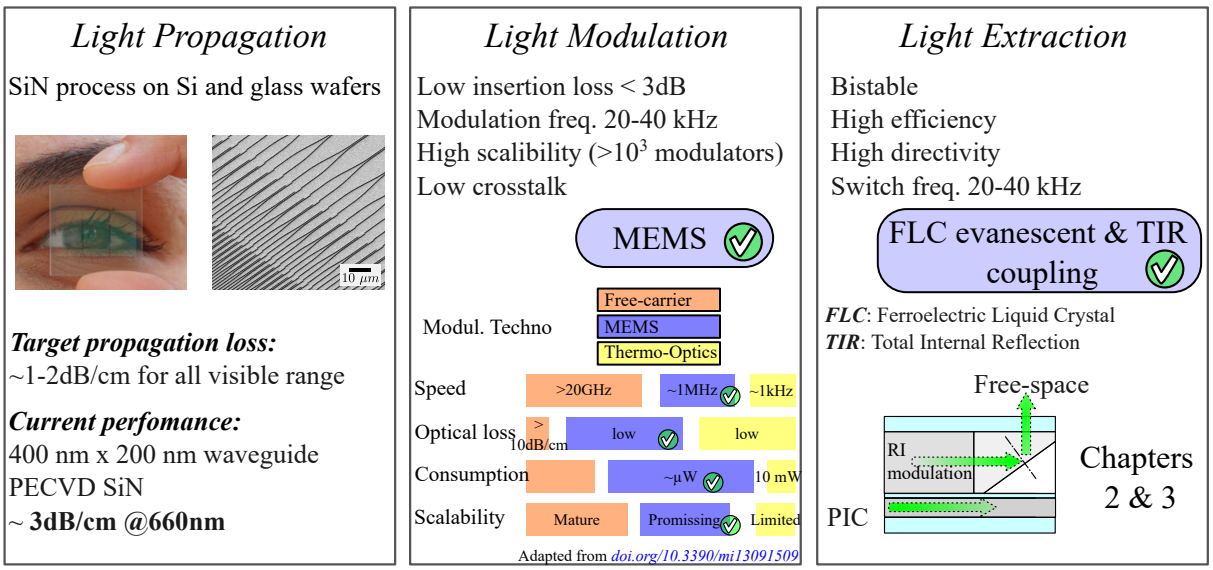

Figure 1.18: Summary of key technological challenges and identified solutions.

1.5 System Design and Requirements

1.5.1 Control of the EyeBox

A directional display has the advantage of efficiently coupling light rays into the optical system (the second block in the NED efficiency evaluation). Moreover, with our concept, we can also address the efficiency in the last block, which relates to the EyeBox and the eye pupil. This section discusses the EB as a pupil-forming configuration using only one lens.

Figure 1.19(a) shows a schematic of an on-axis NED. Since the display is directional, we assume that the central rays of the pixels are directed toward point "V". Points "E" and "V" are conjugate through the lens centered at "C", with a focal length of f = FC. The central rays from each pixel are refracted by the lens and pass through point "E". The divergence field β_0 overlaps at point "E," which corresponds to the position of the eye pupil. Basically, this forms a pupil-forming configuration using a single lens. The EyeRelief is ER = CE. The diameter of this efficient EyeBox is simply $2f\tan(\beta_0)$ [101].

Figure 1.19(b) shows an illustration of an off-axis directional display with a reflective holographic combiner. The pixels are directed toward point "V". The rays are reflected and collimated toward the eye, forming an exit pupil centered at point "E" that is conjugate to "V" by the lens centered at "C".

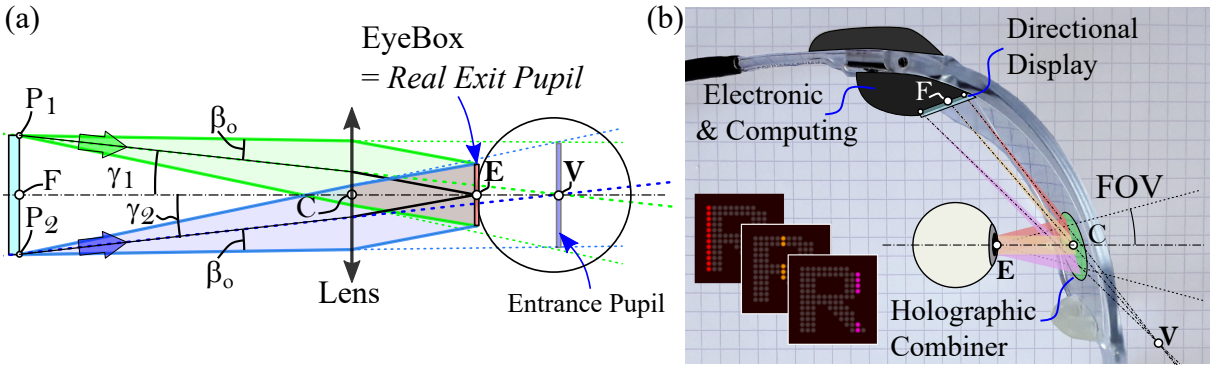

Figure 1.19: (a) EyeBox pupil-forming configuration using a single lens. The directional display rays are directed toward point "V" conjugate to "E", thus the EB as an exit pupil is fixed at the eye pupil (b) Illustration of an application case of an off-axis configuration using a free-space holographic combiner.

If we consider a design case following Figure 1.19(b), with a 15° FoV and an EB diameter of 10 mm, this will determine the panel specifications (β_0, $\gamma_{\max}$, display size, etc.). This is summarized in Table 1.2.

The illustration of the monocular eyewear in Figure 1.19(b) is not a projection of an actual product. This efficient free-space configuration could be interesting for industrial or military applications. The configuration is inspired by designs such as North Focals [102] and Intel Vaunt [103], which use a LBS display engine. However, this setup requires improvement, as the display can be visible to the outside and also the eyelashes could obstruct the light path. An alternative configuration, similar to that of Engo [104], could place the panel near the nose pad instead of the glasses temple, thereby reducing the focal length and display size while maintaining the same FoV.

The takeaway of this section is that a directional display combined with a free-space holographic combiner can provide an efficient way of forming the EyeBox. Further details on the

directional display and the control of the EB can be found in [105].

Table 1.2: Summary of some design specifications for a 15° diagonal FoV and a 10 mm EB diameter. Shaded rows in gray indicate the resulting specifications for the panel and the combiner.

Full Diagonal Field of View	15 degrees
Lens Focal Length (FC)	50 mm
EyeBox Diameter	10 mm
EyeRelief (CE)	20 mm
Angular Resolution (for pixel sizes of 20 μm and 10 μm)	44–88 PPD
Pixel Divergence β_0	5.71 degrees
Maximum Angle of Directivity γ_{max}	4.55 degrees
Display Size	10.8×7.7 mm^2
Holographic Combiner Diameter	>15.3 mm

1.5.2 Pixel Design and RGB

The pixels in this PIC-based panel differ from those in conventional displays. Light is locally "emitted" by means of an extraction component, whose role is to extract the guided light into free space. Figure 1.20(a) shows a schematic where the waveguides act as rows and the activation electrodes as columns. This corresponds to a row-column addressing, where the light in each waveguide is modulated while the corresponding column is activated. The image is formed sequentially, column by column.

In the column direction, we have prismatic strips which act as reflective structures for light extraction. Their minimum spacing is determined by the physical constraints of the evanescent coupling, specifically the "coupling length". This aspect will be discussed in detail in Chapters 2 and 3. For example, the periodic spacing of these strips can start from 5 μm. The spacing between the waveguide rows, on the other hand, is more flexible; the minimum distance is set to avoid mode crosstalk between adjacent waveguides. As an example, the minimum periodic spacing can be around 1.5 μm.

This periodic difference between rows and columns can lead to an asymmetric pixel grid. This is illustrated in Figure 1.20(b) by the red rectangle. It can be seen that the close spacing of the waveguides results in unnecessary oversampling of pixels in one direction, while the spacing of the strips leads to undersampling.

The crossing constraint of the strips (Λ_{ext}) with the waveguides is still satisfied if the strips are rotated by an angle ψ. This is shown in Figure 1.20(c). This inclination relaxes the oversampling caused by the waveguides. As illustrated by the red rectangle, the pixel grid becomes less elongated compared to case (b).

On the right of (b) and (c), a simulated image sampling is shown, comparing the oversampling along the rows for $\psi = 0°$ and the effect of a rotation, for example at $\psi = 60°$, which balances the sampling between the row and column directions.

Before moving to an RGB design, our current focus is on the monochromatic configuration, since some subcomponents (such as the extraction element) must first reach a sufficient level of maturity. We believe that the extraction component developed in this thesis is a key element for future PIC developments, whether in the visible range for microdisplays or at other wavelengths. For example, it could be integrated into Meta front-lit PIC to increase contrast, acting as a local

dimming element.

The monochrome panel may be of interest for military, industrial, or other niche applications. Nevertheless, the RGB question must also be addressed. For color implementation, one straightforward approach is to use three separate RGB transparent panels combined either by vertical stacking or by merging the colors through an X-cube. Alternatively, a single panel could be designed with three different waveguides, one for each color. However, this introduces complexity in the splitting tree, which could increase the overall footprint by a factor of three. To mitigate this, a possible solution would be to use a three-level interlayer waveguide structure, where each division occurs at a different vertical level. At the extraction region (the strips), the light is brought up to a same level by means of a vertical directional coupler [106–108]

Figures 1.20(d) and (e) show RGB waveguides positioned at the same level within the extraction region. In (d), three waveguides are modulated, and a column is activated to extract the three RGB light. In (e), a schematic illustrates the spacing of the RGB waveguides. Note that the waveguide width can differ for each color to adapt the extraction conditions to the RGB wavelengths.

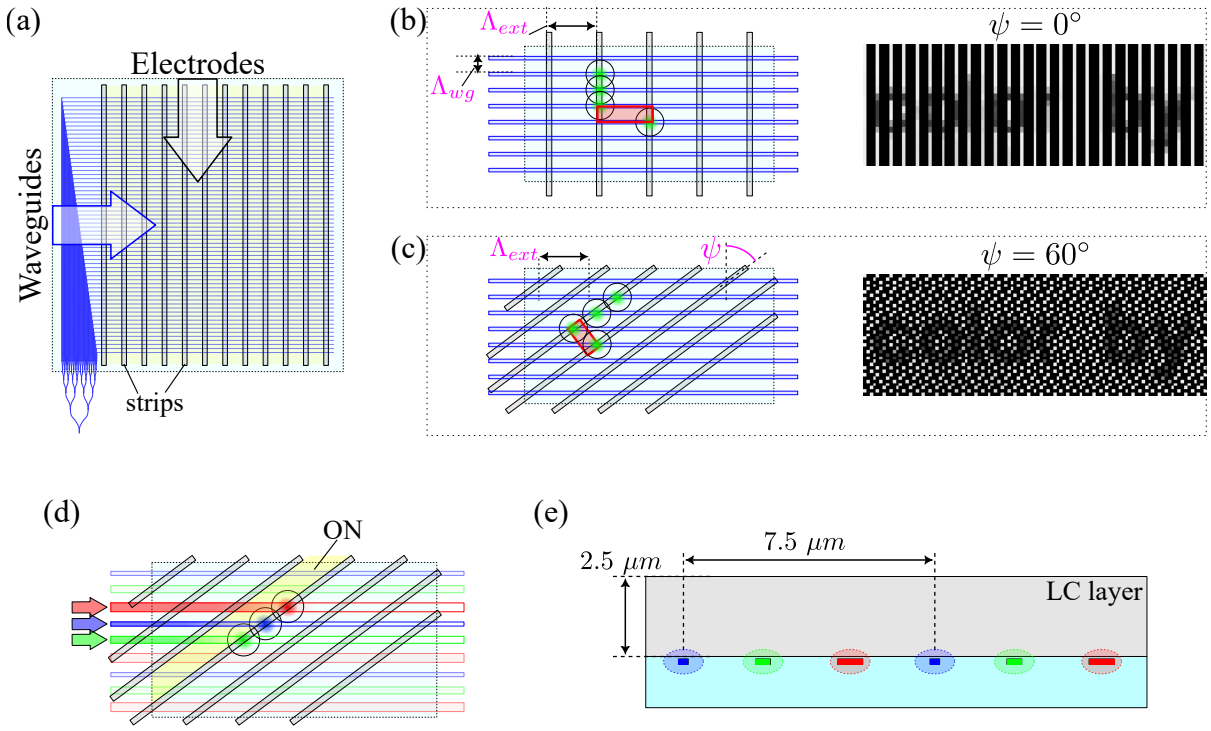

Figure 1.20: (a) Pixel row–column addressing, where the waveguides form the rows and the electrodes form the columns. (b) Asymmetric pixel grid due to oversampling of the waveguides and undersampling of the strips. (c) Inclination of the extraction strips to average the sampling; on the right, the simulated image result. (d) RGB implementation using a single-panel PIC, where the waveguides are positioned at the same level. (e) Schematic cross-section view of the RGB waveguides.

Rotating the strips with respect to the waveguides is an interesting approach for averaging the sampling. However, it is possible that the rays reflected by the prismatic strips become trapped by TIR inside the glass substrate. In fact, the rotation ψ increases the incidence angle with respect to the reflecting plane. An illustration of trapped rays is shown in Figure 1.21(a). In Chapter 4, a more detailed visual representation of the strip operation will be presented.

Nevertheless, the holographic layer can help overcome the trapping conditions by recording a hologram with a reference angle that redirects these rays back into free space, as illustrated in Figure 1.21(b). Recording such a hologram would require the use of a prism to couple the reference beam into the substrate. This configuration is illustrated in Figure 1.21(c), which shows the recording geometry of the pixelated hologram at a reference angle corresponding to the case in (b).

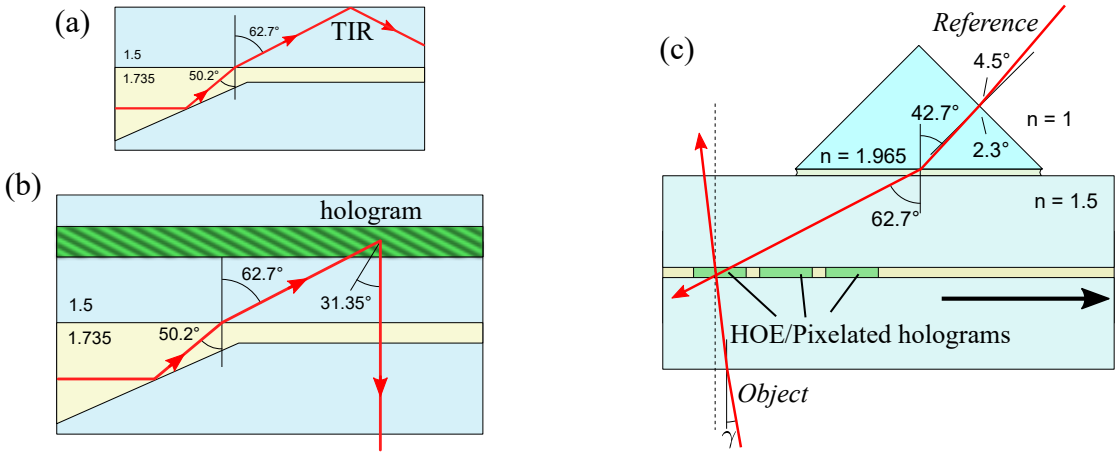

Figure 1.21: (a) TIR-trapped ray after reflection from the strip. (b) Holographic layer including a reference angle to redirect the trapped ray into free space. (c) Holographic recording setup using a prism to couple the reference beam. The object beam defines the direction angles γ.

1.5.3 Dimensioning and Process

This section provides a brief overview of the addressing scheme and explains the need for high-speed liquid crystals (FLCs).

Figure 1.22(a) shows a schematic layout of the PIC panel, including a laser array (example of six emitters) that addresses a set of ten waveguides. We can note that the waveguides are drawn vertically as columns. The signal level in each waveguide is modulated at the modulation stage, while the switching blocks or electrodes are placed below. In (a), the electrodes are inclined at an angle ψ with respect to the waveguides. The letter "R" is displayed as an example.

Only three lasers are activated in pulse mode. The frame displaying the letter "R" is formed sequentially through the activation of the electrodes. Figure 1.22(b) shows a subframe where one switch is active. In this configuration with rotated electrodes, it is possible to activate four electrodes with a single switch because they do not cross the same waveguides. The signal is modulated accordingly, and the corresponding pixels become illuminated. Subsequent subframes are generated by activating the following switches, and the letter "R" appears continuously due to visual persistence.

For the image to appear stable and continuous (to avoid flicker), the sequential activation of all switches N_s must occur at a frequency above 50 Hz. This requires that each active subframe be addressed at a minimum frequency of $N_s \times 50$, and that the liquid crystal respond within this frequency range.

For a dimensioning of the microdisplay panel, we can consider a VGA resolution (640×480 pixels), as shown in Figure 1.22(c). For example, let us assume illumination by an array of 20 laser diodes, each feeding 72 waveguides. The waveguide spacing is set to $\Lambda_{wg} = 2\ \mu$m,

and the strip spacing to $\Lambda_{ext} = 10\ \mu$m. For an inclination angle of $\psi = 63°$, we obtain an effective pixel size of 4.5 μm. We have four electrodes per switch and a total of 215 switches. If we aim to operate at 50 Hz, the required operating frequency of the liquid crystal must exceed 10.8 kHz. FLCs can operate in this range (see chapter 3). The active display area is approximately 2.68×2.15 mm^2.

In Figure 1.22(b), since each of the four electrodes activated by one switch does not cross all the waveguides, the number of electrodes multiplied by the number of waveguides does not directly correspond to the total number of pixels. However, the total number of pixels is given by the number of switches N_s multiplied by the number of waveguides.

Note that in the example given in Figure 1.22(c), the display is very small and therefore not suitable for the free-space configuration shown in Figure 1.19(b). The display size must be increased to achieve the desired FoV, since the focal length is large (50 mm). To reach a display size of approximately 10.8×8 mm^2, the waveguide and electrode spacings must be increased to $\Lambda_{wg} = 7.5\ \mu$m and $\Lambda_{ext} = 37\ \mu$m, respectively.

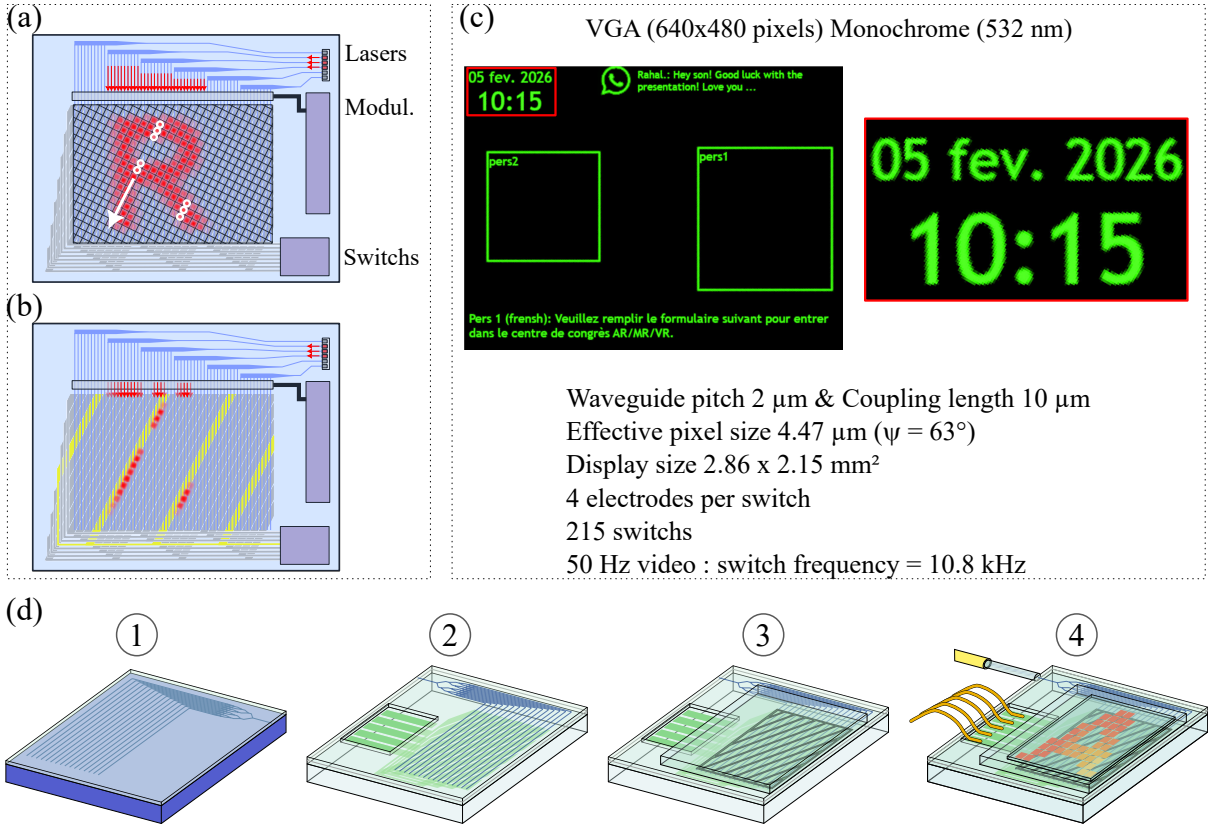

Figure 1.22: (a) Schematic of a PIC panel using a laser array, a modulation stage, and activated electrodes through switches. The letter "R" is generated sequentially. (b) Subframe of the generated "R", where one switch activates four electrodes due to the inclination angle ψ. (c) Example of a VGA display sampled at $\psi = 63°$, showing the full image and a zoomed-in detail. (d) Work process for a future prototype.

Figure 1.22(d) shows a schematic illustration of a prototype fabrication process. (1) Waveguides are designed, fabricated, and characterized on a silicon substrate. The waveguides are made of SiN using standard CMOS processes. (2) The waveguides are then transferred onto a transparent SiO_2 substrate, where the electrodes are integrated through a lithographic process on

ITO (indium tin oxide). (3) The strips are fabricated using a nanoimprint process and reported on top of the PIC, where the liquid crystal is filled in between. (4) Finally, a pre-recorded holographic pixelated layer is laminated onto the extraction region, the electrodes are wire-bonded, and light is coupled into the PIC panel.

1.6 Scope and Purpose of this Research

This directional display project began with my thesis in January 2023. Before that, my supervisor, C. Martinez, was working on a non-conventional holographic display, also based on PIC technology, which used interference between pixels to form a collimated field that directly focused on the retina (a retinal projection display without an optical system [109, 110]). After some conclusions were drawn regarding display contrast, resolution, and power consumption, the project was stopped. The objective of my thesis was therefore to build upon the previous work elements (PIC and holography) a more conventional pixelated display which requires an optical system to form the virtual image [105, 111].

The objectives of my thesis are structured around three main parts: system design, the extraction element, and the pixelization of the hologram (HOE).

System design: Some elements of this part have already been discussed in this chapter. In Chapter 5, we will also present a passive demonstration involving only a pixelated hologram, without the PIC. In the system design stage, I must define, together with my supervisor, a coherent specification for the PIC panel. This specification determines several requirements for other components, such as the extraction element length and operating speed.

Extraction element: This is a central part of my thesis. Extracting light from the waveguide into free space is a key process in our directional display. Chapters 2 and 3 focus on comparing a conventional approach used in the previous project, which involved a diffraction grating. However, at the beginning of this work, we patented a new solution based on evanescent coupling and total internal reflection.

In my theoretical work presented in Chapters 2 and 3, I focused on deriving meaningful equations that provide good estimations, rather than relying solely on intensive simulations. All the theoretical results were validated using 3D FDTD simulations. Chapter 3 concludes with a passive demonstration of this component.

Finally, at the beginning of Chapter 3, I also provide a concise bibliography on ferroelectric liquid crystals, explaining their operating principles and how they will be implemented, with the hope that this thesis may serve and support future research involving the implementation of this type of liquid crystal.

Hologram pixelization: In this part, I used a holographic printer developed in the previous project. My goal was to adjust the setup and the recording automation to record pixelated holograms that encode reflection functions γ, which was successfully achieved (see Chapter 4). Recording divergent or convergent functions is not addressed in this thesis and is left for future work.

The topic of this thesis is multidisciplinary, covering integrated photonics, holography, liquid crystals, and optical systems. I focused on providing concise reminders and key theoretical elements in each discipline.

1.7 Conclusion

Conventional NEDs exhibit efficiencies as low as 40 dB (0.01%). Solving this limitation improves image luminance/brightness while maintaining low power consumption, reduced battery demand, and minimal heat generation. This is especially important for smart eyewear, where the form factor must remain close to that of prescription glasses.

The efficiency chain is not limited to the display surface or its luminous efficacy. It extends from the display itself, through the optical system, and finally to the eye. Matching the étendue of the emission with that of the optical system requires reducing the étendue while maintaining a sufficiently large and efficient EyeBox for comfortable viewing.

Our proposed concept, based on a photonic integrated circuit (PIC), is estimated to achieve an efficiency of about 20 dB, representing a 100 times improvement over conventional approaches.

In this chapter, I presented a historical overview of NEDs evolution. The field is clearly trending toward more compact and efficient eyewear solutions.

The optical architecture of NEDs was described in its simplest form, focusing on virtual image formation, combiners, and microdisplays. Three main technologies; μLED, LCoS, and LBS, were discussed in terms of their operating principles, limitations, and advantages. They are the current solution for high-brightness demand, which is essential for outdoor applications.

Power consumption for each solution was analyzed. Emerging approaches based on LCoS with back-lit PIC illuminators were also discussed, highlighting the growing interest in using PICs in the visible range. My takeaway is that LCoS is currently a mature technology that continues to evolve with increasing performance requirements.

Our proposed directional display concept features pixels, each with a fixed emission direction γ and divergence β. Its operating principle is based on three technological elements: a photonic integrated circuit, active extraction components, and a pixelated hologram. The layout and addressing scheme are also described.

Attention was given to the advantage of controlling the EyeBox by forming a real exit pupil using a single lens. Efficient choice of EyeBox reduces power consumption while maintaining high brightness and comfortable viewing conditions.

In our display architecture, an essential element is the extraction component, which enables out coupling of light from the waveguides into free space. In Chapters 2 and 3, I will discuss this component in detail. We propose an innovative approach based on evanescent coupling and total internal reflection. I will compare this solution with a conventional out-coupling grating. Experimental validation is provided at the end of Chapter 3. Holographic pixelization and the encoding of the reflection angle γ are discussed in Chapter 4, along with experimental results. In Chapter 5, we present a passive prototype of a NED to showcase the importance of directional display on efficiency and brightness.

Chapter 2

Active Component for Light Extraction I

Contents

2.1 Total Internal Reflection **39**
2.1.1 TIR and Evanescent Field 39
2.1.2 Fresnel Reflection and Phase Shift 40
2.2 Waveguide Mode **41**
2.2.1 Eigenvalue Equation and the Effective Refractive Index 41
2.2.2 Mode Profile 44
2.2.3 Mode Extraction and Radiation Decay Constant 45
2.3 Extraction Requirements and Specifications **47**
2.4 Diffraction Grating: Conventional Extraction Approach **48**
2.4.1 Diffraction Orders and k-space 49
2.4.2 Radiation Decay Constant 50
2.4.3 Angular Width of the Extraction 53
2.4.4 Polarization 56
2.4.5 Conclusion 57
2.5 Evanescent Coupling: Innovative Extraction Approach **58**
2.5.1 Overview of the Approach 58
2.5.2 *k*-space: Parallel and Oblique Coupling 59
2.5.3 Evanescent Coupling: Parallel / Directional Coupler 60
2.5.4 Evanescent Coupling: Oblique Coupling 64
2.5.5 Radiation Decay Constant 66
2.5.6 Angular Width of the Extraction 70
2.5.7 Polarization 71
2.5.8 Conclusion 72
2.6 Conclusion **74**

2.1 Total Internal Reflection

Total Internal Reflection (TIR) is a fundamental phenomenon. It is introduced here along with some basic equations, as it will be useful to describe waveguides in an intuitive way.

2.1.1 TIR and Evanescent Field

We consider a plane wave with wavevector $k = \frac{2\pi}{\lambda}$, where λ is the wavelength in free space. Figure 2.1 shows a three-layer structure with refractive indices n_0, n_1 and n_2, respectively. The thickness d of the cover layer is large compared to the wavelength ($d/\lambda > 10$). A ray or plane wave is guided within the structure by TIR at an angle θ_1. The plane wave undergoes total internal reflection at both the upper and lower interfaces only if the incident angle θ_1 is greater than the critical angles of the two interfaces. Using Snell's law, the two critical angles associated with TIR are given by:

$$\theta_{12}^c = \sin^{-1}\left(\frac{n_2}{n_1}\right) \quad \text{and} \quad \theta_{10}^c = \sin^{-1}\left(\frac{n_0}{n_1}\right) \tag{2.1}$$

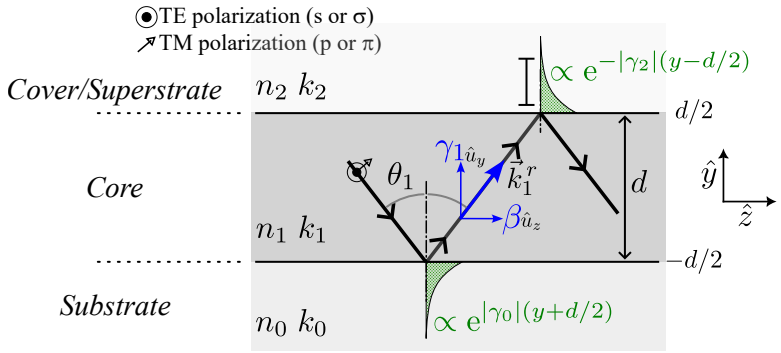

Figure 2.1: A ray is confined in layer 1 by total internal reflection (TIR). At the reflection interface, an evanescent part of the field exists outside layer 1. This evanescent wave decays exponentially.

Even if the wave is fully reflected, there is always an evanescent part of the field outside. At the reflection interface, an exponential decay is illustrated. This decay is rapid and can be on the order of 0.1 μm (for visible wavelengths, with n_1 and n_2 around 2 and 1.5, respectively).

The reflection and refraction properties at an interface are governed by the angle of incidence θ and the polarization state of the wave. The z-axis is defined as the propagation axis. At the boundaries, the longitudinal components of the wave vectors satisfy $\beta = k_1^z = k_0^z = k_2^z$, where β is referred to as the propagation constant. This implies that in all media, the fields share the same z-dependence, given by $\exp(i\beta z)$.

$$\beta = kn_1 sin(\theta_1) \tag{2.2}$$

Under TIR conditions, the propagation constant β satisfies the inequality $n_1 > \beta/k > \max(n_0, n_2)$.

The transverse component γ_j of the wave vector in the j-th medium is defined as

$$\gamma_j(\beta) = k\sqrt{n_j^2 - (\beta/k)^2} = kn_j cos(\theta_j) \tag{2.3}$$

The units of γ_j and β are μm^{-1}. Under TIR conditions, in the core, γ_1 is real and positive. In regions 0 and 2, γ_0 and γ_2 are purely imaginary. The field outside is evanescent. Across a distance $1/|\gamma_j|$ outside layer 1, the field amplitude decays by a factor of $1/e$.

For a wavelength of $0.532\,\mu m$, with $n_1 = 2$, $n_0 = 1.46$, and an incident angle $\theta_1 = 60°$, the characteristic decay length $1/|\gamma_0|$ is $0.162\,\mu m$. This decay is rapid and can be exploited to leak or sense the confined ray through TIR.

2.1.2 Fresnel Reflection and Phase Shift

The reflection and refraction properties depend on the angle of incidence θ_1, or equivalently on the propagation constant β (see Equation (2.2)). They are also influenced by the polarization of the wave, whether it is transverse electric (TE, also called the s wave or σ-wave) or transverse magnetic (TM, also called the p wave or π-wave). We introduce the following polarization coefficient q_k [112].

$$q_k = \begin{cases} 1 & \text{for TE polarization} \\ n_k^2 & \text{for TM polarization} \end{cases} \tag{2.4}$$

The Fresnel reflection coefficient of the electric field (amplitude) is given by the following equation:

$$r_{jk}(\beta) = \frac{q_k\gamma_j - q_j\gamma_k}{q_k\gamma_j + q_j\gamma_k} \tag{2.5}$$

The interface j–k corresponds to the interface where the incident medium is j (for example, $j = 1$ for the core) and the next medium is k (for example, the substrate or the cover).

The phase shift of $-2\phi_{jk} = \arg(r_{jk}(\beta))$ occurs upon reflection. This phase shift is obtained from the phase angle of the Fresnel reflection coefficient and can be expressed as:

$$\phi_{jk}(\beta) = atan(q_j\gamma_k / iq_k\gamma_j) \tag{2.6}$$

The Fresnel reflection coefficient in exponential form is defined with the phase shift as [112]:

$$r_{jk}(\beta) = exp[-i2\phi_{jk}(\beta)] \tag{2.7}$$

In TIR conditions, the phase shift is real and lies in the range $[-\pi, 0]$. In this case, the reflection is total, with $|r_{jk}| = 1$.

The following Figure 2.2 shows the phase shifts at the interfaces. The core, with refractive index $n_1 = 2$, is sandwiched between a substrate $n_0 = 1.5$ and a superstrate $n_2 = 1$. The x-axis represents $n_1 \sin(\theta_1) = \beta/k$. TIR occurs at angles smaller for the interface $(n_1 = 2)/(n_2 = 1)$ than for the $(n_1 = 2)/(n_0 = 1.5)$. When $\beta/k > n_0$, the ray remains trapped inside the core. It is important to note that the phase shift differs between TE and TM polarizations.

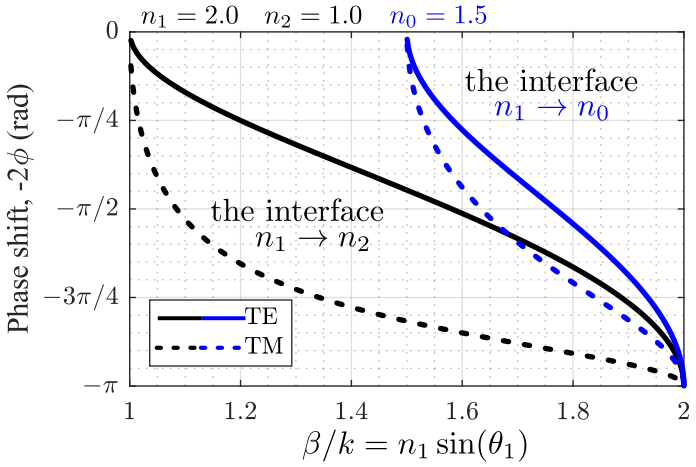

Figure 2.2: Phase shifts at the interfaces of a planar structure, where the core has a refractive index $n_1 = 2$, sandwiched between $n_0 = 1.5$ and $n_2 = 1$. The phase shifts are plotted as a function of β normalized to k.

2.2 Waveguide Mode

The configuration shown previously in Figure 2.1 is called a planar *lightguide*. As we reduce the thickness d, the reflected wave will interfere with itself, resulting in a stationary field profile. This configuration is called *waveguide*. Under TIR $n_1 > \beta/k > \max(n_0, n_2)$, all plane waves propagating at angles θ_1 satisfying this condition are totally reflected, forming a continuum. However, when the thickness d of the lightguide becomes small (on the order of λ), this continuum of possible θ_1 (or equivalently β) breaks into discrete values β_ν. Only specific angles will be allowed. The solutions are called modes. They correspond to a set of transverse mode profiles $\boldsymbol{\mathcal{E}}_\nu(x, y)$ and $\boldsymbol{\mathcal{H}}_\nu(x, y)$ for the electric and magnetic fields, respectively, together with the corresponding propagation constant β_ν, where ν is the mode index.

The fields can be expressed as:

$$\mathbf{E}_\nu(\mathbf{r}, t) = \boldsymbol{\mathcal{E}}_\nu(x, y) \exp(i\beta_\nu z - i\omega t), \tag{2.8}$$

$$\mathbf{H}_\nu(\mathbf{r}, t) = \boldsymbol{\mathcal{H}}_\nu(x, y) \exp(i\beta_\nu z - i\omega t), \tag{2.9}$$

where ω is the angular frequency and $\mathbf{r} = (x, y, z)$.

We define a mode as a propagating field with a transverse distribution whose magnitude and polarization do not depend on the propagation direction z [113]. This is interesting because in a lossless waveguide without any bend (such as a single-mode optical fiber), the transverse profile remains the same regardless of where the waveguide is cut. In other words, the waveguide conserves the Étendue from point A to point B.

To derive the mode solutions, we could start from Maxwell's equations and apply boundary conditions at the dielectric interfaces. However, for simplicity, I will use ray optics to provide an intuitive explanation.

2.2.1 Eigenvalue Equation and the Effective Refractive Index

Consider Figure 2.3, which shows a slab waveguide. We drop the x dependence in the fields, since the waveguide exhibits only one-dimensional transverse confinement, and the guided mode

index reduces to $\nu = m$. In the case of two-dimensional confinement, the mode index would be $\nu = mn$, where m and n are integers.

In Figure 2.3, the ray within the core bounces upward and downward. The **k**-vector can be decomposed into a longitudinal component β (see Equation (2.2)) and a transverse component γ_1 (see Equation (2.3)). In the y-direction, the transverse component of the plane wave interferes with itself. For a mode to exist, a transverse resonance condition of constructive interference must be satisfied. The phase accumulated during a round trip in the thickness core d is $2\gamma_1 d$. Additionally, there are phase shifts at the boundaries due to TIR (see Equation (2.6)), namely $-2\phi_{01}$ and $-2\phi_{12}$. The total phase difference is:

$$\psi(\beta) = 2\gamma_1 d - 2\phi_{01}(\beta) - 2\phi_{12}(\beta), \tag{2.10}$$

This phase function must satisfy constructive interference:

$$\psi(\beta_m) = 2m\pi, \quad \text{where } m = 0, 1, 2, \ldots \tag{2.11}$$

The allowed propagation constant can be found by solving this equation for β. This equation is known as the guidance condition [113] or the eigenvalue equation [114].

The quantity β_m/k is dimensionless and corresponds to an effective refractive index n_{eff}. For a guided mode, n_{eff} must satisfy the TIR condition: $n_1 > n_{\text{eff}} > \max(n_0, n_2)$. The guided mode 'sees' an effective refractive index lower than n_1, since an evanescent part exists outside n_1 in both n_0 and n_2.

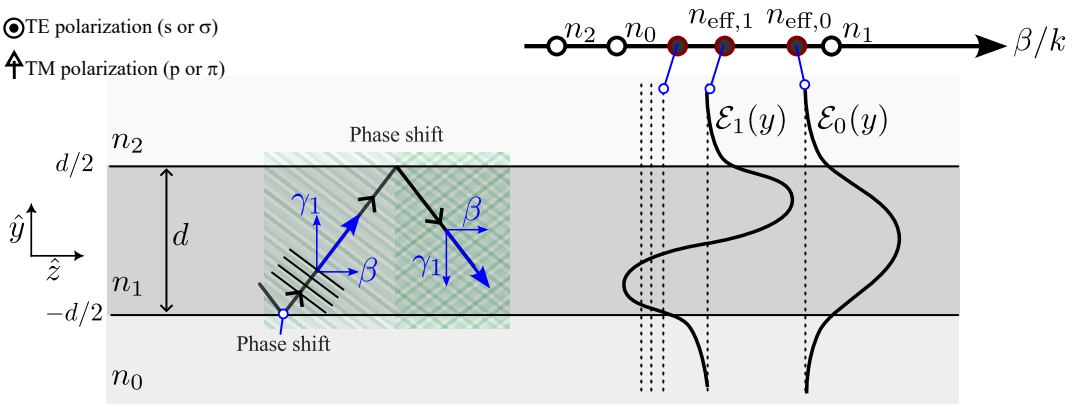

Figure 2.3: Phase condition leading to the eigenvalue equation. The reflections must interfere constructively. The phase accumulated in a round trip is $2\gamma_1 d$. Upon reflection at the interfaces, there is a phase shift that depends on the polarization and the angle of incidence. The solutions are discrete and form guided modes. On the right, an illustration of the fundamental mode ($m = 0$) and the mode ($m = 1$).

The reflection coefficient depends on the polarization; thus, the solutions for TE and TM polarizations are different. Note that the TM polarization is along $\hat{y}$ and the TE polarization is along $\hat{x}$.

We solve the eigenvalue equation for the following example: the refractive indices are $n_0 = 1.5$ for the substrate, $n_2 = 1$ for the superstrate/cover, and $n_1 = 2$ for the core/film. Two film thicknesses, $d = 0.2$ μm and $d = 0.3$ μm are used to show the dependence of the number of guided modes on the thickness. Figure 2.4 shows the solution in terms of the effective

index, $n_{\text{eff}} = \beta/k$, as a function of wavelength. The mode number $m = 0$ corresponds to the fundamental mode.

Note that for $d = 0.2\ \mu$m (black curves), only the fundamental modes TE_0 and TM_0 exist. For a thickness of $d = 0.3\ \mu$m, the effective indexes of the fundamental modes are higher, and an additional mode appears: $m = 1$. As can be observed, the TM_1 mode ceases to exist at wavelengths above $0.55\ \mu$m, and similarly, the TE_1 mode vanishes around $0.65\ \mu$m.

Outside the TIR condition, the modes are called radiative modes. They propagate in the substrate and/or the superstrate and are therefore not confined within the core of the waveguide. More generally, the effective index can be interpreted as a weighted average of n_0, n_1, and n_2, determined by the spatial distribution of the field.

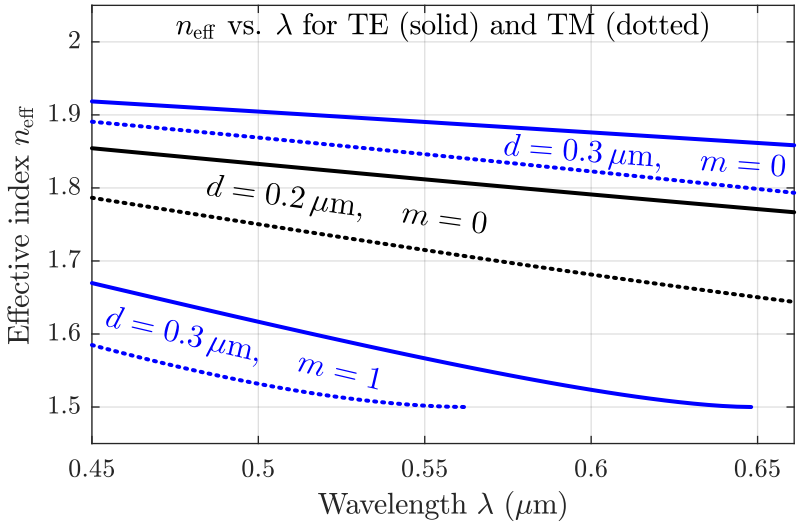

Figure 2.4: Dispersion of the effective index as a function of the wavelength and the thickness d. The refractive indices of the substrate, core, and cover are $n_0 = 1.5$, $n_1 = 2$, and $n_2 = 1$, respectively.

In addition to the intrinsic materials dispersion of the refractive index $n(\lambda)$, the effective index n_{eff} also exhibits dispersion with respect to both the wavelength and the geometry of the waveguide $n_{\text{eff}}(\lambda, d)$. For a waveguide supporting multiple wavelengths (e.g., RGB), each wavelength will correspond to a different effective index. For three separate waveguides, it is possible to adjust the geometry of each one so that the three colors (RGB) have the same effective index. If the materials exhibit absorption, characterized by a non-zero extinction coefficient (i.e., $\text{Im}(n_i) > 0$), then the effective index becomes a complex number. In this case, the imaginary part of n_{eff} is directly related to the absorption losses in the waveguide. To avoid uncontrolled modal interferences, it is preferable to design the waveguide geometry so that only the fundamental modes (TE_0 and TM_0) are supported.

The effective index n_{eff} is one of the most important parameters in this study. All the phenomena involved in extraction, such as the interaction between a guided mode and a grating, and the coupling of modes from one waveguide to another, depend on the effective index. The equation (2.11) used to solve for n_{eff} is quite simple and only valid for a slab geometry. In the general case, simulation tools must be used to find the eigenvalues $n_{\text{eff},\nu}$ and the corresponding field profiles $\mathcal{E}_\nu(x, y)$ (eigenvectors). Lumerical® solvers, such as FDE (Finite-Difference Eigenmode), can be used. For propagation and simulating interactions, FDTD (Finite-Difference Time-Domain) can be used.

2.2.2 Mode Profile

To find the mode field profile $\mathcal{E}_\nu(x, y) = [\mathcal{E}_x, \mathcal{E}_y, \mathcal{E}_z]_\nu$, Maxwell's equations must be solved with the appropriate boundary conditions applied at the interfaces. In the case of a slab waveguide, the vector field is invariant along the x-direction (planar). The x-component of the electric field for TE polarization, $\mathcal{E}_x(y)$ follows the spatial profile described below.

$$\mathcal{E}_x(y) \propto \begin{cases} \cos\left(\gamma_1 \frac{d}{2} - a\right) \exp\left[-|\gamma_2|\left(y - \frac{d}{2}\right)\right], & y > \frac{d}{2}, \\ \cos\left(\gamma_1 y - a\right), & -\frac{d}{2} < y < \frac{d}{2}, \\ \cos\left(\gamma_1 \frac{d}{2} + a\right) \exp\left[|\gamma_0|\left(y + \frac{d}{2}\right)\right], & y < -\frac{d}{2}, \end{cases} \tag{2.12}$$

In the core, there is an oscillatory term. The parameter a is a phase factor that depends on all transverse components of the wave vector (γ_0, γ_1, and γ_2).

At this stage, it is clear that, for a guided mode, the transverse components outside the core are purely imaginary. Therefore, we will drop the absolute value notation $|\gamma|$. Since we know that for a guided mode $n_{\text{eff}} > n_0$, n_2, we redefine γ_0 and γ_2 in a positive form as follows:

$$\gamma_i = \frac{2\pi}{\lambda}\sqrt{n_{\text{eff}}^2 - n_i^2}, \quad i = 0, 2 \text{ for the substrate and the cover.} \tag{2.13}$$

The field outside the waveguide is evanescent. For a decay outside the core by a factor of $1/e$, we define the effective thickness of the waveguide for TE polarization as:

$$d_{\text{eff}} = d + \frac{1}{\gamma_0} + \frac{1}{\gamma_2} \tag{2.14}$$

In Figure 2.5(a), we show an example of the electric field profile for TE and TM polarizations. We plot the magnitude $|\mathcal{E}| = \sqrt{\mathcal{E}_x^2 + \mathcal{E}_y^2 + \mathcal{E}_z^2}$ as a function of the transverse position y. The TE field is continuous because the electric field is tangential to the boundary, whereas the TM field is discontinuous because the electric field is normal to the boundaries. The thickness of the core is $d = 0.2$ μm. The refractive indices n_0, n_1, and n_2 are 1.5, 2, and 1, respectively. The wavelength is $\lambda = 0.532$ μm. The effective indices for TE and TM are 1.819 and 1.728, respectively.

Figure 2.5(b) shows the mode profile of a waveguide with thickness $d = 0.2$ μm and width $w = 0.3$ μm. The waveguide is buried in the substrate n_0, below the cover n_2, with a separation of $s = 0.05$ μm below the white horizontal line. The mode is TE with $n_{\text{eff}} = 1.705$. The polarization is along the x-direction. The electric field is discontinuous along x and continuous along y.

Figure 2.5(c) the mode profile of TM with $n_{\text{eff}} = 1.663$. The polarization is along the y-direction. The electric field is discontinuous along y and continuous along x.

The mode confinement describes how strongly the field is concentrated within the core. This depends on the refractive index contrast of the waveguide through n_{eff} and γ. A high-index-contrast waveguide allows multiple waveguides to be placed close together without significantly perturbing the guided modes, as the overlap of the evanescent fields in neighboring waveguides becomes negligible. To extract the power within the waveguide, the evanescent part can be used. For example, in 2.5(b) and (c), the cover can incorporate a structure that interacts with the evanescent part and causes the mode to leak out.

In Figure 2.5(a), the fraction of the field magnitude inside the waveguide is 68.4% for TE and 52.1% for TM. The intensity fraction $|\mathcal{E}|^2$ is 86.2% and 63.8% for TE and TM, respectively.

In Figures 2.5(b) and (c), the fraction of the field magnitude inside the waveguide is 41.3% for TE and 34.9% for TM. The intensity is 69% and 58.4% for TE and TM, respectively. Above the core, in the cover, the magnitude fraction is 6.3% for TE and 10.6% for TM, while the intensity is 1.2% and 4.44% for TE and TM, respectively. When increasing n_2 from a refractive index of 1 to 1.5, the field magnitude fraction in the cover increases to 12.7% for TE and 16.7% for TM.

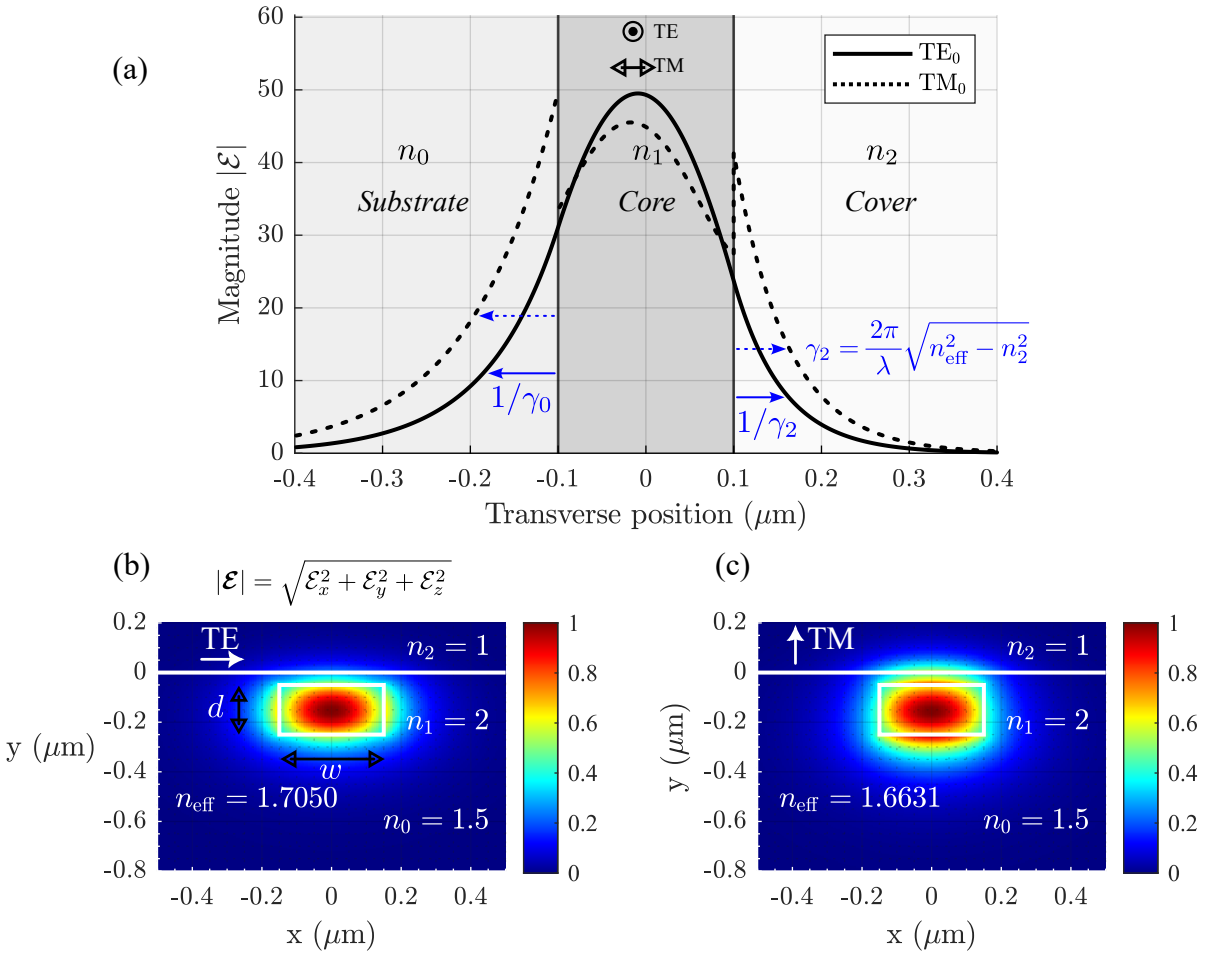

Figure 2.5: Mode profiles of the fundamental TE and TM modes. The magnitude of the electric field is shown: (a) for a slab waveguide, (b) and (c) for a 2D waveguide at 0.05 μm under the substrate surface. The waveguide thickness is $d = 0.2$ μm and the width is $w = 0.3$ μm. The refractive indices of the substrate n_0, the core n_1, and the cover n_2 are 1.5, 2, and 1, respectively. For (a), the effective indices for the TE_0 and TM_0 modes are 1.819 and 1.728. The wavelength is 0.532 μm. (a) is plotted using 1-D mode solver OMS, and (b) and (c) are plotted using Lumerical® FDE.

2.2.3 Mode Extraction and Radiation Decay Constant

A guided mode is invariant along the direction of propagation, since the propagation constant β is real (see Equation (2.8)). In our system, we need to extract the mode at a certain point from the waveguide. At this stage, a perturbation is required to allow the mode to leak out.

In Figure 2.6(a), a schematic top view is shown. A mode in a waveguide propagates from A to B. The mode is invariant, and the same amount of power is present at B as at A (we neglect propagation and bend losses). The other waveguides pass through an extraction zone from A to C where the mode is coupled out. At this stage, the mode inside the waveguide attenuates as a function of z.

Inside the extraction region, the propagation constant is a complex number. The imaginary part α_r is the radiation decay constant. The propagation constant should be replaced by the following expression:

$$\beta \rightarrow (\beta + \delta\beta) + i\alpha_r \tag{2.15}$$

$\delta\beta$ is real and can be positive or negative. This term emphasizes that the propagation constant can differ slightly in the extraction region. It is generally neglected.

In terms of the effective index, we can write this equation as follows.

$$n_{\text{eff}} \rightarrow \left(n_{\text{eff}} + \delta n\right) + i\,\frac{\alpha_r}{k} \tag{2.16}$$

$1/\alpha_r$ has units of μm and, in a manner similar to $1/\gamma$, it provides a characteristic length for extraction. The subscript "r", for radiation is used because the mode is coupled to radiation modes.

Figure 2.6(b) presents a side view of the extraction function. The propagation perturbation occurring in the extraction region is shown as a shaded box. As the mode enters the extraction region, the amplitude inside the waveguide decays exponentially. This decay is described as follows:

$$\frac{dA(z)}{dz} = -\alpha_r A(z) \tag{2.17}$$

In terms of power, we can write the decay rate as follows:

$$\frac{dP(z)}{dz} = -2\alpha_r P(z) \tag{2.18}$$

The radiation can occur at a specific angle within a certain cone or at multiple different angles, such as upward in the cover and downward in the substrate.

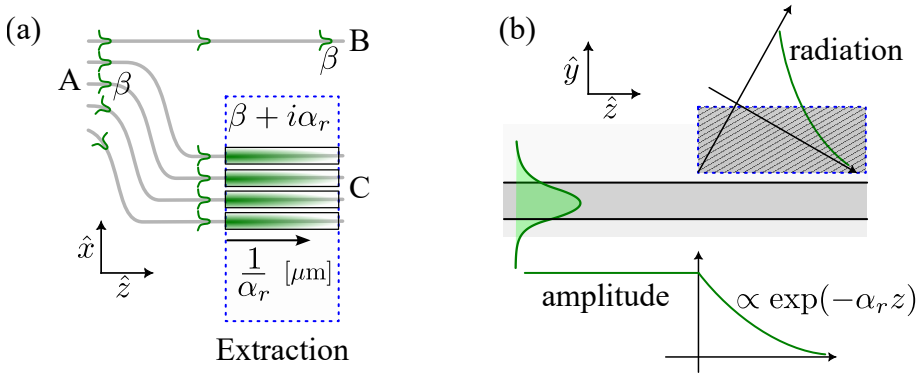

Figure 2.6: (a) Propagation from A to B is invariant. From A to C, in the extraction zone, the modes are coupled out. The propagation constant β is now complex and is replaced by $\beta + i\alpha_r$, where α_r is the radiation decay constant. (b) Side view: the extraction zone is shown as a shaded box. The mode is extracted into a radiation mode. The amplitude inside the waveguide decays exponentially.

For $\alpha_r = 0.01\ \mu\text{m}^{-1}$, at a distance of $1/\alpha_r = 100\ \mu\text{m}$, the amount of power remaining within the waveguide is $\exp(-2) = 13.5\%$. This means that at 100 μm of extraction length, 86.5% of the power is coupled to radiation modes. These modes are found through a phase-matching equation, which will be detailed for our extraction strategies.

2.3 Extraction Requirements and Specifications

This section defines the requirements of the extraction function. In our micro-display, extraction occurs at the level of each pixel. The mode must be extracted to free space, locally and actively under an applied voltage.

Figure 2.7 shows a schematic of the waveguides represented as rows and the extraction components as columns. A modulation stage sets the levels in waveguides 1 and 4. The third column is activated, and extraction occurs. The image is formed sequentially. In the following frames, the remaining columns are activated. To avoid flicker, the image must be formed at a minimum refresh rate of 50 Hz [31]. Depending on the number of columns or resolution, this sets a minimum response speed for the extraction component ($\approx 100\,\mu$s).

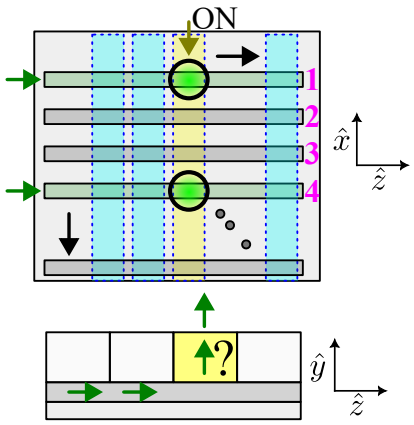

Figure 2.7: Waveguides as rows and extraction as columns.

The extraction must be efficient and directive, as shown schematically in Figure 2.7. The extraction should be upward, and the totality of light should be extracted. The coupling to radiation modes must favor a single direction.

The extraction must be efficient over a short extraction length. A short extraction length implies a high radiation decay constant. For example, $\alpha_r = 0.1\ \mu\text{m}^{-1}$ corresponds to an extraction length of $1/\alpha_r = 10\,\mu$m for 86.5% power extraction.

Here is an overview of the expected extraction specifications for our μdisplay design:

→ **Extraction length** ($1/\alpha_r$): $10 - 20\,\mu$m

→ **Directivity**: A single extraction direction is required for efficiency and to avoid parasitic signals that could reduce contrast.

→ **Speed**: Approximately $100\,\mu$s. The active element in this component is the liquid crystal (LC). Nematic LCs are generally too slow for this, so ferroelectric liquid crystals are preferred. These are introduced in the following chapter 3.

→ **Divergence**: The extraction angular width must be well understood and controlled.

→ **RGB**: Ideally, the component should work for RGB.

→ **Polarization**: The mode is polarized. It is advantageous for the extraction to preserve this polarization, especially in design configurations where polarization is essential (LCoS, LC, etc.).

→ **Contrast**: Local active extraction must provide good contrast relative to the neighboring OFF states.

→ **Integration and tolerance**: The component must remain practical and maintain good performance despite the tolerances of the fabrication.

In the following sections, I discuss two components: the first based on a diffraction grating and the second based on evanescent coupling and refraction. Our second approach is innovative and has been patented during this work.

2.4 Diffraction Grating: Conventional Extraction Approach

A diffraction grating is a passive optical component with a periodic structure that diffracts incident monochromatic light into different directions depending on the grating period, or disperses broadband light into its spectral components. In integrated optics, diffraction gratings are used in a variety of applications, including emitter structures in laser devices such as distributed feedback (DFB) lasers and distributed Bragg reflector (DBR) lasers [115, 116]. In coupling between modes, by providing an additional phase-matching term qK to assist in coupling between modes within the same waveguide or between adjacent waveguides in directional couplers [114, 117, 118]. Diffraction gratings also serve as wavelength filters, reflectors, deflectors, etc. The list is not exhaustive [119]. One specific use case considered in this section is the use of a grating as an **in/output coupler**, allowing optical coupling between a waveguide and free space [119, 120].

In Figure 2.8(a) a guided mode is extracted at a specific angle with a certain divergence. In (b) a side view is shown. The period of the grating is Λ. $K = \frac{2\pi}{\Lambda}$ is the z-component of the grating vector. The refractive index of the grating is n_g.

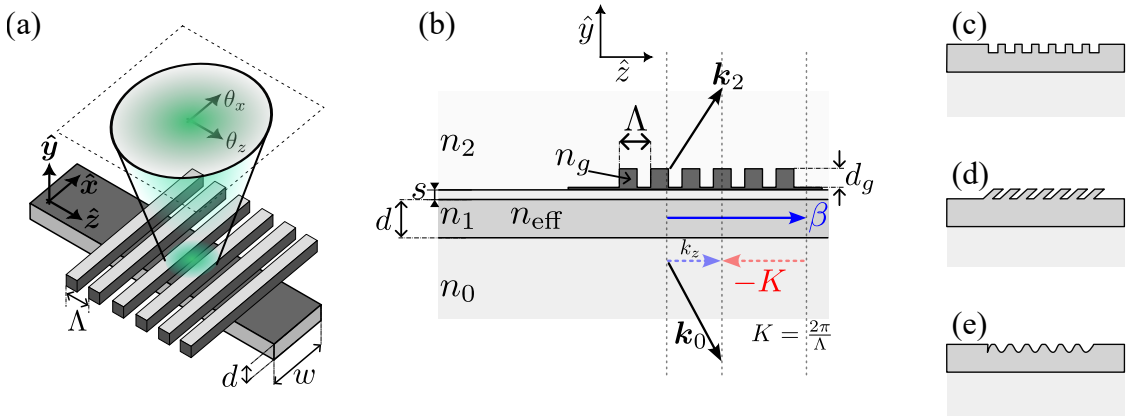

Figure 2.8: (a) Diffraction grating on the cover of the waveguide. The periodic perturbation causes the mode to couple to free space. (b) Side view. The grating wavevector $K = \frac{2\pi}{\Lambda}$ acts as an additional propagation constant to assist phase matching between the mode propagation constant β and the longitudinal component of the radiated wavevector. (c), (d), and (e) Other types of diffraction gratings on a waveguide.

To extract the mode, a phase-matching condition must be satisfied between the propagation constant β and the longitudinal component of the wave vector in the radiation direction.

As shown in (b), the magnitude of β is greater than the magnitude of the longitudinal component $k_{i,z}$ of the wave vector in free space $\boldsymbol{k}_i$. Here, $i = 0, 2$ denotes the substrate and the cover, respectively. The phase-matching is the difference $\Delta\beta = k_{i,z} - \beta < 0$. The coupling is possible and optimal only for $\Delta\beta = 0$. The grating through $K = \frac{2\pi}{\Lambda}$ assist in satisfying the phase matching between $k_{i,z}$ and β. In the case of a periodic perturbation with period Λ, the phase-matching condition of the coupled-mode theory can be expressed as follows [121].

$$k_{iq,z} = \beta - qK, \quad i = 0, 2 \tag{2.19}$$

q is an integer representing the diffraction order. Under small perturbation, β is approximately equal to the propagation constant of the mode before entering the extraction region.

We can normalize the equation using $k = \frac{2\pi}{\lambda}$ to express the diffraction order angles (measured with respect to the normal, $\hat{y}$):

$$n_i \cdot \sin(\theta_{iq}) = n_{\text{eff}} - q \cdot \frac{\lambda}{\Lambda}, \quad i = 0, 2 \text{ and } q \in \mathbb{N}^* \tag{2.20}$$

The energy distribution among the diffraction orders q depends on the shape of the grating profile; rectangular (Figure 2.8(a) and (c)), slanted (Figure 2.8(b)), sinusoidal (Figure 2.8(e)), triangular, and others. This distribution is directly related to the Fourier components of the periodic structure of the grating.

For a given diffraction order, achieving greater directionality, which means more energy is radiated into the cover than into the substrate, depends on the introduction of a transverse asymmetry in the grating. Constructive or destructive interference effects can improve this directionality [122], as seen in blazed and slanted gratings [123].

2.4.1 Diffraction Orders and k-space

The equation (2.20) can be intuitively understood using k-space. k-space, or reciprocal space, is a convenient way to represent changes in the direction of the wave vector $\boldsymbol{k}_i$ when going from one medium i to another medium j. The wave vector $\boldsymbol{k}_i$ in medium i has the same magnitude regardless of its direction. It lies on the surface of a sphere whose radius $k_i = kn_i$ is determined by the refractive index n_i. Here, $k = \frac{2\pi}{\lambda_{\text{vacuum}}}$ is the magnitude of the wave vector in vacuum. Different media have different sphere radii, defined by their respective n_i. Figure 2.9(a) shows the k-space normalized by k, where an example of Snell's law is illustrated. Assume that $n_j < n_i$. The sphere of the medium i is larger than the medium j. The beam refracted from medium i to medium j retains the same longitudinal component. In the sphere representation, this corresponds to projecting the wavevector along the normal direction $\hat{n}$ until it intersects the radius sphere n_j. If this translation does not reach any point on the surface n_j (the longitudinal component exceeds n_j), TIR occurs, as illustrated by the red beam.

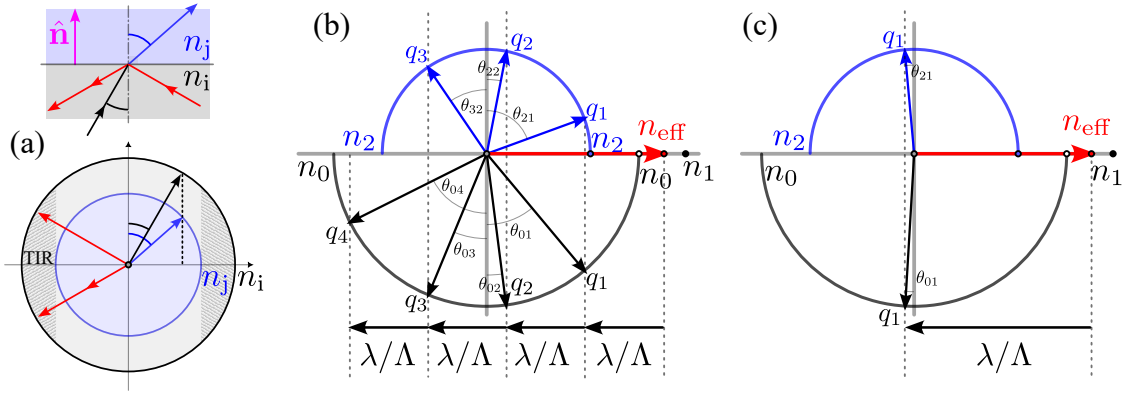

Figure 2.9: (a) Refraction and TIR visualized in k-space. (b) Multibeam coupling of n_{eff} into the cover and the substrate. The grating assists through the term λ/Λ to couple n_{eff} into different orders q. (c) Two-beam coupling.

The equation (2.20) is illustrated in Figure 2.9(b). The mode is represented by n_{eff}. The blue semicircle represents the cover, while the black semicircle of radius n_0 represents the substrate. Since there is no intersection of n_{eff} with the two semicircles, the mode is guided. However,

the grating assists the coupling by adding the term qK. The normalized term is $q\lambda/\Lambda$. For first order, $q = 1$, the mode couples to radiation directions in the cover at an angle θ_{21} and in the substrate at an angle θ_{01}. Similarly for $q = 2$ and $q = 3$. For $q = 4$, the fourth order is possible only in the substrate.

The power distribution into different orders depends on the shape of the grating and the number of the order. The radiation decay constant is the sum of the decay constants corresponding to coupling into all diffraction orders in both the substrate and the cover: $\alpha_r = \sum_{i,q} \alpha_{i,q}$.

Controlling directivity and thus ensuring efficiency requires designing the coupling condition so that only the first order is available. The grating period is thus reduced so that the grating supports only one diffraction order in each medium. This is shown in Figure 2.9(c). Now we have $\alpha_r = \alpha_{0,1} + \alpha_{2,1}$. Downward radiation is always present unless the grating shape is designed to favor a single direction. For a binary grating, the upward and downward efficiencies are equal [124].

For first-order ($q = 1$) vertical out coupling, where $\theta_{i,1} = 0$, the condition $\Lambda = \lambda/n_{\text{eff}}$ must be satisfied. This condition holds for both the cover and the substrate. However, it is generally preferable to avoid $\theta_{i,1} = 0$, since the same grating period also satisfies a second-order ($q = 2$) at $\theta_{i,2} = -90°$, which corresponds to a counter-propagating mode.

2.4.2 Radiation Decay Constant

Rather than relying directly on numerical simulations, it is convenient to have an analytical expression for the radiation constant to gain insight into the influence of each parameter of the grating and the waveguide. Coupled-mode theory or leaky-wave analysis provides the key characteristics for that [119, 124, 125].

In the following, we will limit the analytical treatment to the first diffraction order, so that $\alpha_r = \alpha_{0,1} + \alpha_{2,1}$. Additionally, only the decay constant for TE polarization will be expressed. Readers interested in further details may refer to [119], pp. 83–94.

For the waveguide, the required parameters include the refractive indices of the substrate n_0, the waveguide n_1, the cover n_2, thickness of the waveguide d, the wavelength λ, and the effective index of the mode n_{eff}. For the grating, we need the refractive index n_g, the period Λ, and the grating thickness d_g.

In the following equation, we define $\bar{n}_g$ as the volume-averaged refractive index of the grating, since it is surrounded by the cover. The parameter ff represents the filling factor.

$$\bar{n}_g = \sqrt{ff \cdot n_g^2 + (1 - ff) \cdot n_2^2} \tag{2.21}$$

The evanescent decay of the mode in the grating layer is characterized by the transverse component:

$$\gamma_g = k\sqrt{n_{\text{eff}}^2 - \bar{n}_g^2} \tag{2.22}$$

The transverse component of the radiated wave vector in the grating medium is:

$$k_{2,y} = \frac{2\pi}{\Lambda_\alpha} = k\sqrt{\bar{n}_g^2 - \left(n_{\text{eff}} - \frac{\lambda}{\Lambda}\right)^2} \tag{2.23}$$

Λ_α is the transverse spatial period of the first diffracted order in the grating medium. This quantity will explain the interference caused by discontinuities at the upper and lower interfaces

of the grating, which gives rise to oscillations as a function of the thickness of the grating d_g (Fabry–Pérot).

The following is an expression for the radiation decay constant for the first diffraction order ($q = 1$) for TE polarization [124, 125]:

$$\alpha_r = \begin{cases} \dfrac{2}{\lambda n_{\text{eff}}} \cdot \dfrac{n_1^2 - n_{\text{eff}}^2}{n_1^2 - n_2^2} \cdot [n_g^2 - n_2^2]^2 \cdot \dfrac{\Lambda_\alpha}{d_{\text{eff}}} \cdot \left(\dfrac{d_g}{\lambda}\right)^2, & \text{if } d_g \lesssim \gamma_g^{-1} \quad (1) \\ \dfrac{1}{2\pi^2 \lambda n_{\text{eff}}} \cdot \dfrac{n_1^2 - n_{\text{eff}}^2}{n_1^2 - \bar{n}_g^2} \cdot \dfrac{[n_g^2 - n_2^2]^2}{2n_{\text{eff}} - \frac{\lambda}{\Lambda}} \cdot \dfrac{\Lambda_\alpha}{d_{\text{eff}}} \cdot \dfrac{\Lambda}{\lambda}, & \text{if } d_g \gtrsim \gamma_g^{-1} \quad (2) \end{cases} \tag{2.24}$$

Depending on the penetration depth $1/\gamma_g$ relative to the thickness of the grating d_g, two cases arise. If the grating is shallow, such that $d_g \lesssim \gamma_g^{-1}$, the radiation decay constant varies proportionally to the square of the grating thickness $\alpha_r \propto d_g^2$. If $d_g \gtrsim \gamma_g^{-1}$, a saturation regime is reached.

The radiation scales with the square of the refractive index contrast, $[n_g^2 - n_2^2]^2$. If the refractive index of the grating matches the cover, no outcoupling occurs ($\alpha_r = 0$). In the following chapter, this will be discussed in the context of active extraction. The cover will be replaced by a liquid crystal layer (LC) such that $n_2 = n_{\text{LC}}(\text{Voltage})$.

For equation (2.24), no residual layer or gap is assumed between the grating and the waveguide. However, the key characteristics remain the same.

We begin by applying the expression from equation (2.24) to the examples presented by Tamir [124] and Nishihara [119]. Figure 2.10(a) shows an example of the simulated decay constant versus the depth of the grating groove d_g. The solid lines represent results from the FDTD simulations performed using the parameters shown in the schematic. These results are consistent with those reported by Tamir [124]. In his article, he applied a rigorous approach at only a few discrete points.

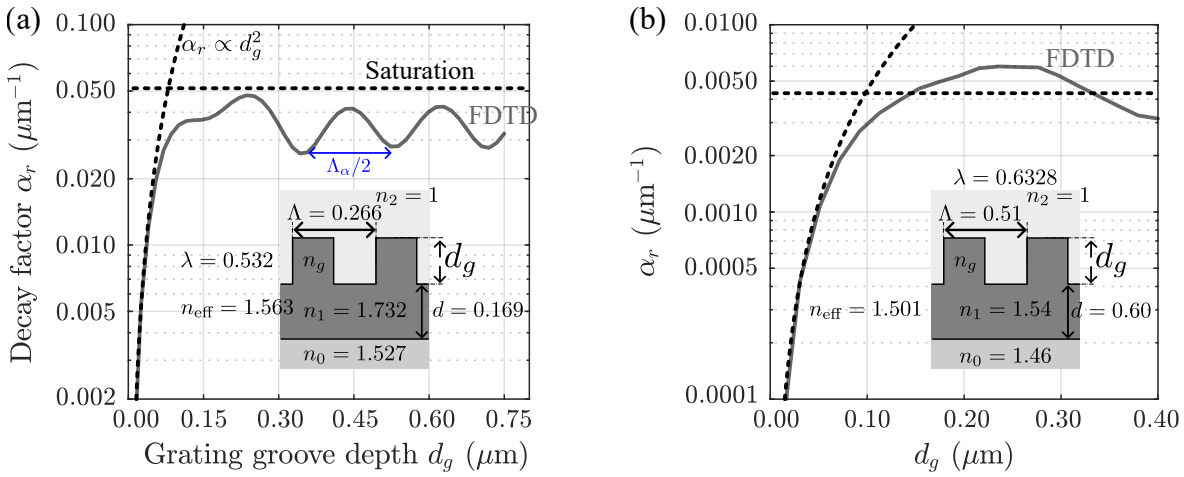

Figure 2.10: (a) Radiation decay constant as a function of the grating thickness d_g. I reproduced the same results as Tamir (1977) [124]. The solid line shows the FDTD simulation, while the dashed line corresponds to the analytical expression given by Equation (2.24). (b) I reproduced similar results to those reported by Nishihara (1988) [119].

The dashed lines correspond to values computed using the analytical decay expression. Oscillations as a function of grating thickness are also observed. The period of these Fabry–Pérot

oscillations corresponds to half the transverse spatial period in the grating $\Lambda_\alpha/2$ (see equation (2.23)).

Figure 2.10(b) shows an example using the parameters provided in [119]. Our FDTD simulation results, represented by the solid line, match those reported by Nishihara. In his book, he employed a rigorous analysis based on space-harmonic expansions, which corresponds to what is now commonly known as Rigorous Coupled-Wave Analysis (RCWA). Similarly, the dashed lines correspond to values computed using the analytical decay expression. The analytical results match closely with the simulation.

The equation (2.24) is consistent with the simulations, and I reproduced similar results with our FDTD simulation, in agreement with Tamir and Nishihara. The equation is compact and easy to implement. The expression for TM, not shown here, can be found in [124]. The expression is valid for the first order; a more general expression can be found in Nishihara's book [119].

We now consider an example related to our waveguide. Figure 2.11 presents FDTD simulations of the decay constant for both TE and TM polarizations, shown by the solid black and blue lines, respectively. In Figure 2.11(a), the simulation is two-dimensional (slab). In (b), it is three-dimensional with a waveguide width of $w = 0.3\,\mu$m. The refractive indices are $n_0 = 1.5$, $n_1 = 2$, $n_2 = 1$, and $n_g = 1.5$. The grating period Λ is chosen to produce an outcoupling angle of 2° in the cover for a wavelength $\lambda = 0.532\,\mu$m.

Figure 2.11(a) shows that the decay constant for TE polarization is approximately equal to that of TM. The dashed curves represent the analytical solutions plotted in both regimes: $\alpha_r \propto d_g^2$ and the saturation. The values α_r are around 0.007–0.01 μm^{-1}, corresponding to a characteristic extraction length of 143–100 μm. The radiated power is divided equally between the substrate and the cover.

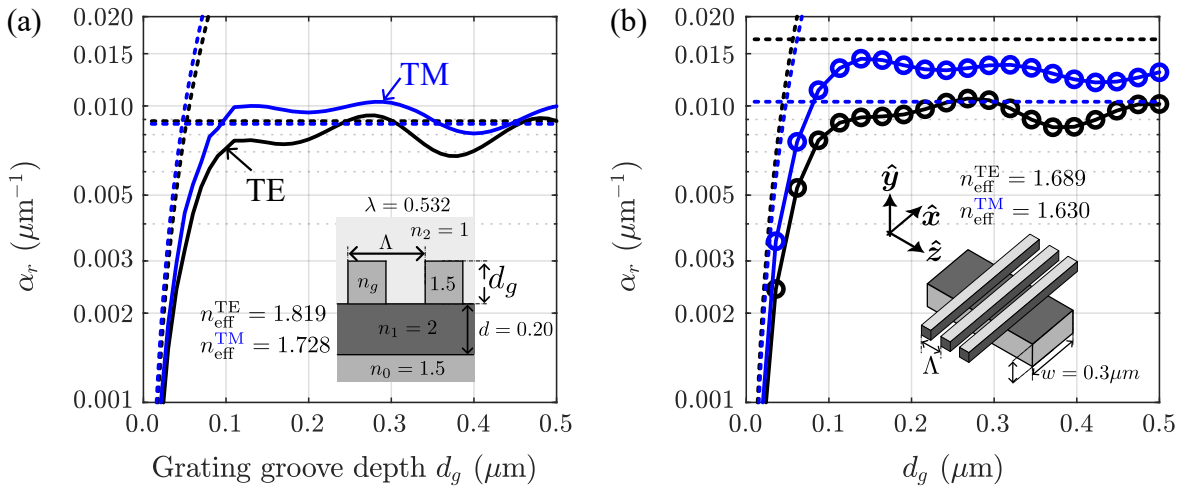

Figure 2.11: Radiation decay constant as a function of the grating thickness d_g. (a) 2D FDTD simulation. The solid line shows the simulation results, while the dashed line represents the analytical expressions. The waveguide and grating parameters are illustrated in the schematic. (b) 3D FDTD simulation. The n_{eff} in the analytical equation is replaced by the effective index for a waveguide with a width of $w = 0.3\,\mu$m.

The analytical equation is valid only for the slab configuration. In Figure 2.11(b), which corresponds to the 3D case, this equation is not satisfied. However, the effective indices from the 3D geometry are used to compute the dashed analytical curves. The results show a deviation between the analytical saturation and the 3D FDTD results. However, the values of α_r remain

approximately at the same level as in the slab case. The analytical expression for α_r is valid only under the perturbation approach, and this limitation should be kept in mind.

Figure 2.12 presents a comparison between simulation and the analytical expression of α_r, plotted as a function of the thickness of the waveguide, using solid and dotted curves, respectively. Only the saturation regime is considered, with a fixed grating thickness of $d_g = 0.3\,\mu$m.

Reducing the thickness d increases the penetration of the mode outside the waveguide, resulting in greater interaction with the grating and increased extraction. This effect is observed in the solid curves for both TE (black) and TM (blue) polarizations.

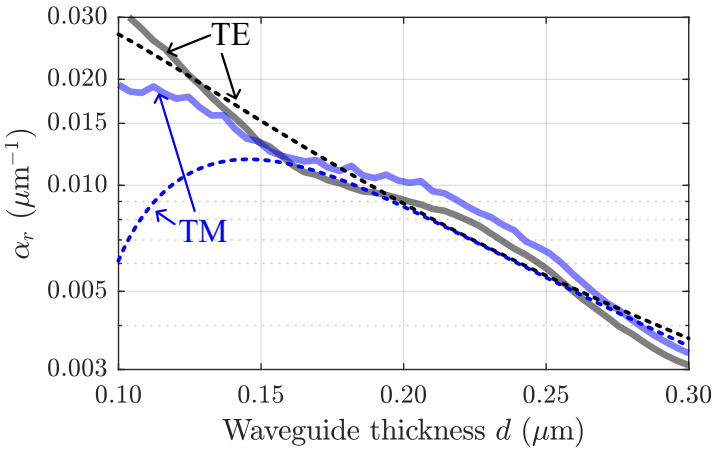

Figure 2.12: Radiation decay constant as a function of the grating thickness d. Comparison of the 2D FDTD simulation (solid line) and the analytical expression (dashed line). The grating thickness is $d_g = 0.3\,\mu$m. The dashed line shows the saturation expression of Equation (2.24) for TE and TM polarizations. The other parameters are similar to those in Figure 2.11(a).

However, the analytical expression for TM begins to underestimate radiation as the waveguide thickness decreases, indicating that the interaction is no longer in the weak perturbation. In asymmetric waveguides ($n_0 \neq n_2$), existing modes are cut off below certain critical thicknesses. For example, in this case, the TM mode is cut off first at approximately 82.2 nm, followed by the TE mode at around 45 nm.

2.4.3 Angular Width of the Extraction

The grating through $\frac{2\pi}{\Lambda}$ assists in phase matching between the guided mode propagation constant and the longitudinal component of the radiation. The grating "slows down" the mode by $\frac{2\pi q}{\Lambda}$, where q is the diffraction order.

We must note that the coupling is a resonant phenomenon, and we must expect a phase-matching bandwidth. Unlike guided modes, which have discrete propagation constants, radiation modes form a continuous spectrum of propagation constants. Phase matching with a longitudinal radiation constant occurs with a finite width $\Delta\beta$. This is illustrated in Figure 2.13(a).

In this section, the equations involved are inspired by Norton [125] and Ulrich [112]. The wavevector diagram is presented on the right side of Figure 2.13(b). We know from Section 2.2.3 that the propagation constant β in the extraction region takes a complex form: $\beta \rightarrow \beta + i\alpha_r$. The propagation constant in the waveguide is denoted β_{eff}. The periodicity of the grating Λ introduces spatial diffraction orders by shifting β_{eff} by integer multiples of $2\pi/\Lambda$.

The shaded blue region represents the range of longitudinal components corresponding to radiation modes. Two diffraction orders are shown: β_1 and β_2. As illustrated, this vector diagram lies in the complex plane, with real and imaginary axes.

The excitation of a radiation mode is a resonant phenomenon. The corresponding resonance points are poles. For example, if we consider the first order in the diagram, the pole is a complex number. According to coupled-mode theory, this pole is given by $\beta_1 + i\alpha_r$, where the imaginary part α_r represents the radiation decay constant for that order.

Near this pole, the amplitude of transmission from the guided mode to the radiation order is proportional to the following:

$$t(k_z) \propto \frac{1}{k_z - (\beta_1 + i\alpha_r)} \tag{2.25}$$

The power transmission is therefore proportional to:

$$|t(k_z)|^2 \propto \frac{1}{1 + \dfrac{(k_z - \beta_1)^2}{\alpha_r^2}} \tag{2.26}$$

This is a Lorentzian expression, whose full width at half maximum (FWHM) is $2\alpha_r$. The transmission is sketched in Figure 2.13(b) as a function of the longitudinal wave vector component. Two resonance peaks correspond to the coupling to orders $q = 1$ and $q = 2$. Each peak has a different width of $2\alpha_r$.

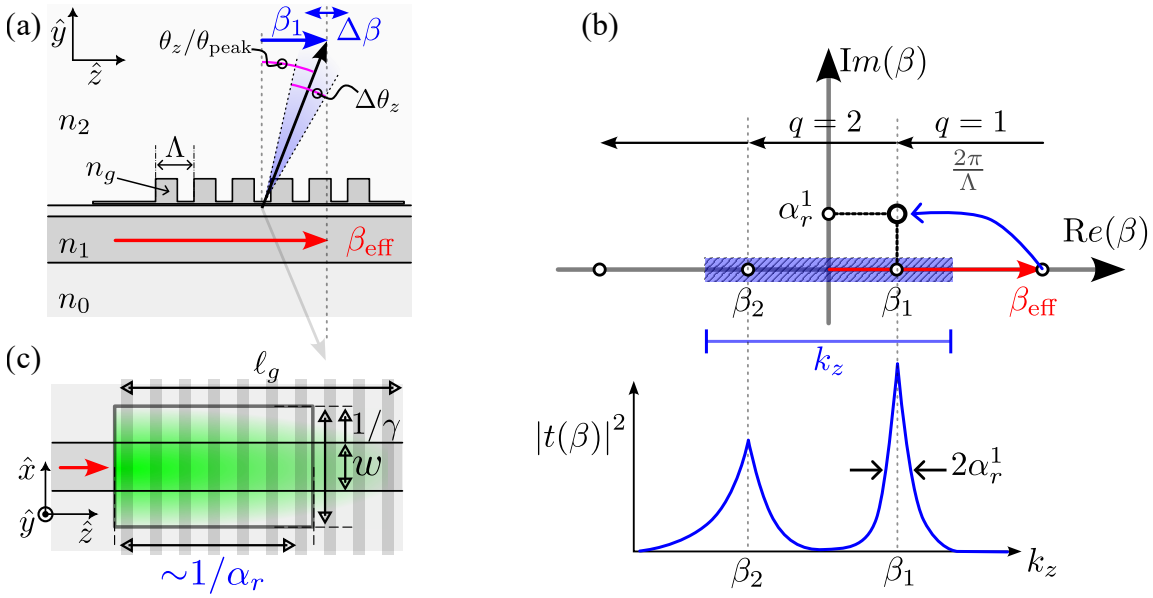

Figure 2.13: (a) Illustration of the resonance width $\Delta\beta$ of the phase matching assisted by the periodic grating between β_{eff} and β_1. (b) Illustration of the phase matching or coupling between β_{eff} and a complex pole $\beta_1 + i\alpha_r^1$. (c) Illustration of the effective aperture of the near-field, which defines the extraction divergence in the far-field.

We can use the two half-maximum angles, $\arcsin[(\beta_1 \pm \alpha_r)/(n_2 k)]$, to obtain $\Delta\theta_z$, the divergence in the z-direction. This divergence occurs within the cover medium with a refractive index of n_2. Note that the divergence is centered on the order angle given by $\theta_{\text{peak}} = \arcsin\big(\beta_1/(n_2 k)\big)$

(Equation (2.20)). By differentiating θ_{peak} and knowing that $\Delta\beta_1 = 2\alpha_r$, we obtain the following expression in degrees [125]:

$$\Delta\theta_z\,(^\circ) \;=\; \frac{180}{\pi}\,\frac{\lambda\,\alpha_r}{\pi n_2\,\cos\theta_{\text{peak}}}, \tag{2.27}$$

For $\alpha_r = 0.02\,\mu\text{m}^{-1}$, $\theta_{\text{peak}} \approx 0^\circ$, $\lambda = 0.532\,\mu$m, and $n_2 = 1.5$, the resulting angular divergence is $\Delta\theta_z \approx 0.13^\circ$, which is narrow.

If we consider the diffraction profile of a square aperture of size a illuminated with a uniform amplitude, the resulting diffraction pattern follows a function of $sinc^2$. The FWHM of this diffraction is found at $2\sin(0.443\,\lambda/(n_2 a))$, or, under the small angle, at $0.886\,\lambda/(n_2 a)$.

In Equation (2.27), the relationship between $\Delta\theta_z$ and α_r can be interpreted as follows: The radiation near the waveguide extends over a characteristic length of approximately $1/\alpha_r$. This length can be regarded as an effective aperture. To match this equation with a uniformly illuminated aperture diffraction, the approximate length to consider is $0.886\pi/\alpha_r \approx 2.75/\alpha_r$. At this distance, only 6.2% of the guided amplitude remains in the waveguide. Figure 2.13(c) shows an illustration of the aperture that defines the divergence. The width is given by the physical width of the waveguide w plus the transverse attenuation $2/\gamma$.

Note that, to fully extract the mode, the length of the grating ℓ_g must be much greater than the characteristic extraction length $\gg 1/\alpha_r$. If $\ell_g < 1/\alpha_r$, the effective aperture will be defined by ℓ_g and not by $1/\alpha_r$.

Figure 2.14 shows an example of 3D FDTD simulation of the far-field.

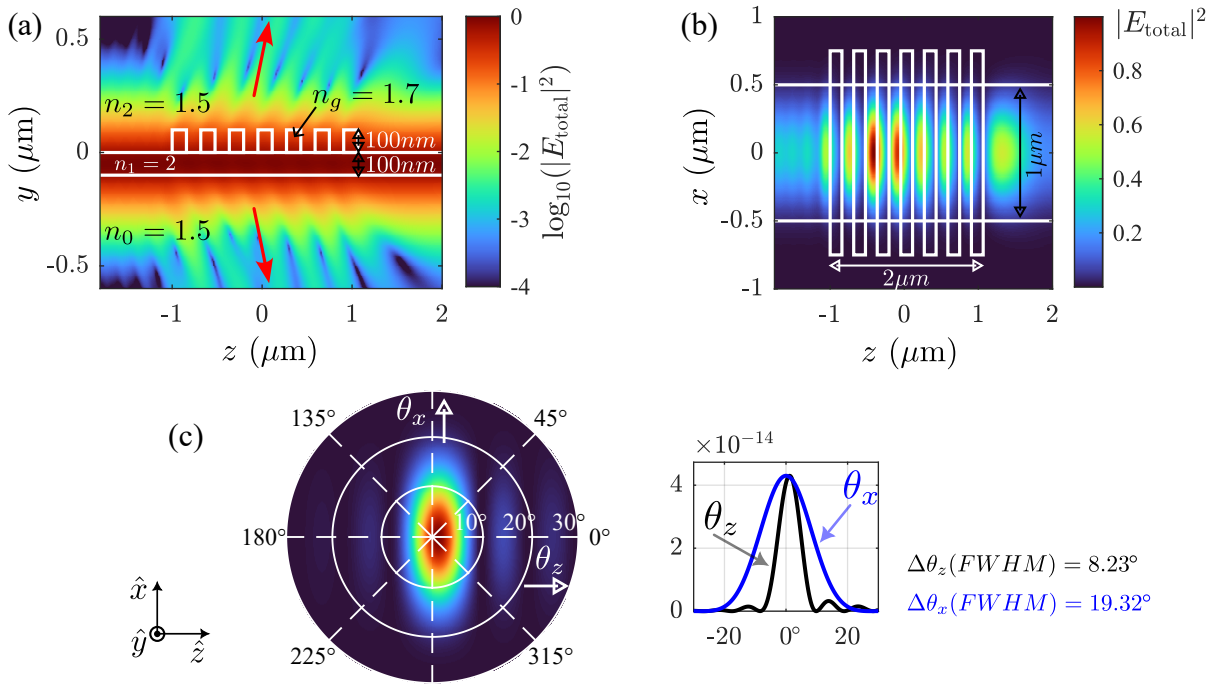

Figure 2.14: (a) Side view of a grating with a waveguide (logarithmic scale). (b) Top view of the near field. (c) Far-field distribution of the extracted radiation (divergence).
$n_0 = 1.5$, $n_1 = 2$, $n_2 = 1.5$, $\lambda = 0.532\,\mu$m, TE fundamental mode, $d = 0.1\,\mu$m, $d_g = 0.1\,\mu$m, $w = 1\,\mu$m, $\ell_g = 2\,\mu$m, $\alpha_r = 0.027\,\mu\text{m}^{-1}$

Figure 2.14(a) shows a side view on a logarithmic scale. The orders in the cover and the substrate are depicted by the red arrows. The grating period is set so that the first diffraction

order occurs at an angle of $\theta_z \approx 1°$. The guided mode is TE (along $\hat{x}$). We have $\alpha_r = 0.027\,\mu\text{m}^{-1}$ and $1/\alpha_r \approx 37\,\mu\text{m} \gg \ell_g = 2\,\mu m$. Only 5.2% of the optical power is extracted.

Figure 2.14(b) shows the near-field profile. The waveguide and grating structures are outlined with white lines. The power monitor is positioned close to the grating to capture both the evanescent decay of the guided mode and the local effect of the grating. The effective aperture can be taken as $2\,\mu\text{m} \times 1\,\mu\text{m}$. We neglect $1/\gamma \sim 0.1\,\mu\text{m}$ since the waveguide width is large. Figure 2.14(c) shows the far-field profile. The angular spread in the z-direction is approximately half that in the x-direction. We plot intensity profiles around the maximum in both directions. The solid black line corresponds to θ_z, with a half-width of 8.23°. The solid blue line corresponds to θ_x, with a half-width of 19.32°. Using the diffraction formula $0.886\lambda/(n_2 a)$ for a rectangular aperture of $2\,\mu\text{m} \times 1\,\mu\text{m}$, we get $\Delta\theta_z = 9.05°$ and $\Delta\theta_x = 18.4°$. As an approximation, this is in good agreement with the simulation.

2.4.4 Polarization

In microdisplays that use polarization modulation, such as LCDs and LCoS or in our application, where liquid crystals are used to modulate the extracted light, it is important to understand the polarization extinction ratio (PER). PER describes the ratio between the desired and undesired polarization. The intensity of the far-field can be decomposed as $|E_{\text{total}}|^2 = |E_x|^2 + |E_y|^2 + |E_z|^2$. The desired polarization along $\hat{x}$ can be achieved by increasing the weight of the $|E_x|^2$ component. The PER is angle-dependent. For polarization along $\hat{x}$, PER corresponds to the ratio $|E_x|^2/(|E_y|^2 + |E_z|^2)$.

Figure 2.15 (a) shows the far-field for the guided TE mode. The total intensity profile $|E_{\text{total}}|^2$ is plotted on a logarithmic scale to highlight the lobes of the oscillatory characteristic of aperture diffraction. On the right, a schematic of the grating and the waveguide are presented. TE is along $\hat{x}$. The extraction is shown with two arrows. We expect the polarization to be along $\hat{x}$. Each intensity component is plotted separately. The components are normalized by the maximum of the total intensity $\max(|E_{\text{total}}|^2)$. This maximum is at the angle of extraction $\theta_z \approx 1°$. The far-field is computed inside the medium with $n_2 = 1.5$ and is cropped to a 30° window.

The $|E_x|^2$ component is dominant, indicating that the polarization is well preserved. The PER exceeds 1,000:1 in the center of the far-field. The overall PER within this 30° window is around 1,000:1.

Figure 2.15 (b) shows the far-field for the guided TM mode. On the right, a schematic of the grating and the waveguide are presented. TM is along $\hat{y}$. The extraction angle is $\theta_z \approx 1°$, very close to vertical; thus, we expect the polarization of the extracted signal to be predominantly along $\hat{z}$. Compared to TE, the intensity exhibits some differences. Around $\theta_z \approx 50°$, a secondary lobe reaches 18% of the maximum intensity. In fact, the TM mode is vertically polarized, making it more sensitive to discontinuities as it interacts with the grating. This is observed in the oscillation lobes, which are slightly more pronounced than in the TE case. Note that the length of the grating is only 2 μm (7 ridges of the grating), which also explains the secondary lobes. If we increase the grating length, the main diffraction lobe becomes much more dominant.

The dominant intensity component is $|E_z|^2$. The overall PER within this 30° window is around 15:1, which is very low. This is due to the component $|E_x|^2$. The impact of the component $|E_y|^2$ on the PER occurs around the angle $\theta_z = 50°$, which is outside of this window.

When designing gratings, the polarization behavior should be considered. TE polarization

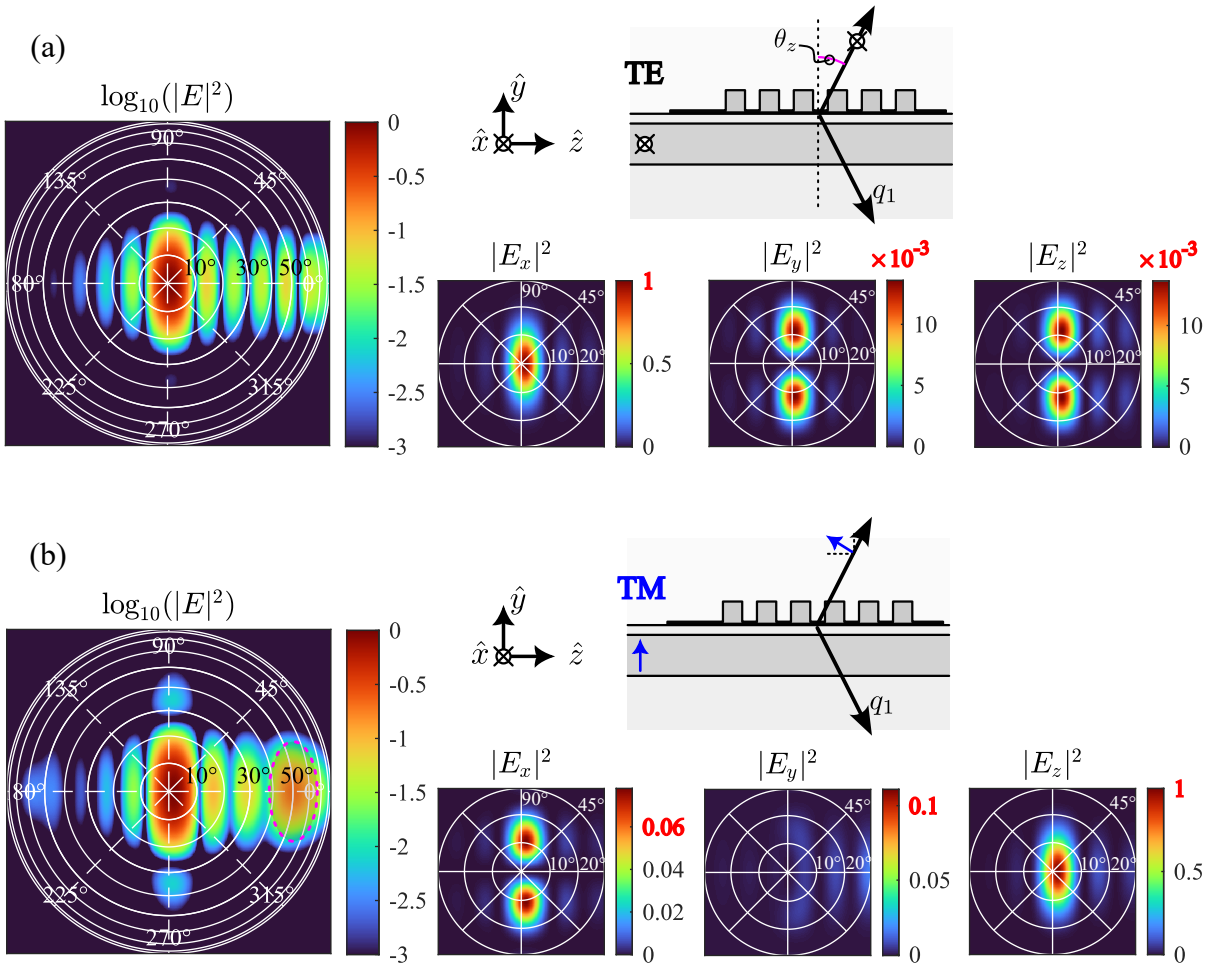

Figure 2.15: (a) TE guided mode (along $\hat{x}$). The total intensity is given by $|E_{\text{total}}|^2 = |E_x|^2 + |E_y|^2 + |E_z|^2$ and is plotted on a logarithmic scale. $|E_x|^2$, $|E_y|^2$, and $|E_z|^2$ are shown separately over a divergence window of 30°. (b) TM guided mode (along $\hat{y}$); the rest is similar to (a). The components are normalized by the maximum of the total intensity $\max(|E_{\text{total}}|^2)$. The waveguide and grating parameters are: $n_0 = 1.5$, $n_1 = 2$, $n_2 = 1.5$, $n_g = 1.7$, $\lambda = 0.532\,\mu$m, $d = 0.1\,\mu$m, $d_g = 0.1\,\mu$m, $w = 1\,\mu$m, $\ell_g = 2\,\mu$m, $\alpha_r = 0.027\,\mu\text{m}^{-1}$.

yields better performance compared to TM.

2.4.5 Conclusion

In this section, I discussed the extraction by a diffraction grating. The activation will be addressed in the following chapter 3, after the introduction of the ferroelectric liquid crystal (FLC). A typical value for the extraction length with this approach is $1/\alpha_r = 100\,\mu$m. For single-order diffraction, radiation exists in both the cover and the substrate. The divergence is directly related to the effective aperture defined by $1/\alpha_r$ and the effective width of the waveguide w_{eff}. The extraction polarization of the TE yields better performance than that of the TM mode. The grating equation (Eq. (2.20)) and the radiation decay constant (Eq. (2.24)) are wavelength dependent. RGB with the same extraction angle requires three waveguides with the same n_{eff}.

2.5 Evanescent Coupling: Innovative Extraction Approach

The component described here is patented by us. It offers several advantages for light extraction. In the first section, I provide an overview of its working principle, followed by a discussion of the physical details in the subsequent sections.

2.5.1 Overview of the Approach

In Figure 2.16(a), I show an illustration of the working principle of our innovative approach. The mode is coupled from the waveguide with refractive index n_1 to another layer with refractive index n_3. Within this layer, an inclined interface reflects the radiation into free space by total internal reflection (TIR). The key elements are the following: the value of n_3 is locally increased and represents the liquid crystal. The inclined interface is a prismatic structure immersed in n_3. The layer with refractive index n_3 can be considered as a second waveguide above the main waveguide. In general, as we will see later, due to the thickness and width of this layer, we may refer to it as a lightguide.

In Figure 2.16(a), we show four regions. In region (1), the value of n_3 is low and close to the value n_2. The evanescent part of the mode reaches this layer. As the mode enters region (2), n_3 is locally increased. The coupling strength depends on the separation s. This parameter will be important for the radiation constant α_r. In region (3) the radiation is incident from a high index medium to a low index medium. By TIR, the radiation is extracted into the free space. In region (4), the value of n_3 is low.

Figure 2.16(b) shows the composition of this structure. (A) is our photonic chip, where the waveguides route the light from the laser source to the pixels. (B) is a chip that contains only the prismatic structures. These are fabricated using high-refractive-index resin and nanoimprint lithography (NIL). (C) is a liquid crystal layer sandwiched between (A) and (B).

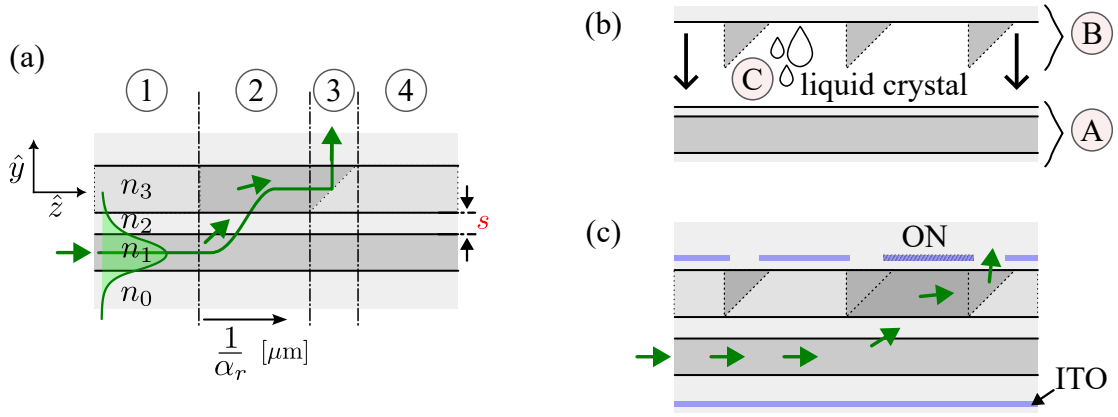

Figure 2.16: (a) Working principle of this innovative approach. The mode in the layer n_1 reaches the layer of refractive index n_3 through its evanescent part. The value of n_3 can be locally increased, as shown in region (2), allowing the mode to leak into this layer. n_3 represents a liquid crystal. In region (3), a prismatic interface reflects the radiation into free space by total internal reflection. (b) Composition: (A) the waveguides chip, (B) a transparent substrate with the prismatic structure, and (C) a liquid crystal. (c) An applied voltage locally increases n_3 to enable extraction.

Figure 2.16(c) shows the activation process. Indium tin oxide (ITO) electrodes are activated, and the ON state locally increases the refractive index. The mode is then coupled and extracted

by TIR. When this electrode is deactivated and the next one is activated, the TIR shifts by one column. In our μdisplay, the image is formed sequentially, column by column.

2.5.2 *k*-space: Parallel and Oblique Coupling

The coupling of modes from one waveguide to another is possible, but it requires a phase-matching condition. Coupled-mode theory (CMT) [115, 121, 125, 126] provides well-established results.

For simplicity, suppose that two waveguides are close enough for the evanescent field of one to reach the other. In order to couple the power from one mode to another, these two modes must have the same propagation constant β. This can be illustrated by the following analogy. Imagine two trains moving in the same direction. If they travel at the same speed and are close enough, two people on the trains can exchange objects and communicate. Air friction is neglected. When phase matching is satisfied, the power transfer between the two modes is optimal.

In Figure 2.17(a), the mode β_{eff} is coupled into the high index layer n_3. β_{eff} is phase-matched with the longitudinal component k_z. The coupling angle θ_3 is given by:

$$\theta_3 = \arcsin\left(\frac{n_{\text{eff}}}{n_3}\right). \tag{2.28}$$

Since coupling requires the matching of longitudinal components, this coupling can also be called *longitudinal coupling* [121].

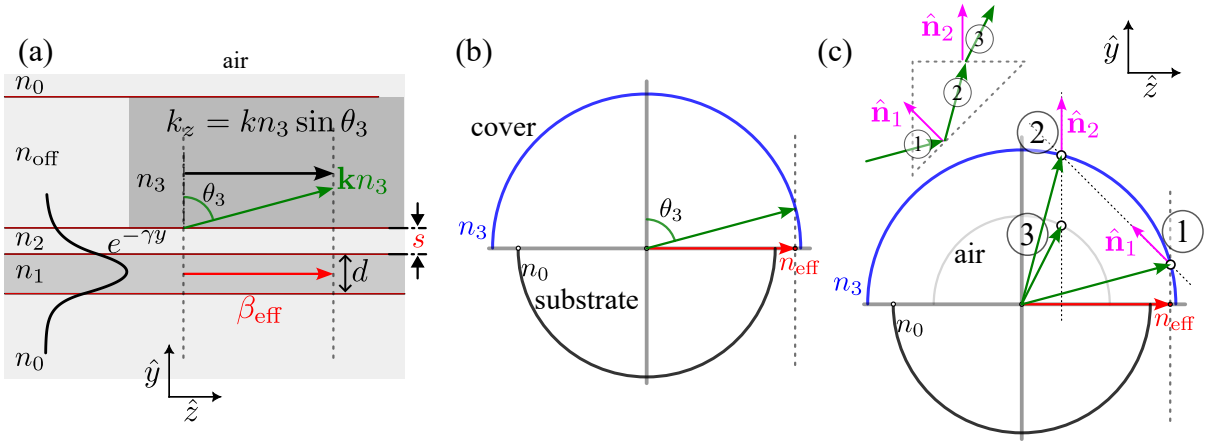

Figure 2.17: (a) Evanescent coupling of the guided mode β_{eff} and the phase-matching condition $n_{\text{eff}} = n_3 \sin(\theta_3)$. (b) *k*-space representation of this coupling. (c) *k*-space of the coupling and the effect of the prism on the coupled vector.

In Figure 2.17(b), I show *k*-space representation. n_3 must be at least greater than or equal to n_{eff} ($n_3 \geq n_{\text{eff}}$). The coupling is then possible. The angle θ_3 is found by translating n_{eff} until it intersects the perimeter of the circle n_3. Refer to Section 2.4.1 in the grating section if you are not familiar with this representation.

In Figure 2.17(c), I show the result of the prismatic interface. The prism reflects the incident radiation. $\hat{n}_1$ denotes the normal to the first interface. To find the new angle after reflection, project the tip of the vector from (1) to (2) until it intersects the perimeter of the circle n_3. When extracting to air, project the tip from (2) to (3) until it intersects the perimeter of the circle for air.

The evanescent coupling from Figure 2.17(a) can also be used in reverse as an in-coupler to couple an incident collimated beam into the guided mode, usually by using a high-index prism. This is known as a prism coupler. The articles by Ulrich and Tien [112, 127] discuss this in detail. Ulrich's work is of particular interest as the analytical expressions he derived match our simulation results. This provides valuable insight into the influence of each parameter. In (a), the separation s, or the gap between the waveguide and the high index layer, is the key parameter. The coupling depends on the evanescent field. The radiation constant α_r for this component has an exponential dependence on s and the penetration of the field $1/\gamma$, as $\exp(-2\gamma s)$. This will be discussed in the section of radiation decay constant.

The refractive index n_2 of the separation layer must be lower than n_1 so that the mode in the core is confined. The mode couples through this separation by optical tunneling [121]. In the reverse case, as a prism in-coupler, the incident beam must satisfy the TIR condition at the interface $n_3 \rightarrow n_2$ so that the evanescent part excites the mode.

In Figure 2.17(a), we used the propagation constant β_{eff} in the extraction region. This is a good approximation; however, a slight change $\delta\beta$ must be taken into account, as shown in Equations (2.15) and (2.16). This will be discussed later.

The operation of the prismatic structure on the coupled radiation shown in Figure 2.17(c) is only intended to prepare the reader. In the following section, I discuss the coupling characteristics in a flow similar to the extraction by a diffraction grating. The full picture of the prismatic structure and the component with the liquid crystal is discussed in the next chapter.

Let us give the following definitions based on the value of θ_3:
→ **Parallel Coupling**: $\theta_3 = 90°$ or $n_{\text{eff}} = n_3$. If the dimensions (thickness and width) of the n_3 layer are small and similar in size to the waveguide, the condition $n_{\text{eff}} = n_3$ for parallel phase matching must be replaced by $n_{\text{eff},1} = n_{\text{eff},3}$, where these two are the effective indices of the mode in waveguide 1 (lower) and waveguide 2 (upper, layer n_3). The condition $n_{\text{eff}} = n_3$ implies that we consider the n_3 layer as a lightguide, meaning it can support tens or even a larger number of modes. The number of modes $N \times M$ supported by a channel guiding structure with core refractive index n_3 and substrate and cover of index n_0 can be estimated by [121]:

$$N_{\text{TE}} = N_{\text{TM}} \approx \left\lfloor \frac{2}{\lambda} d \sqrt{n_3^2 - n_0^2} \right\rfloor, \quad M_{\text{TE}} = M_{\text{TM}} \approx \left\lfloor \frac{2}{\lambda} w \sqrt{n_3^2 - n_0^2} \right\rfloor \tag{2.29}$$

d and w are the thickness and width of the waveguide. For $n_3 = 1.8$, $n_0 = 1.5$, $\lambda = 0.532\,\mu$m, $d = 2\,\mu$m, and $w = 10\,\mu$m, we get $N = 7$ and $M = 37$, giving a total number of 259 modes.
→ **Oblique Coupling**: $\theta_3 < 90°$. The coupled radiation has a transverse component and, depending on the thickness of the n_3 layer, it can be reflected at the upper interface.

2.5.3 Evanescent Coupling: Parallel / Directional Coupler

Our innovative extraction component was inspired by a common component used in integrated photonics. The directional coupler where the power can be transferred from one waveguide to another, either in the plane (xz) or vertically.

Figure 2.18(a) presents two waveguides, a and b. The power is in the waveguide a in the mode β_a. As this waveguide approaches the other, the evanescent field in the waveguide a excites the mode β_b in the waveguide b.

The longitudinal component must be matched ($\delta = 0$) for optimal coupling, where δ the

phase matching condition is:

$$2\delta = (\beta_b \pm \delta\beta_b) - (\beta_a \pm \delta\beta_a) \tag{2.30}$$

$\delta\beta$ is the slight change in the propagation constant in the coupling region.

In Figure 2.18(a), we illustrate the coupling constants κ. Those can be determined from the coupled-mode theory (CMT). κ has the same dimension as the propagation constant β (units of μm^{-1}). κ_{ab} describes the coupling strength from a to b, and κ_{ba} from b to a. κ_{aa} is the self-coupling term for a, which is $\delta\beta_a$. Similarly, $\kappa_{bb} = \delta\beta_b$. To find the coupling constants, the field distributions of the modes a and b are needed, as well as the refractive index profile. κ is calculated as an overlap of the fields. Some equations can be found in [121, 126]. The integrals are taken over the perturbation region; outside the waveguide, the mode is exponentially evanescent. Consequently, these constants depend on the separation s and follow an exponential trend: $\kappa \propto \exp(-\gamma s)$.

Figure 2.18(b) shows the effective indices of the waveguides a and b. In (1), there is phase matching between the fundamental modes. If we propagate this mode and approach the second waveguide, the transfer is possible. In (2), there is a phase mismatch; the coupling is not efficient and will depend on the value given by Equation (2.30). In (3), there is no available possibility for coupling.

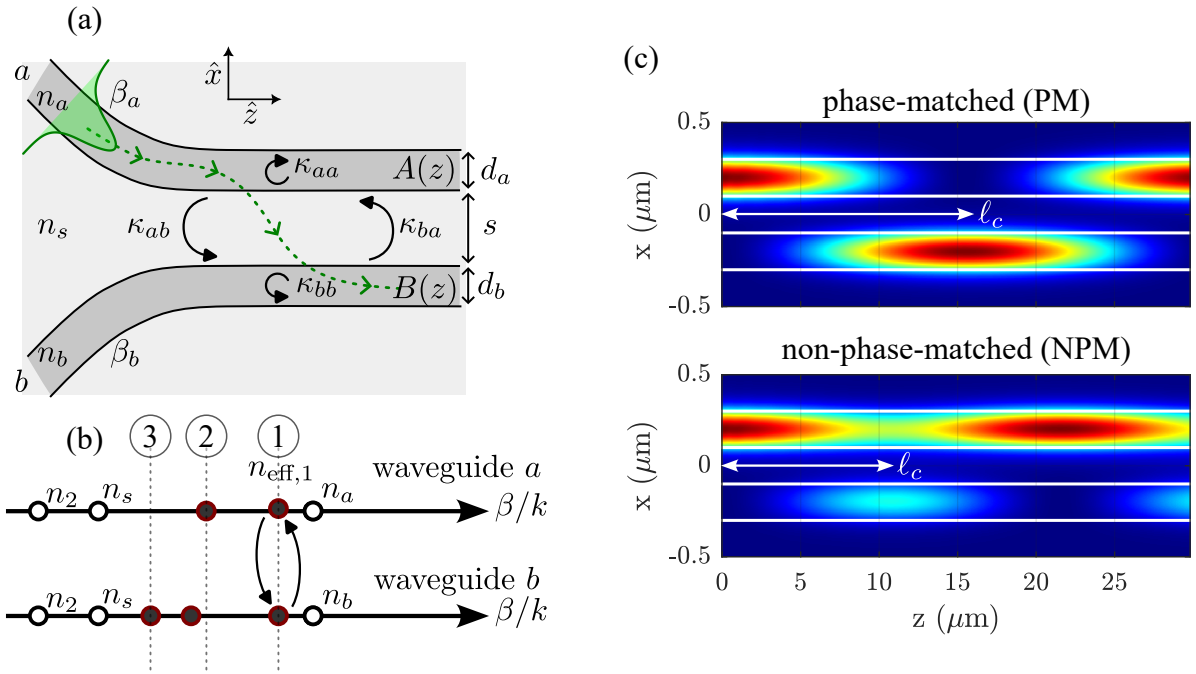

Figure 2.18: (a) Schematic of a directional coupler showing the coupling constants κ. (b) Phase-matching conditions between the modes in waveguide a and waveguide b. (c) Simulation of a directional coupler under phase matching. Below, a mismatch case is shown where the refractive index difference between the waveguides is 0.02.

Here is an expression for the coupling constant κ for the fundamental modes in symmetric waveguides under weak perturbation, cf. [126]:

$$\kappa = 2\frac{\sqrt{n_1^2 - n_s^2}}{n_{\text{eff}}\, d_{\text{eff}}} \exp\left\{-\gamma\left(s + \frac{d}{2}\right)\right\} \tag{2.31}$$

The word **symmetric** means that $n_1 = n_a = n_b$ and $d = d_a = d_b$, so $\kappa = \kappa_{ab} = \kappa_{ba}$.

We can think of κ (μm^{-1}) in a way similar to the radiation decay constant α_r. In this case, $1/\kappa$ is also a characteristic length of the coupling. Using CMT, we can solve the system for the amplitudes $A(z)$ and $B(z)$ in waveguides a and b [121]. We consider the initial condition where the power is in the waveguide a before entering the coupling region: $A(z = 0) = A_0$ and $B(z = 0) = 0$.

The efficiency of the coupling can be written as follows:

$$\eta = \left|\frac{B(z)}{A(0)}\right|^2 = \frac{1}{1 + \left|\frac{\delta}{\kappa}\right|^2} \sin^2\left(\kappa.z\sqrt{1 + \left|\frac{\delta}{\kappa}\right|^2}\right) \tag{2.32}$$

The maximum coupling efficiency is given by:

$$\eta_{\max} = \frac{1}{1 + \left|\frac{\delta}{\kappa}\right|^2} \tag{2.33}$$

In phase matching ($\delta = 0$), 100% transfer is possible. As presented in Equation (2.32), the coupling efficiency depends on the propagation distance z, the coupling coefficient κ, and the phase mismatch δ. The quantity $\eta(z)$ oscillates as a function of z, which means that the power is transferred back and forth between the waveguides a and b. These oscillations are periodic. The maximum power transfer occurs at coupling distances $z = (2m + 1)\,\ell_c$, where $m \in \mathbb{N}$ and ℓ_c is the characteristic coupling length, given by half the oscillation period:

$$\ell_c = \frac{\pi}{2\kappa\sqrt{1 + \left|\frac{\delta}{\kappa}\right|^2}} \tag{2.34}$$

The maximum efficiency $\eta_{\max}(\delta)$ follows a Lorentzian profile, which is typical of resonance phenomena. The bandwidth FWHM (full width at half maximum) of this resonance profile is given by 2κ.

In Figure 2.18(c), an FDTD simulation of directional coupling is presented. A phase-matched case is shown where the waveguides are kept symmetric. Symmetric coupling is by default always phase matched. In the second simulation, we introduced **asymmetric** coupling by reducing the refractive index of the waveguide b by 0.02. As a result, the coupling is no longer optimal and full transfer does not occur.

In Figure 2.19(a), the coupling efficiency is plotted as a function of the propagation distance z. Two cases are considered: a phase-matched condition ($\delta = 0$) and a phase-mismatched condition ($\delta = 0.11\ \mu m^{-1}$). The coupling coefficient is set to $\kappa = 0.095\ \mu m^{-1}$ to match the conditions used in the previous Figure 2.18(c).

In Figure 2.19(b), the Lorentzian profile of the maximum coupling efficiency is plotted as a function of the phase mismatch normalized by the coupling constant κ. The full width at half maximum (FWHM) of this curve is equal to 2.

For symmetric waveguides where waveguides a and b have the same geometry and materials, the phase-matching condition is always satisfied, regardless of the wavelength. The maximum coupling efficiency at the coupling length reaches 1. Only the coupling length depends on the wavelength.

For asymmetric coupling, the phase-matching condition is not automatically satisfied. The propagation constants, or the effective indices, are different, and the dispersion $n_{\text{eff}}(\lambda)$ is also

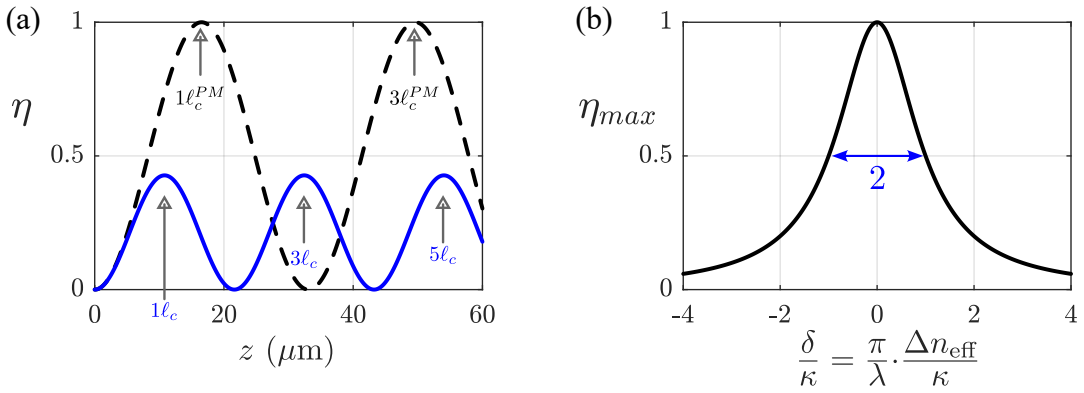

Figure 2.19: (a) Power exchange for $\kappa = 0.095\ \mu\text{m}^{-1}$: phase-matched case ($\delta = 0$, dashed) and phase-mismatched case ($\delta = 0.11\ \mu\text{m}^{-1}$, solid blue). (b) Lorentzian profile of the maximum coupling efficiency.

different. However, at a fixed wavelength, n_{eff} can be designed by tuning the geometry of one waveguide to achieve phase matching. A section on asymmetric directional couplers can be found in the Appendix.

In the schematic shown in the previous Figure 2.18(a), the waveguides are aligned in the same $\hat{x}$-direction. However, our component has two levels: the first level contains the waveguides for light distribution, and the second level is the liquid crystal layer, as illustrated in Figure 2.16. We couple the light in the $\hat{y}$-direction. From the first level to the second. The layers n_3 and n_1 are therefore asymmetric.

The directional coupler is a fascinating component, as it enables the transfer of power from one guiding structure to another. This component, which is common in integrated photonics, inspired us for our extraction principal. After transferring the power, the prismatic structure redirects to free space, without diffraction orders involved.

However, the n_3 layer is large in width (slab) and in thickness (1–3 μm), and supports a large number of modes. This is large compared to the waveguides of geometry (200 $nm \times 300\ nm$). The power does not bounce back and forth as in a directional coupler. In phase matching, the power **leaks** into the n_3 layer with a certain divergence that depends on the resonance width (through α_r, which we will discuss further) and the width of the waveguide.

In the following sections, as we will see in the leakage. The radiation decay constant of leakage will have the form $\alpha_r \propto \exp(-2\gamma s)$. This is quite close to κ (Equation (2.31)) of the directional coupler, which describes the strength of the coupling and the involvement of the evanescent part in exponential form.

The general term *evanescent coupling* is used, since the phenomenon involves γ. This includes the directional coupling and the leakage assisted by the evanescent part. To distinguish the nature of the leakage from that of the directional coupler, I used the word "parallel" and "oblique". For parallel, the coupling angle is 90°. The radiation direction is parallel to the propagation constant of the mode. For both parallel and oblique, the coupling occurs through leakage, with no back-and-forth oscillation.

2.5.4 Evanescent Coupling: Oblique Coupling

The leakage condition is $n_3 \geq n_{\text{eff}}$. The longitudinal component of the mode matches a radiation at an angle given by $\theta_3 = \arcsin(n_{\text{eff}}/n_3)$. $\theta < 90°$ is oblique for $n_3 > n_{\text{eff}}$. As n_3 increases, the obliquity also increases.

To consider the n_3 layer as a free propagation zone, its dimensions should be infinite. However, such a condition is not feasible in simulations, especially in FDTD methods, which are computationally expensive with size. A practical approach is to apply certain approximations, perform convergence tests, or assume that a free propagation regime is achieved when the dimensions are much larger than the wavelength, typically when $\gg 10\lambda$.

The following 3D FDTD simulation in Figure 2.20 shows the coupling angles for $n_3 = 1.8$ and $n_3 = 1.9$. The mode is the fundamental TE with $n_{\text{eff}} = 1.701$ and dimensions $d = 0.2\ \mu$m and $w = 0.3\ \mu$m. The layer n_3 starts at $z = -4.5\ \mu$m. For $z \leq -4.5\ \mu$m, the refractive index is $n_2 = 1.46$. The boundaries of the n_3 layer (upper and edges) are set to absorb the fields, allowing leakage without reflections.

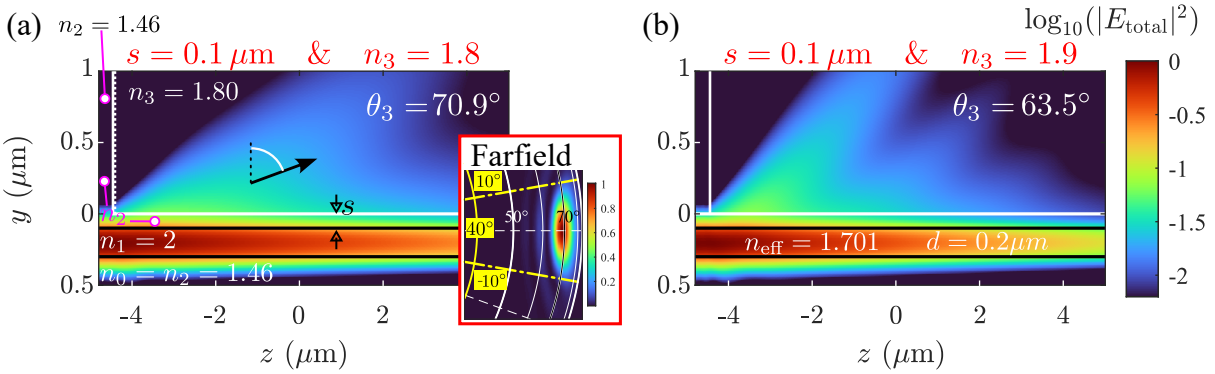

Figure 2.20: Evanescent coupling into the high-index layer n_3. The coupling is oblique at an angle $\theta_3 = \arcsin(n_{\text{eff}}/n_3)$. (a) For $n_3 = 1.8$. (b) For $n_3 = 1.9$. The remaining parameters are indicated in the figure. The waveguide width is $w = 0.3\ \mu$m and $\lambda = 0.532\ \mu$m.

In the following Figure 2.21, I present some visual cuts of the coupling. (a) shows the profile in the waveguide. The power is attenuated as a function of z. (b) shows the leakage profile within the n_3 layer; this cut is at $y = 2\ \mu$m. Here, $y = 0$ is set as the start of the n_3 layer. Additional cuts at different positions y are shown in (c). As y increases, the red spot shifts in the z-direction and increases in size in both directions. The shift occurs simply due to the coupling angle θ_3. The increase in size is caused by the divergence around the coupling angle.

In Figure 2.21(d), a transverse profile of the coupling is shown in the high-index layer n_3. $z_\ell = 0$ marks the beginning of the layer. The narrow profile around ($x = 0$, $y = 0$) is the evanescent part coming from the waveguide below (not shown). The evanescent part tunneling through the separation $s = 0.1\ \mu$m excites the leakage. As z_ℓ increases, more leakage occurs. These figures are normalized to show the profile distribution. A percentage coupling is indicated. At $z_\ell = 0$, the coupling is 0%; the evanescent part of the mode is not included since it is part of the guided mode. The percentage values are calculated based on the attenuation of the guided mode. The mode power decays in the form $\exp(-2\alpha_r z)$ (see Section 2.2.3 for the definition of α_r). Here, $\alpha_r = 0.1\ \mu\text{m}^{-1}$.

The main information required is as follows: first, the angle θ_3 or θ_{peak}. In contrast to diffraction, we have a single peak. The angle can be found approximately using n_{eff} and n_3.

Second, α_r, which gives us the longitudinal extent of the spot in the near field. The size in the other direction can be estimated using the mode width. Third, the divergence, which is related to α_r. With this information, the evolution of the spot can be estimated at different positions.

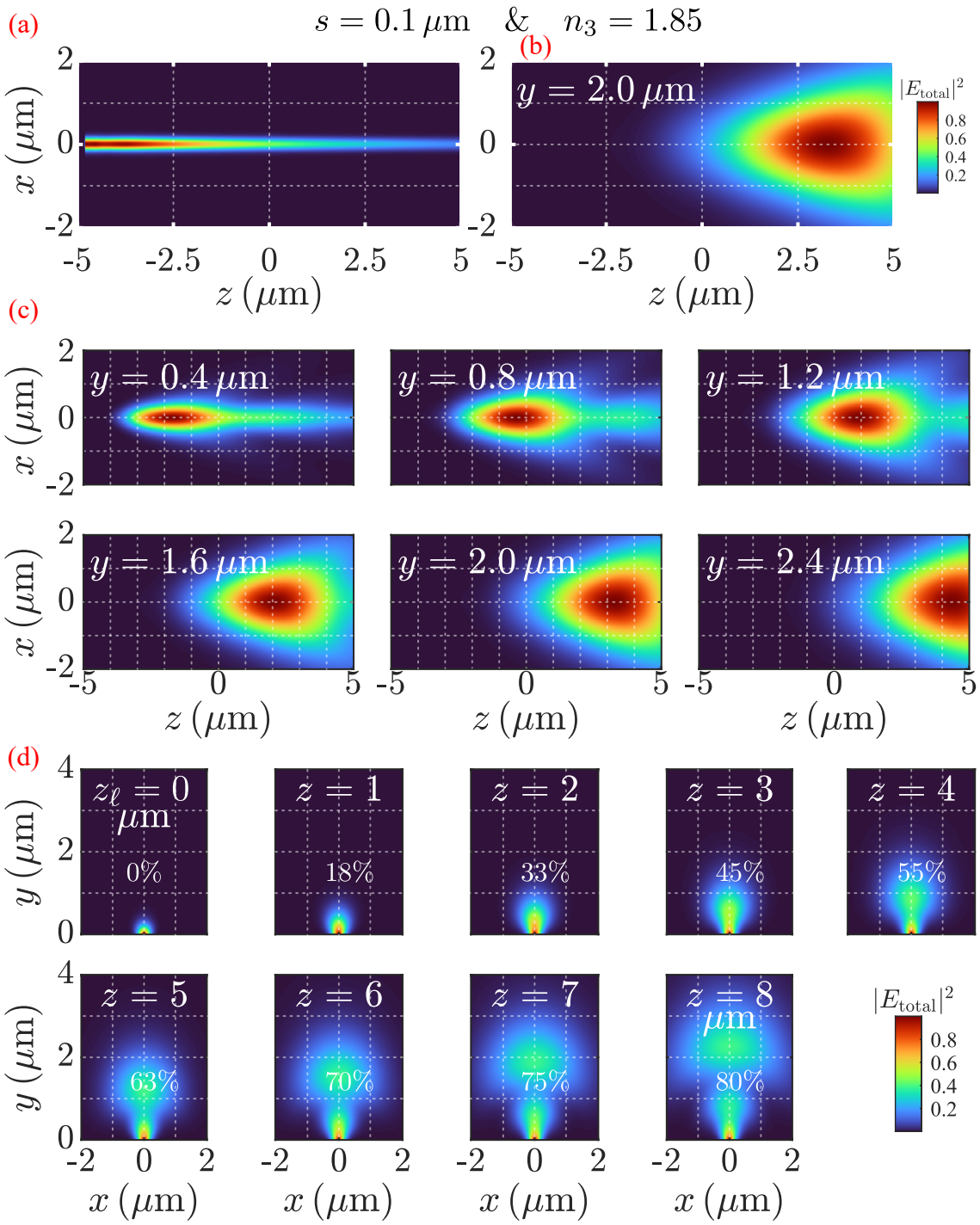

Figure 2.21: Evanescent coupling into the high-index layer n_3. Different cuts are presented: (a) the waveguide profile in the (xy) plane. (b) the high-index layer n_3 at $y = 2\,\mu$m ($y = 0$ starts at the beginning of the n_3 layer). (c) different (xy) cuts for various y positions. (d) the transverse profile in the high-index layer at different coupling distances. The percentages do not include the power from the evanescent part from the waveguide.

2.5.5 Radiation Decay Constant

We are interested in the radiation decay constant α_r, which describes the rate at which power leaks into the high-index layer. For prism in-couplers, Liu [121] mentioned that α_r has an exponential dependence of the form $\exp(-2\gamma_2 s)/d_{\text{eff}}$, where s is the separation between the waveguide and the high-index layer and $\gamma_2 = \frac{2\pi}{\lambda}\sqrt{n_{\text{eff}}^2 - n_2^2}$. Elsewhere, using a combination of wave and ray optics, Tien and Ulrich [127] present a detailed theory of the prism–film coupler. Ulrich paper [112] provides insightful results. In his paper, Ulrich uses a plane-wave expansion analysis. I will use his results in the reverse case, to couple from the n_1 layer to n_3.

In the following analysis, the equations are valid for a slab structure but can be extended to 3D with a good approximation, provided that the change in n_{eff} is taken into account.

Let $k_z = \beta = kn_3 \sin(\theta_3)$ be the longitudinal component in the high-index layer. In phase matching, $\beta = \beta_{\text{eff}}$, where β_{eff} is the propagation constant in the waveguide n_1.

We define the following important coupling parameter h as:

$$h = \exp(-\gamma_2 s) \tag{2.35}$$

Other relevant equations include the Fresnel coefficient in Equation (2.5), the phase shift upon reflection in Equation (2.6), and the eigenvalue equation in Equation (2.10).

According to Eq. (58) in [112], the decay constant α_r is given by:

$$\alpha_r = \sin(2\phi_{12}) \sin(2\phi_{32}) \cdot \frac{2}{\chi} h^2 \tag{2.36}$$

where $\chi = -\frac{\partial \psi}{\partial \beta}$, ψ is the eigenvalue function defined in Equation (2.10), and ϕ_{ij} are the phase shifts upon reflection at the interface ij, as described in Equation (2.6).

Based on his analysis, Ulrich demonstrates a resonance phenomenon as a function of β. When the wave is incident at certain values of β or angle θ_3, a guided mode in the waveguide is excited. This occurs through a transfer function $t(\beta)$.

In Figure 2.22(a), I reproduce the same example from the article (Fig. 3 in [112]) to show the consistency of our MATLAB implementation. The vertical axis represents the energy density excitation inside the waveguide, which is proportional to $|t(\beta)|^2$. The horizontal axis is the normalized longitudinal component. The structure in (a) is multimode: at certain angles θ_3, we observe peaks corresponding to the resonances. These resonance points match the effective indices of the guided modes. As shown, the structure supports three TE modes, labeled with the subscript m. Three curves are plotted for three different separation values s. As s increases, the peak positions move closer to the exact effective indices of the waveguide modes, and the energy density increases.

At resonance, the value of beta can be written as:

$$\beta^{(pole)} = \beta_{eff} - \sin(2\phi_{12}) \cos(2\phi_{32}) \cdot \frac{2}{\chi} h^2 \tag{2.37}$$

In phase matching β does not exactly match the value of β_{eff}. As s increases, the coupling parameter h decreases and the resonance position shifts toward the guided mode propagation constant. The sign of the shift can be positive or negative; it depends on $\cos(2\phi_{32})$, since $2\phi_{32} \in [0, \pi]$.

Figure 2.22(b) shows a single-mode waveguide with thickness $d = 0.2\,\mu$m, and refractive indices $n_0 = 1.46$, $n_1 = 2$, $n_2 = 1.46$, and $n_3 = 2$, at a wavelength of 0.532 μm. The shift as

a function of s is opposite to the previous case. The peak resonance position of $s = 60\,\text{nm}$ is close to the effective index of the waveguide: $n_{\text{eff}} = 1.834$.

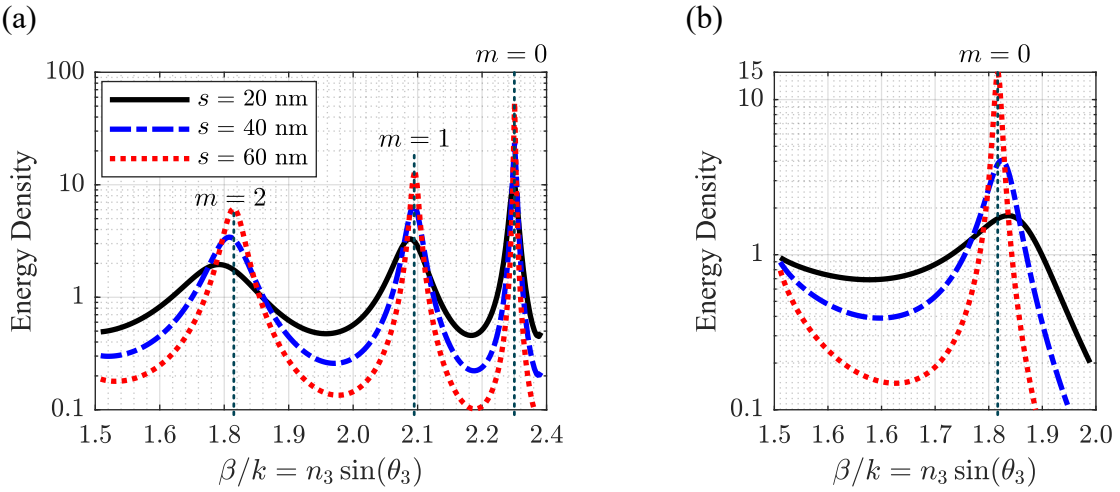

Figure 2.22: (a) Reproduction of Fig. 3 in [112], with $\lambda = 0.6328\,\mu$m, $n_0 = 1.52$, $n_1 = 2.35$, $n_3 = 2.87$, $n_2 = 1.00$, $d = 0.500\,\mu$m, TE polarization. (b) Our example: $\lambda = 0.532\,\mu$m, $n_0 = 1.46$, $n_1 = 2$, $n_2 = 1.46$, $n_3 = 2$, $d = 0.2\,\mu$m, TE polarization, $n_{\text{eff}} = 1.8329$.

In the following analysis, we verify the dependence of α_r versus the separation s, which is expected to be $\alpha_r \propto \exp(-2\gamma_2 s)$. Figure 2.23 shows a 2D FDTD simulation of α_r as function of s.

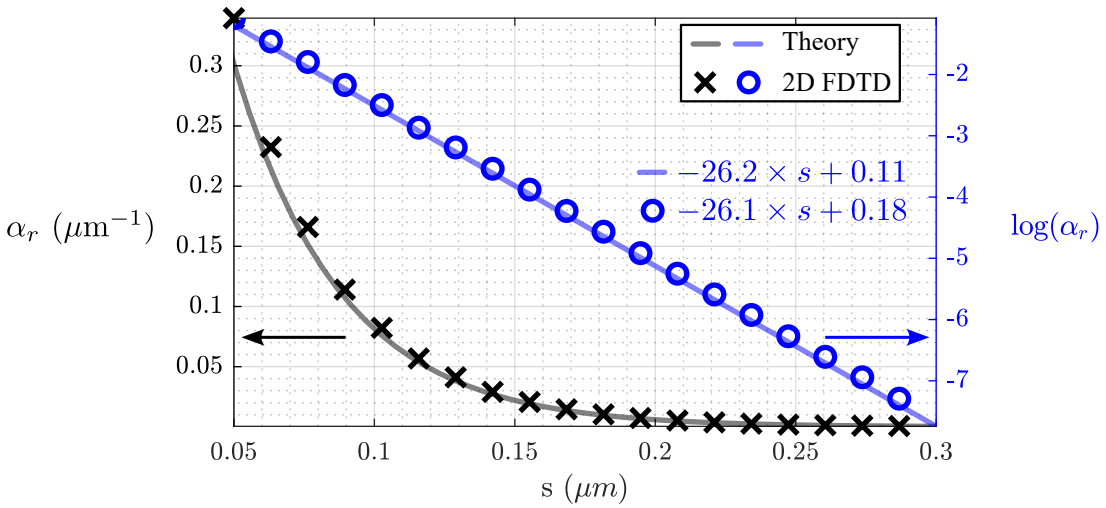

Figure 2.23: Radiation decay constant α_r as function of the separation s. Solid line is the theoretical model. The crosses are the simulations points. $\lambda = 0.532\,\mu$m, $n_0 = 1.46$, $n_1 = 2$, $n_2 = 1.46$, $n_3 = 2$, $d = 0.2\,\mu$m, TE polarization, $n_{\text{eff}} = 1.8329$

The solid line represents the theoretical model from before, while the crosses correspond to simulation results of the 2D FDTD. As expected, α_r varies exponentially with the separation s. On the right axis, we plot $\log(\alpha_r)$ to visualize its linear dependence on s, which is clearly observed. Circular markers indicate the simulated data points. The slope corresponds to $2\gamma_2$. Using $n_{\text{eff}} = 1.8329$ and $n_2 = 1.46$, we obtain a slope of -26.2, which is in good agreement with the values shown in the figure.

α_r are one order of magnitude higher for evanescent coupling compared to the grating. In the latter, the maximum values of α_r were around 0.01–0.02 μm^{-1}. In evanescent coupling, the values reach 0.1–0.4 μm^{-1}. The extraction length is thus approximately ten times shorter.

In Figure 2.24, I present results for the 3D geometry, with a waveguide width of $w = 0.3$ μm. (a) for TE with $n_{\text{eff}} = 1.7011$ and (b) for TM with $n_{\text{eff}} = 1.6686$.

To obtain theoretical predictions, I extended the slab model by adapting the core refractive index n_1. I applied the effective index method: in the x-direction, I considered a refractive index profile of 1.46 | 2 | 1.46 with $w = 0.3$ μm. I computed the effective index of the corresponding slab mode and used it as the new core refractive index n_1 in the y-direction. For example, for the guided TE mode, I first computed the effective index of the TM mode along x, obtaining $n_{\text{eff}} = 1.8698$, which replaced $n_1 = 1.8698$ in the slab model. Similarly, for the TM guided mode, I used the effective index of the TE mode along x, which is 1.9013, to replace n_1 in the theoretical slab calculation.

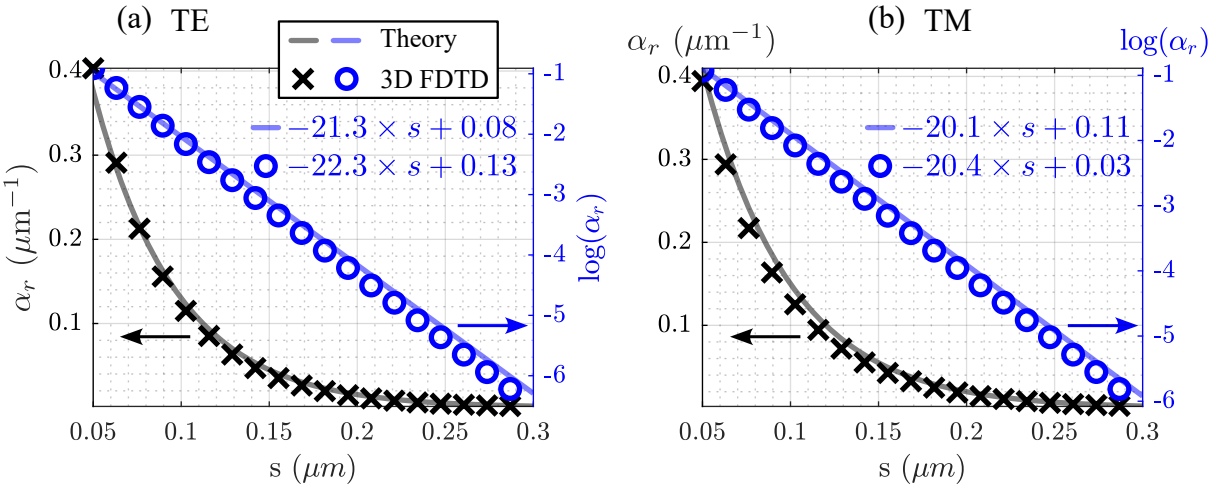

Figure 2.24: Radiation decay constant α_r as function of the separation s. Solid line is the theoretical model. The crosses are the simulations points. $\lambda = 0.532\,\mu$m, $n_0 = 1.46$, $n_1 = 2$, $n_2 = 1.46$, $n_3 = 2$, $d = 0.2\,\mu$m, $w = 0.3\,\mu$m. (a) is TE. (b) is for TM mode.

Compared to the slab case, the effective indices in this geometry are lower, indicating that the modes are less confined. This is reflected in the slightly higher values of α_r (about 1.2 times). The slopes of the simulation results are −22.3 for TE and −20.4 for TM. The theoretical slopes are −21.3 and −20.1, which show close agreement with the simulations. For the slab case, the agreement is even better. TE and TM exhibit approximately similar values of α_r.

As demonstrated earlier in equation (2.28), the refractive index n_3 plays a significant role in determining the extraction angle. n_3 also plays an important role in the radiation decay constant α_r. In Figure 2.25, this dependency is depicted. Markers represent simulated data points. The lines correspond to the theoretical predictions. The black curves are for TE and the blue curves are for TM. Figure 2.25(a) and (b) for the separations $s = 0.1$ μm and 0.05 μm, respectively. There is a clear threshold associated with the coupling condition $n_3 \geq n_{\text{eff}}$. The value of α_r increases with n_3 and reaches saturation.

The theoretical predictions do not perfectly fit the 3D simulation; however, they follow the same dependencies. The difference is due to the estimate n_{eff} and the adaptation of the slab model to the 3D simulation. In slab geometries, the theory matches the simulation very well. The theoretical model is presented here to demonstrate its usefulness for quick analysis.

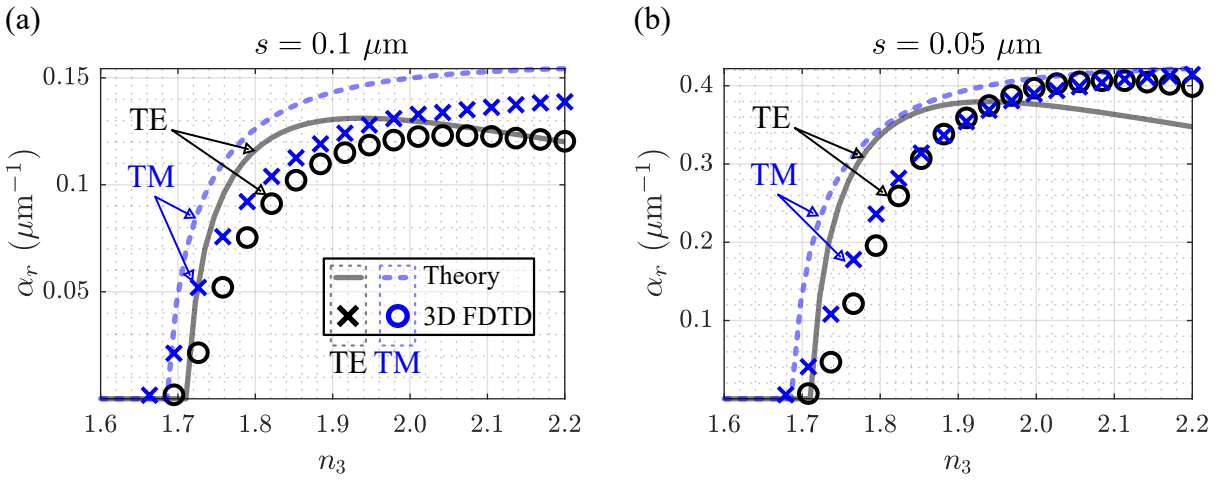

Figure 2.25: Radiation decay constant α_r as function of n_3. Solid line is the theoretical model. The crosses are the simulations points. $\lambda = 0.532\,\mu$m, $n_0 = 1.46$, $n_1 = 2$, $n_2 = 1.46$, $d = 0.2\,\mu$m, $w = 0.3\,\mu$m. (a) for $s = 0.1\ \mu$m. (b) for $s = 0.05\ \mu$m.

There is a trade-off between the coupling rate α_r and the coupling angle. As n_3 increases, the coupling angle deviates further from the longitudinal direction 90°. In (b), considering the TE mode with $n_{\text{eff}} = 1.7011$, and for $n_3 = 1.708$, the coupling angle is 84.8° (calculated using Equation (2.28)), but α_r remains low at 0.007 μm^{-1}. When $n_3 = 1.737$, α_r increases to 0.05 μm^{-1}, and the coupling angle decreases to $\theta_3 = 78.3°$.

In directional couplers, it is possible to achieve high values of the coupling constant κ. This is particularly interesting because it allows maintaining a 90° coupling angle while also achieving a high α_r. α_r and κ have the same physical interpretation, as they are related to an extraction/coupling length. However, in order to reach high κ, the thicknesses of the two waveguides must remain small, since κ depends on both the separation s and the thickness of the waveguide, as shown in the equation for symmetric coupling (2.31).

For our evanescent coupling, the thickness of the high-index layer is relatively large compared to that of the waveguide. This explains the low value of α_r for a high value θ_3 close to 90°.

According to the weak coupling approximation in [112], for accurate results, equation (2.35) must satisfy $h \leq 0.1$. In our case, this condition implies a minimum separation value of $s > 0.1\ \mu$m. However, even outside this limit, the theoretical equation provides very good results for rapid prototyping.

2.5.6 Angular Width of the Extraction

Near the poles, the Lorentzian expression for transmission is proportional to:

$$|t^{(\text{pole})}(\beta)|^2 \propto \frac{1}{1+\left(\dfrac{\beta-\beta^{(\text{pole})}}{\alpha_r}\right)^2} \tag{2.38}$$

This expression is similar to that given for the grating in Equation (2.26). The full width at half maximum (FWHM) of this resonance is $2\alpha_r$.

Similar to Equation (2.27), we can write the divergence in the z-direction as follows:

$$\Delta\theta_z\ (^\circ) = \frac{180}{\pi}\cdot\frac{\lambda\,\alpha_r}{\pi n_3\,\cos\theta_{\text{peak}}}, \tag{2.39}$$

In Figure 2.26(a), the far-field in the z-direction is plotted for three different separation values s. The solid curves correspond to a fit using the Lorentzian expression given in equation (2.38), while the dotted curves represent the results of a 2D FDTD slab simulation.

The curves for $s = 0.10$ and $0.15\ \mu$m fit well to the theoretical model. For $s = 0.05\ \mu$m, the positions and shapes of the peak show some discrepancies. In this later, the weak coupling approximation is indeed not valid as $h > 0.1$.

I calculate FWHM $= \Delta\theta_z$ of these curves and plot in Figure 2.26(b) the divergence in the z-direction as a function of s. The cross markers correspond to the simulation results, while the solid gray line represents the theoretical prediction based on α_r and Eq. (2.39). The theory matches the simulation. The divergence $\Delta\theta_z$ is directly related to the characteristic length $1/\alpha_r$. Recall that this length represents the distance over which only e^{-2} of the power remains in the waveguide.

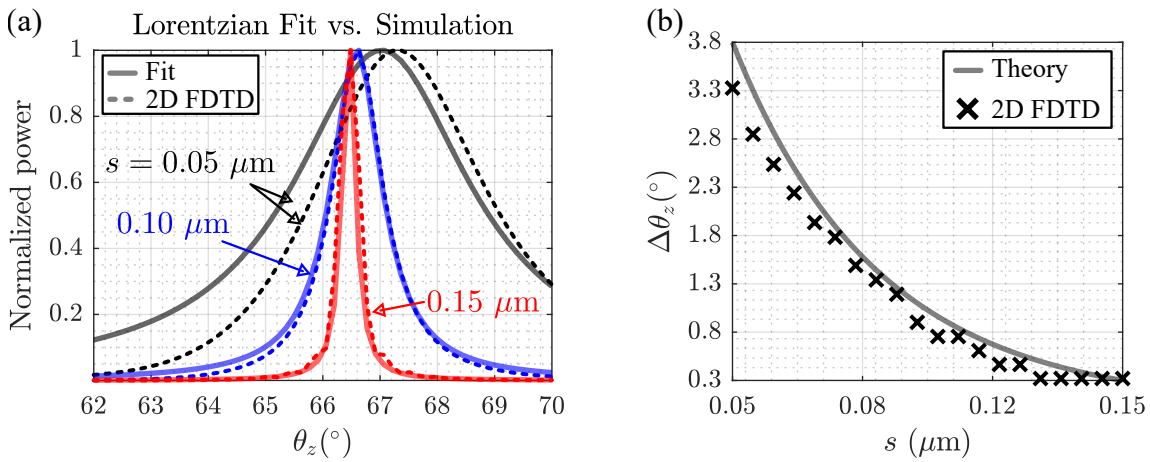

Figure 2.26: (a) Far-field in the z-direction for different s. The 2D FDTD results are fitted with a Lorentzian expression (Eq. (2.38)). The FWHM $= \Delta\theta_z$ is calculated for each s and plotted in (b). $\lambda = 0.532\,\mu$m, $n_0 = 1.46$, $n_1 = 2$, $n_2 = 1.46$, $n_3 = 2$, $d = 0.2\,\mu$m, TE polarization, $n_{\text{eff}} = 1.8329$.

The width in the x-direction, $\Delta\theta_x$, depends on the effective mode width. Figure 2.27 shows the 3D FDTD results for $\Delta\theta_x$. As the width w increases, $\Delta\theta_x$ decreases. We fitted the data with a diffraction model $\arcsin\big((\lambda/n_3)/w_{\text{eff}}\big)$, where w_{eff} is the effective width of the mode calculated using n_{eff}.

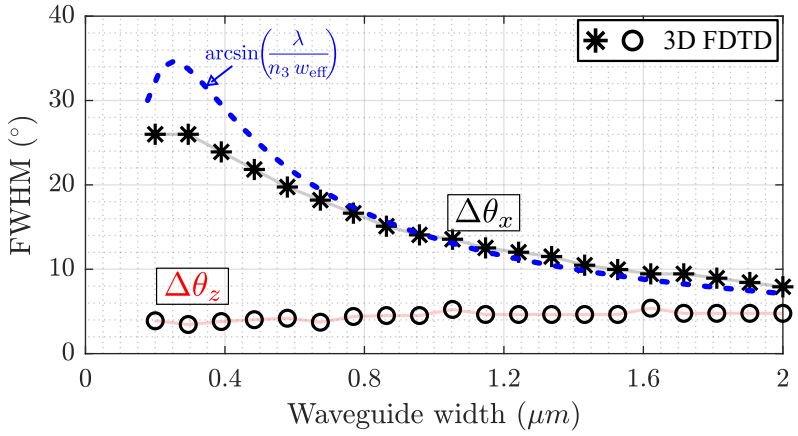

Figure 2.27: The angular size of the divergences $\Delta\theta_x$ and $\Delta\theta_z$ as a function of the waveguide width w. $\Delta\theta_x$ is directly related to the extent of the mode in the x-direction, or the effective width w_{eff}. The dashed lines are fits using a simple diffraction model. w_{eff} is calculated using n_{eff} and the evanescent depth $1/\gamma$. $\lambda = 0.532\,\mu$m, $n_0 = 1.46$, $n_1 = 2$, $n_2 = 1.46$, $n_3 = 2$, $d = 0.2\,\mu$m, TE polarization and $s = 0.05\,\mu$m.

Note that as the width of the waveguide is reduced, n_{eff} decreases and the penetration depth of the evanescent part, $1/\gamma$, increases outside the waveguide. The diffraction model using w_{eff} provides a good approximation and requires only knowledge of n_{eff}. However, for more precise results, one may calculate the mode profile in the x-direction and extract the exact effective width w_{eff}.

The divergence can be interpreted as the far-field angular size resulting from the near field spot size of the coupled field. This spot size can be estimated using n_{eff} and α_r.

Note: In the simulation, the divergence depends on the size of the high-index n_3 box. As the box transverse size increases, more angles can be coupled. In Figure 2.27, I used a box with a thickness of 6 μm and a width of 20 μm. This is time-consuming for simulations such as FDTD. Since the divergence in the z-direction is small compared to that in the x-direction, the box width must be increased for more accurate results. In practice, the high-index layer n_3 is a slab. For good estimates, it is recommended to use the diffraction model, as illustrated by the dashed curve.

2.5.7 Polarization

In Figure 2.28, the far-field is decomposed into its individual intensity components. The components are normalized by the maximum of the total intensity $\max(|E_{\text{total}}|^2)$.

In Figure 2.28 (a), the guided mode is TE (along $\hat{x}$). The $|E_x|^2$ component is important, indicating that the polarization is well preserved. The polarization extinction ratio (PER) is on the order of 1,000:1. The intensity distributions of the components are not identical. In the center of the spot, the PER exceeds 1,000:1, indicating an even stronger polarization contrast.

In Figure 2.28 (b), we present the corresponding results for the TM (along $\hat{y}$). The resulting polarization is decomposed along $\hat{y}$ and $\hat{z}$. The coupling angle θ_{peak} is 68.42°. To obtain the polarization fraction along $\hat{y}$ and $\hat{z}$, we simply decompose using $\sin^2(\theta_{\text{peak}})$ and $\cos^2(\theta_{\text{peak}})$, respectively. This yields a decomposition of approximately 86.5% along $\hat{y}$ and 13.5% along $\hat{z}$. If $\theta_{\text{peak}} = 90°$ for the case of parallel coupling, the polarization can be fully preserved along $\hat{y}$.

This component is more intuitive even for TM, as the intensity distribution depends only on

the coupling angle. The component exhibits better polarization performance than extraction by the grating, which, in the case of TM polarization, yields a low extinction ratio.

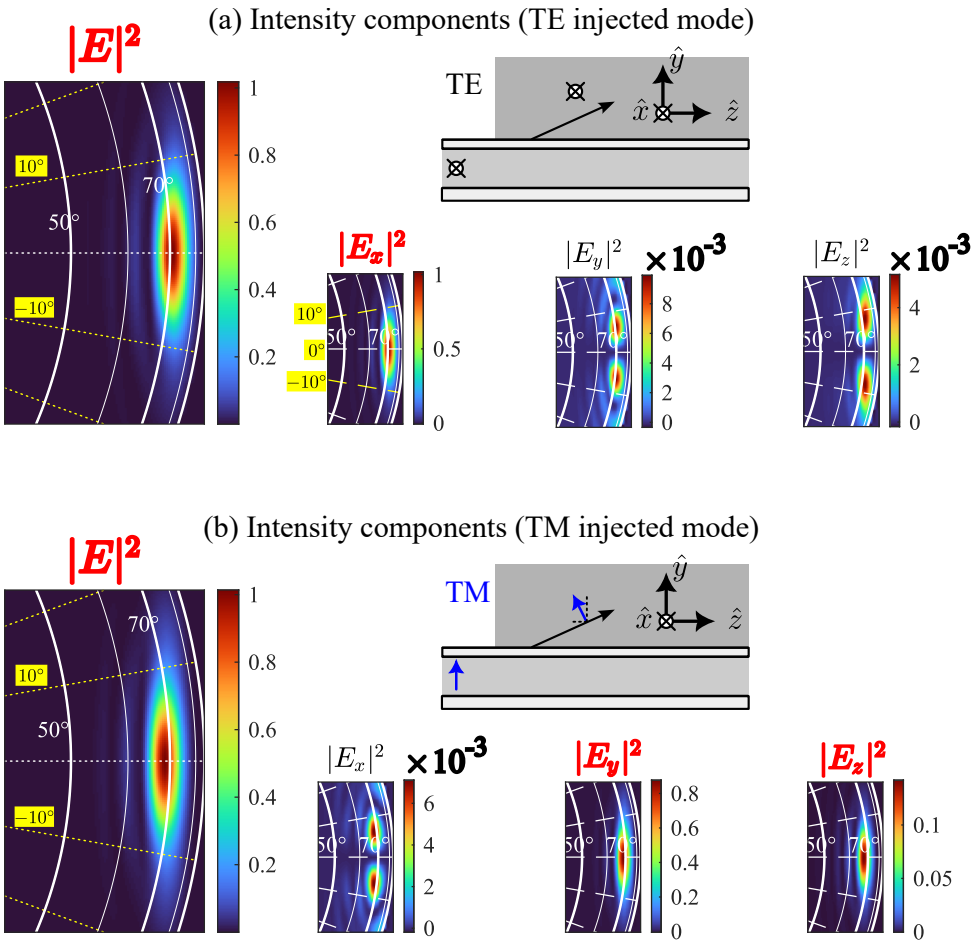

Figure 2.28: Decomposition of the far-field intensity. (a) TE guided mode (along $\hat{x}$). The total intensity is given by $|E_{\text{total}}|^2 = |E_x|^2 + |E_y|^2 + |E_z|^2$. $|E_x|^2$, $|E_y|^2$, and $|E_z|^2$ are shown separately around the extraction angle. (b) TM guided mode (along $\hat{y}$). The components are normalized by the maximum of the total intensity $\max(|E_{\text{total}}|^2)$. The parameters are: $n_0 = 1.46$, $n_1 = 2$, $n_2 = 1.46$, $n_3 = 1.8$, $\lambda = 0.532\,\mu$m, $d = 0.2\,\mu$m, $w = 0.3\,\mu$m, $s = 0.1\,\mu$m, $n_{\text{eff}}(\text{TE}) = 1.701$, $n_{\text{eff}}(\text{TM}) = 1.669$. The transverse size of the n_3 layer is $2 \times 2\,\mu\text{m}^2$.

2.5.8 Conclusion

In this section, I discussed the extraction using an innovative approach that combines evanescent coupling with a prismatic structure. I focused on the key characteristics of the coupling. The full configuration with the prismatic structure is discussed in the following chapter, after the introduction of the ferroelectric liquid crystal.

This approach provides values of α_r about 10 times higher than by diffraction, where a typical decay length of $1/\alpha_r = 10\,\mu$m can be achieved. There are no diffraction orders, unlike in the grating approach. The divergence, in a similar manner, is related to the effective aperture defined by $1/\alpha_r$ and the effective waveguide width w_{eff}.

The polarization is well preserved after coupling for both TE and TM modes. The evanescent coupling is wavelength-dependent. The RGB operation requires three waveguides with the same n_{eff}.

In this section, I also provided key compact equations that can be used for quick prototyping and understanding the dependencies. This was made possible by compiling foundational works from the 1970s, such as that of Ulrich [112]. Using simulations, I verified the equation and highlighted the physics of the coupling through the evanescent component γ. In fact, the key parameters can be reduced to the value of n_{eff}, which is the most important element.

To conclude, I provide Figure 2.29, which shows $\alpha_r(n_3, d, \lambda)$ as a function of the separation s. These figures come from my analytical analysis of the evanescent coupling behavior described in the literature [112]. They were calculated using MATLAB and verified through FDTD simulations in Lumerical®.

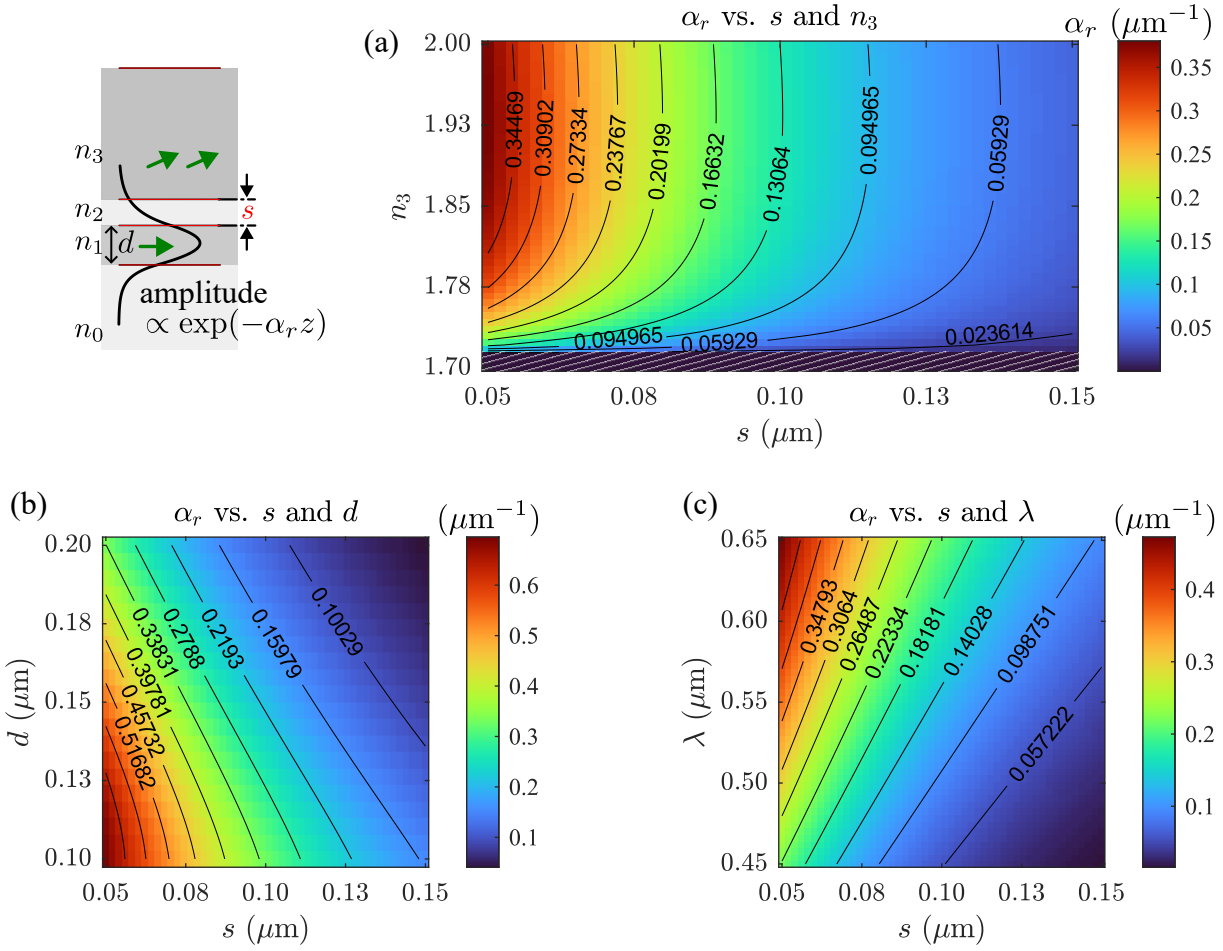

Figure 2.29: (a) $\alpha_r(n_3, s)$. (b) $\alpha_r(d, s)$. (c) $\alpha_r(\lambda, s)$. Nominal parameters: core thickness $d = 0.2\,\mu$m; refractive index profile $n_0|n_1|n_2|n_3 = 1.46|1.87|1.46|1.8$; TE polarization. n_2 is adjusted to match $n_2 = 2$ using the effective index method for a width $w = 0.3\,\mu$m.

In (a), α_r as a function of n_3 and s. The coupling starts at $n_3 \geq n_{\text{eff}}$. $\alpha_r(n_3, s)$ increases with n_3 and decreases with s. In (b), $\alpha_r(d, s)$ decreases with the thickness of the waveguide d because n_{eff} increases and the depth $1/\gamma$ of the evanescent part is reduced. In (c), $\alpha_r(\lambda, s)$ increases with wavelength. To obtain a similar α_r for RGB, three separate waveguides must be used with different geometries.

2.6 Conclusion

In this chapter, I started with a brief introduction to the waveguide mode and the evanescent part outside the waveguide, characterized by the depth $1/\gamma$, where $\gamma = \frac{2\pi}{\lambda}\sqrt{n_{\text{eff}}^2 - n_2^2}$. Here, n_2 is the refractive index (RI) of the cover. The mode can be extracted by introducing a perturbation in the cover. As the evanescent field reaches the perturbation, extraction becomes possible.

I used a useful parameter, α_r, the radiation decay constant, which characterizes the amplitude attenuation of the mode as $\exp(-\alpha_r z)$ when the mode is extracted during propagation. This parameter α_r (in units of μm^{-1}) gives a characteristic extraction length $1/\alpha_r$, corresponding to the extraction of 86.5% of the power $(1 - e^{-2})$.

For our approach using a photonic chip as a microdisplay, light must be extracted locally and actively. To extract light, I discussed two solutions: the grating outcoupler and the evanescent coupler with a prismatic structure. The latter has been patented by us and satisfies many extraction requirements that conventional outcoupler grating solutions do not.

For the grating, α_r varies as a function of the RI contrast:

$$\alpha_r \propto (n_g^2 - n_2^2)^2 \tag{2.40}$$

where n_g and n_2 are the RI of the grating and the cover, respectively. α_r can be modulated by changing n_2, for example, by using a liquid crystal as the cover. This will be discussed in the next chapter.

For the evanescent coupler, we have:

$$\alpha_r \propto \exp(-2\gamma s) \tag{2.41}$$

where s is the separation between the waveguide and the high-index layer n_3. The coupling requires a small separation ($s \leq 1/\gamma$) in order for the evanescent field to reach the n_3 layer. In addition, It requires $n_3 \geq n_{\text{eff}}$ to couple to a radiation direction.

Our approach provides α_r values about 10 times higher than those achieved with the grating outcoupler, with a typical decay length of $1/\alpha_r = 10\,\mu\text{m}$. Moreover, there are no diffraction orders, unlike in the grating approach, and the light is coupled only in the upper part of the propagation space.

I discussed other important aspects such as divergence and polarization. The divergence is simply related to the size of the near-field. The latter is related to $1/\alpha_r$ and the effective waveguide width.

It is important to note that I provided both the simulation and analytical treatment. The analytical results were verified by FDTD simulations. This analytical study represents a comprehensive work that combines my understanding with a compilation of key literature. In the bibliography, you will find carefully selected references.

In the following chapter, liquid crystals (LCs) are introduced, with a special focus on ferroelectric LC. Then, I discuss the activation of the extraction, including both the outcoupling grating and the evanescent coupling with TIR. The prismatic structure is examined in more detail with visual representations. I will present some design equations for the complete component, followed by a demonstration of passive extraction based on this new innovative structure.

Chapter 3

Active Component for Light Extraction II

Contents

3.1 Motivation for Liquid Crystal Integration **77**
3.1.1 Birefringence 77
3.1.2 Liquid Crystal Phases 78
3.1.3 Chiral Smectic C Phase and Ferroelectricity 79
3.1.4 Driving Mode and Bistability 80
3.1.5 Response Time: Ferroelectrics versus Nematics 81
3.1.6 Temperature Dependence 82
3.1.7 Packaging and Defects 83
3.1.8 Liquid Crystal and Integrated Photonics 84
3.1.9 Conclusion 86
3.2 Active Component for Light Extraction **87**
3.2.1 Operation Modes 87
3.2.2 Grating Filled with Liquid Crystal 88
3.2.3 Evanescent Coupling Modulation and TIR 92
3.2.4 Parallel Coupling: Asymmetric Directional Coupler 94
3.2.5 Oblique Coupling: Design and Trade-offs 95
3.2.6 Oblique Coupling: TIR in 3D 96
3.2.7 Full Extraction Efficiency Simulation 99
3.3 Results: Passive Extraction Demonstration **102**
3.3.1 Fabrication Process of a Passive Sample 102
3.3.2 Wet Etching of Silicon and Nanoimprint Results 103
3.3.3 Overview of the Layout: PIC and NIL Chips 105
3.3.4 Experimental Protocol Using a Goniometer 107
3.3.5 Results and Analysis 108
3.3.6 Perspectives 112
3.4 Conclusion **113**

3.1 Motivation for Liquid Crystal Integration

The high birefringence of Liquid Crystals (LCs), along with the ability to dynamically tune it with respect to the polarization of the guided mode, are the key properties motivating our use of LCs. In this section, we first describe the concept of birefringence, then provide a brief introduction to this broad field by focusing on two typical phases: nematic and smectic C liquid crystals. We emphasize on their operating principles, their electro-optic response (speed), temperature dependence, packaging considerations, typical defects, and propagation losses.

3.1.1 Birefringence

Liquid Crystals have interesting properties that can be leveraged in our component. First, LC molecules are anisotropic. In a medium, these molecules can exhibit long-range orientational order. As a result, the LC medium becomes anisotropic and exhibits birefringence: a wave propagating through it experiences a refractive index (RI) that depends on the orientation of the electric field, i.e., its polarization. Second, LC molecules can be dynamically reoriented by an external field through an applied voltage. Consequently, this RI can be tuned in real time.

In an anisotropic medium, *birefringence* Δn is defined as the difference between the two extreme values of the RI. Typically, liquid crystals exhibit high values of Δn, ranging from approximately 0.05 to 0.45.

Figure 3.1(a) shows the optical indicatrix of a uniaxial medium. The principal axis along z also called the *optical axis* is the extraordinary axis. A linearly polarized wave aligned with this principal axis remains linearly polarized in the same direction and experiences the extraordinary RI n_e. Similarly, a wave polarized in the x-y plane remains linearly polarized and experiences the ordinary RI n_o.

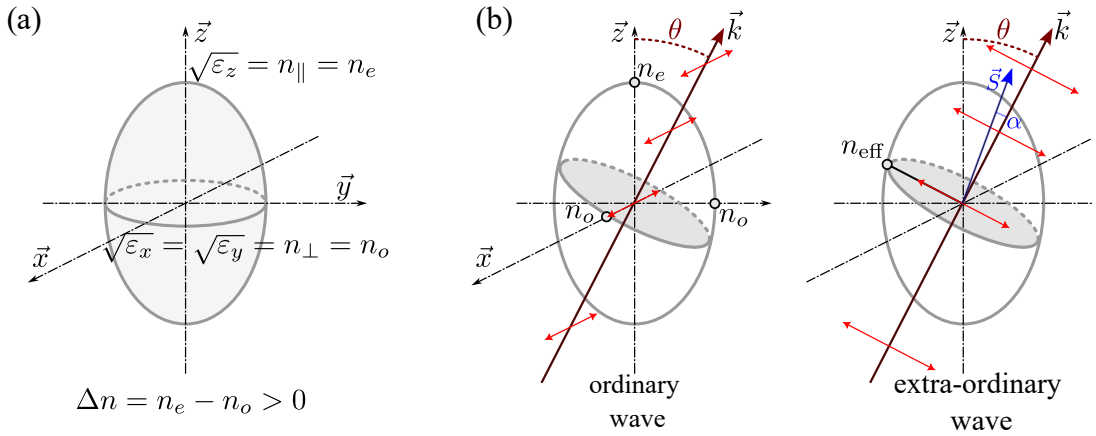

Figure 3.1: (a) Optical indicatrix (index ellipsoid) of optically positive uniaxial medium. (b) Determination of the indices of refraction of the ordinary wave and the extra-ordinary wave

Figure 3.1(b) shows an optical wave propagating obliquely with respect to the indicatrix, at an angle θ. In this case, there are two normal modes. The first is the *ordinary wave*, whose polarization lies entirely in the x-y plane. Regardless of the angle θ, this wave experiences a constant refractive index equal to n_o. The second mode is the *extraordinary wave*, with polarization lying in the plane containing the optical axis z. The RI for this wave depends on the angle θ and is given by:

$$n_{\text{eff}} = \frac{n_o n_e}{\sqrt{n_o^2 \sin^2\theta + n_e^2 \cos^2\theta}} \tag{3.1}$$

In the case of the extraordinary wave, a *walk-off* (deviation angle) may occur between the wavevector $\vec{k}$ (the direction of phase propagation) and the Poynting vector $\vec{S}$ (the direction of power flow). This phenomenon is common in anisotropic media [121, 128]. The deviation angle α of $\vec{S}$ with respect to $\vec{k}$ for the extraordinary wave is given by:

$$\alpha = \tan^{-1}\left(\frac{n_o^2}{n_e^2}\tan\theta\right) - \theta. \tag{3.2}$$

At $\theta = 0°$, $n_{\text{eff}} = n_o$, and at $\theta = 90°$, $n_{\text{eff}} = n_e$. For $\theta = 45°$, with $n_o = 1.54$ and $n_e = 1.73$, we obtain $n_{\text{eff}} = 1.63$ and a walk-off angle $\alpha = -6.6°$. For a propagation distance of 20 μm, the beam is deviated by -2.3 μm.

3.1.2 Liquid Crystal Phases

Liquid crystals represent a vast and fascinating field. Displays and light modulators such as LCDs, LCoS are only a small fraction of the commonly known applications. LC molecules (*mesogen*) are typically organic compounds that combine fluidity with a certain degree of long-range order. Physicists study how these mesogen self-organize to form liquid crystal phases, how defects emerge, and what optical properties arise in different phases. Chemists, meanwhile, design and synthesize molecular structures that, for example, exhibit a stable target phase over a specific temperature range, with desired birefringence.

The commonly known phases of matter are solid, liquid, and gas. Liquid crystal phases lie between solid and ordinary liquid. They are sometimes referred to as *mesophases*, from the Greek *mesos* (middle). This is depicted in Figure 3.2. Within the liquid crystalline domain, we illustrate the smectic-C (SmC), smectic-A (SmA), and nematic phases. The organization order decreases with increasing temperature. The molecules are represented by rod-like shapes.

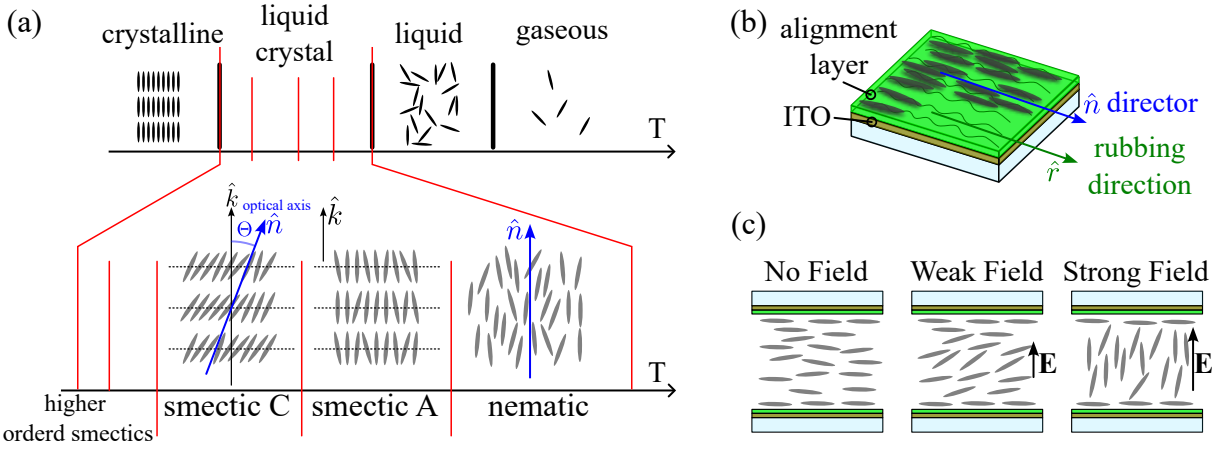

Figure 3.2: (a) Phase transitions and liquid crystals. (b) Schematic showing the alignment of LC. Rubbing the polyimide surface realigns the LC molecules along the rubbing direction. (c) Illustration of the effect of the external electric field **E** on the LC molecules.

The nematic phase is the most widely used in display technologies. This phase exhibits long-range orientational order described by the director $\hat{n}$, which defines the average alignment

direction of the molecules. This director is also the optical axis. As shown in the schematic, thermal fluctuations prevent the molecules from being perfectly aligned with $\hat{n}$. When the temperature decreases, an additional type of order can emerge: long-range positional order in one dimension, forming layers. The vector $\hat{k}$ illustrates the layer normal. You can think of this structure as a stack of two-dimensional liquids. In the smectic C (SmC) phase, the molecular director $\hat{n}$ is tilted at an angle Θ with respect to the layer normal $\hat{k}$.

The director $\hat{n}$, which corresponds to the optical axis of this anisotropic medium, can be set in a desired direction. This is analogous to fixing a boundary condition (BC), and the term used is *anchoring*. This is typically achieved by using alignment layers, such as mechanically rubbed polyimide films or photoalignment techniques. By coating the surrounding surfaces. The BC of the surfaces extends to the bulk through the viscoelastic properties of the LC.

In the nematic phase, when an external electric field is applied, the induced polarization in the medium generates an electric torque on the director. For the director to reorient, the electric torque must overcome both the elastic restoring torque and the viscous resistance of the medium, which are influenced by the boundary conditions and the LC properties.

3.1.3 Chiral Smectic C Phase and Ferroelectricity

In a dielectric medium, the electric polarization $\mathbf{P}$ is a measure of the density of the dipole moment. Dipoles tend to align with an external electric field due to the torque $\mathbf{P}\times\mathbf{E}$. Polarization can either be induced by an external field or can be spontaneous.

The presence of spontaneous polarization in a medium can be leveraged to achieve fast switching times. The nematic phase, because of its symmetry, does not exhibit spontaneous polarization, nor does the smectic C (SmC) phase.

However, when a *chiral* dopant is added to SmC, the resulting phase is the *chiral* smectic C phase (SmC*). In this phase, the director $\hat{n}$ rotates helically around the normal smectic layer $\hat{k}$, as shown in Figure 3.3(a). The tilt plane lacks mirror symmetry, allowing spontaneous polarization $\mathbf{P}_s$ to exist. The direction of this polarization is given by $\mathbf{P}_s = P_0\,\hat{k}\times\hat{n}$. $\mathbf{P}_s$ cancels out over one pitch of the helical structure, which prevents the appearance of macroscopic polarization and, consequently, ferroelectricity.

A ferroelectric medium has macroscopic polarization even in the absence of an external field. In 1980, Clark and Lagerwall [129] demonstrated that in a suitable geometry where the helix in SmC* can be suppressed if the cell is sufficiently thin (a few micrometers). This prevents $\mathbf{P}_s$ from averging to zero. The cell thickness must be smaller than the pitch of the helix [130]. Under these conditions, SmC* can be ferroelectric, as illustrated in Figure 3.3(b). The smectic layers are perpendicular to the substrates, and the molecules are anchored in the plane. Only two stable states of macroscopic polarization exist, and switching between them is possible by applying an electric field. This geometry is called a surface-stabilized ferroelectric liquid crystal (SSFLC) cell.

Unlike nematic, the operation of SmC* does not allow grayscale operation. The structure is bistable. However, the response time can be up to 10 to 100 times faster than that of the nematic phase.

Figure 3.3(c) shows an example of planar alignment with in-plane switching. The surface anchoring should be strong enough to suppress the helical rotation at the surface. This can be achieved using rubbed polyimide layers or, more simply, obliquely evaporated inorganic surfaces such as SiO_2 [130]. Depending on the sign of the applied electric field, the director

rotates between two stable states. In LCD devices, to achieve maximum contrast between white and black pixels, the tilt angle Θ is set to 22.5°. This is made possible through molecular synthesis and engineering of ferroelectric liquid crystal (FLC) materials [131].

In our case, we are primarily interested in the change of the refractive indices with respect to the guided mode, which is a different approach from that used in LCDs (crossed polarizers and a half-wave plate). A larger tilt angle of 45° would be interesting, as it allows the use of full birefringence Δn. However, achieving such a rotation may reduce the response time because of rotational viscosity.

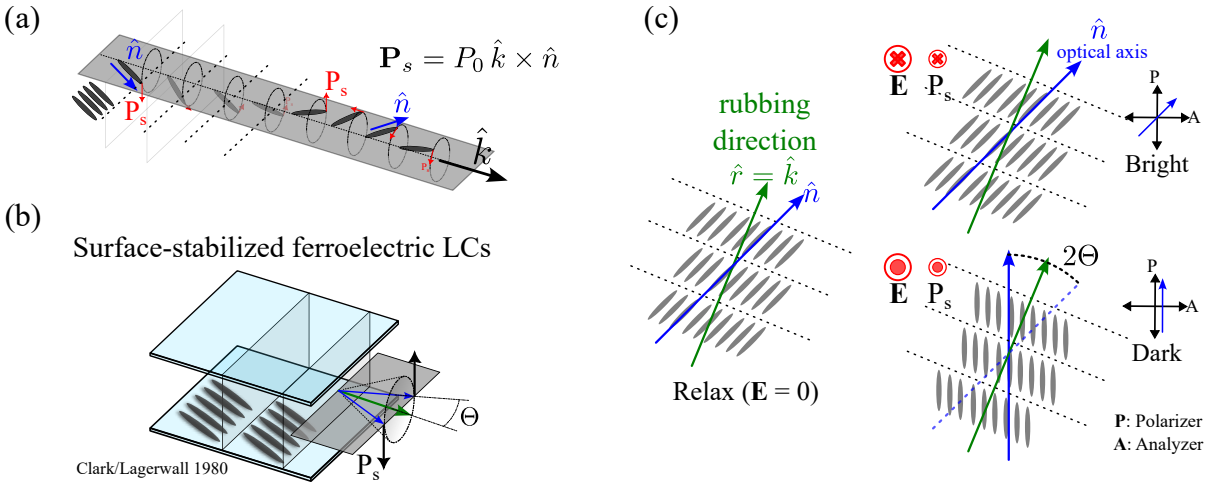

Figure 3.3: (a) Chiral smectic C phase (SmC*): the director $\hat{n}$ and the polarization vector rotate along the smectic layer normal. (b) Surface-stabilized ferroelectric liquid crystals (SSFLC): the cell is thin enough to suppress the helix, resulting in a macroscopic polarization. (c) Example of molecular alignment in the relaxed state. By applying an electric field (up or down), the director switches between two bistable states. A crossed polarizers configuration is shown, where the transmission appears bright if the director is oriented between the polarizer *P* and the analyzer *A*.

3.1.4 Driving Mode and Bistability

In smart glasses, where the displayed content does not require constant updating, such as date, text messages, or notifications. In this case, bistability offers the potential benefit of low power consumption [132].

Figure 3.4(a) illustrates the switching behavior of ferroelectric liquid crystals (FLCs) and their hysteretic response. Note that in the relaxed state ($E = 0$), the director maintains its orientation, demonstrating bistability. The full tilt angle $2\Theta_d$ in the driven state can be slightly different from $2\Theta_r$ in the relaxed state. In (b), we show the typical transmission or light intensity when the molecules are placed between two crossed polarizers. (c) presents two possible driving modes. First, in direct driving, the electric field is continuously applied to maintain the desired state. Second, pulsed driving, a voltage pulse is used to switch the state, after the field is removed ($E = 0$). The director then relaxes to a slightly lower tilt angle, but the state remains stable because of bistability.

The threshold for switching depends on both the magnitude and duration of the pulse. In passive matrix displays, a pulse length of 10 μs may require tens of volts to achieve switch-

ing [130]. In contrast, for nematic liquid crystals, the threshold is directly defined by a threshold voltage. Typical threshold voltages for nematic materials are on the order of 1 V [133].

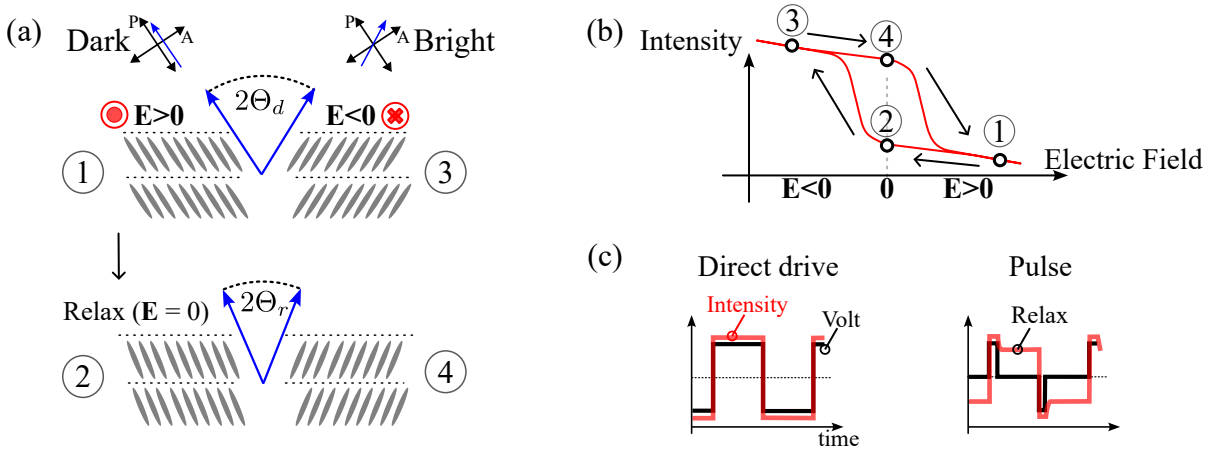

Figure 3.4: (a) By applying an electric field (up or down), the director switches between two bistable states (1) and (3). In the relaxed state ($E = 0$), the director maintains its orientation (bistability). The full tilt angle $2\Theta_d$ in the driven state can be slightly larger than $2\Theta_r$ in the relaxed state. (b) Hysteretic switching of the transmission when the LC is placed between crossed polarizers. (c) Two possible driving schemes: direct driving and pulsed driving.

3.1.5 Response Time: Ferroelectrics versus Nematics

The response time of nematics is typically around 10 ms at best. Ferroelectrics, however, can be much faster, with response times in the range of 10–100 μs [130].

Response Time: Nematics

The total response time is the sum of the ON and OFF times, τ_{on} and τ_{off}, respectively. The electro-optic effects in nematics are nonpolar, meaning they do not respond to the sign of the electric field, unlike ferroelectric materials. While an electric field is required to switch ON, switching OFF cannot be achieved by simply reversing the field direction. Instead, relaxation to the OFF state occurs passively and is governed by elastic restoring forces due to surface anchoring. The speed of OFF time depends on the elastic constants of the material K and its rotational viscosity γ.

The following equation [133] presents the time constants for switch-on and switch-off. The switch-on time constant τ_{on} depends on material parameters such as the dielectric anisotropy $\Delta\varepsilon$ and the rotational viscosity γ. Here, d is the thickness of the liquid crystal cell. The switching time is inversely proportional to the square of the applied voltage V^2. The value of τ_{on} can typically be less than 1 ms. The switch-off time constant τ_{off} is a purely viscoelastic process, governed by the ratio γ/K, where K is the splay elastic constant. The OFF time is generally slower and can exceed few milliseconds. Addressing schemes combining IPS and VA modes have been proposed to reduce the OFF time [134, 135], but it remains on the order of 1 ms. The quadratic dependence on the cell gap d is particularly interesting. In conventional LCD displays, the cell gap is typically around 4 μm. In our case, we can use a smaller gap (~1 μm or less), which leads to improved response times.

$$\tau_{\text{on}} \propto \frac{\gamma d^2}{\varepsilon_0 \Delta\varepsilon V^2}, \quad \tau_{\text{off}} \propto \frac{\gamma d^2}{K} \tag{3.3}$$

Response Time: FLC

The characteristic response time of FLC is given by the following equation, where E is the electric field, P_s is the spontaneous polarization, and γ_{eff} is the effective rotational viscosity:

$$\tau = \frac{\gamma_{\text{eff}}}{P_s E} \tag{3.4}$$

The subscript "eff" in γ_{eff} indicates that the viscosity is dependent on the tilt angle Θ. FLC with a large tilt angle exhibit lower response times. As shown in the expression below, the effective rotational viscosity increases with the square of the sine of the tilt angle:

$$\gamma_{\text{eff}} = \gamma \sin^2(\Theta) \tag{3.5}$$

The switching speed increases with both the spontaneous polarization and the applied electric field. P_s is a molecular property, while γ is a property of the medium. Increasing the ratio P_s/γ significantly improves the response speed. There is thus a trade-off between speed and tilt angle.

Note that FLC or liquid crystal materials, in general, are not universal; their properties, such as P_s, Θ, Δn, and phase stability over temperature, all depend on molecular synthesis and design [136]. During the past two decades, significant improvements in the properties of the nematic liquid crystal have been achieved, driven largely by the development of LCD technology [130]. In contrast, FLC received less attention during that period. However, interest in FLC has recently resurged, particularly with the growing demand for microdisplays based on FLCoS (ferroelectric liquid crystal on silicon) technology [62], which drives improvements in switching speed, defect stability, and overall performance.

3.1.6 Temperature Dependence

In near-eye displays, a wide operating temperature range is essential, especially for military applications that must operate under cold and hot conditions. The properties of liquid crystals are strongly temperature dependent. Parameters such as phase stability, response time, tilt angle, dielectric anisotropy, elastic constants, and rotational viscosity vary with temperature. This is a critical consideration, as the intended operating temperature range may limit the target application of our micro-display development.

In Figure 3.5, we present an example of the temperature dependence of some properties of smectic C*. Figures (a) and (b) show data from Nabadda *et al.* [137]. The helical pitch of the Smectic C* phase is approximately 1 μm. The tilt angle reaches a high value of 45°. However, the small pitch makes it challenging to stabilize the helix within a practical cell thickness for surface-stabilized ferroelectric liquid crystal (SSFLC), since the helix pitch must be larger than the cell gap.

Figure (c) presents results from Mathew *et al.* [131], showing a target tilt angle of 22.5°, suitable for intensity modulation under crossed polarizers. They characterized three FLC materials, showing a decrease in tilt angle with increasing temperature. The critical temperature T_c of phase transition, ranges from 43°C to 66.2°C.

Figure (d), from Charisoulis *et al.* [62], shows the switch-on time as a function of temperature for different cell gaps (CG). At room temperature, the response time is about 50–100 μs, but it increases significantly at lower temperatures.

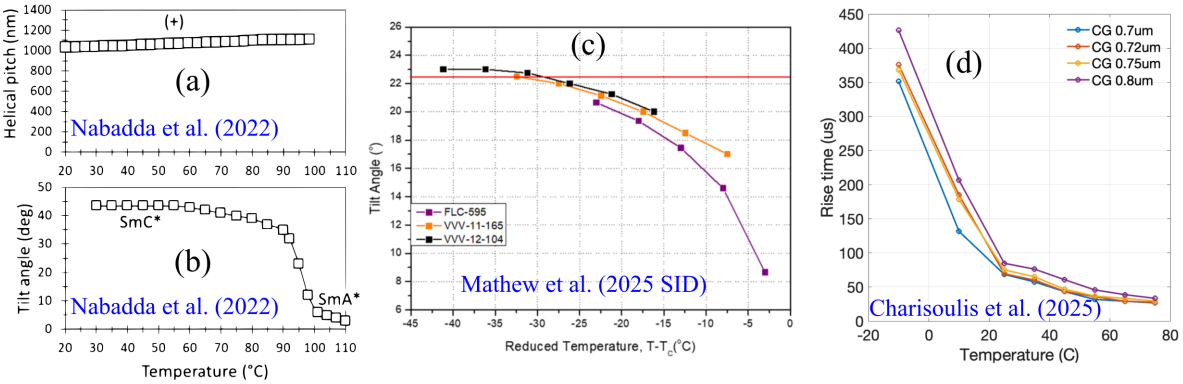

Figure 3.5: (a) and (b) reprinted from Nabadda *et al.* [137]: (a) helix pitch of the Smectic C* phase versus temperature. (b) large tilt angle of 45° versus temperature, showing a wide temperature range for the SmC* phase up to 80°C before phase transition. (c) Reprinted from Mathew *et al.* [131]: tilt angle versus temperature with a target value of 22.5° for different FLC materials; the critical temperature T_c of the phase transition varies from 43°C to 66.2°C. (d) Reprinted from Charisoulis *et al.* [62]: switch-on time as a function of temperature for different cell gaps (CG).

3.1.7 Packaging and Defects

Liquid crystal integration occurs at later stages of the fabrication process. First, we fabricate the photonic chip, either on a CMOS-compatible 200-mm or 300-mm wafer scale. Then, the liquid crystal is integrated. The key steps of LC integration are as follows: First, a polyimide layer is spin-coated. This layer serves to anchor the LC molecules by defining the boundary conditions. The alignment direction of the LC is fixed. This can be achieved through mechanical rubbing, photoalignment, or oblique evaporation. LC is then filled into the gap between the photonic chip and a cover glass. The cell thickness is set by spacers, which can be either patterned photoresist or photonic structures on the cover glass. The LC is filled with its isotropic phase (at high temperature). Upon cooling, a phase transition occurs to the desired working phase, typically nematic or smectic C*. This step, referred to as the baking process, is crucial for achieving a good and uniform alignment of the LC molecules.

In theory, LC baking-filling process may seem intuitive; however, in practice, it is a critical and delicate process, particularly when it comes to controlling LC defects. Liquid crystal can exhibit various types of defects, which can be thought of as analogous to those in solid crystals (e.g., dislocations, vacancies, and others). However, LC defects are more complex [138]. The types of defects depend on the LC phase. For example, nematic and smectic C* phases exhibit different defect textures. These defects must be carefully controlled and, ideally, eliminated in our application, as they scatter light and degrade the display performance.

FLC is used in a surface-stabilized configuration, as shown in the geometry in Fig. 3.6(a), where the smectic C* layers ideally form a perfect *bookshelf* structure. However, in practice, the layers often bend into a V-shape, forming what is known as a chevron structure, as illustrated in Fig. 3.6(b). The orientation of the chevron can occur in two ways, denoted C1 and C2,

depending on the direction of rubbing. Zigzag defects appear where the C1 and C2 regions meet, as shown schematically in Fig. 3.6(c). Almost all ferroelectric liquid crystal cells exhibit these defects [138]. These zigzag defects cause light scattering and reduce display contrast. To minimize this, the chevron direction should be uniform [130], which can be achieved by carefully controlling the *pretilt angle* at the alignment surfaces. For example, a high pretilt angle favors the formation of C1 chevrons [130]. It is also important to ensure smooth and planar surfaces, as well as to apply slow cooling during the phase transition (nematic to SmA to SmC*) [139].

In Fig. 3.6(d), zigzag defects are shown under crossed polarizers [140].

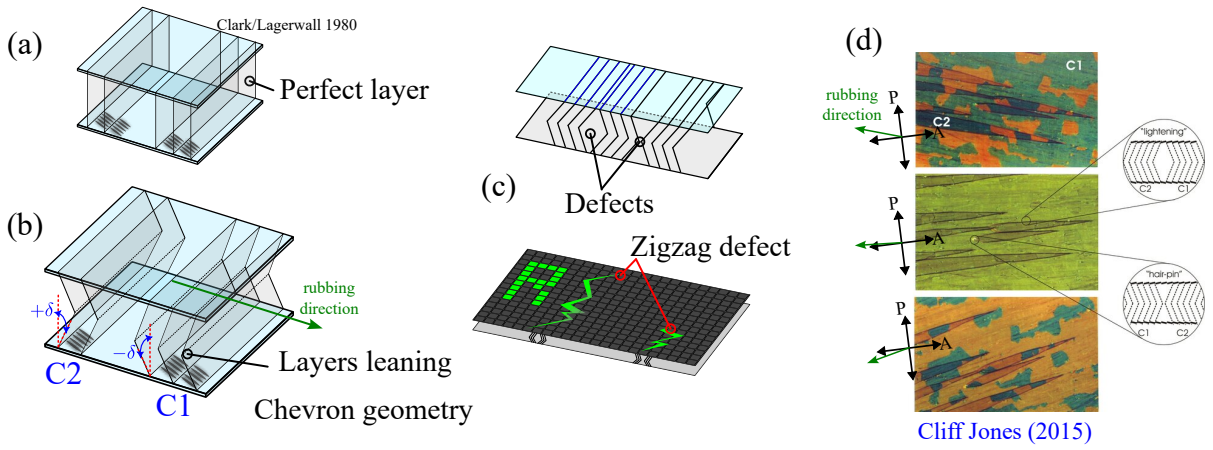

Figure 3.6: (a) Surface-stabilized ferroelectric liquid crystals (SSFLCs) with SmC* layers forming an ideal *bookshelf* structure. (b) Layer leaning and chevron formation; two possible chevron structures, C1 and C2. (c) The coexistence of C1 and C2 leads to the formation of zigzag defects and light scattering. (d) Reprinted from Jones [140]: zigzag defects observed under crossed polarizers.

FLCs have proven their potential due to their fast switching speed. In contrast to nematic displays, which have reached a high level of maturity, ongoing developments focus on FLC materials with improved stability, such as thermal stability, chevron-free, shock stability, and packaging robustness. This progress is largely driven by the advantages of FLCoS microdisplays [62, 141].

3.1.8 Liquid Crystal and Integrated Photonics

The integration of liquid crystals with optical waveguides dates back to the early 1970s, with works by Channin in 1973 [142, 143], Sheridan in 1974 [144], and Chenming in 1974 [145]. Because of their electro-optical effects and high birefringence, liquid crystals have been extensively investigated for modulation applications. High birefringence enables short modulation lengths, allowing for a high integration density. However, in telecommunication application, LC speed remains a bottleneck compared to other modulation technologies, such as thermo-optic modulators (up to 10 kHz), plasma dispersion modulators (20 GHz and above), and MEMS-based modulators (around 1 MHz).

In Fig. 3.7(a), an example of one of the earliest uses of nematic liquid crystals as an active waveguide layer is shown. Light is coupled into the LC layer using a prism and out-coupled at the end. In Fig. 3.7(b), an example of an active directional coupler is shown, where light can couple from one waveguide to another. The author proposed using an FLC as the active separation layer. In Fig. 3.7(c), an example is shown where a nematic liquid crystal is used for modulation in the visible range. By switching the orientation of the liquid crystal, the effective index of the

waveguide changes, enabling a tunable phase shift. In Fig. 3.7(d), the use of a liquid crystal as a phase shifter for low power consumption is illustrated, with an application in creating programmable waveguide circuits. In Fig. 3.7(e), FLC is used to achieve bistable switching between two effective refractive indices. By using FLC as the cladding for the waveguide and grating, a tunable wavelength filter is demonstrated. In the relaxation state ($E = 0$), the optical state is preserved even after the applied voltage is removed.

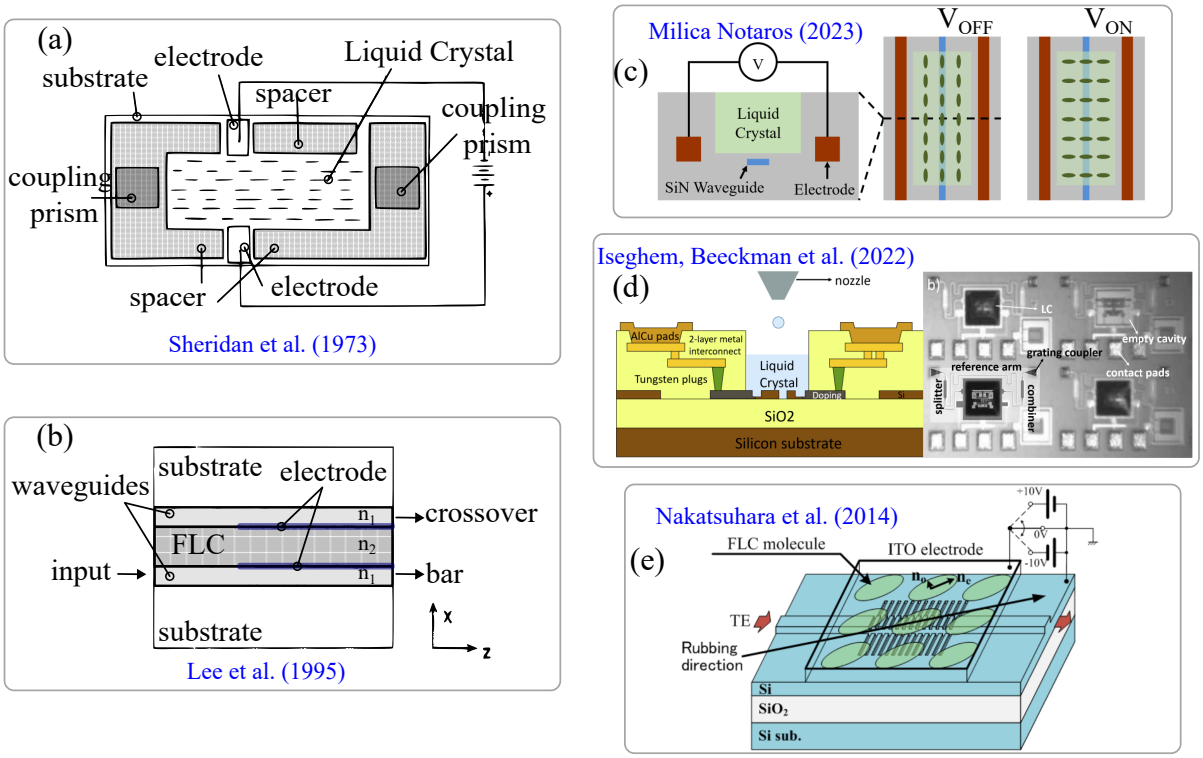

Figure 3.7: (a) Reprinted from [144]: first use of nematic liquid crystals as an active waveguide film. (b) Reprinted from [146]: proposed active directional coupler using FLC. (c) Reprinted from [147]: use of liquid crystals as a phase shifter in the visible range. (d) Reprinted from [148]: use of liquid crystals in telecommunications and programmable photonics. (e) Reprinted from [149]: use of FLC and bistability for a tunable wavelength filter.

In LCD displays, light passes through a thin cell (typically 5–10 μm), and attenuation due to absorption and scattering in the LC layer can be neglected. However, in photonic circuits, light interacts with the LC medium over much longer distances, ranging from a few micrometers up to 1–2 cm. Therefore, the value of propagation losses becomes significantly more important.

The propagation loss in dB/cm can be separated into *absorption* and *scattering* losses. In nematic LC, Channin1973 [142, 143] reported scattering losses of 30–40 dB/cm, significantly higher than the 1 dB/cm losses reported by Sheridan1974 [144] at a wavelength of 0.63 µm. Absorption losses are low in both isotropic and nematic phases, around 0.04 dB/cm in the visible range [150]. The results reported by Wu1987 [150] are in agreement with those of Channin1973, confirming the presence of high scattering losses in the nematic phase. High scattering losses are attributed to thermal fluctuations in the orientation of the director $\hat{n}$. Alessandro2021 [151] reported propagation losses of 6–8 dB/cm.

For smectic A phase, Giallorenzi1976 [152] showed that scattering is several orders of magnitude lower than in nematic phase, with propagation losses around 2 dB/cm.

We will use a liquid crystal as a cover layer for the waveguide, which should result in significantly lower propagation losses. Assuming bulk LC propagation losses of approximately 2 dB/cm or 10 dB/cm, and considering a configuration in which the LC is placed as a cover layer at a distance of 50 nm from a SiN waveguide (300 nm $\times$ 200 nm), the estimated propagation losses for the TE mode are approximately 0.06 or 0.3 dB/cm, respectively. For the TM mode, the losses are expected to be 0.12 or 0.6 dB/cm. These values do not take into account additional propagation losses due to absorption or sidewall roughness in the SiN waveguide itself.

3.1.9 Conclusion

In this section, we introduced liquid crystals, with a particular focus on the nematic and smectic C* phases. Nematic LC are well-established in the display industry because of their high level of maturity. Smectic C* LC, when surface-stabilized (SSFLC), is used as ferroelectric liquid crystals (FLC). FLC are promising for fast electro-optic applications thanks to their submillisecond response times (typically 10–100 μs), whereas nematics are limited by slower response times (10 ms).

Our interest lies in the integration of LC with integrated photonics to create active components. By combining the results of the previous chapter with the electro-optic effects of nematic or FLC materials, we aim to develop active light extraction elements, where the extraction of light can be modulated by an applied voltage.

In the following table 3.1, we provide a brief summary of the main advantages and disadvantages of nematic compared to FLC.

	Nematic	FLC
Response time	On (<1 ms), Off (~10 ms)	Fast (10–100 μs)
Gray scale	Possible	Bistable
Temperature range	Wide	Moderate
Packaging and defects	Mature	Sensitive to defects (chevron)
Cell gap	Not critical	Requires small gap (below 2 μm)
Propagation loss (in LC)	High (10 dB/cm)	Medium (2 dB/cm)
Power consumption	Medium	Low

Table 3.1: Comparison of the main characteristics of nematic and ferroelectric liquid crystals (FLCs).

3.2 Active Component for Light Extraction

The high birefringence and electro-optic effect of liquid crystals will be leveraged to achieve active components for light extraction.

In the previous Chapter 2, I discussed the physics of passive extraction components. The components include a diffraction grating and an evanescent coupler, which can be either parallel (directional) or oblique. The activation of these components is illustrated in Figure 3.8. The grating is impregnated with a liquid crystal (LC), which allows dynamic control of its refractive index (RI) (with respect to the polarization of the guided mode). This can be used either to match the index of the grating and suppress diffraction or to enhance the RI contrast and increase the extraction. In the evanescent coupler, the RI of the LC layer can be tuned to match or exceed the effective index of the waveguide. When the indices are matched, the coupling is parallel. When the layer index is higher, oblique coupling occurs. To couple light into free space (air), a prismatic component is required to redirect the guided light by total internal reflection (TIR).

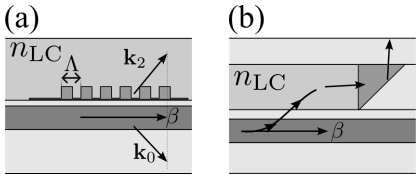

Figure 3.8: (a) Grating impregnated with liquid crystal. (b) Tunable evanescent coupling.

In this section, I discuss the activation of the grating and the evanescent coupling with LC. I present simulation results and some design considerations. The end of this chapter provides some experimental results in passive mode without LC. This work sets the foundation for future studies that will incorporate LC, especially FLC.

The goal of our component is to extract light efficiently and over a short distance ($\propto$ 10–20 μm). Its length will be related to the pixel pitch. The component must meet these objectives without compromising the performance of the micro-display and within reasonable fabrication tolerances. We should note that this component is not restricted to display applications only (e.g., Datacom, OPA for LiDAR, and dimming for LCoS [61], etc.).

3.2.1 Operation Modes

The modes of operation of light extraction depend on the polarization of the guided mode and the orientation of the LC. Figure 3.9(a) shows a waveguide with an associated coordinate system. The LC is located in the cover layer of the waveguide. The propagation direction is $\hat{z}$. The TE and TM polarizations are along $\hat{x}$ and $\hat{y}$, respectively. Labels (1) and (2) illustrate two different LC orientations. Depending on the polarization, the guided mode experiences different refractive indices. For example, in (1), the TE mode "sees" the extraordinary index n_e and the ordinary index n_o in configuration (2). The TM mode experiences the opposite.

Depending on electrode position, alignment conditions, and LC phase, different operation modes can be achieved. Figure 3.9(b) shows an example of operation modes. The ON and OFF states correspond to the polarization experiencing high and low refractive indices, respectively. We suppose an initial tangential alignment along $\hat{z}$. Both the TE and the TM polarizations experience a low RI n_o and are in the OFF state. In the nematic case, If the electrodes form a capacitor, applying a voltage causes vertical alignment (VA). Under this condition, the TE mode is OFF and the TM is ON. If the electrodes are positioned on the same plane, we operate in in-plane switching (IPS). In this, the TE mode is ON and the TM is OFF.

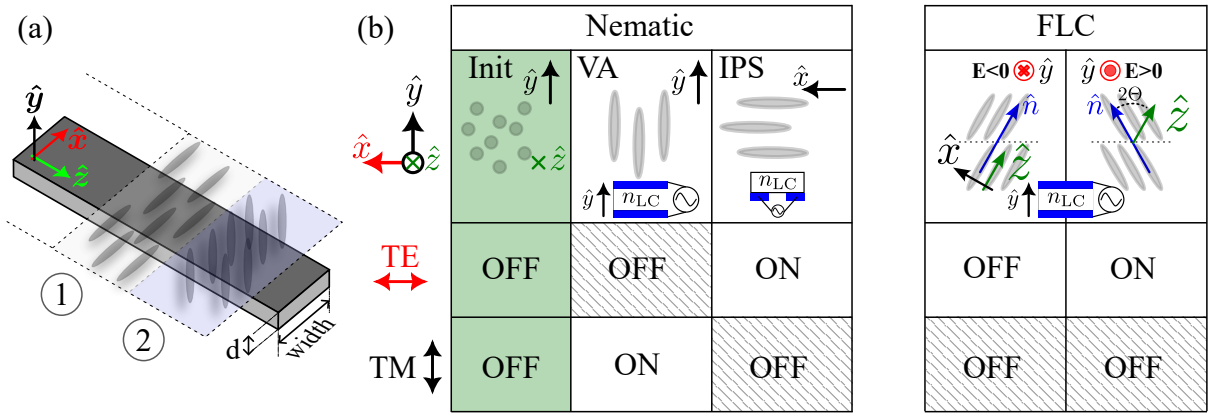

Figure 3.9: (a) A waveguide with a reference frame. Propagation is along $\hat{z}$. TE and TM are along $\hat{x}$ and $\hat{y}$, respectively. (1) and (2) illustrate examples of LC orientations in the waveguide cover. (b) An example of operation modes. The ON and OFF states correspond to the guided mode experiencing high and low refractive indices, respectively.

In the case of FLC, the LC are in a capacitor configuration, and the reorientation occurs in-plane. The TE mode experiences the ordinary index n_o for $E < 0$. When $E > 0$, the experienced effective RI is between n_o and n_e. The value of this RI depends on the full tilt angle. Equation (3.1) can be used by replacing θ with 2Θ. The TM mode is always OFF in this configuration.

3.2.2 Grating Filled with Liquid Crystal

In Figure 3.10(a), a guided mode with propagation constant β_{eff} is shown. The grating, with period Λ, introduces a periodic perturbation. Some diffraction orders, q_1 and q_2, are illustrated. The grating cover is filled with a LC. The operating modes, LC alignment, and electrodes are not shown in this schematic for clarity. In the previous chapter, I defined a decay factor α_r (units of μm^{-1}), which describes the decay of the amplitude of the guided mode as it propagates, following $\exp(-\alpha_r z)$. The power decay follows $\exp(-2\alpha_r z)$. For a guided mode with a diffraction grating, this decay factor depends on the RI contrast between the grating (n_g) and the LC (n_{LC}):

$$\alpha_r \propto (n_g^2 - n_{\text{LC}}^2)^2 \tag{3.6}$$

In RI matching where $n_{\text{LC}} = n_g$, the decay factor α_r is zero and the grating effect is erased. As n_{LC} increases relative to n_g, light extraction increases. To enable deactivation (OFF) and activation (ON) of the grating, the RI of the grating n_g must match n_o or n_e of the LC. In previous work [153, 154], we used the nematic LC 5CB with $n_o = 1.54$ and $n_e = 1.73$, and set $n_g = n_o = 1.54$ at a wavelength of 532 nm. However, this component has some limitations. For this binary grating, the first diffraction order is approximately equally split, with 50% of the power between the cover and the substrate. The thickness of the grating d_g can be used to increase α_r. However, there is saturation for $\alpha_r(d_g)$. As discussed in the previous chapter, this saturation occurs around $d_g = 0.1$–0.2 μm. For a high index contrast of 0.5 (with $n_g = 1.5$ and $n_{\text{cover}} = 1$), the decay factor α_r is limited to approximately 0.01–0.015 μm^{-1}. This corresponds to extraction lengths $1/\alpha_r$ greater than 67 μm. Note that the birefringence of 5CB is only $n_e - n_o \approx 0.2 < 0.5$.

In Figure 3.10(b), the normalized k-space is shown. The guided mode is represented by n_{eff}. The beam directions allowed in the substrate are represented by a semicircle of radius n_0. In the cover region, we have a domain shaped like half a coconut. The cover consists of a LC layer whose RI varies between two values. The normalized grating vector is also shown, with magnitude λ/Λ. As shown in (b), the first diffraction order is close to the vertical direction, the angular variation as n_{LC} changes is small. It is possible to observe a second diffraction order when the maximum value of n_{LC} is high compared to λ/Λ. This is illustrated by the order q_2, which will be trapped in the LC layer by TIR.

If $n_{\text{LC}} \geq n_{\text{eff}}$, an unwanted evanescent coupling may occur. This is illustrated by the green vector; the mode n_{eff} leaks in the LC layer. Moreover, the decay factor α_r of the evanescent coupling can exceed the diffraction. To prevent this parasitic evanescent coupling, the maximum value of n_{LC} must be lower than n_{eff}.

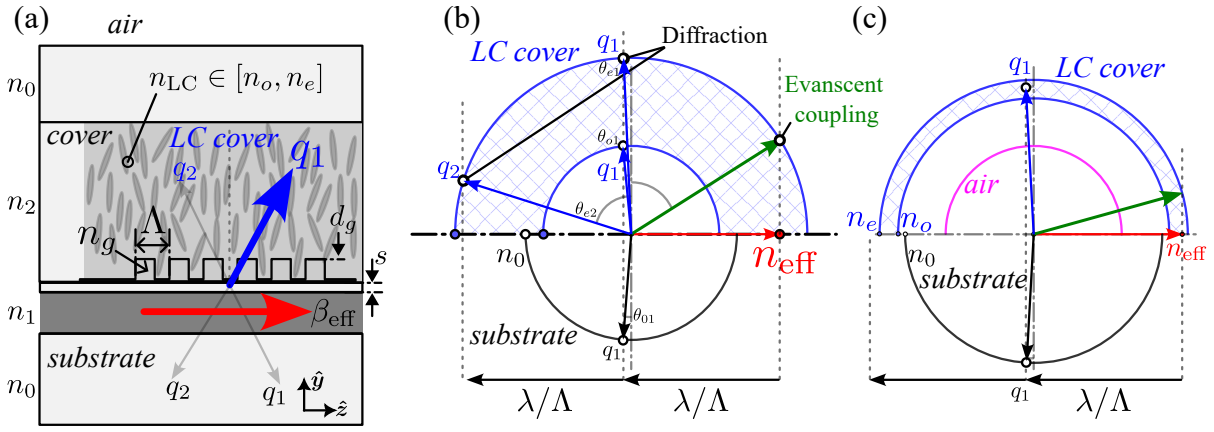

Figure 3.10: (a) Diffraction grating impregnated with LC. The propagating mode couples to different radiation orders. (b) k-space showing the normalized propagation directions, with $k_0 = 2\pi/\lambda_0$. The propagation mode is represented by n_{eff}. The blue half-coconut represents the available angles in the cover, as n_{LC} can vary. If n_{LC} is larger than n_{eff}, evanescent coupling occurs, leading to losses. (c) Scaled k-space using LC 5CB, with $n_o = 1.54$ and $n_e = 1.73$.

In Figure 3.10(b), the half-coconut blue domain representing the LC layer is exaggerated for illustration purposes. In (c), we present a scaled k-space diagram, where the cover corresponds to the LC 5CB. The substrate $n_0 = 1.46$, the air $n_{\text{air}} = 1$, and the effective index is $n_{\text{eff}} = 1.704$. The period Λ is chosen to diffract light near, but not exactly along, the vertical direction, to avoid a second order q_2 which will correspond to the backward-guided mode.

If we increase n_{LC} beyond n_{eff}, a longitudinal phase match component for evanescent coupling becomes possible (the green vector). This effect is parasitic and undesirable. Thus, the RI of the LC should remain below such $n_{\text{LC}} < n_{\text{eff}}$.

We consider the following 3D FDTD simulation shown in Figure 3.11. We plot the first-order diffraction efficiency in the upward direction, above the cover, expressed as a percentage %. The length of the grating is 20 μm. A schematic of the simulation is shown inside the plot area. The width of the waveguide is 0.3 μm, and the guided mode is TE (along $\hat{x}$), with an effective index $n_{\text{eff}} = 1.704$. The thickness of the grating is $d_g = 0.2$ μm. In the schematic, the two red arrows represent the first-order diffraction. A power monitor placed above the LC layer measures the upward diffraction. The black arrow inside the LC layer corresponds to the evanescent coupling,

which is trapped by TIR. Note that there is a transition loss when the mode enters and exits the active LC layer. This is illustrated by the green diffraction arrows. A monitor placed at the end expands the incident field in the injected mode. This allows us to quantify the overall losses due to diffracted order, evanescent coupling, and transition loss.

The RI of the grating is 1.55, and the RI of the LC varies from 1.50 to 1.80. For this grating length, the maximum diffraction efficiency reaches 10%. At RI matching, the efficiency drops to 0.2%. This residual value is due to the transition loss from $n_2 = 1.46$ to $n_{\mathrm{LC}} = 1.55$. This residual diffraction affects the contrast in the display. In practice, it occurs during transitions between the OFF and ON states, corresponding to the change from low to maximum n_{LC}.

The black dashed curve represents the theoretical model introduced in the previous chapter. As shown, it fits well with the FDTD simulation. However, the model does not account for transition losses. The operating wavelength is 532 *nm*.

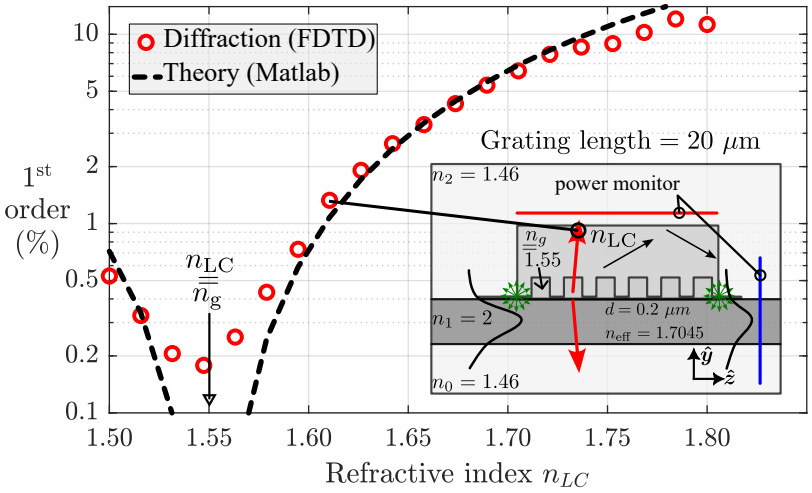

Figure 3.11: First-order diffraction efficiency as a function of the RI of the LC (n_{LC}). The condition $n_{\mathrm{LC}} = n_g$ corresponds to grating erasure (OFF). The schematic shows the simulation parameters. The width of the waveguide is 0.3 μm. The thickness of the grating is $d_g = 0.2$ μm. $\lambda = 532$ nm

In Figure 3.12(a), we plot the decay factor α_r as a function of n_{LC}. The results obtained from the expansion monitor after the active LC are shown as cross markers. The circle markers represent the decay factor of the first diffraction order (both in the upward and downward directions). To estimate the upward diffraction efficiency from α_r for a grating length ℓ_g, we can use the expression $\left(1 - \exp(-2\alpha_r \ell_g)\right)/2$. The factor $2\alpha_r$ accounts for the decay of the power, and the division by 2 corresponds to the fraction of the power diffracted upward. For example, with $\alpha_r = 0.005$ $\mu\mathrm{m}^{-1}$ and $\ell_g = 20$ μm, the upward efficiency is approximately 9.1%.

In (a), the hatched region corresponds to $n_{\mathrm{LC}} \geq n_{\mathrm{eff}}$, where unwanted evanescent coupling occurs. In (b) and (c), the power profile is shown for $n_{\mathrm{LC}} = 1.65$ and $n_{\mathrm{LC}} = 1.8$, respectively. The diffraction order is represented by two red arrows. In (c), the evanescent coupling is indicated by a black arrow. This later is trapped within the LC layer and can interact with the grating, resulting in diffraction in unwanted directions, which reduces the display contrast.

In index matching, the total loss from all contributions is approximately 0.0002 $\mu\mathrm{m}^{-1}$. For a grating length of 20 μm, this results in an overall loss of 0.8%, of which approximately 0.2% leaks upward. From (a), the contribution of the evanescent coupling to the decay factor α_r is

approximately three times higher than that of the grating itself ($\sim 0.02 - 0.005 > 0.005\ \mu\text{m}^{-1}$).

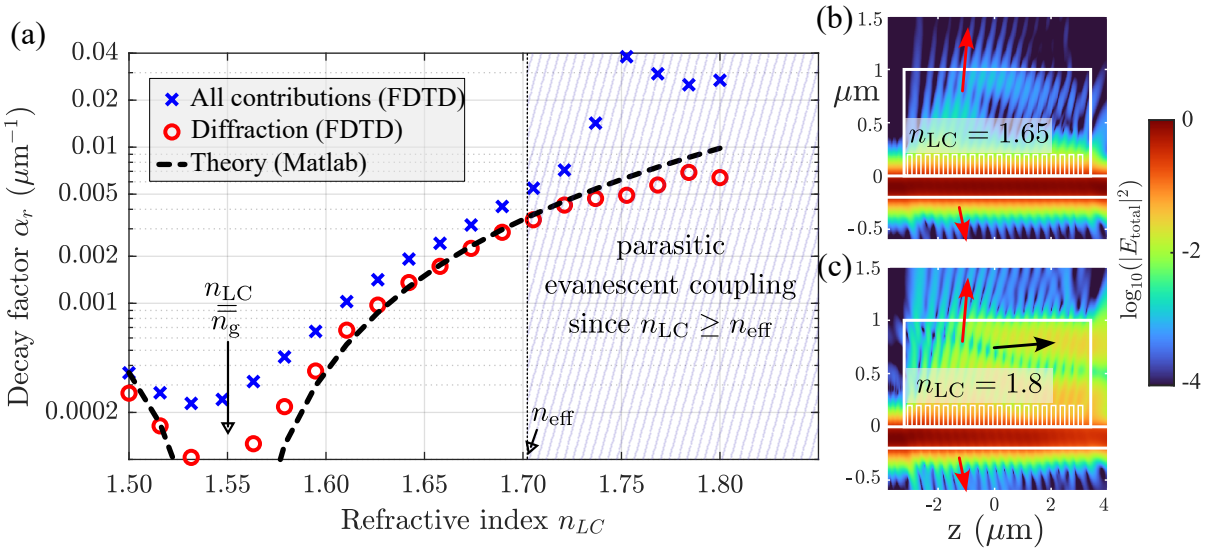

Figure 3.12: (a) Decay factor as a function of n_{LC}. The hatched region indicates possible evanescent coupling. (b) Diffraction profile showing the unwanted downward order. (c) At high n_{LC}, evanescent coupling occurs, as indicated by the black arrow.

Boundary Conditions and Grating Ghost Effect:

Refractive index matching requires precise control of the RI of the grating. This can be achieved, for example, by using a sol-gel process, where the index is tuned by mixing SiO_2 (low index) and TiO_2 (high index). A mismatch will create a residual grating that we call a grating ghost effect [153].

In Figure 3.13, we present a simulation of the grating filed with a nematic LC under applied voltage. The gray bar represents the RI of the LC. The colored bar indicates the voltage distribution. The LC orientation is illustrated by the arrows. The applied electric field reorients the LC, changing its RI from 1.54 to 1.73. At the boundaries, strong surface anchoring forces the LC to maintain an index of 1.54, that is, the switch is not complete. This reduces the RI contrast and, consequently, the diffraction efficiency. Since the alignment is not perfect within the groves, a grating ghost effect occurs. This simulation is obtained through a finite element method (FEM) using COMSOL*.

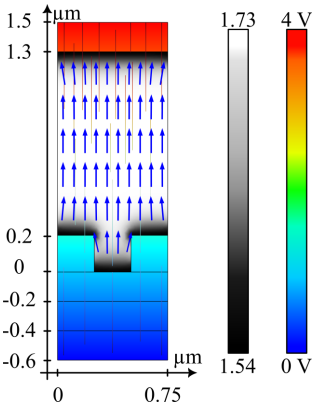

Figure 3.13: Grating Ghost Effect.

A grating filled with LC is a promising structure for active light extraction. However, low values of the decay factor α_r (order of $\alpha_r \sim 0.001\ \mu\text{m}^{-1} \rightarrow 1/\alpha_r \sim 1$ mm) and the presence of ghost effects of a grating are limiting factors. This structure is therefore not suitable for ferroelectric liquid crystals (FLCs), as grating undulations can increase the chances of defects.

*In COMSOL Multiphysics, I applied the Euler–Lagrange equation to the free energy density of the nematic LC [155, 156] (Oseen–Frank model with electrostatic and surface contributions). The resulting differential equations were then implemented in COMSOL through the PDE modules.

There exists a configuration different from the grating index matching, in which the grating is separated from the waveguide by a distance $s \sim 0.5\ \mu$m. The LC is used to actively tune the evanescent field of the mode. This component exhibits even lower α_r. More details are available in [153, 154]. In this section, we conclude that a diffraction grating filled with LC is not suitable for our needs. Other extraction characteristics, such as the angular extraction width, wavelength dispersion, and polarization sensitivity, are discussed in the previous chapter. The following section focuses on our innovative and patented approach based on evanescent coupling. This new component offers several advantages.

3.2.3 Evanescent Coupling Modulation and TIR

Unlike the diffraction component, where the grating interacts directly with the guided mode, this component operates differently. Here, the guided mode leaks first into the cover layer, and then a prismatic structure redirects the leaked power to free space via total internal reflection (TIR). Figure 3.14(a) shows the cover composed of an LC layer and a prismatic structure with refractive index n_p. By increasing the RI of the LC compared to the effective index of the guided mode n_{eff}, the mode can be coupled to the cover layer. The coupled/leaked mode has an effective index equal to n_{LC}. This approximation is valid since the LC layer is relatively thick (t_p = 1–2 μm) compared to the waveguide ($\sim 0.2\ \mu$m).

When the RI of the guided mode n_{eff} and the leaked mode n_{LC} are matched, the coupling is considered *parallel*. That is, the propagation constants are parallel (green arrows). This is illustrated in (a) by 90°. When $n_{\text{LC}} > n_{\text{eff}}$, we consider the coupling as *oblique*. Both phenomena are related to the evanescent part of the guided mode in the LC layer.

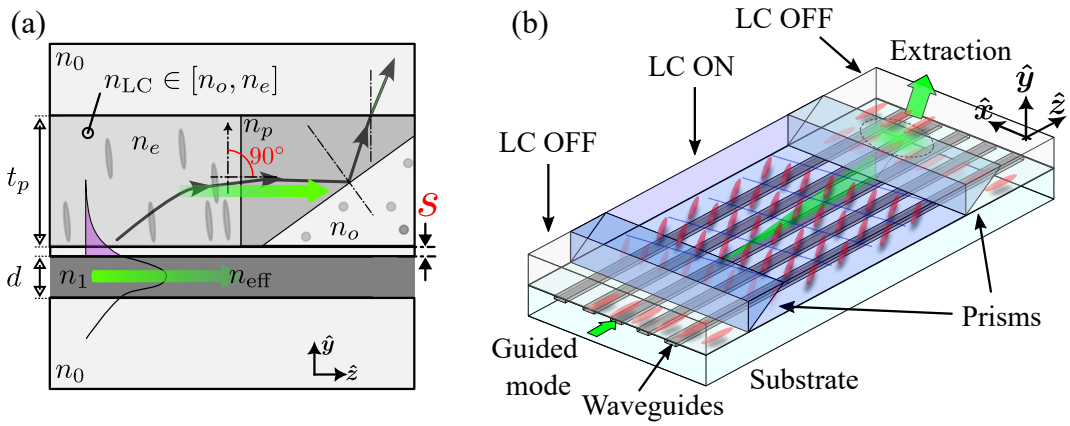

Figure 3.14: (a) Directional coupling: the coupled mode, shown with a blue arrow, is parallel to the guided mode. The prism extracts the incident mode by total internal reflection (TIR). (b) Schematic of FLC impregnated within a photonic chip along with the prism strips.

Figure 3.14(b) shows a schematic that includes the waveguides, the LC layer, and the prisms. The LC represents FLC. By applying an electric field, the guided mode is leaked into the cover layer which afterward is reflected to the free space by TIR.

Prism TIR condition

Figure 3.15(a) shows a prism used to reflect guided mode at the interface between the refractive indices n_p and n_o. The angle $\beta = \frac{\pi}{2} - \alpha$ represents the incidence of the beam relative to the

normal of the interface (not to be confused with the propagation constant). We need TIR at this interface and transmission to free space at the second interface n_p/n_2. Using TIR conditions and the relation $\gamma = 2\beta - \frac{\pi}{2}$, we get the following condition for extraction:

$$\arcsin\left(\frac{n_o}{n_p}\right) \leq \beta < \frac{\pi/2 + \arcsin(n_2/n_p)}{2} \tag{3.7}$$

For $n_p = 1.8$ and $n_2 = n_o = 1.46$, we have $54.2° \leq \beta < 72.1°$. In terms of α, this corresponds to $17.9° < \alpha \leq 35.8°$. Here, t_p and ℓ_p are the thickness and length of the prism structure. These two lengths are related by $\tan(\alpha) = t_p/\ell_p$. Figure 3.15(b) shows a simulated TIR by the prism, where the incident mode is a TE at a wavelength of 532 nm. The dimensions are $\ell_p = 2\,\mu$m and $t_p = 1\,\mu$m, which corresponds to $\alpha = 26.6°$.

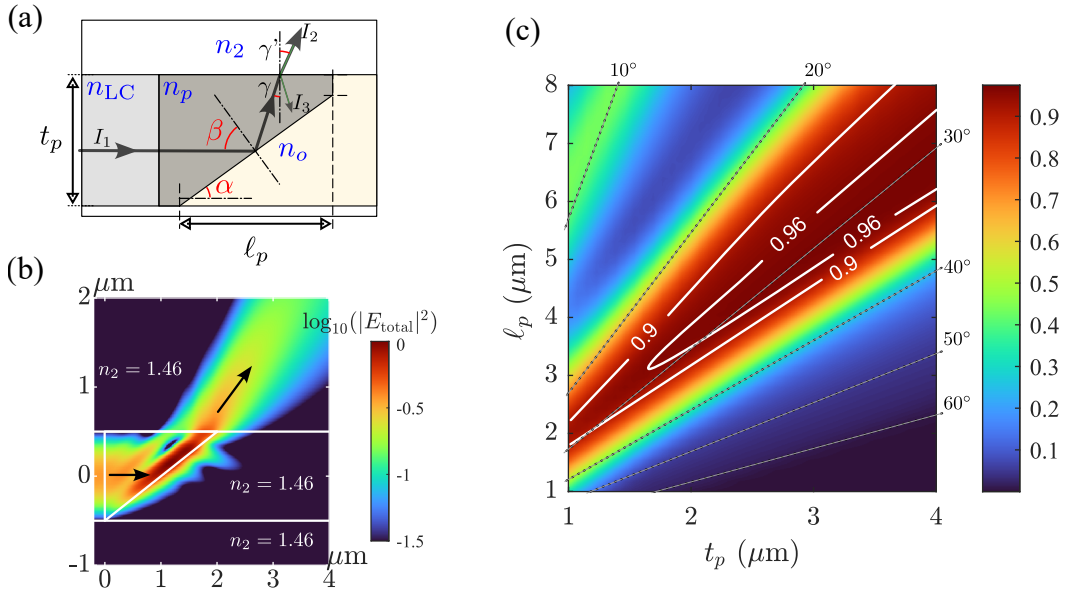

Figure 3.15: (a) Micro-prism structure and total internal reflection (TIR) condition as a function of various parameters. (b) FDTD simulation of TIR for an incident TE mode. (c) 2D FDTD simulation of TIR with an incident TE mode, showing the influence of the length and the thickness of the prism.

Figure 3.15(c) presents the simulated efficiency of the prism as a function of ℓ_p and t_p. The color bar indicates the transmission to the free space, normalized by the incident power of the mode. The dotted lines represent the angles α. The TIR range of α is consistent with Equation (3.7). It is possible to achieve an efficiency of 96% for a prism thickness $t_p \geq 2\,\mu$m. The losses are due to the evanescent parts of the incident power, which interact with the corners of the prism and are not reflected. The difference between n_p and n_{LC} should be small to minimize Fresnel reflections, which are around 0.04% in the case of $n_p = 1.8$ and $n_{LC} = 1.73$, and 1% for $n_p = 1.8$ and $n_2 = 1.46$.

In Equation (3.7), the RI n_o should be replaced by n_{LC} in the OFF state. For example, with $n_o = 1.54$, we obtain $\alpha_{max} = 31.2°$ instead of 35.8°. This reduces the angular spread of the cone shown in Figure 3.15(c). Increasing the prism n_p will shift the cone down to higher angles of α.

For parallel coupling, Equation (3.7) is sufficient to estimate the working range of the prism. The overlap of the incident power with the thickness of the prism, along with the Fresnel coefficients, can be used to estimate the efficiency of the prism.

3.2.4 Parallel Coupling: Asymmetric Directional Coupler

In the previous chapter, we discussed the directional coupler and how the coupling length or α_r is exponentially related to the separation s (see Fig.3.14(a) for the location of s). The coupling is considered *symmetric* when the two waveguides are symmetric; they have the same geometry and materials. In the case of an *asymmetric* directional coupler, it is possible to achieve an operating point where the coupling is optimal. This occurs under the phase-matching condition, that is, when the effective indices of the two waveguides are equal. Symmetric waveguides are always phase-matched. Recall that the dispersion of $n_{\text{eff}}(\lambda)$ differs in asymmetric waveguides. For a fixed wavelength, the geometry of the waveguide (thickness and width) can be designed so that n_{eff} matches that of the second waveguide. In our case, the second waveguide is considered to be the LC layer, with its own effective index $n_{\text{eff2}} \sim n_{\text{LC}}$. For optimal RGB coupling, three waveguides are needed, one for each color. The waveguides should be designed to satisfy the condition $n_{\text{eff}}(\lambda) = n_{\text{LC}}(\lambda)$, where n_{LC} is taken in the ON state.

Figure 3.16(a) illustrates the dispersion of n_{eff} as a function of wavelength and waveguide geometry. The thickness is fixed at $d = 0.22\,\mu$m. The width of the waveguide varies from 0.2 to 0.5 μm. The waveguide material is Si_3N_4, based on data from the Lumerical® FDE (Finite Difference Eigenmode). The waveguide is buried in SiO_2. The effective index n_{eff} of the fundamental mode decreases with increasing wavelength and increases with waveguide width. The effective index n_{eff} of the TE mode is slightly larger than that of the TM mode. Suppose that the RI of the ON state of the LC is $n_{\text{LC}} = 1.75$. For the TE mode, we need to follow the isoline corresponding to $n_{\text{eff}} = 1.75$. This defines a specific waveguide width for each wavelength: 0.21, 0.31, and 0.5 μm for wavelengths $\lambda = 0.450$, 0.532, and 0.627 μm, respectively. The waveguides should be separated by at least 1.5 μm to avoid crosstalk. This sets the total width required for RGB to approximately 5.5 μm.

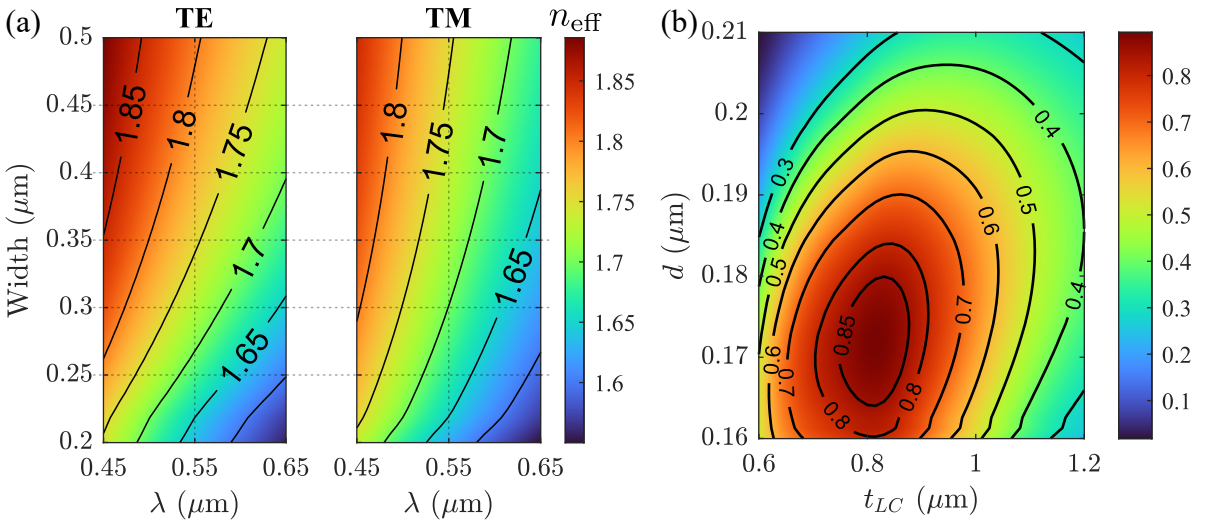

Figure 3.16: (a) Dispersion of the effective index n_{eff} as a function of waveguide geometry and wavelength. The waveguide of thickness 0.22 μm is buried in SiO_2. The core material is Si_3N_4, based on Lumerical® material data. (b) Coupling efficiency into the LC layer of a directional asymmetric coupler. 2D simulation with a waveguide thickness of 0.2 μm and a RI of 1.95. The second waveguide is a LC with a RI of 1.8. The separation between the two waveguides is 0.05 μm.

Figure 3.16(b) shows the directional coupling efficiency into the LC layer. The coupling

length is set to $\ell_c = 10\ \mu$m, with a separation of $s = 0.05\ \mu$m. The waveguide operates at $\lambda = 532\ n$m with a RI of 1.95, while the LC RI is set to 1.8. This value was chosen for low ℓ_c; using a lower RI for the LC would require increasing t_{LC} to achieve phase matching since the waveguide RI is high. However, the coupling constant ($\kappa \propto 1/\ell_c$) of the fundamental mode in the LC layer, through evanescent coupling, decreases as t_{LC} increases. In the LC layer, we use a mode expansion monitor to calculate the power coupled into the fundamental LC mode. The simulation is two-dimensional, which is equivalent to a slab waveguide configuration. The efficiency can be up to 90%. The tolerance ($d \pm \Delta d$) for an efficiency of 85% around the optimal value is Δd =9 nm for the waveguide thickness and 64 nm for the thickness of the LC layer. The asymmetric directional coupler is sensitive to fabrication tolerances. The optimal coupling efficiency of 90% and the optimal TIR efficiency of 96% (Fig.3.15(c)) result in a total efficiency of 86.4%. Other tolerances, such as variations in the RI of the materials, make phase matching in this asymmetric structure more sensitive. The expected overall efficiency may be lower than the optimal value of 86.4%. However, the remaining light is still guided and not leaked. This is advantageous, as the losses do not contribute to parasitic light (which would reduce contrast). We must recall that the decay factor for diffraction is much lower. For a grating length of $\ell_g = 20\ \mu$m, the upward extraction efficiency is only 9.1%.

3.2.5 Oblique Coupling: Design and Trade-offs

Oblique coupling is less constrained than parallel coupling. The condition is simple and requires the refractive index of the LC layer to be higher than the effective index of the guided mode, that is, $n_{\text{LC}} > n_{\text{eff}}$. In this case, the leakage occurs at an angle $\theta = \sin^{-1}(n_{\text{eff}}/n_{\text{LC}})$ lower than 90°.

Figure 3.17(a) is taken from the previous chapter, where I show the decay constant α_r as a function of the RI of the LC layer. We must recall that α_r is related to leakage efficiency. For a given propagation length ℓ, the leakage efficiency is given by $(1 - \exp(-2\alpha_r \ell)) \times 100\%$. The quantity $1/\alpha_r$ is the characteristic length for 86.5% of power leakage. In Figure 3.17(a), for $n_{\text{LC}} = 1.85$, we have $1/\alpha_r = 3.33\ \mu$m. The corresponding angle is $\theta = 67.1°$ for $n_{\text{eff}} = 1.704$.

Figure 3.17(b) shows the full coupling length, denoted ℓ_c, which includes the prism length ℓ_p. The figure indicates the prism thickness ($t_p \approx t_{\text{LC}}$), the length ($1/\alpha_r$), and the coupling angle θ. These parameters can be designed to achieve high extraction efficiency.

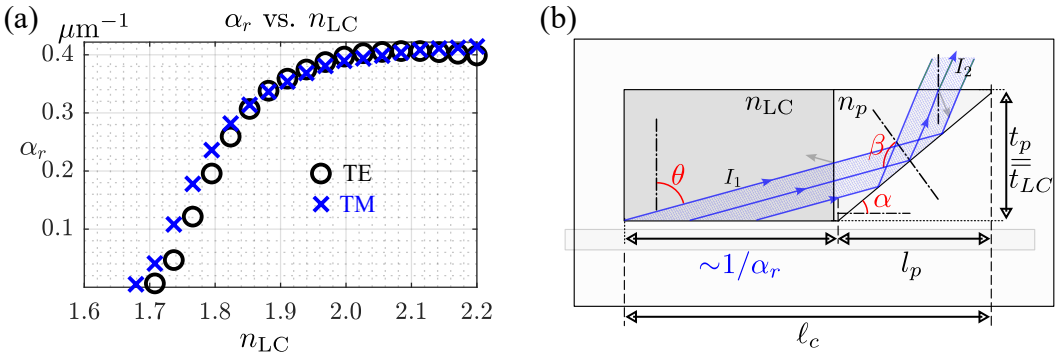

Figure 3.17: (a) Decay factor as a function of the refractive index of the LC layer. (b) The coupling angle θ and the prism parameters can be designed to extract the leaked energy.

The first and last rays within the required leakage length ($1/\alpha_r$ or more) should remain within the TIR interface. If α_r and θ are known, a condition can be set on the thickness t_p. The position

of the first ray on the TIR interface depends on α_r, θ, and α the angle of the prism.

Taking $\ell_c = 1/\alpha_r + \ell_p$, $t_p = \ell_p \tan(\alpha)$, and $t_p = \ell_c \tan\left(\frac{\pi}{2} - \theta\right)$, we can derive the following condition on thickness t_p:

$$t_p \geq \frac{(1/\alpha_r)\tan(\alpha)}{\tan(\alpha)\tan(\theta) - 1} \tag{3.8}$$

For the point $n_{\mathrm{LC}} = 1.85$, we have $1/\alpha_r = 3.33$ μm and $\theta = 67.1°$. For a prism angle $\alpha = 45°$, this implies that $t_p \geq 2.43$ μm. This corresponds to an expected extraction efficiency of approximately 86.5% (without considering Fresnel reflections and the efficiency of the prism). A thickness $t_p = 2$ μm or less is suitable for FLC. To reduce t_p, both the angle θ and the decay factor α_r should be high. However, both depend on n_{LC}, and may vary in opposite directions.

Note that the TIR condition remains the same as in Equation (3.7). However, the angle β is no longer parallel to the propagation direction, as in the case of the parallel coupling. The relation between β and α is now given by: $\beta = (\pi - \theta) - \alpha$. Since the incident angle β increases, a prism with an angle of 45° where $\ell_p = t_p = 2$ μm satisfies the TIR condition for $\theta = 70°$.

3.2.6 Oblique Coupling: TIR in 3D

The leakage is centered on the angle θ, with a divergence. The size of this divergence is related to the extraction length $\sim 1/\alpha_r$ and the mode width in the waveguide. A more detailed physical derivation can be found in the previous Chapter 2 (Section 2.5.6). TIR and transmission should be considered for all incident angles within this divergence cone. Analytical analysis is somewhat complex. I will use MATLAB to provide a more visual understanding.

In Figure 3.18(a), we recall the Fresnel coefficients and TIR. Solid lines represent the transmittance for TE and TM polarizations, shown in blue and red, respectively. Dashed curves represent the reflectance. Before TIR, transmission depends on the polarization and angle of incidence. In contrast, the TIR region forms a perfect plateau. The incident angle on the surface of our prism must be above the critical angle. In Figure 3.18(b), a 3D-view of a prism structure is shown. In practice, we may be limited in the choice of the angle α, defined between the base and the facet of the prism. For example, wet etching of silicon results in the formation of inclined facets with excellent optical quality. Depending on the orientation of the silicon crystal planes, two angles are typically obtained: 54.74° or 45° [157]. I will only consider these two values.

If we consider $\alpha = 45°$, the angle of incidence of the ray A ($\beta = 45°$) does not satisfy the TIR condition when going from $n = 1.8$ to $n = 1.5$ (below the critical angle).

Note that, by rotating the prism around $\hat{y}$, the angle of incidence can increase to $\beta' > \beta$. This is illustrated by ray B, which rotates at an angle ψ with respect to ray A. This rotation increases the likelihood of TIR. However, as ψ increases, the incident angle of the reflected ray γ also increases.

To understand how we can extract the rays that are coupled out from the waveguide and are incident on the prism facet, I will provide a 3D visualization. First, we need to define the angular space that will be used to represent the rays incident on the prism. Figure 3.18(c) and (d) show the definition of the angle θ_y, measured with respect to $\hat{z}$ in the (yz) plane, and the angle θ_x, measured with respect to $\hat{z}$ in the (xz) plane. Our angular space will be defined on the basis of these angles θ_x and θ_y.

To outcouple the ray into air, the requirements labeled (1) and (2) in Figure 3.18(c) must be satisfied: first total internal reflection, then transmission.

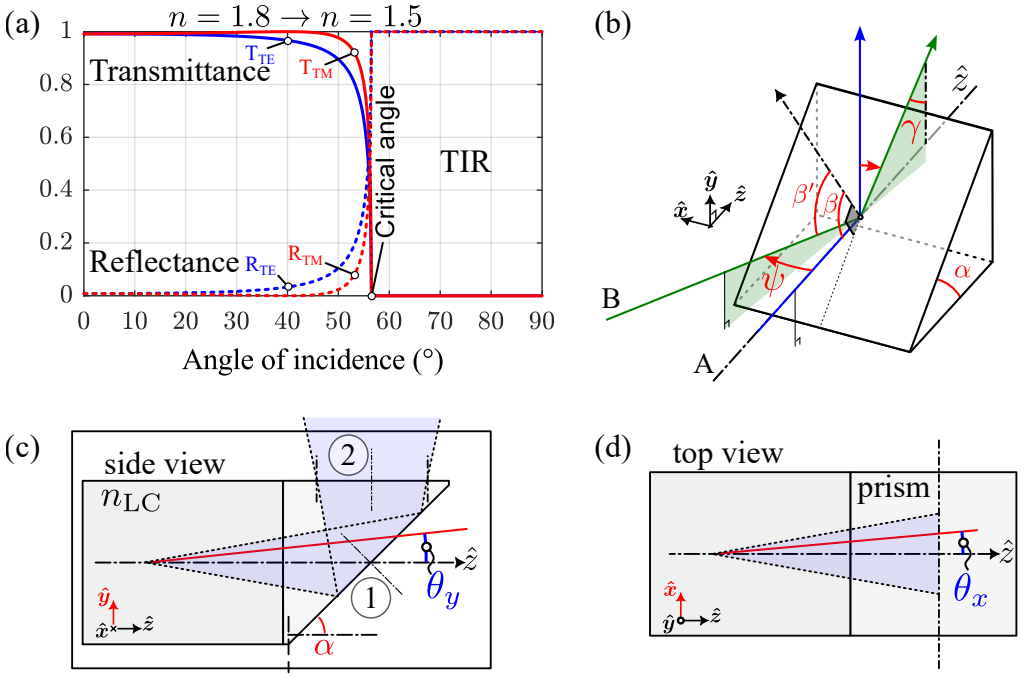

Figure 3.18: (a) Fresnel coefficients plotted as a function of the incident angle. (b) Visual representation of the prism structure. Rotating the prism by an angle ψ increases the incident angle ($\beta' > \beta$), thereby the likelihood of TIR. (c) Side view of the prism and the definition of θ_y. Required conditions: (1) TIR first, and (2) transmission second. (d) Top view and the definition of θ_x.

In Figure 3.19, I provide a visual representation of these TIR and transmission requirements. Polar plots represent the angular space of incidence, cropped to a cone of 60°. The center point corresponds to a ray propagating along $\hat{z}$. The angles between this ray and the $\hat{x}$- and $\hat{y}$-axes are denoted by θ_x and θ_y, respectively.

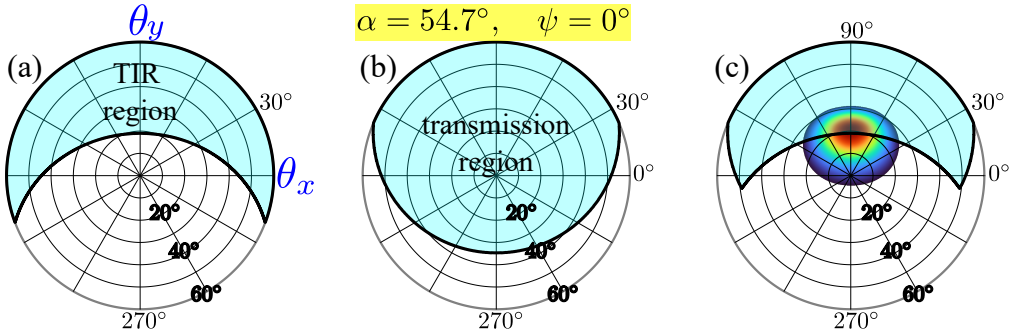

Figure 3.19: Visualization of the prism response. The polar plot represents the space of incident rays, with the center corresponding to a ray along $\hat{z}$. (a) shows the blue region where the rays satisfy the TIR condition. (b) shows the region where the rays satisfy the transmission condition at the second interface. (c) shows the region where the rays can be extracted. The power lobe corresponds to the far-field of a leakage occurring at an angle around $\theta_y = 20°$ (or $\theta = 70°$).

The blue regions are represented as binary conditions: if the ray falls within it, it is extracted,

without indicating how much % of the ray is extracted. The TIR is binary, as it is a plateau. The transmission is not binary; Fresnel coefficients must be applied. Nevertheless, it can be considered binary for rays that are far from the boundaries (critical angles).

Note: Do not confuse the extraction angle θ (in Fig. 3.17(b) or Eq. (2.28)) with the angular space coordinates θ_x and θ_y. In fact, $\theta = 90° - \theta_y$.

The angle of the prism is $\alpha = 54.74°$. The rotation angle of the prism is $\psi = 0°$. The first plot (a) shows the region where TIR is possible. For example, the central ray lies outside the TIR region and it is not totally reflected. As the ray angle increases in the $\hat{y}$ direction (i.e., θ_y), the incident angle also increases, making TIR possible. At $\theta_y \sim 20°$, the ray enters the TIR region. Similarly, if the prism is rotated, or equivalently, if the central ray is rotated in the $\hat{x}$ direction, TIR becomes possible for $\theta_x \sim \pm 45°$.

The second plot (b) shows the region where transmission is possible. This represents the second requirement to extract the rays from the structure. To separate this condition from the first one, the incident space is reflected as if the prism acts as a mirror of an angle α. For example, the centered ray, when reflected, is within the transmission region.

The third plot (c) shows both conditions since the rays must respect TIR and transmission. Inside this space, we show a far-field representation of the leaked power. Extraction occurs around $\theta_y = 20°$ ($\theta = 70°$). The far-field is projected along the $\hat{z}$ direction. The power distribution in the polar plot illustrates the extraction divergence. Here, the mode is extracted using $n_{\text{LC}} = 1.85$. The extraction length is $1/\alpha_r = 3.33$ μm. The full divergence in the $\hat{y}$ direction is approximately 15° inside the high index layer. The divergence in the $\hat{x}$ direction is larger due to the small waveguide width, with a total divergence of $\sim 50°$. For successful extraction, the regions of TIR and transmission must overlap with this far-field. Approximately 50% of the far-field lies within this overlap.

This plot does not capture the full image of the extraction. The incident rays must first touch the prism facet. In fact, increasing the extraction angle θ_y improves the overlap. However, there is a trade-off with the need to reach the prism of thickness t_p, as discussed in the previous section (Equation (3.8)). It is recommended to use extraction angles θ_y below 20° to maintain a reasonable thickness t_p.

In Figure 3.20, we present interesting results when considering a prism angle of 45°. Here, we show results for different values of ψ. In the first row (a,b,c). The TIR condition is lower than before. At $\theta_y \sim 10°$, the ray enters the TIR region. The transmission condition is symmetric around the central ray, since $\alpha = 45°$. The angular radius corresponds to the critical angle. The overlap between the far-field and the prism condition is greater than before with an angle of $\alpha = 54.74°$.

By rotating the prism at an angle ψ, the condition can be shifted toward the far-field of the extraction in the LC layer. In the second row (d,e,f), we show the results for $\psi = 40°$. The central point lies within the TIR region. The transmission region is shifted to the right. Increasing ψ increases the likelihood of TIR, as the incident angle β increases. However, the chance of transmission decreases since the incident angle γ on the subsequent surface also increases. In (f), the overlap is good.

Figures (g), (h) and (i) show the results for $\psi = 20°$, 60° and 80°, respectively. In this particular case of $\alpha = 45°$, the extraction region shifts horizontally by the same amount as ψ. The maximum and minimum shifts that include the central ray (for parallel coupling) occur at $\psi \approx 54°$ and $\approx 35°$, respectively.

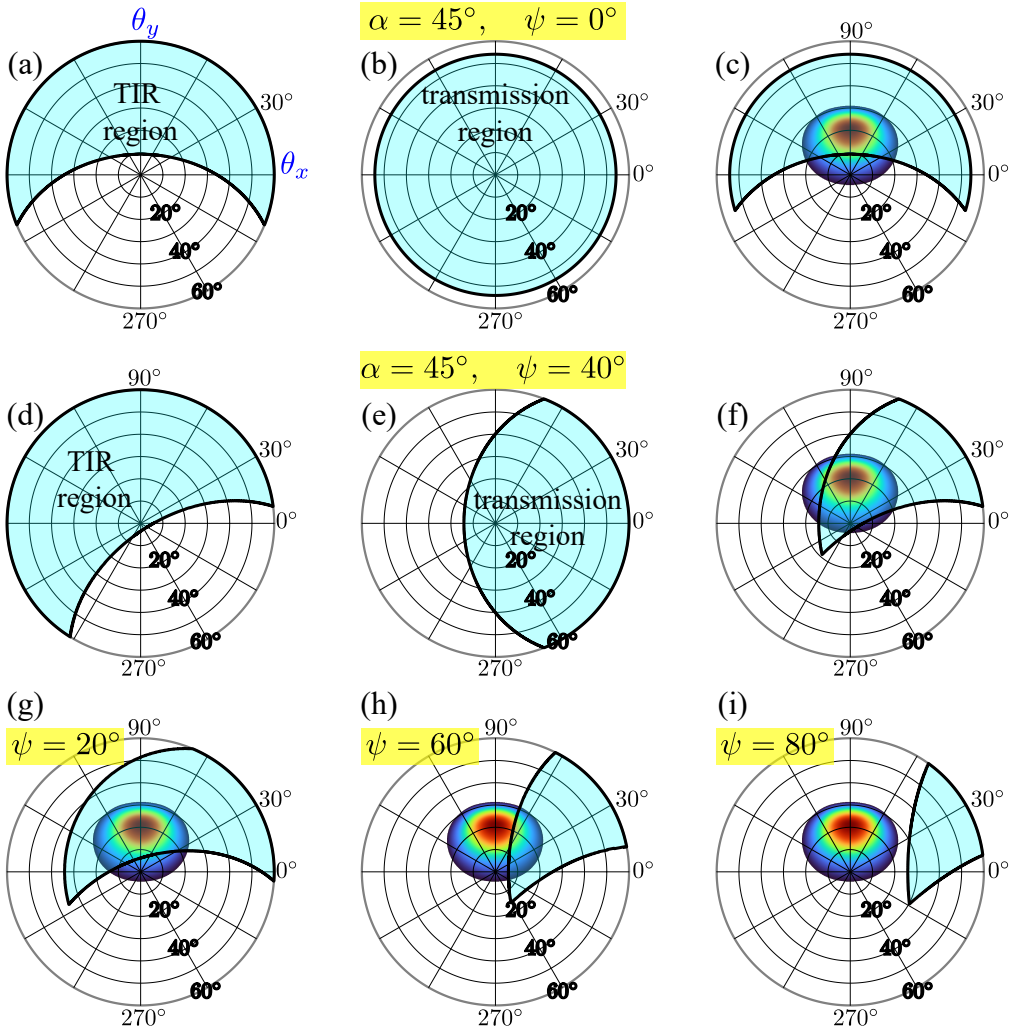

Figure 3.20: Visualization of the prism response for a prism angle $\alpha = 45°$. The polar plot represents the space of incident rays, the center corresponding to a ray along $\hat{z}$. The prism rotation around the $\hat{y}$-axis is defined by the angle ψ. Figures (a) and (d) show the regions where the rays satisfy the TIR condition. Figures (b) and (e) show the regions where the rays satisfy the transmission condition at the second interface. Figures (c), (f), and the last row (g, h, i) show the regions where the rays can be extracted. The power lobe corresponds to the far-field of a leakage occurring at an angle around $\theta_y = 20°$ (or $\theta = 70°$). The transition occurs between refractive indices of 1.8 and 1.46.

The angle 45° is particularly interesting, especially when taking into account the possibilities introduced by varying ψ. In this representation, I did not include how the rays are refracted in air or at which angle. This was left as a perspective work, which must also account for the hologram that can center the extraction to the normal.

3.2.7 Full Extraction Efficiency Simulation

In Figure 3.21, I show the total extraction efficiency as a function of n_{LC} and the total length of the component ℓ_c. The angle of the prism is 45° with $\ell_p = t_p = 2$ μm and $\psi = 0°$. A horizontal line on the y-axis indicates the effective index of the guided mode. The wavelength is 0.532 μm.

In practice, the LC layer is a slab waveguide. However, the size of the simulation window cannot be infinite. Taking into account the divergence and the propagation length, a reasonable

width can be set to ensure the overlap of the extraction with the prism interface. For 3D FDTD simulations, the simulation size is computationally expensive. Therefore, we fixed the simulation width to 3 μm and used two different waveguide geometries to have two different divergence.

In (a), the width and thickness of the waveguide are 0.3 μm and 0.2 μm, respectively. The mode is TE, with $n_{\text{eff}} = 1.704$. In (b), the width and thickness of the waveguide are 1 μm and 0.12 μm, respectively. The mode is TE, with $n_{\text{eff}} = 1.701$. The separation distance is $s = 0.05$ μm. In (a) and (b), the maximum extraction efficiencies are 63% and 76%, respectively. This efficiency is achieved for n_{LC} values between 1.8 and 1.9. This efficiency can also be achieved for lower values of n_{LC} by reducing the effective index of the waveguide.

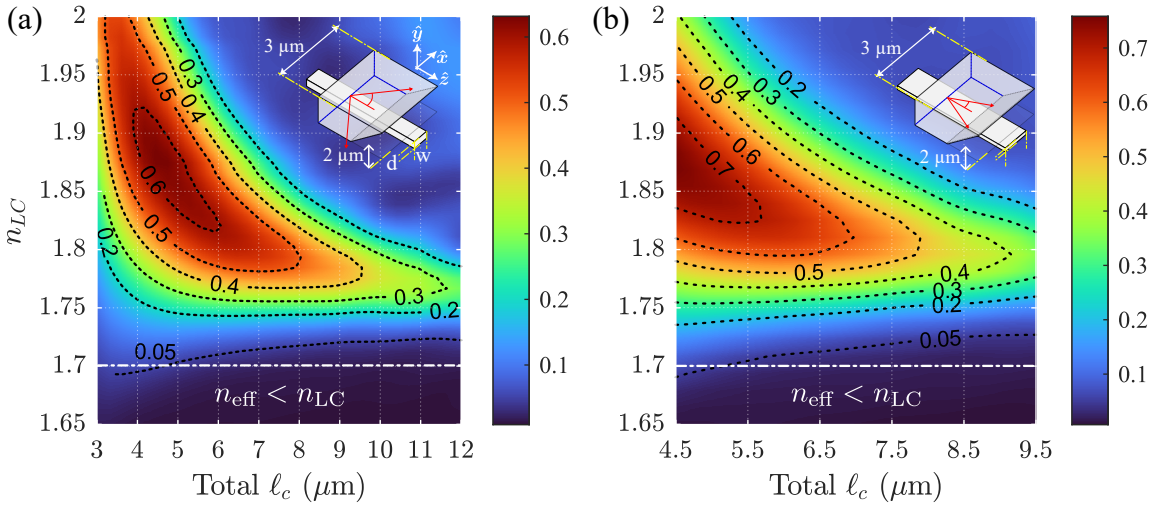

Figure 3.21: 3D FDTD simulation of full extraction efficiency via evanescent coupling (including the prism), as a function of LC RI and total extraction length (including the length of the prism). The waveguide index is 2. The geometry is buried in RI = 1.46. The wavelength is 0.532 μm. The width of the FDTD box is 3 μm. In (a), the width and thickness of the waveguide are 0.3 μm and 0.2 μm. In (b), the width and thickness of the waveguide are 1 μm and 0.12 μm, respectively. The mode is TE, with $n_{\text{eff}} = 1.704$ for (a) and $n_{\text{eff}} = 1.701$ for (b). The separation distance is $s = 0.05$ μm. The maximum extraction efficiencies are 63% and 76% for (a) and (b), respectively. The difference in efficiency is due to the difference in leakage divergence relative to the FDTD box fixed at a width of 3 μm.

Figure (b) exhibits an efficiency higher than (a), because the waveguide width is larger, resulting in reduced divergence. This difference is due to the limited width of the simulation. Taking a point from (a) at $n_{\text{LC}} = 1.85$ and $\ell_c = 5$ μm, the efficiency converges to 75% as a function of the simulation width for widths greater than 7 μm. The remaining power lost in the waveguide is approximately 13–17%. The additional loss of about 9% occurs at the prism with the incident divergence.

Extracting the remaining guided power would require increasing both the extraction length and the thickness of the prism (see Equation (3.8)). However, it is interesting to note that the remaining guided power is low and does not contribute to parasitic extraction, which would otherwise impact contrast.

Oblique coupling offers a wider range of flexibility in choosing the coupling length. This length can be tuned by adjusting the separation distance s. The coupling conditions are also more relaxed than those required for phase matching with the parallel coupling. The total efficiency for both mechanisms can exceed 60%. The maximum efficiency reaches 86.4% for the parallel

coupling and 76% for the oblique coupling. The minimum total extraction length can be as short as 5 μm. This length can be increased to achieve a higher ℓ_c by appropriately selecting α_r. This, in turn, depends on the separation s, the effective index n_{eff}, and the refractive index of the LC layer n_{LC}. Details on how each parameter influences α_r can be found in the previous chapter.

Figure 3.22 shows a simulation of this component using the nematic liquid crystal 5CB under an applied voltage. The results were obtained using COMSOL. The applied voltage reorients the LC, changing its refractive index from 1.54 to 1.73. The blue arrows indicate the LC director. The upper electrode is positioned to provide an adiabatic transition of the refractive index, which can be observed near the tip of the prism. The waveguide "sees" a gradual increase in n_{LC}, which reduces diffraction effects at the transition between ON and OFF pixels.

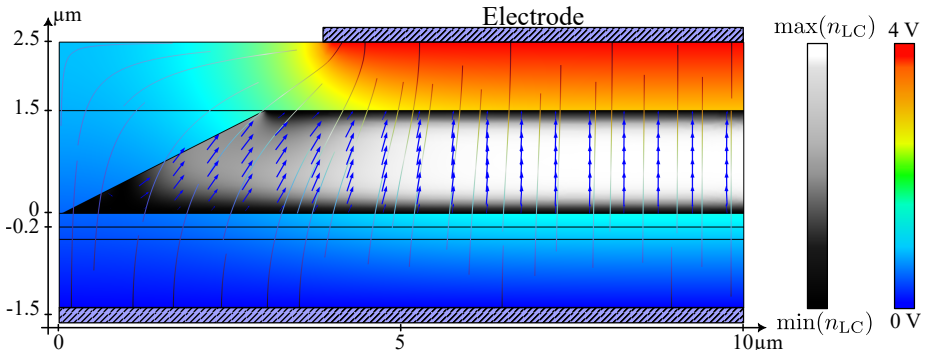

Figure 3.22: An example of RI distribution under applied voltage. The LC is strongly anchored to the surface (Dirichlet boundary condition). The blue arrows indicate the LC director.

Note that the tip of the prism has a slight impact on the contrast. For a separation of $s = 0.05$ μm, with $n_p = 1.73$ and in the OFF state where $n_{\text{LC}} = 1.54$, we have an upward transmission of 0.1%. This can be reduced by increasing the separation s.

Conclusion

In this section, I presented an innovative concept that enables efficient extraction over shorter lengths compared to diffraction gratings. The approach combines evanescent coupling with TIR and it was patented during the PhD. The following table summarizes some of the key results.

	α_r (μm^{-1})	Efficiency ($\ell_c = 10$ μm)	Tuning Parameters	Tolerance	LC	Pol.	λ (nm)
Grating + LC	0.005	<10%	Δn, n_{eff}, d_g	Good	Nematic	TE	depends
Parallel Coupling	<0.2	≈85%	s, n_{eff}	Low	Nematic and FLC	TE and TM	depends
Oblique Coupling	>0.2	≈75%	s, n_{eff}, n_{LC}	Good	Nematic and FLC	TE and TM	depends

Table 3.2: Summary of extraction strategies.

3.3 Results: Passive Extraction Demonstration

3.3.1 Fabrication Process of a Passive Sample

To validate the concepts developed in this chapter, we propose a passive test sample. The electro-optical approach using liquid crystals has not been treated experimentally in my thesis. Nevertheless, I have provided some basic theoretical elements that could serve for a potential follow-up thesis. The idea of this passive approach is to replace the high-index layer with a passive material, namely a resin. Evanescent coupling and total internal reflection (TIR) will be demonstrated using the microstructure described in Figure 3.23(a).

The structure shown in green is a strip with a thickness h_r and a fixed width. The facets, or sidewalls, are tilted at an angle α. The structure is fabricated on a transparent substrate using Nanoimprint Lithography (NIL). The block (1) is referred to as the NIL chip. This component is then glued to a photonic integrated circuit (PIC), illustrated by the block (2). The adhesive is a UV-curable glue with a RI of $n_{\text{glue}} = 1.54$ that fills the space around the NIL structure.

Our goal is to obtain facets of optical quality. To achieve this, we use wet etching of silicon followed by replication through NIL. The NIL material must exhibit very high transparency to minimize propagation losses, and its RI must fall within the desired value ($n_{\text{NIL}} \geq n_{\text{eff}}$).

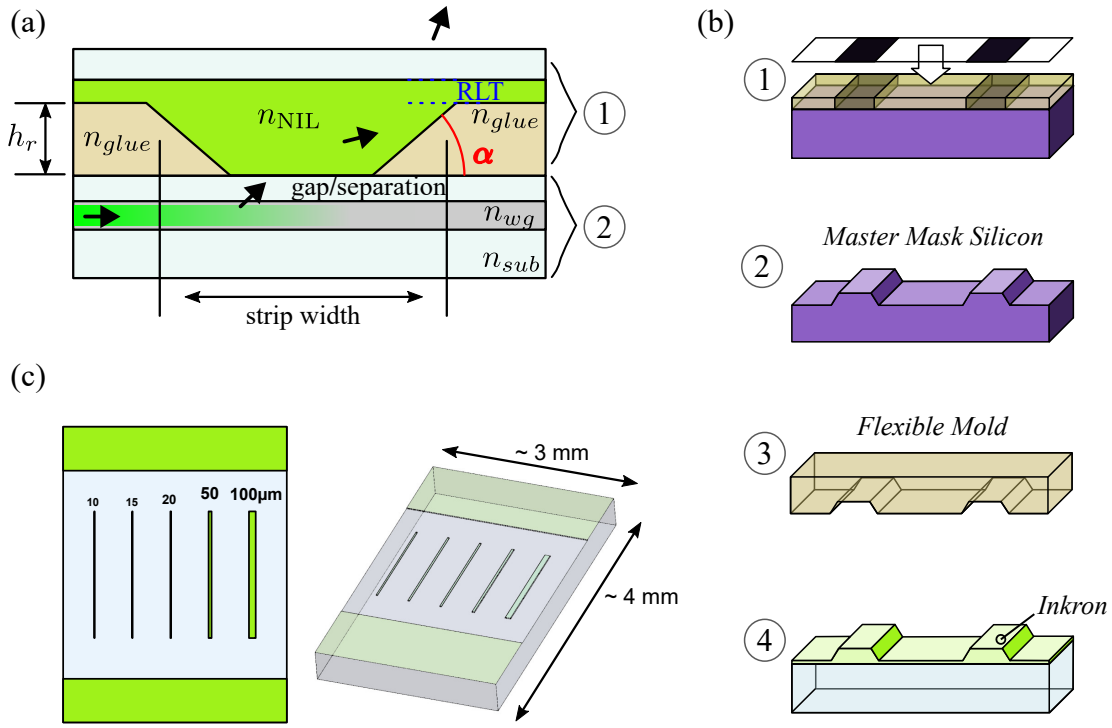

Figure 3.23: (a) Description of the passive sample used to demonstrate evanescent coupling and TIR: **{1}** The Nanoimprint Lithography (NIL) chip. **{2}** The Photonic Integrated Circuit (PIC). (b) Fabrication process of the passive sample. **{1}** Lithography, **{2}** wet etching results, **{3}** mold fabrication, and **{4}** NIL replication. (c) Chips of size 3 × 4 mm^2 are diced, each containing strips of 10, 15, 20, 50, and 100 μm.

We collaborated with in-house laboratories specialized in NIL and wet etching to test several materials and to evaluate their compatibility with the dimensions of our microstructure. The

typical thickness of the structure is about h_r =2 μm. In the schematic, a residual layer thickness (RLT) is indicated.

In Figure 3.23(b), the fabrication process is described:

(1) **Lithography:** a lithographic mask with strips of different widths is used for the wet etching of silicon.

(2) **Wet etching:** following targeted wafer crystal plane, this process reveals strips with optically smooth facets at α = 45° or 54.74°. This enables the fabrication of the master structures.

(3) **Mold replication:** for NIL, a flexible mold is replicated from the master.

(4) **Resin imprinting:** this mold is then used to reproduce the structure in a high-index resin.

For the materials, several resins were evaluated. From Norland, we tested NOA170 with a RI of 1.7 in the visible range. From HighRI Optics, we tested the resin Nano1.9-P with an RI of 1.9. From Inkron, we tested the resin IOC-135-C55 with an RI of 1.8. Compared to the other resins, the Inkron material allowed us to replicate the structures faithfully, with very few defects. We therefore chose the Inkron resin.

Once the NIL process is completed, chips of size 3×4 mm^2 are diced, as indicated in Figure 3.23(c). Each chip contains five strips with widths of 10, 15, 20, 50, and 100 μm.

3.3.2 Wet Etching of Silicon and Nanoimprint Results

Figure 3.24(a) presents a schematic of the strip composed of the RI Inkron resin. The sidewalls must exhibit optical quality to act as mirrors for TIR. Two sidewall angles, 45° and 54.74°, can be obtained by anisotropic wet etching of silicon (Si).

The development of these planes depends on the type of Si wafer (e.g., (100)-Si) and its orientation during lithography with respect to the strip. For a strip patterned in the standard orientation relative to the wafer notch, etching produces sidewalls at 54.74°. To obtain sidewalls at 45°, the wafer or mask must be rotated by 45° relative to the notch [158].

Anisotropic etching of silicon is widely employed in the fabrication of micromirror structures. A selection of relevant studies on etching at 45° and 54.74° is provided in [157, 159, 160].

This work has been carried out in collaboration with colleagues in CEA Leti specialized in wet etching, who evaluated two anisotropic etching solutions: KOH/IPA and TMAH/Triton.

Based on their results, KOH/IPA was selected because it produces best surface quality. Silicon masters were subsequently fabricated in both orientations to obtain the two corresponding sidewall angles.

In Figure 3.24(b), microscope images of 20 μm-wide strips are superimposed, illustrating the results of 45° (top) and 54.74° (bottom) etches. we can note that, depending on the mask orientation relative to the wafer, the crystalline structure exposed at the bottom differs. The top strip was oriented at 45°.

Figure 3.24(c) presents SEM views of the etched sidewalls of the silicon master. The strip shown features 45° sidewalls, a thickness of 2.5 μm, and a width of 50 μm. The sidewalls exhibit good optical quality with minimal residue.

From this Si master, a flexible mold was fabricated by colleagues in CEA Leti specialized in NIL. The mold is used to replicate the strips in Inkron resin with a RI of 1.808 at 532 nm.

Figure 3.24(d) shows the sidewalls of the Inkron NIL replication, while Figure 3.24(e) presents an SEM cross-section of the strip. This strip is the results of a 10 μm mask opening. The measured width of the resulting strip is approximately 13.5 μm. This difference is attributed

to the etching process of silicon, which extends slightly beneath the mask. The thickness of the replicated structure is 2.34 μm. The replicated angle is 42.5° instead of 45°, which can be explained by shrinkage during UV curing of the resin (about 8%).

The key result is the good optical quality of the facets, essential for the total internal reflection.

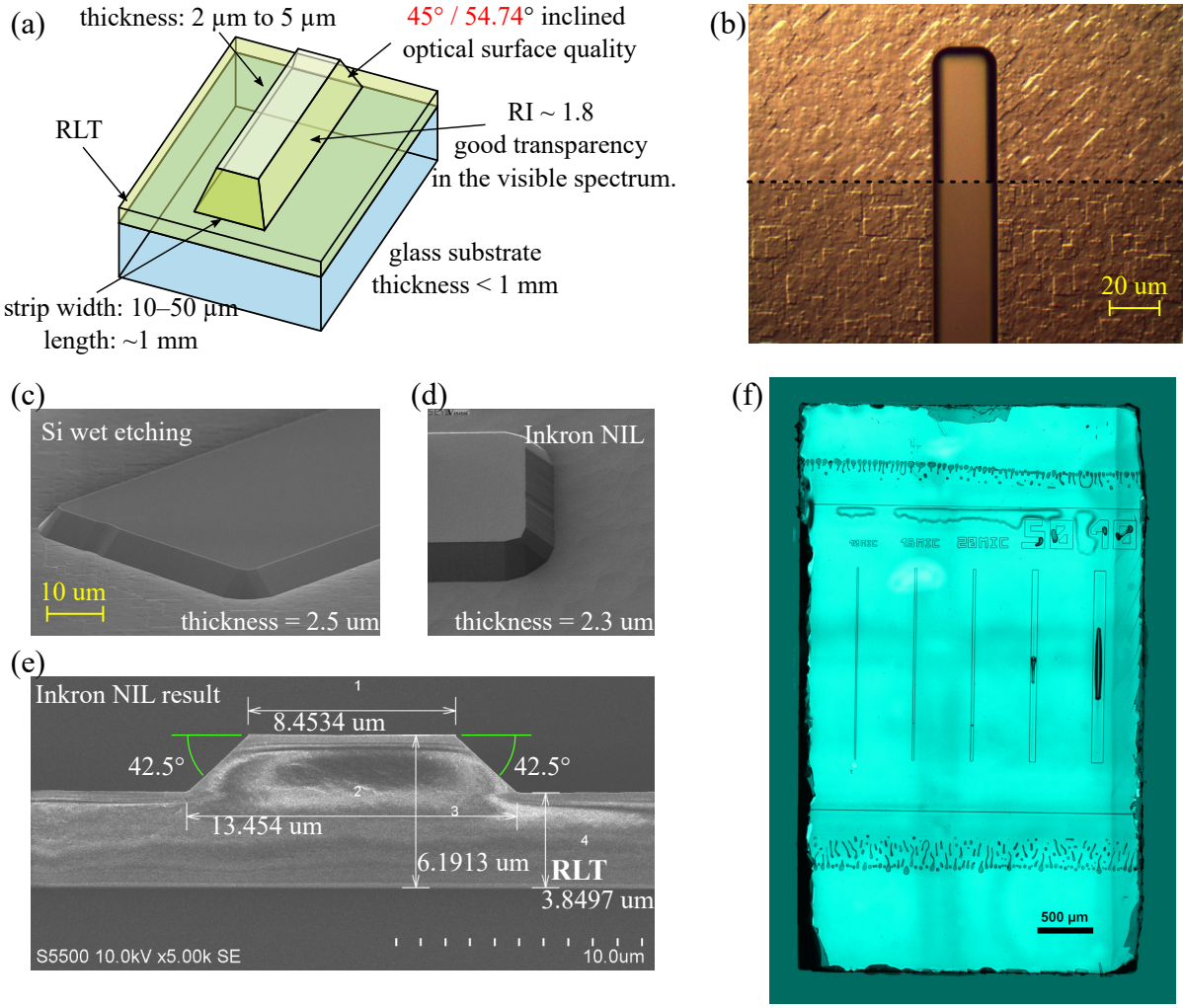

Figure 3.24: (a) Schematic of the strip characteristics: transparent high-index resin with sidewalls (facets) at 45° or 54.74°, exhibiting optical surface quality. (b) Superposition of two photographs of the 20 μm strip after the Si etching: Sidewalls at 45° (top) and 54.74° (bottom). The focus is set at the bottom of the etched cavity (around the strip). (c) SEM view of Si wet etching results. (d) SEM view of a replication result obtained by NIL using Inkron resin. (e) SEM cross-section of a 10 μm strip in Inkron resin. (f) Stitched optical microscope image of the final NIL chip.

We performed ellipsometry measurements using a Woollam M2000-DI to determine the RI and the extinction coefficient k of the NIL structure. The measured coefficient was $k \leq 10^{-6}$ for wavelengths in the range 0.45–1.5 μm, indicating that the absorption losses are below 1 dB/cm. We can note that these values are below the typical ellipsometric sensitivity ($k \sim 10^{-4}$–10^{-3}). Since ellipsometry provides an *indirect* measurement, the precision and reliability of the extracted k values should be verified using complementary techniques.

After the process on the 200 mm glass substrate, the patterns of interest were diced. Figure 3.24(f) shows the cutting results of our NIL chip (3 × 4 mm^2), where five strips are visible.

The Inkron resin provides excellent results with very good uniformity in the pattern development of the strips. However, slight filling defects can be observed, with the appearance of a central bubble in the widest strips (systematically on the 50 μm and 100 μm strips). Strips with widths of 10, 15, and 20 μm are generally perfectly replicated on the whole 200 mm glass wafer.

The subsequent step involves bonding the NIL chip onto a PIC.

3.3.3 Overview of the Layout: PIC and NIL Chips

The off-the-shelf PIC used in this work is shown in Figure 3.25(a). This PIC was originally developed by the team for a different project [99]. I identified some building blocks that can be used in our case. The PIC is fabricated using a CMOS process with silicon nitride (SiN) waveguides deposited by PECVD (Plasma Enhanced Chemical Vapor Deposition) on 300 mm wafers. The waveguides are buried in silicon oxide (SiO_2). Through molecular bonding, the PIC is transferred from the silicon substrate (left image) onto a glass substrate (right image), after which the silicon is removed, making the PIC transparent.

This PIC was developed on a 300 mm platform to reduce waveguide sidewall roughness and thereby minimize propagation losses. However, in this platform the only available method for SiN deposition was PECVD rather than LPCVD (Low Pressure CVD). As a result, the PIC exhibits unexpectedly high propagation losses of 25 dB/cm at 532 nm, which are not attributed to roughness, but to absorption of SiN. More details on the development of this PIC can be found in [99]. Nevertheless, the PIC remains operational at 660 nm, where the propagation losses are 3.5 dB/cm. The waveguide profile is rectangular, with a thickness of 200 nm and widths ranging between 300 and 400 nm.

A typical value of the effective index is around $n_{\text{eff}} \approx 1.7$ at 532 nm for TE polarization, considering $n_{\text{SiN}} = 2.0$ and $n_{\text{SiO}_2} = 1.46$.

Our NIL chip is mounted onto this PIC and bonded using NOA68 UV glue with a RI of 1.54. The white arrow in Figure 3.25(a) indicates the bounding of the NIL chip onto this PIC.

Figure 3.25(b) presents a schematic of this bonding. The NIL chip is represented by the rectangle with five strips. The schematic below represents a portion of the PIC layout. The orange lines represent the waveguides, while the green lines correspond to waveguides on a second level beneath the orange ones. We focus only on the first-level waveguides.

The block of interest begins at point (1), which includes a grating in-coupler grating used to couple light from an external optical fiber. In region (2), light is divided into 64 waveguides through a cascade of MMIs (multimode interferometers), as indicated by the arrows. The NIL strips can be aligned with these waveguides, as shown at point (3), where the 10 μm strip first interacts with the waveguides. An assembly protocol was developed to orient the strips at a fixed angle and position relative to the waveguides. Finally, at point (4), a grating out-coupler extracts all the remaining guided light. Note that the NIL strips in region (3) do not cover all the waveguides, leaving some uncovered to provide a reference signal at the out-coupler.

I used the term "separation" in the previous Chapter 2 to denote the "gap" that separates the waveguide from the high-index layer. These two terms are interchangeable. This is illustrated in Figure 3.23(a). In our transparent PIC, the waveguide has a SiO_2 top cladding (superstrate) with a thickness of approximately 30 nm. If the NIL chip and the PIC are bonded in optical contact, the gap would be 30 nm. However, a relevant question concerns achieving optical contact (i.e., the absence of an air gap between the chips). To investigate this, we used an optical microscope to analyze Newton fringes.

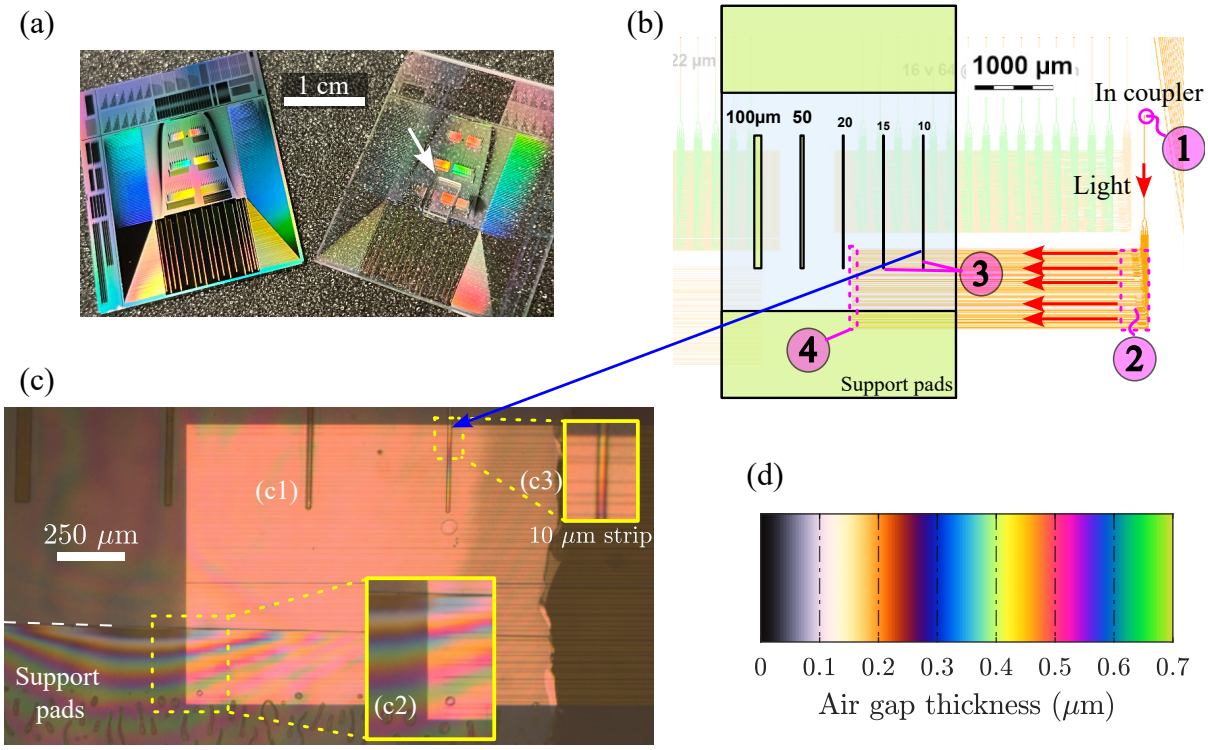

Figure 3.25: (a) Off-the-shelf PIC used for passive extraction. On the left: SiN waveguides buried in SiO_2 on a silicon substrate. On the right: PIC transferred onto a transparent glass substrate. The arrow indicates the NIL chip bonded to the PIC. (b) Schematic layout showing the alignment between the NIL chip and the PIC. (c) Microscopic image of the strip alignment with respect to the waveguides. (d) Simulation of reflected white light as a function of the air gap between two glass substrates.

Figure 3.25(c) shows a microscope image of the NIL chip on the PIC, taken before dispensing the UV glue. The alignment is maintained using a 3D-printed holder.

The strips are visible; (c1) corresponds to the 15 μm strip. The brighter rectangular zone (white–orange) indicates the waveguides. Two strips (c1) and (c3) cover about one-third of the upper portion of these waveguides. This image can be linked to the previous Figure 3.25(b). On the left side of the bright zone lies region (4), which contains the out-coupling grating.

Note that the NIL chip includes support pads at the top and bottom with the same thickness as the strip. (c2) shows a zoomed-in view of the contact at the lower support, where color fringes are observed. These Newton rings indicate the presence of an air gap between the chip and the PIC, resulting from wavelength-dependent interference. Figure 3.25(d) presents a simulation of reflected white light as a function of the air gap between two glass substrates, where darker colors indicate optical contact.

In (c2), the air gap is seen to increase from top to bottom. The 15 μm strip in (c1) and the two strips on the left are thus in optical contact, while the 10 μm strip shown in (c3) is not. Comparison with the colors in Figure 3.25(d) suggests that this 10 μm strip has an air gap of approximately 100–200 nm. The actual separation for the evanescent coupling would be the sum of the air gap and the thickness of the top cladding of 30 nm.

This strip is closer to the edges. We can note that the dicing process was not perfect, as seen by the removed resin at the edges in Figure 3.24(f). In addition, bonding with the PIC was carried out manually, which may have introduced imperfections. The presence of microscopic particles can hinder the establishment of proper optical contact. This explains the observed air

gap in the 10 μm strip. As a result, this later exhibits an air gap of approximately 200 nm due to its proximity to the edges, whereas the 15 μm strip (c1) achieves full optical contact.

In the final step, NOA68 UV glue with a refractive index of 1.54 is dispensed to replace the air and seal the bonding.

3.3.4 Experimental Protocol Using a Goniometer

The sample is mounted in a goniometer setup. Figure 3.26(a) shows a schematic of the characterization setup. Light from an optical fiber at 532 nm (green) or 660 nm (red) is coupled into the PIC through a grating coupler. The red arrows indicate the propagation direction.

The extraction characteristics are measured under imaging conditions: a camera equipped with an objective lens rotates around the extraction axis, with θ denoting the observation angle. A grayscale iDS CMOS monochrome camera (8-bit dynamic range with sensor size 6.4 × 4.6 mm) is used for characterization.

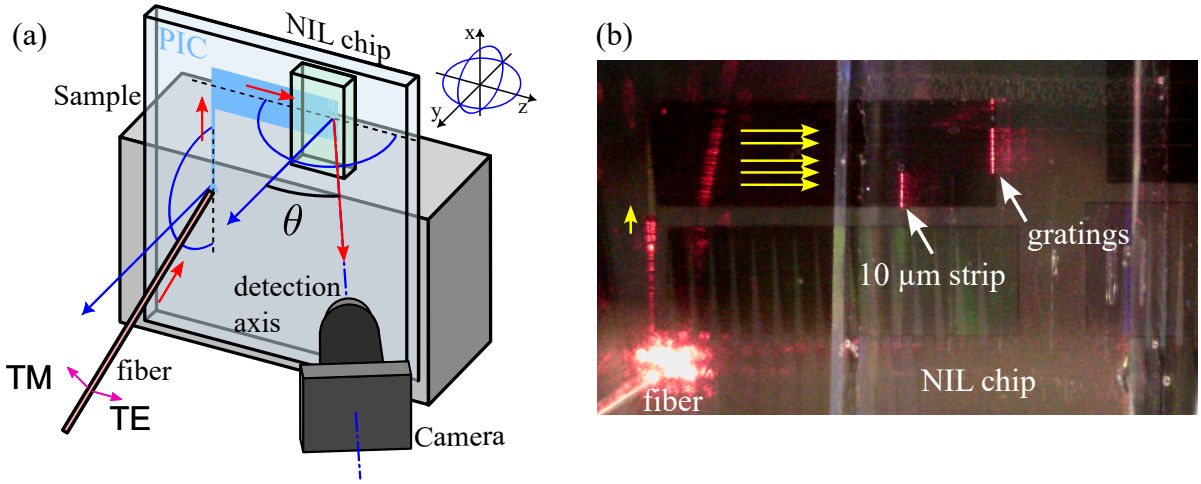

Figure 3.26: (a) Characterization setup using a goniometer. The signal from the fiber is coupled into the sample, and the extraction is measured in the near field using an iDS grayscale camera with an objective lens. (b) Image captured with a Dino-Lite color camera showing the extraction. The 10 μm strip extracts the light.

Before I proceed with the angular measurement, I use a Dino-Lite digital microscope camera to capture a large field-of-view color image. Figure 3.26(b) shows the image obtained using the red wavelength. The intense spot in the lower-left corner corresponds to the reflection from the input optical fiber. The propagation direction is indicated by the yellow arrows. The bright region near the first arrow corresponds to the MMIs used for light division. Additional red spots can also be observed, originating from stray light caused by coupling, reflections, and interactions with microstructures.

Following the arrow direction, we enter the bonding region between the NIL chip and the PIC. The key result is observed at the position of the 10 μm strip, where the extracted light is clearly visible. In relation to Figure 3.25(c), we observe that no light is extracted from the 15 μm strip.

At the end, we have out-coupling grating. Extraction from the gratings can be observed in the region where the waveguides path is not covered by the strip.

This image is a qualitative demonstration of the extraction using our concept of evanescent coupling and TIR. In the following, I provide additional results showing that the extraction is localized at each waveguide. and that the extraction using the strip occurs in one direction, in contrast to the grating. I show the intensity profile in 1D and present FDTD simulations to fit and support the experimental results.

3.3.5 Results and Analysis

Evaluation of the Extraction Directionality

Figure 3.27 shows images captured with a high resolution monochrome camera. Figure 3.27(a) presents an image of the extraction from both the strip and the out-coupling grating.

In (a1), a close-up view of the strip is shown. The yellow arrow indicates a bubble defect in the glue, located at the end of the strip. This bubble will serve as a useful reference to locate the strip. The waveguides appear as horizontal lines. It should be noted that the waveguides are not uniformly distributed and are grouped into four families with widths of 370, 380, 390, and 400 nm. The strip is visible, with the extraction localized at the waveguide positions and along the second sidewall of the strip.

(a2) shows the extraction at the out-coupling grating. Some waveguides do not exhibit any extraction, which can be correlated with the colored fringes observed in the microscope image of Figure 3.25(c2). In this region, the NIL chip support has the same RI as the strip, and the waveguide signal is coupled through evanescent coupling.

A binary out-coupling grating diffracts light symmetrically into two directions, upward and downward. In contrast, our approach is directional, as the reflected light is extracted in one direction. Figure 3.27(a) shows the camera focused on the front of the sample. Since the sample is transparent, a mirror was placed behind it to observe the rear of this sample. Figure 3.27(b) shows the corresponding image obtained when focusing on the reflection from the mirror. In other words, (a) represents the forward direction, whereas (b) corresponds to the backward direction. In (b), the yellow arrow marks the position of the strip.

It can be observed that, unlike the forward direction in (a), no extraction appears in the backward direction in (b). However, for the out-coupling grating, identical extraction is observed in both directions. Unlike the conventional binary grating, our extraction is therefore fully directional as expected.

In the goniometer setup, I measured the angular characteristics of the strip extraction by rotating the camera around the extraction points. Figure 3.27(c) shows an example of the results as a function of the angle θ. A first scan was performed to identify the angle at which the intensity is highest. For example, at a wavelength of 532 nm, the maximum intensity was observed around 50°. The laser power was then reduced to avoid saturation at this maximum, and a second scan was performed at different angles.

I carried out this characterization at 532 nm because, for the red wavelength (660 nm), the corresponding angle is larger. Measuring at higher angles increases the obliquity factor, leading to stronger image distortion. Despite the high propagation losses in the green, extraction is measured at different angles. Noted that Figures 3.27(a), 3.27(b), and 3.27(c) were all obtained at 532 nm. In Figure 3.27(c), the grayscale image was falsely colored in green to emphasize the used wavelength.

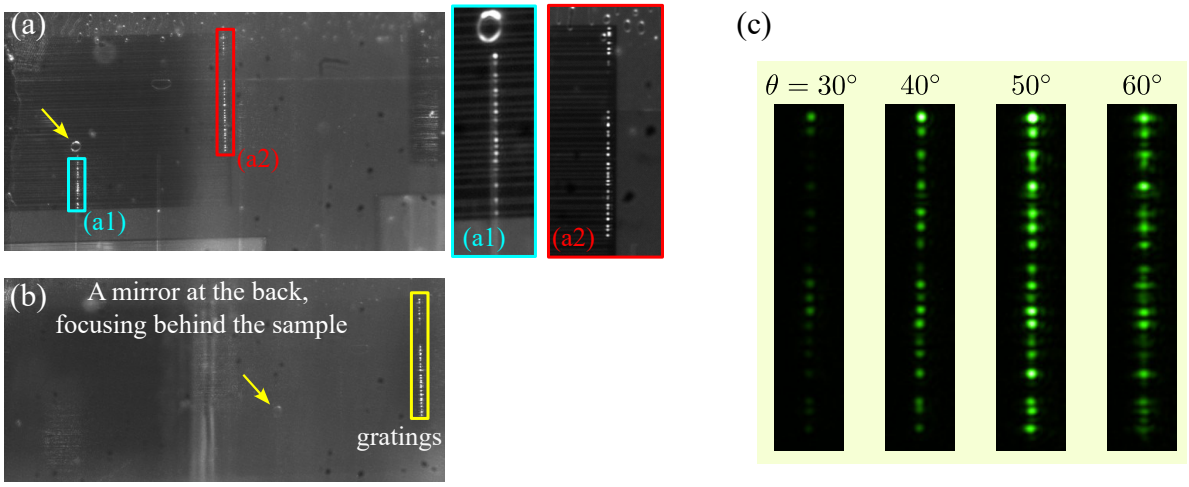

Figure 3.27: (a) Image of the extraction: (a1) localization of the extraction at the 10 μm strip, and (a2) the out-coupling grating extraction. (b) Image of the extraction in the backward direction, showing that the grating extracts light in both directions, in contrast to our directional strip. (c) Image of the strip extraction at different observation angles.

Measurement of the Intensity 1D Profile

The second step consisted of processing the images using MATLAB. For each extraction point, the pixel values are integrated. Since these points correspond to different waveguides widths, the resulting integrations as a function of angle are grouped according to the corresponding waveguide widths.

In Figure 3.28, the angular characteristics of the extraction are presented for the group of waveguides with a width of 400 nm.

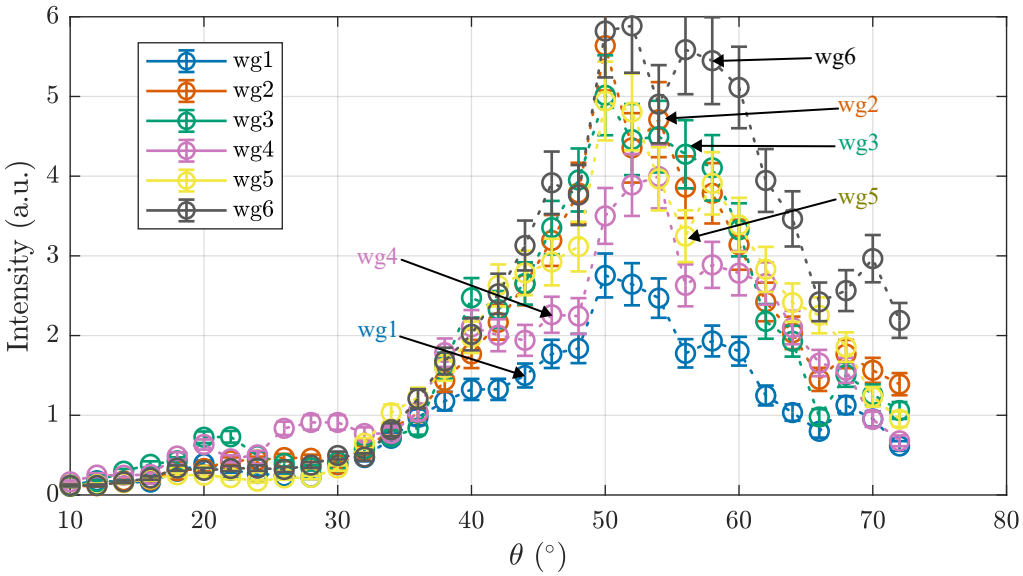

Figure 3.28: Experimental results of the strip extraction. The intensity is plotted as a function of θ (or θ_z), the angle along the propagation direction. All waveguides have the same width of 400 nm.

The extraction is centered around 50°. The results for the different waveguides show similar

profiles but with varying peak heights. This can be explained by differences in the gap, as shown by the variations in fringe color.

Theoretically, using geometrical optics, the extraction angle in air can be expressed by the following equation:

$$\gamma_{\text{out}} = \arcsin\left(n_{\text{NIL}} \sin\left(2\alpha + \arcsin\left(\frac{n_{\text{eff}}}{n_{\text{NIL}}}\right)\right)\right) \tag{3.9}$$

where γ_{out} is the extraction angle in air, n_{NIL} is the refractive index of the resin, α the strip angle, and n_{eff} the effective index of the waveguide. Using $n_{\text{eff}} = 1.7$, $n_{\text{NIL}} = 1.808$, and $\alpha = 42.5°$, the calculated extraction angle is 49.6°. This agrees with the experimental measurement.

In Figure 3.28, the FWHM of the extraction is around 20°. Theoretically, if a sidewall thickness of 2.34 μm at an angle of 42.5° is considered as the diffraction limit, the corresponding length size is $a = 2.34/\sin(42.5°) = 3.46$ μm. Using the diffraction formula in the resin of RI $n = 1.8$, we get $\arcsin\left(\frac{\lambda}{n \cdot a}\right) = 8.83°$.

The extraction angle inside the resin is $\gamma_{in} = 24.9°$, which corresponds to 49.6° outside in air. Applying Snell's law for $\gamma_{in} \pm 8.83/2$ when refracting from $n = 1.8$ to $n = 1$ (air) gives extraction angles of 61.82° and 39.05°. The theoretical FWHM can therefore be expected to be approximately $61.82° - 39.05° = 22.77°$. This is consistent with the experimental results.

The hypothesis that the sidewall length of the prism acts as the element that limits diffraction in the propagation direction can be justified. In fact, along this direction, it was shown in my theoretical analysis that the divergence of the evanescent coupling is directly related to the leakage length ($1/\alpha_r$). However, after evanescent coupling, reflection from the sidewall can also act as a limiting factor for diffraction. In this case, the length of the sidewall is small compared to the leakage length.

Measurement vs FDTD Simulations

In Figure 3.29(a) I show a scaled schematic of the functional strip. This strip corresponds to a width of 10 μm. The wet-etching process results in a total etching width of 13.45 μm, while the effective interaction width is 8.32 μm.

Two rays are plotted. The first ray is not reflected by the facet due to the large strip width, whereas the second ray hits the facet and is reflected and refracted into free space. When the separation (gap) is small (around 50 nm), the interaction is strong and the leakage length ($\propto 1/\alpha_r$) becomes smaller than the strip width. In this case, the extraction into air is expected to be very low.

Based on the observed fringe colors, the gap remains within the evanescent field range (100–300 nm). Some evanescent coupling can therefore be expected. low extraction is also expected, as the evanescent coupling is not strong and the interaction width of 8.32 μm is sufficient to allow some rays to be extracted.

In Figure 3.29(b), a 3D FDTD simulation of the intensity profile along the propagation direction is presented. The goal is to verify the experimental intensity distribution. The legend indicates the gap values, which range from 50 nm to 400 nm.

The intensity is not localized at 50° for a gap of 50 nm. At this value, the strip width is larger than the leakage length, resulting in an extraction efficiency of only 0.7%. However, the profile becomes more localized around 50° for larger gap values. This confirms the Newton

fringes observed in the air gap. It should be noted that the overall simulated efficiency remains relatively low, between 5% and 10%. In Figure 3.29(c), the simulated results are normalized and plotted together with the experimental data. The simulations are in good agreement with the experimental results.

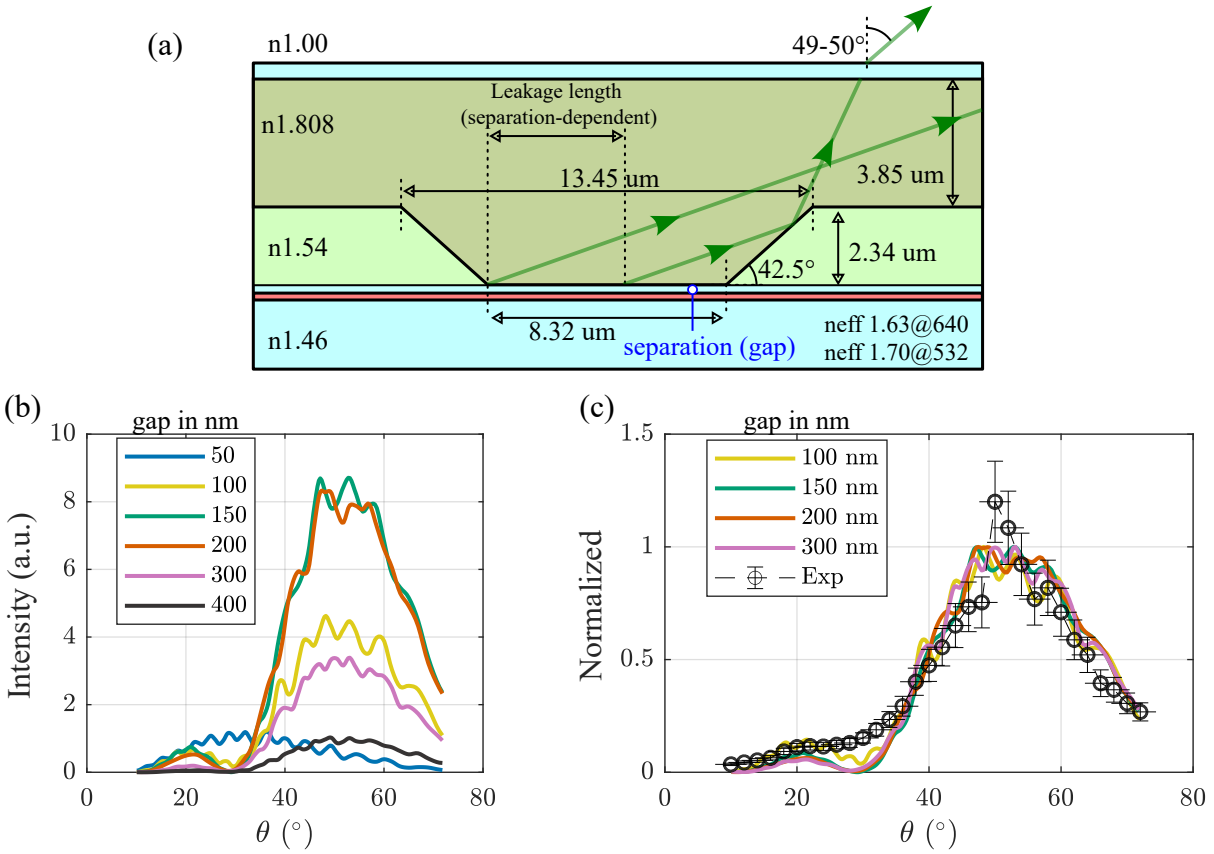

Figure 3.29: (a) Scaled schematic of the 10 μm strip. (b) 3D FDTD simulation of the extraction as a function of the separation (gap). (c) Normalized simulation overlaid with the experimental intensity profile.

Besides the good agreement observed in the intensity profile, it would be interesting to experimentally verify the extraction efficiency and compare it with the simulations. This was left as a perspective for future work. The current imaging setup can be used to estimate the extraction efficiency using the grating out-coupler, which has an extraction efficiency of about 50%. The idea is to measure the intensity profiles from both the strip and the grating, then integrate these intensities over the solid angle to obtain the extracted power. Ideally, the intensity should be measured in both directions, $I(\theta_z, \theta_x)$. It should be noted that propagation losses, Fresnel coefficients, and the relative intensity amplitudes must also be taken into account. The camera gray level can be used to estimate the relative amplitude of the extraction between the grating and the strip by measuring the gray level at $\theta_z = 50°$ for the strip and at the extraction angle of the grating.

In my theoretical analysis, I provided design insights to maximize light extraction (Eq. (3.8)). It should be noted that this sample did not include any of the design procedures introduced in this chapter, as many parameters were unknown at the time of its development. Nevertheless, this sample provided a key result for validating the principle of the extraction component.

3.3.6 Perspectives

This passive extraction demonstration is important, as it validates our new concept based on evanescent coupling followed by total internal reflection (TIR) into free space.

Our first results are promising, but it is important to further investigate this component and integrate the liquid crystal for active operation.

Here are some perspectives for future experiments:

→ First, for the Inkron resin, we could use the strip with an angle of $\alpha = 54.74°$, as the extraction will be closer to the vertical direction. This will facilitate the extraction measurements.

→ Since we already have the masks, we should test higher etched thicknesses t_p (>2.5 μm). This will reduce the strip width and increase the facet size, allowing more rays to be extracted. It would also be interesting to evaluate the replication fidelity of the Inkron resin for larger thicknesses.

→ Improve the goniometer setup to perform 2D angular scans. The current measurements provide only a 1D scan along the propagation direction. In the perpendicular direction, the divergence depends on the mode width.

→ Improve the bonding protocol to achieve optical contact, especially for strips near the edges of the NIL chip. Assessing contact under the microscope using Newton's fringes is a simple yet powerful method to estimate the thickness of the air gap.

→ Rotate the strip with respect to the waveguide by an angle ψ and perform a 2D intensity measurement. This modifies the TIR/transmission condition for the extraction. For the same strip width, as ψ increases, the interaction width also increases. However, the extraction angle will deviate in a different direction. Perform a 2D angular scan to characterize this.

→ Identify a protocol to measure the extraction efficiency and verify the results using FDTD simulations.

The masks and the PIC used in this thesis were not specifically designed for the purpose of this demonstration. To move a step forward, my design equations should be applied while taking into account the current functional resin. A new set of masks should be developed using strip with varying widths. Ideally, to test the impact of the gap and also the extraction divergence, a new generation of waveguides should also be developed with varying widths (0.3–1 μm) and with different cladding thicknesses (separation = 50–200 nm). Here are some perspectives for the new masks while keeping the same PIC:

→ Use of a new lithography mask with strip widths below 10 μm.

→ Testing of new resins with different refractive indices.

→ Transition toward the prismatic structure and the use of index-matching liquids for passive extraction.

→ Progress toward the implementation of liquid crystals.

It is worth noting that, Inkron resin, with a RI of $n = 1.8$ at 532 nm, exhibits low absorption in the infrared (IR) region around 1550 nm. This opens the door to potential applications beyond the visible range. The new component could therefore be explored for optical signal routing in telecommunications and datacom systems. When combined with holographic optical elements (HOEs), it could also be used in laser scanning applications such as LiDAR operating at 850 nm. In addition, it may find use for dimming in μdisplays such as LCoS with PIC [61]. The exploration of these possible applications is left for future work.

3.4 Conclusion

We demonstrate for the first time the operation principal of a new type of photonic component. Our innovative extraction component is based on evanescent coupling followed by total internal reflection into free space.

Active extraction from a guided mode in a photonic integrated circuit (PIC) into free space remains a major challenge for many applications, such as our directional display concept. This component is a key element, since unlike diffraction gratings, it enables high-efficiency light extraction over a very short distance (<10 μm).

In the previous and current chapters, I presented key theoretical elements comparing our component with an out-coupling grating in terms of extraction length, directionality, divergence, integration, RGB operation, polarization, and fabrication tolerance. I summarized the key dependencies on a critical parameter, the decay constant α_r, to provide a coherent comparison. Only our innovative component meets our display requirements, achieving an extraction length below 10 μm with an efficiency exceeding 60%.

This chapter then proceeded to discuss the activation process. I provided a comprehensive overview of ferroelectric liquid crystals (FLCs). We are particularly interested in this bistable phase due to its high operation speed (<100 μs). This may help overcome one of the principal limitations in the use of nematic liquid crystals (response time > 10 ms). Key takeaways include: FLCs are fast, bistable, low-power consumption, require a small cell gap (2 μm) to exhibit ferroelectricity.

In the design process, I focused on providing equations that are independent of FDTD simulations. The only parameter that needs to be simulated is the effective index of the guided mode. All other parameters are defined through simple analytical equations. The new component involves a multiparameter design and may present trade-offs between enhancing the evanescent coupling and achieving (TIR). These analytical developments will provide a foundation for future design work.

We finally carried out experiments to validate our innovative approach. The demonstration was carried out using high refractive index resin by fabricating strips with sidewall angles of 45° and 54.74°. The process used wet etching of silicon, which produced good quality surfaces. The NIL process was then used to replicate the structures using Inkron resin. The sample was bonded to a photonic chip, and light extraction was successfully validated after fiber coupling.

The extraction angle is 50° with a divergence of 20°, measured using a goniometer setup. The experimental results are in good agreement with the simulations.

This static demonstration opens the perspective for a dynamic implementation of this new extraction component using liquid crystals.

In the following chapter, we will explore the next step after light extraction. μholograms encoding optical functions are positioned at the extraction points. These elements redirect the extracted light. This is important to add directionality to the emission, especially when the extraction component leads to complex angles. I will discuss the recording of such μholograms and present some experimental results.

Chapter 4

Holographic Pixelization

Contents

4.1 Preliminary Physics **115**
4.1.1 Holography 115
4.1.2 Volume Bragg Gratings (VBGs) 116
4.1.3 Encoding Reflection Angles and k-space 118
4.2 Simulations: PSM and Kogelnik **120**
4.2.1 VBG as an Array of Parallel Stacked Mirrors (PSM) 122
4.2.2 RCWA Comparison 124
4.2.3 Spectral and Angular Selectivity 129
4.3 Recording Materials **130**
4.3.1 Photopolymers and Silver Halides 130
4.3.2 Exposure and Refractive Index Modulation 131
4.3.3 Mechanical Stability 133
4.4 Holographic Printer **134**
4.4.1 Objective 134
4.4.2 Holographic Printers 134
4.4.3 Setup Description 135
4.4.4 Automation 137
4.5 Characterization and Results **138**
4.5.1 Microscopic and Macroscopic Views 138
4.5.2 Reconstruction of the Encoded Focus 139
4.5.3 Replication and Perspectives 140
4.6 Conclusion **143**

4.1 Preliminary Physics

Holography is both visually impressive and physically complex. Just placing a child in front of a volume hologram often leads to amazement. But behind this visual effect, there is a mix of physical principles: diffraction effects caused by the repeating patterns inside the material, and geometric effects related to the way these patterns are oriented. There is also a contrast between the high temporal coherence needed to record a hologram and the fact that no such coherence is required to view it.

The goal of this section is to introduce some preliminary physics, focusing in particular on how reflection angles are encoded in a hologram and the representation of on-Bragg and off-Bragg conditions in k-space.

4.1.1 Holography

When introducing a hologram to kids, students, or adults, I always get the same reaction: looking through the film, they see a floating 3D object. Sometimes, they even turn the holographic plate as if trying to reach the virtual object.

In conventional imaging, the information of relative optical paths (relative phases) of different points on the object is lost. However, in holographic imaging, the full information in the wave field scattered by the object can be recorded. This includes the phase and the amplitude.

Given that a recording film responds only to intensity, the phase information is converted into intensity by interfering the object wave with a reference wave. The intensity at each point in the resulting interference pattern depends both on the phase and the amplitude of the object wave [161].

After the recording process, the object is reconstructed by illuminating the hologram with the same reference wave. Note that the word *hologram* refers to the pattern recorded within the holographic film.

In general, holography is the process of recording the interference pattern between two coherent light waves. The application of holographic imaging is compelling and sparks genuine amazement. However, our focus is not on this artistic aspect of holography. We are interested in holography as a process for recording optical functions.

For example, one can record a component such as a lens or a slanted mirror. The holographic recording will exhibit optical properties close to those of the original component. The word "close" is deliberately used, as the efficiency, spectral response (wavelengths) and angular selectivity of the hologram may vary. These aspects will be discussed later.

Some refer to this hologram that records an optical function as Volume Bragg Gratings (VBGs) or Holographic Optical Elements (HOEs). [162–164].

Figure 4.1(a) shows the conventional principle of recording a reflection hologram, where the object and reference beams are on opposite sides of the holographic plate. Figure 4.1(b) shows the reconstruction of the hologram using the same reference beam.

In holography, the interference pattern is recorded as a modulation of the refractive index (phase hologram) or a modulation of absorption (amplitude hologram), or both. I illustrate this principle using the analogy shown in Figure 4.1(c), involving sand and a table. The vibration pattern of a stationary profile can be visualized using sand particles. After stopping the vibration, the sand retains the same profile.

Figure 4.1(d) shows holographic imaging samples I recorded for kids visiting our lab.

Figure 4.1(e) shows the objective of this chapter. I recorded micro-holographic elements, where each element encodes a reflection function. Throughout this chapter, we will explore the underlying physics and the printing process.

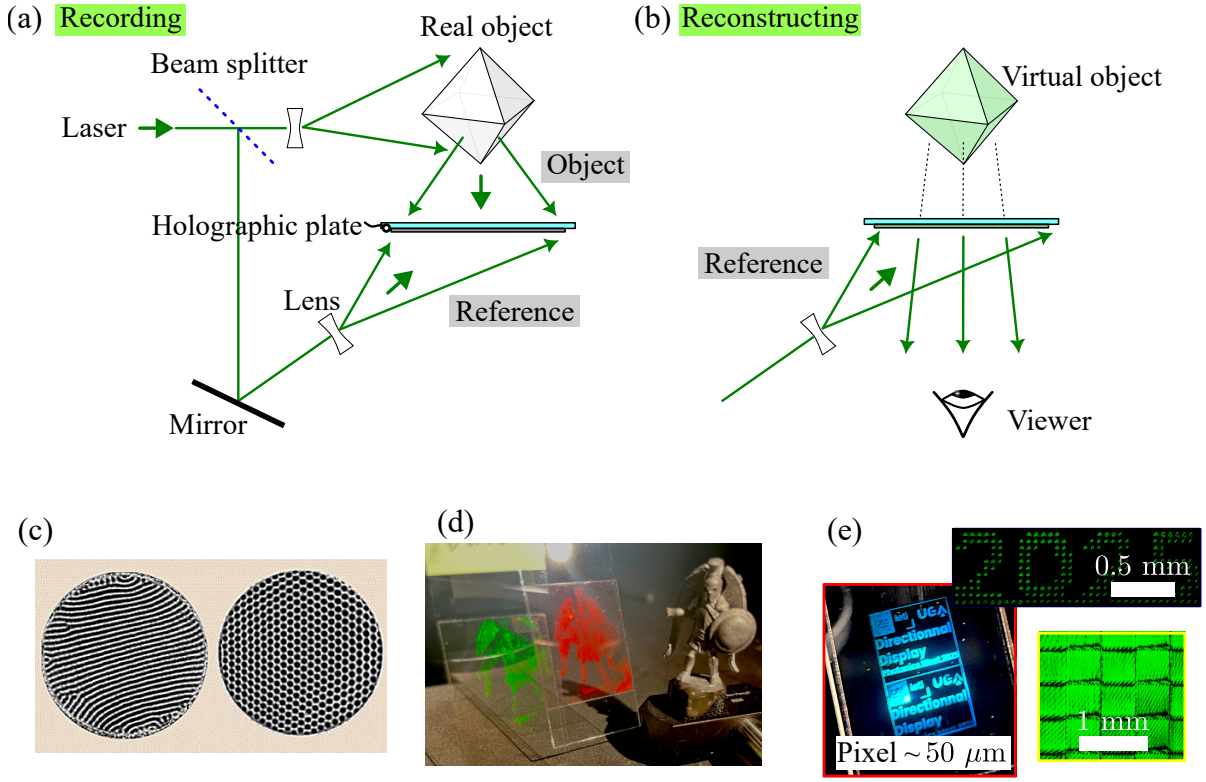

Figure 4.1: (a) Conventional recording process of a hologram. (b) Playback/reconstruction/reading of the hologram. (c) Pattern in the sand [165] and vibration-induced structures. (d) Example of holographic imaging: on the right, a heroic fantasy miniature; on the left, holograms of the miniature recorded with a green and a red laser. (e) Example of a pixelated holograms, representing the goal of this chapter.

4.1.2 Volume Bragg Gratings (VBGs)

Consider a holographic film exposed by a pair of waves: an object wave $A(\mathbf{r})e^{i\mathbf{k}_A\cdot\mathbf{r}}$ and a reference wave $B(\mathbf{r})e^{i\mathbf{k}_B\cdot\mathbf{r}}$, where $\mathbf{r}$ is the position vector, A and B are the amplitudes, and $\mathbf{k}_A$ and $\mathbf{k}_B$ are the wave vectors for the central directions of waves A and B.

The interference pattern $\left|A(\mathbf{r})e^{i\mathbf{k}_A\cdot\mathbf{r}} + B(\mathbf{r})e^{i\mathbf{k}_B\cdot\mathbf{r}}\right|^2$ leads to a local change in the refractive index as follows [166]:

$$\begin{aligned} n(\mathbf{r}) &= n_0 + \beta_1\left(|A|^2 + |B|^2\right) + \Delta n\cos(\mathbf{r}\cdot\mathbf{K}_{\text{holo}}), \\ \Delta n &= \beta_2|AB^*| \end{aligned} \tag{4.1}$$

The grating vector is defined as $\mathbf{K}_{\text{holo}} = \mathbf{k}_A - \mathbf{k}_B$. The refractive index varies periodically along the direction of $\mathbf{K}_{\text{holo}}$, with an amplitude of Δn. The coefficients β_1 and β_2 characterize the response of the medium to the intensity.

Figure 4.2(a) shows the recording of a transmission hologram, where the object and reference beams are on the same side of the hologram. The interference fringes are oriented along the $\hat{x}$ direction. The fringe period Λ is related to the grating vector $\mathbf{K}_{\text{holo}}$ by:

$$|\mathbf{K}_{\text{holo}}| = \frac{2\pi}{\Lambda}. \tag{4.2}$$

Figure 4.2(b) shows the recording of a reflection hologram. In this case, the fringes are oriented more parallel to the surface. Reflection holograms behave like multilayer filters. $\mathbf{k}_{\text{in}}$ and $\mathbf{k}_{\text{out}}$ represent the incident (reading) and diffracted beams, respectively.

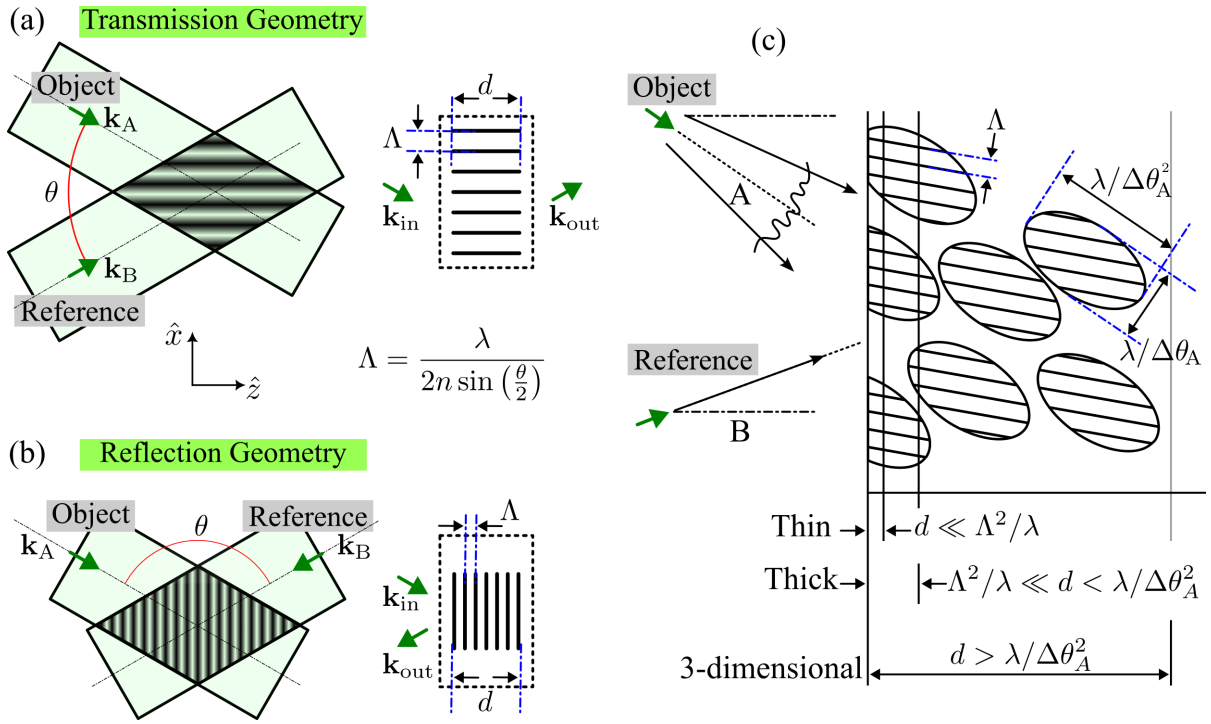

Figure 4.2: (a) Transmission Volume Bragg Grating (VBG), where the fringes are nearly perpendicular to the surface. During the recording process, the object and reference beams are on the same side. (b) Reflection VBG, where the fringes are more parallel to the surface. In this case, the object and reference beams are on opposite sides. (c) From Zel'dovich [167]: spatial scales of interference inhomogeneities within the recording medium.

We represent only one diffracted beam, since higher orders are suppressed by the Bragg condition. This is the case in our recording scheme. The Bragg regime depends on the interaction length within the hologram. As the hologram thickness d increases, higher diffraction orders vanish due to destructive interference.

Holograms are classified into two categories, thin holograms and volume holograms. Thin holograms operate in the Raman–Nath diffraction regime, where energy is distributed among multiple diffraction orders. However, Volume hologram operate in the Bragg regime, where energy is primarily concentrated in the first diffraction order. The distinction between these two regimes is often based on a factor $Q \sim \lambda d/\Lambda^2$, introduced by Klein and Cook in 1967 [168], or on the higher-order criterion proposed by Moharam and Young in 1978 [169]. We can note that the boundaries between thin and thick holograms remain subject of research [170, 171].

The fringes in (a) and (b) are the interference between two plane waves. Real holograms of an extended object will have a superposition of fringes in different directions. As shown in Figure 4.2(c), if we zoom in on the registering medium of a hologram and assume that the object $|A(\mathbf{r})|^2$ contains inhomogeneities due to the coherent summation of object points of

random phases, we get speckle. Speckle is not the focus of this chapter [78]. However, this representation is interesting, as it shows that the actual fringes can be contained within individual speckle elements when $\Lambda \ll \lambda/\Delta\theta_A$.

The size of these elements is determined by $\Delta\theta_A$. $\Delta\theta_A$ is the angular width of the illuminated portion of the object, as seen from the surface of the hologram.

Zel'dovich [166, 167] used this representation to classified holograms as thin or thick based on the relevance of diffraction and interference effects along the thickness of the medium. Let us briefly give a recall of the Fresnel length ℓ_{FR}. For an aperture of size a, when the propagation distance after the aperture is smaller than $\ell_{\mathrm{FR}} = a^2/\lambda$, simple geometric optics can be used. However, at distances $z \gg \ell_{\mathrm{FR}}$ from the aperture, diffraction effects become significant and must be taken into account. Assuming the characteristic feature size of the interference pattern is a, the hologram is considered *thin* if the thickness $d \ll \ell_{\mathrm{FR}}$, and *thick* if $d \gg \ell_{\mathrm{FR}}$. An example of such a feature size is the grating period, $a = \Lambda$, leading to the condition that a hologram is thick when $d \gg \Lambda^2/\lambda$. Which is consistent with the classification based on the Klein factor Q. Zel'dovich also proposed another classification, referred to as *three-dimensional*, based on the inhomogeneity size of speckle elements, given by $a = \lambda/\Delta\theta_A$. The hologram is three-dimensional when $d \geq \lambda/\Delta\theta_A^2$.

Note that the classification into thin and volume holograms is important, as it determines the diffraction regime. Thick holograms operate under the Bragg condition, which is the case in our work. At resonance (i.e., under the Bragg condition), diffraction occurs only for specific combinations of incident angle and wavelength. The physical thickness of the hologram we use is approximately $\approx$ 14–15 μm.

In our recording setup, we use lenses and mirrors only; no diffusing elements are involved. Therefore, no inhomogeneities are assumed. The term $|A|^2 + |B|^2$ in equation (4.1), known as the *intermodulation* term, can be considered constant. As a result, the variation in the local refractive index is solely due to the *crossmodulation* term, which has a period Λ. The equation can thus be simplified as:

$$n(\mathbf{r}) = n_0 + \Delta n \cos(\mathbf{r} \cdot \mathbf{K}_{\mathrm{holo}}) \tag{4.3}$$

Here, n_0 is the DC component of the refractive index of the medium.

4.1.3 Encoding Reflection Angles and k-space

We use the hologram to encode reflection functions, as illustrated in Figure 4.3(a). In the recording process, a reference plane wave interferes with a tilted object plane wave. This tilt is represented by the angle γ. The interference produces fringes with a specific period Λ and orientation. Both of these characteristics are contained in the amplitude and direction of the grating vector $\mathbf{K}_{\mathrm{holo}}$.

In the reading process, using the same reference wave $\mathbf{k}_{\mathrm{in}}$ reproduces a diffracted wave $\mathbf{k}_{\mathrm{out}}$ with the same direction as the original object wave.

In practice, the goal is to encode reflection functions at the microscopic scale, where each micro-hologram is recorded separately with its own specific reflection angle. Figure 4.3(b) shows a hologram illuminated by a reference wave; each micro-hologram reflects a portion of the incident wave in its encoded direction.

These reflection properties arise from reflection and interference processes, specifically Bragg resonance; they are not the result of conventional mirror reflection. Unlike a mirror, the

holographic reflection depends on both the wavelength and the incident angle of the reading beam. However, one may think of each micro-hologram as a slanted mirror oriented in a different direction, where the normal to the mirror corresponds to the grating vector. This analogy holds only at Bragg condition.

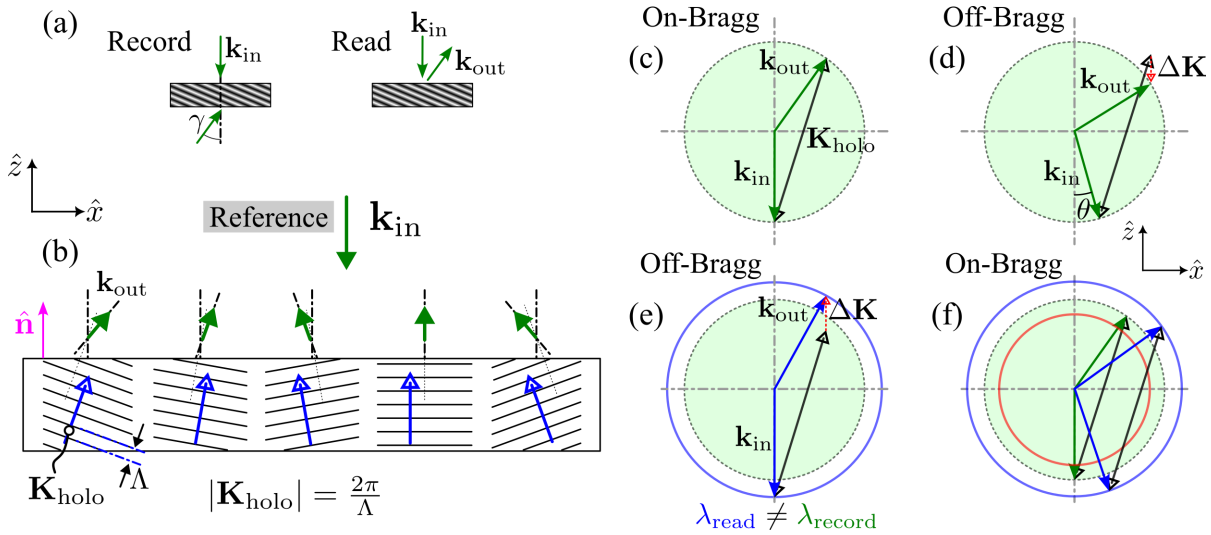

Figure 4.3: (a) Recording a reflection angle γ. (b) The goal of this chapter: recording micro-holograms, each with a different reflection angle. (c) k-space representation of the Bragg condition. The grating vector, incident beam, and diffracted beam form a closed triangle. (d) Off-Bragg condition: the incident beam is deviated from the original reference beam. (e) Off-Bragg condition when using a different wavelength. (f) The Bragg condition can be satisfied at different wavelengths, but at different angles, and only if $|\mathbf{K}_{holo}| \leq 2|\mathbf{k}_{read}|$, where $|\mathbf{k}_{read}|$ is the radius of the k-space sphere at that wavelength.

Figure 4.3(c) shows the k-space representation of the Bragg condition. Consider $\mathbf{k}_{in}$ as the reference wave and $\mathbf{k}_{out}$ as the object wave. The vectors $\mathbf{k}_{in}$, $\mathbf{k}_{out}$, and $\mathbf{K}_{holo}$ form an isosceles triangle. Upon reading with the same reference wave, the Bragg condition is satisfied when these three vectors form a closed triangle:

$$\mathbf{k}_{out} = \mathbf{k}_{in} + \mathbf{K}_{holo} \tag{4.4}$$

Note that an incident wave with $-\mathbf{k}_{out}$ (opposite to the direction of $\mathbf{k}_{out}$) will be diffracted into $-\mathbf{k}_{in}$. Replacing $\mathbf{K}_{holo}$ with $-\mathbf{K}_{holo}$ also satisfies the Bragg condition. In this sense, $\mathbf{K}_{holo}$ can be considered a directionless vector, consistent with the principle of optical reversibility.

Both $\mathbf{k}_{in}$ and $\mathbf{k}_{out}$ are wavelength-dependent. The Bragg condition can be satisfied for some wavelengths, but at different angles.

Figure 4.3(d) shows an example of an off-Bragg condition. The same wavelength is used (the k-space sphere has the same radius $|\mathbf{k}_{record}|$), but the incident angle differs by an amount θ.

When adding the grating vector $\mathbf{K}_{holo}$, the resulting vector ends outside the surface of the k-space sphere. However, the diffracted beam cannot change its wavelength and must therefore lie on the surface. The direction of $\mathbf{k}_{out}$ is adjusted by introducing a mismatch vector $\Delta\mathbf{K}$, which is oriented along the surface normal $\hat{\mathbf{n}}$ [172, 173].

The diffraction angle under off-Bragg conditions is given by:

$$\mathbf{k}_{out} = \mathbf{k}_{in} + \mathbf{K}_{holo} + \Delta\mathbf{K} \tag{4.5}$$

Figure 4.3(e) shows an example of an off-Bragg condition when using a different wavelength. When a shorter wavelength is used for reading (resulting in a larger k-space sphere), the vector $\mathbf{k}_{\text{in}} + \mathbf{K}_{\text{holo}}$ requires a mismatch vector to reach $\mathbf{k}_{\text{out}}$. Note that any deviation from the Bragg condition, whether in angle or in wavelength, results in a drop in diffraction efficiency.

Outside the Bragg condition, diffraction either does not occur or occurs with significantly reduced efficiency. The rate at which efficiency drops depends on the magnitude $|\Delta\mathbf{K}|$ and the angular and spectral selectivity of the hologram, which will be discussed in the following simulation sections.

Figure 4.3(f) illustrates the on-Bragg condition for two wavelengths: green and blue. The green vectors correspond to those used during the recording process. For the blue incident wave, an appropriate incident angle allows the Bragg condition to be satisfied. The red sphere represents a longer wavelength (a smaller k-space radius). No configuration is possible to satisfy the Bragg condition, since the amplitude of $\mathbf{K}_{\text{holo}}$ exceeds the diameter of the sphere.

Volume gratings exhibit strong angular selectivity in the case of transmission VBGs, and strong wavelength selectivity for reflection VBGs. The thickness d and the refractive index modulation Δn determine how rapidly the efficiency drops outside the Bragg condition. These two parameters define the "strength of the grating" [174].

4.2 Simulations: PSM and Kogelnik

The problem we consider is the diffraction efficiency of the diffracted wave relative to that of the incident wave, under both on-Bragg and off-Bragg conditions. For example, we want to understand how the efficiency drops when the incident plane wave is oblique relative to the recording angle, or when the reading wavelength λ_c (c for "construction") differs from the recording wavelength λ_r. We also aim to simulate slanted reflection volume holograms, where the grating vector is tilted with respect to the surface normal of the sample. We focus exclusively on the case of pure phase sinusoidal gratings, where the refractive index is modulated with an amplitude Δn, as shown in the previous equation (4.3).

In 1969, Herwig Kogelnik [175] derived a coupled-wave theory for volume Bragg gratings in both transmission and reflection geometries. The model is valid in the Bragg regime and consists of two coupled waves: the incident wave (zeroth order) and the first diffracted order. The analytical solution provides good prediction of the diffracted beam.

In the previous chapter, we saw the results of coupled-mode theory applied to directional couplers. In the coupling equations, the coupling constant provides an estimate of the coupling length required to achieve maximum efficiency.

For volume holograms, Kogelnik's coupling constant is given by the following expression:

$$\kappa = \frac{\pi \Delta n}{\lambda_c} \tag{4.6}$$

$1/\kappa$ (with units of micrometers) defines a characteristic interaction length for the coupling efficiency. Using a hologram with a thickness on the order of a few multiples of $1/\kappa$ results in strong coupling between the incident and diffracted wave.

For $\Delta n = 0.03$ and a reading wavelength $\lambda_c = 0.532$ μm, we obtain $\kappa = 0.177$ μm^{-1}, corresponding to a characteristic length $1/\kappa = 5.64$ μm.

As a function of the thickness of the hologram d, the reflection efficiency of the on-Bragg at the reading wavelength λ_c equals the recording wavelength λ_r, is given by:

$$\eta = \tanh^2(\kappa d) \tag{4.7}$$

For $d = 14\ \mu$m, $\Delta n = 0.03$, and $\lambda_c = 0.532\ \mu$m, we get a diffraction efficiency of $\eta = 0.97$.

The product κd is often referred to as the *grating strength* [174], which characterizes the effectiveness of the grating. A larger Δn or a thicker hologram leads to a higher grating strength and consequently, better diffraction efficiency. Note that, as we will see, the angular and spectral selectivity are also dependent on both Δn and d.

Klein's criterion for distinguishing between thin and volume holograms assumes a low index modulation Δn. In particular, the factor Q does not include Δn. In my view, for reflection hologram, the distinction should instead be based on the coupling constant κ and the grating period Λ. If we consider that diffraction and interference effects become significant when the interaction length exceeds the Fresnel length $\ell_{\mathrm{FR}} = \Lambda^2/\lambda_c$, then a hologram can be considered in the Bragg regime (volume) if $1/\kappa \gg \ell_{\mathrm{FR}}$, which leads to the condition:$\rho = \frac{\lambda_c^2}{\Lambda^2 \Delta n} \gg 1$. This is similar to the expression proposed by Moharam and Young [169].

In our case, with $\Delta n \approx 0.03$, $\lambda_c = 0.532\ \mu$m, and $\Lambda \approx 0.18\ \mu$m, we obtain $\rho \approx 291$. Since the hologram thickness d is greater than $1/\kappa$, we can confirm that our holograms operate in the Bragg regime. Therefore, Kogelnik's analytical model can be reliably applied. The validity of this will also be demonstrated using rigorous coupled-wave analysis (RCWA).

RCWA is a computational method typically used for analyzing periodic structures. It is based on Maxwell's equations and provides accurate results. We use the RCWA solver provided by Lumerical software.

RCWA should be used when the Bragg condition is not satisfied, as the analytical two-coupled-wave model neglects higher diffraction orders.

Ratcliffe in 2012 [176–178] proposed an alternative approach to Kogelnik's two-coupled-wave theory. His model, PSM (Parallel Stacked Mirrors), is based on summing Fresnel reflections from an infinite number of discontinuities in the refractive index profile of the volume hologram. In my view, although much less well known than Kogelnik's model, Ratcliffe's approach offers valuable insight, as it is based on Fresnel coefficients. Moreover, its results are consistent with computational simulations. It is also capable of analytically describing multiplexed reflection volume holograms in wavelengths and angles.

4.2.1 VBG as an Array of Parallel Stacked Mirrors (PSM)

We present here the analytical expression for the diffraction efficiency of a slanted volume Bragg grating in reflection, based on Ratcliffe's PSM model. [176–178]

We define the propagation constant of the reading wave in the holographic material:

$$\beta = \frac{2\pi n_0}{\lambda_c} \tag{4.8}$$

As well as the ratio α between the reading wavelength λ_c (c for "construction") and the recording wavelength λ_r:

$$\alpha = \frac{\lambda_c}{\lambda_r} \tag{4.9}$$

We need to define the recording angle θ_r and the slant angle ψ. In Figure 4.4(a), we illustrate how θ_r is defined: both the reference and object waves are tilted by the same angle with respect to the surface normal of the holographic film. The k-space diagram shows the corresponding orientation of the grating vector $\mathbf{K}_{\text{holo}}$. Note that θ_r affects only the magnitude of $\mathbf{K}_{\text{holo}}$, not its direction.

To introduce the slant angle ψ, the hologram is rotated relative to the normal surface. This is shown in Figure 4.4(b). The magnitude of $\mathbf{K}_{\text{holo}}$ remains the same, but its direction is tilted by the slant angle ψ.

In the reading process, we use the subscript c (for "construction") to denote the reading wavelength λ_c and the reading angle θ_c. Note that θ_c is measured with respect to the grating vector $\mathbf{K}_{\text{holo}}$. Figure 4.4(c) shows an incident plane wave of wavelength λ_c at an angle $\theta_c - \psi$ relative to the surface normal. In Ratcliffe's PSM model, the hologram is treated as an infinite series of infinitesimal discontinuities in the direction of $\mathbf{K}_{\text{holo}}$. Fresnel reflection coefficients are applied at each interface, and a set of two coupled-wave equations is derived.

From [177], p. 447, we need the following PSM coefficients:

$$\begin{aligned} c_R &= \frac{\cos\theta_c \cos(\theta_c - \psi)}{\alpha \cos\theta_r}, \\ c_S &= -\frac{\cos\theta_c \cos(\theta_c + \psi)}{\alpha \cos\theta_r}, \\ \vartheta &= 2\beta \left(1 - \frac{\cos\theta_c}{\alpha \cos\theta_r}\right) \cos^2\theta_c \end{aligned} \tag{4.10}$$

The reflection efficiency for σ polarization (transverse electric) is expressed in the following form:

$$\eta_\sigma = \frac{\kappa^2 \sinh^2(d\Upsilon)}{\kappa^2 \sinh^2(d\Upsilon) - c_R c_S \Upsilon^2} \tag{4.11}$$

Where:

$$\Upsilon^2 = -\frac{\vartheta^2}{4c_S^2} - \frac{\kappa^2}{c_R c_S} \tag{4.12}$$

κ is Kogelnik's constant, defined in Equation (4.6). The result for p polarization is obtained by the simple transformation $|\kappa| \to |\kappa \cos(2\theta_c)|$.

ϑ in Equation (4.10) is a detuning parameter. It is a function of both the recording and reconstruction parameters and it describes how far we are from the Bragg condition in terms of

angle and wavelength. For an unslanted grating ($\psi = 0°$), the Bragg condition is satisfied when $\cos(\theta_c) = \alpha \cos(\theta_r)$, which corresponds to $\vartheta = 0$.

In our recording configuration, as shown in Figure 4.4(d), the reference is parallel to surface normal, while the object beam is tilted by an angle γ. The magnitude of the grating vector is adjusted by choosing $\theta_r = \gamma/2$, and its direction is set by fixing $\psi = \gamma/2$. This construction is illustrated in the k-space representation.

$$\theta_r = \psi = \gamma/2 \tag{4.13}$$

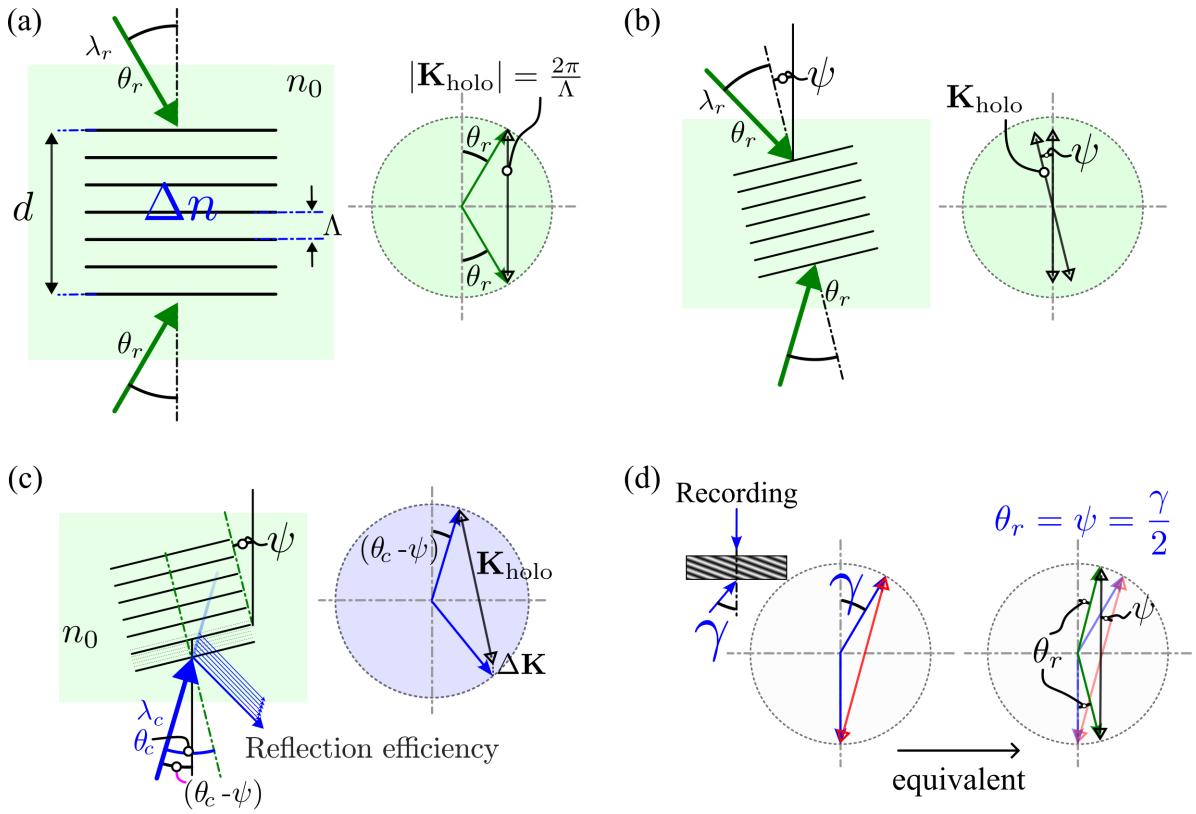

Figure 4.4: (a) Definition of the recording angle θ_r: it determines the magnitude of the grating vector as $|\mathbf{K}_{\text{holo}}| = 4\pi n_0 \cos(\theta_r)/\lambda_r$. (b) Same grating, but slanted from the surface normal by an angle ψ. (c) The reconstruction process with a wavelength λ_c and angle θ_c. θ_c is defined with respect to the grating direction. The PSM model is based on using Fresnel coefficients and treating the grating as a series of discontinuities. (d) Adapting our recording configuration to the PSM parameters: to record a slant angle γ, we set $\theta_r = \psi = \gamma/2$.

4.2.2 RCWA Comparison

Spectral Analysis

In this section, I compare the PSM model with the Kogelnik model using RCWA simulations. Figure 4.5 shows the reflection efficiency as a function of the reading wavelength λ_c. This figure illustrates the spectral selectivity of the hologram. The recording wavelength is $\lambda_r = 0.532\ \mu$m, and the reading angle matches the recording angle, so the Bragg condition is satisfied when $\lambda_c = \lambda_r$. The full width at half maximum (FWHM) of this selectivity is approximately 13.5 nm.

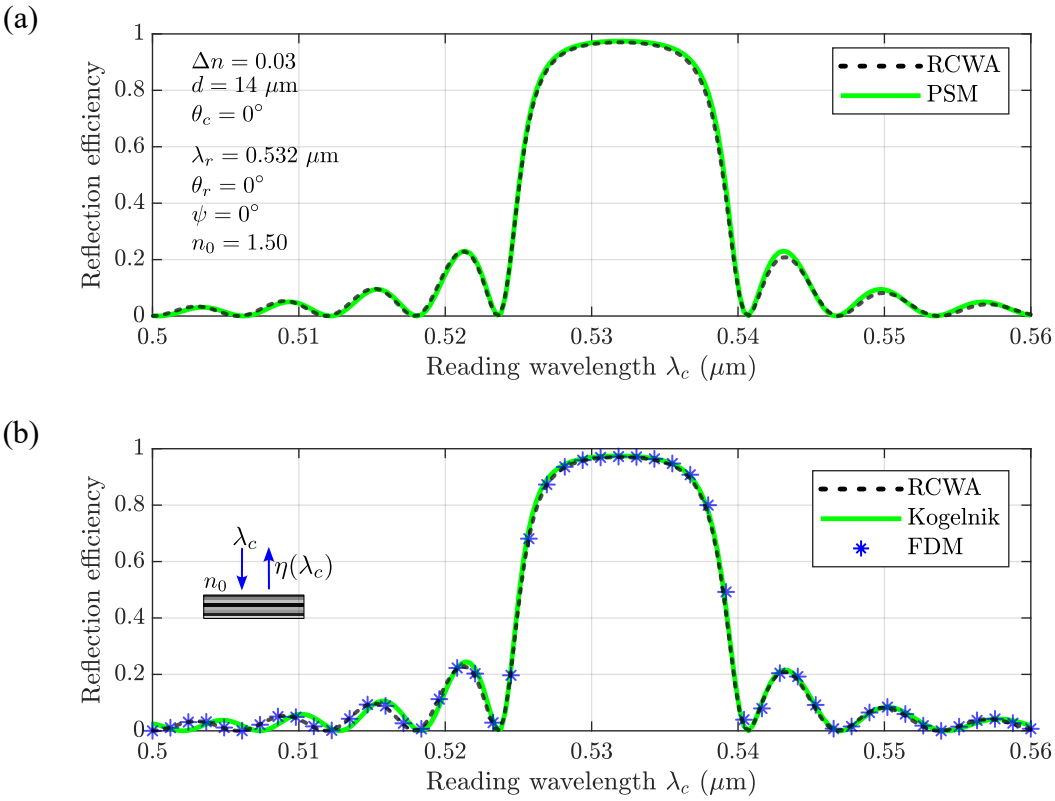

Figure 4.5: (a) Comparison between the RCWA simulation and the PSM model. The reflection efficiency is plotted as a function of the reading wavelength λ_c. The recording parameters and the reading angle are indicated in the figure. (b) Comparison with Kogelnik's model. Additional numerical results are shown as star markers, obtained using a finite difference method (FDM) based on the Runge–Kutta algorithm.

Figure 4.5(a) shows a comparison between the PSM model and RCWA simulations. Note that both PSM and Kogelnik's models are analytical and computationally efficient, whereas RCWA is more time-consuming. The PSM model matches the simulation results, including the off-Bragg response with the oscillations in the efficiency curve.

Figure 4.5(b) provides a comparison between Kogelnik model and RCWA simulations. Numerical results based on a finite difference method using the Runge–Kutta algorithm are also included. The Runge–Kutta method was applied to the Helmholtz equation with boundary conditions similar to those used by Ratcliffe [176].

The RCWA simulations, performed using Lumerical, and the numerical finite difference method (FDE) implemented in MATLAB are consistent with each other. The solid curve represents Kogelnik's analytical results. The central region of spectral selectivity of the hologram

is well matched. A slight deviation is observed in the oscillations on the left side, where Kogelnik's model differs from the simulations. In contrast, the PSM model provides a better fit to these oscillations compared to Kogelnik.

The PSM model is used experimentally to fit the spectral measurements of the efficiency obtained with a spectrometer. The fit provides information about the refractive index modulation Δn and the thickness of the hologram d. This will be discussed in Section 4.3.2, where we have studied the efficiency of the hologram as a function of the exposure of the recording.

Figure 4.6 presents an example of an unslanted holographic sample. The experimental results are plotted as the solid black curve. The solid green curve and the dashed curves are plotted using the PSM model.

At the Bragg condition, which corresponds to the wavelength of maximum efficiency, the reflection efficiency is obtained from Equation (4.7). Efficiency is directly related to the product κd or simply $\Delta n \cdot d$.

For example, the maximum efficiency of the experimental curve is $\eta = 97.2\%$ at $\lambda_c = 0.530\,\mu$m. This efficiency imposes a fixed value on the product $\Delta n \cdot d = \tanh^{-1}\left(\sqrt{\eta}\right) \frac{\lambda_c}{\pi} \approx 0.417\,\mu$m. To find Δn and d, the other required information is the spectral selectivity, which corresponds to the width of the experimental curves.

The PSM curves in Figure 4.6 correspond to different thicknesses d, with Δn fixed in each to yield the same efficiency. The curve with $d = 15\,\mu$m fits the experimental oscillations the best, with a slight difference in the central region. It should be noted that the spectral selectivity is analyzed in Section 4.2.3.

The experimental recording wavelength is $\lambda_{r,\text{exp}} = 0.532\,\mu$m. The spectral measurement shows a response centered at $\lambda_{r,\text{PSM}} = 0.530\,\mu$m. This slight spectral shift is due to a negligible thickness shrinkage (and thus a change in Λ) after polymerization of the photopolymer.

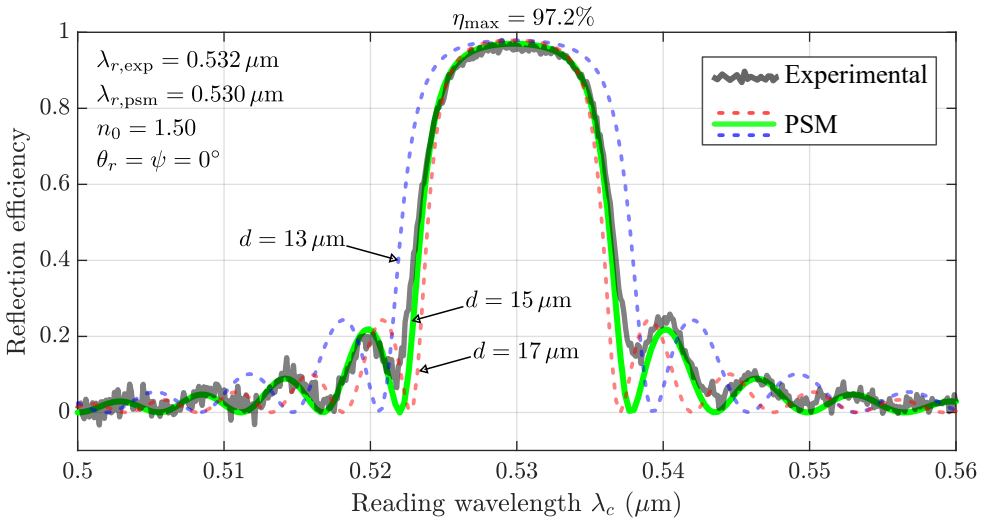

Figure 4.6: Example of the spectral response of a holographic sample (Bayfol HX200 photopolymer) with PSM results. The product $\Delta n \cdot d$ is fixed to match the reflection efficiency (Equation (4.7)). For $d = 13$, 15, and 17 μm, the corresponding values of Δn are 0.032, 0.029, and 0.025, respectively.

Angular Analysis

Figure 4.7 shows the comparison of the angular selectivity. The reflection efficiency is plotted as a function of the reading angle θ_c for $\lambda_c = \lambda_r$. The full width at half maximum (FWHM) of this angular selectivity is approximately 18.4°.

We can note that the reflection efficiency, the refractive index modulation Δn, the grating thickness d, and the angular and spectral selectivity are interrelated. This point will be addressed in Section 4.2.3. These notions are important, as the hologram is not an emissive component but is illuminated externally. The spectral width and divergence of the illumination must fall within the selectivity of the hologram to ensure high efficiency.

Figure 4.7(a) shows the comparison between RCWA and PSM model. The latter fits the simulation results well, including the oscillations observed under strong off-Bragg conditions. Similarly, Figure 4.7(b) shows the comparison between RCWA and Kogelnik. The latter fits the simulation results well. A slight negligible difference can be observed under strong off-Bragg conditions.

The reading angle θ_c is measured inside the hologram, which has a refractive index of $n_0 = 1.50$. Snell's law can be applied to determine the corresponding reading angle in air. The angular selectivity in air is wider: $2 \arcsin(\sin(18.4°/2) \times 1.50/1) \approx 27.8°$.

Note that these results correspond to an unslanted grating.

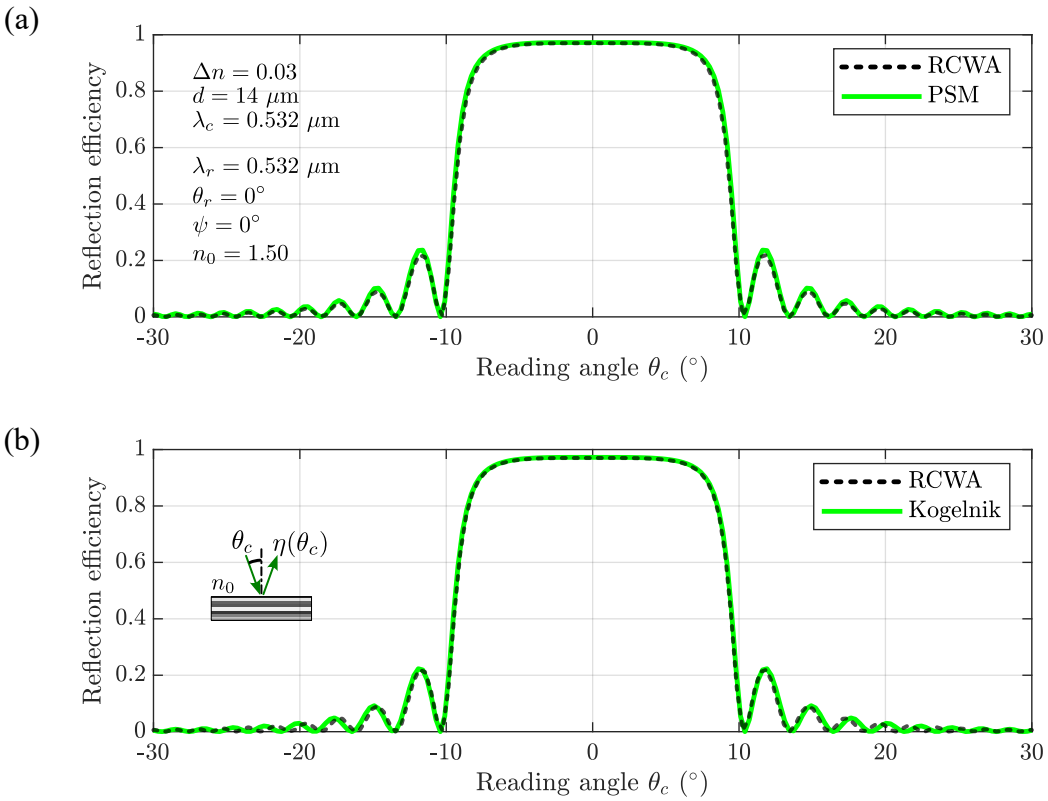

Figure 4.7: (a) Comparison between the RCWA simulation and the PSM model. The reflection efficiency is plotted as a function of the reading angle θ_c. The recording parameters and the reading angle are indicated in the figure. (b) Comparison with Kogelnik's model. θ_c is measured inside the hologram, where $n_0 = 1.50$. The grating is unslanted.

The following Figure 4.8 shows the angular response of the efficiency for a slanted grating.

(a) for $\gamma = 20°$ and (b) for $\gamma = 40°$. A schematic of the recording process is shown, with the recording parameters indicated in the figure. This efficiency is inside the material n_0 and does not include the transition to air. Snell's law and Fresnel equations must be applied. For example, $\gamma = 20°$ corresponds to $\gamma_{\text{air}} = 30.9°$ in air for the refraction: $n = 1 \rightarrow n_0 = 1.50$.

For a slanted hologram, the angular selectivity is divided into half. Whereas, in the case of an unslanted hologram, the angular response did not distinct between the object and the reference since they overlap. An incident reference wave near normal incidence will be efficiently reflected. Similarly, an incident object wave near the recording angle γ will also be efficiently reflected. For this angular selectivity we have two parts: one is centered around 0° (reference) and the other around −20° (object).

For the reference at 0°, it can be observed that the selectivity is not centered on 0°. This can be explained by the mismatch vector $\Delta\mathbf{K}$. For a slanted grating, $|\Delta\mathbf{K}(\delta\theta_{\text{read}})|$ is not a symmetric function. This can be understood by analyzing the magnitude of $\Delta\mathbf{K}$ in k-space.

In Figure 4.8(a), the angular selectivity around the reference and object directions is approximately 9.8° and 10.2°, respectively, showing a slight asymmetry.

In Figure 4.8(b), where the slant angle is larger, the angular selectivity is narrower: around 4° for the reference and 5.1° for the object. This is attributed to the increased perceived thickness of the hologram with respect to the incident angle.

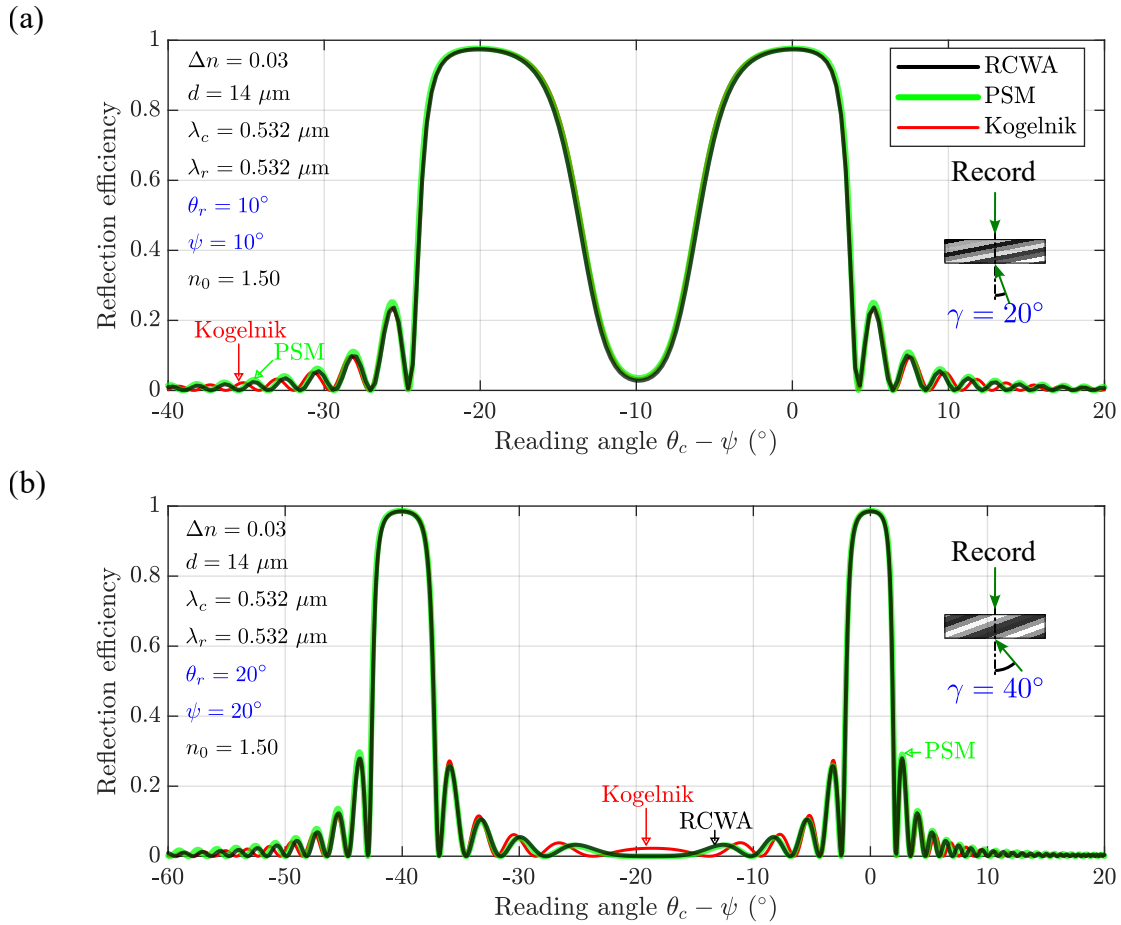

Figure 4.8: Reflection efficiency as a function of the reading angle. Slanted holograms and their impact on angular selectivity are illustrated. The recording angles are $\gamma = 20°$ for (a) and 40° for (b).

As discussed in Section 4.1.3, the Bragg condition is wavelength-dependent. Different wavelengths can satisfy the Bragg condition, but at different angles.

When using LED source or a broad wavelength source with a large angular divergence, the Bragg condition can be satisfied at different angles within this divergence for different wavelengths.

In the following Figure 4.9, I present experimental results of the angular response of a hologram. The recording wavelength is $\lambda_r = 0.532\,\mu$m, while three different wavelengths are used to read this unslanted grating.

For a given reading wavelength, the corresponding reading angle that satisfies the Bragg condition can be easily determined using k-space. In the case of this unslanted grating, a reading (construction) wavelength $\lambda_c > \lambda_r$ does not satisfy the Bragg condition.

In Figure 4.9(a), as the reading wavelength λ_c decreases below the recording wavelength $\lambda_r = 0.532\,\mu$m toward the blue at $\lambda_c = 0.483\,\mu$m, the corresponding angle θ_c that satisfies the Bragg condition increases. We can also note that the angular selectivity decreases. The angle θ_c is measured in the air.

In Figure 4.9(b), we show a fit of the experimental results for $\lambda_c = 0.483\,\mu$m using the PSM model, which matches the measurements very well.

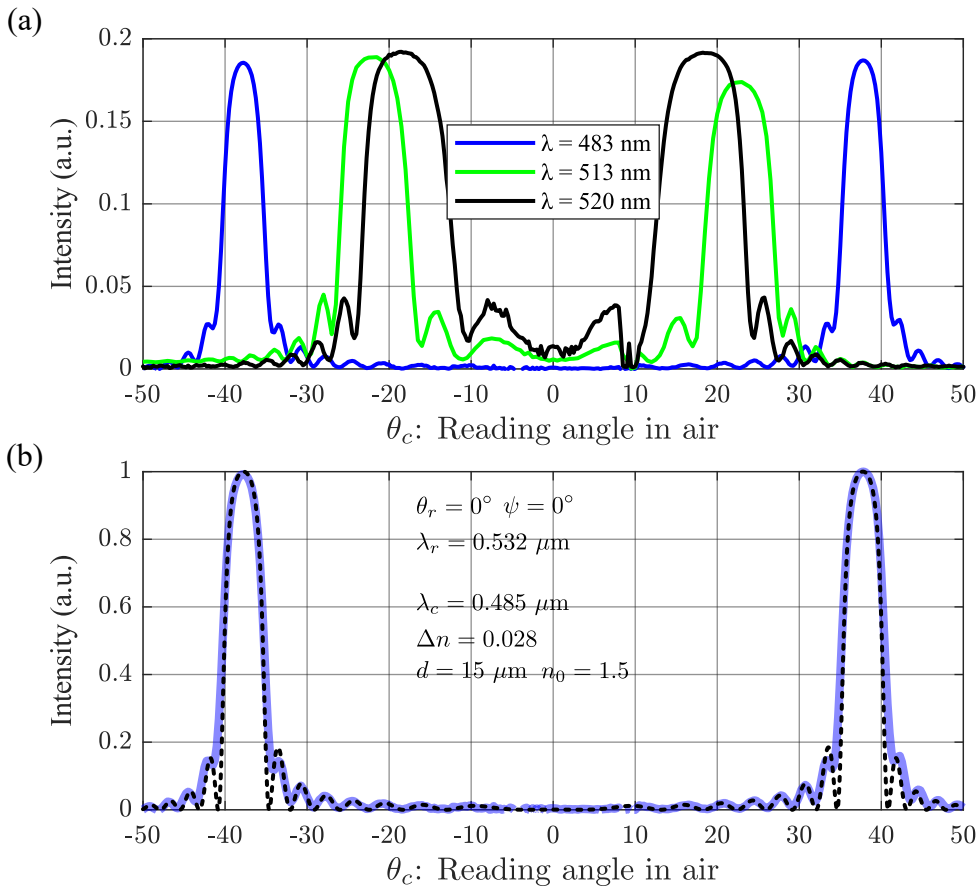

Figure 4.9: Reflection measurements as a function of the incident angle for an unslanted grating recorded at 0.532 μm. Three different wavelengths are used for the reading process. (a) Experimental results. (b) Example of a fit using the PSM model.

4.2.3 Spectral and Angular Selectivity

Reflection volume holograms are highly selective in wavelength but less selective in angle, whereas transmission volume holograms exhibit the opposite behavior [174, 179]. This selectivity can be advantageous for certain applications [180]. In other cases, such as lightguide combiners in augmented reality based on VBGs, the angular selectivity and reflection efficiency may present a trade-off over the incident Field of View (FoV). However, angular and wavelength multiplexing in VBGs can help overcome some of these limitations [181–183].

Multiplexing in holography is the process of recording multiple functions within the same hologram. For example, using different slant angles or different wavelengths. In our case, to extend to RGB, color multiplexing is envisaged. The hologram must be three times thicker to maintain the same reflection efficiency for the three colors. For example, if we assume a maximum modulation of $\Delta n = 0.03$ and aim to multiplex the wavelengths 0.440, 0.532, and 0.640 μm with the same efficiency of 98%, a thickness of $d \approx 46\,\mu$m is required, where the modulation of the refractive index of 0.03 is distributed as 0.0082, 0.0099, and 0.0119 for each wavelength, respectively (calculated by Equation (4.7)) However, as the thickness increases, the selectivity width decreases. Another method to overcome this is by stacking three holographic films, each for a wavelength [184].

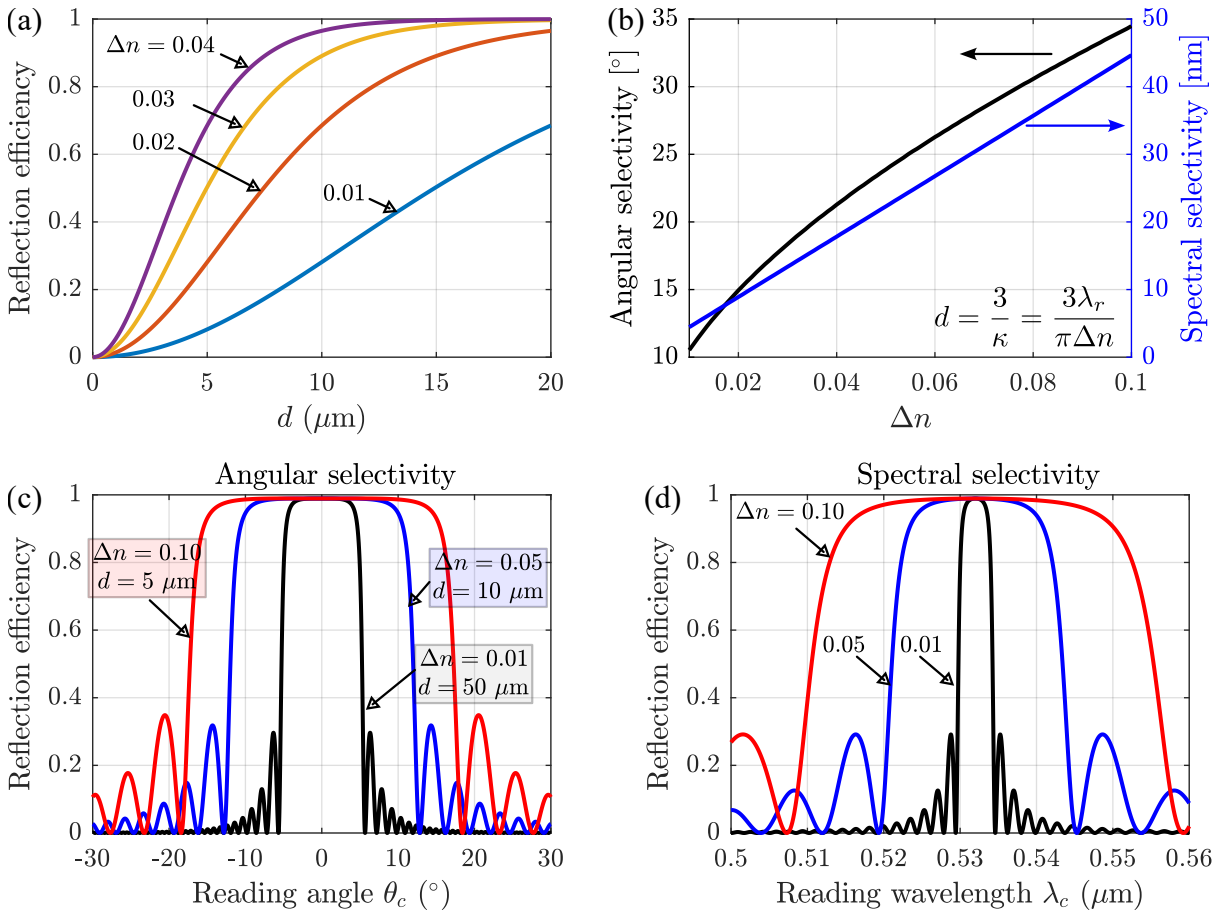

Figure 4.10: (a) Reflection efficiency as a function of the hologram thickness d and the refractive index modulation Δn. (b) Angular and spectral selectivity as a function of Δn. The thickness d is adjusted for each Δn to maintain 99% reflection efficiency. (c) Example of the angular response of the hologram for selected values of Δn. (d) Example of the spectral response. These results are simulated using PSM.

Reflection efficiency, refractive index modulation Δn, grating thickness d, and angular and spectral selectivity are interrelated. Figure 4.10 provides some simulation results of these relationships. (a) shows that the efficiency increases with both thickness d and modulation Δn. (b) shows that the angular and spectral selectivity increase with modulation Δn. The thickness d is chosen as $3/\kappa$ to keep a consistent reflection efficiency of 99%.

Figures 4.10(c) and (d) show the angular and spectral reflection profiles, respectively, for selected values of Δn and d used in (b).

As a general rule of thumb, reducing the thickness decreases the reflection efficiency but increases the width of the angular and spectral selectivity. To restore efficiency at a lower thickness, Δn must be increased.

In our case, with a photopolymer that provides $\Delta n = 0.03$ and a thickness of approximately 14 μm, the reflection efficiency is around 97%. The spectral selectivity is approximately 13 nm. For an unslanted grating, the angular selectivity is about 18.4° inside the hologram medium with refractive index $n_0 = 1.50$. In air, the angular selectivity is higher, around 27.8°. As the slant angle increases, the angular selectivity decreases. In the hologram medium (n_0), for a recording angle $\gamma = 20°$ (which corresponds to a recording angle of 30.86° in air), the angular selectivity is about 10° (which corresponds to 2 arcsin $(\sin(10°/2) \times 1.50/1) \approx 15°$ in air).

4.3 Recording Materials

4.3.1 Photopolymers and Silver Halides

Photopolymers

The formation of the hologram in a photopolymer is illustrated in Figure 4.11. Unexposed photopolymers initially contain monomer entities. During exposure, the monomers polymerize in regions of high intensity. Monomers in low-intensity regions migrate toward the polymerized areas due to the concentration gradient [185] or via osmosis [171]. As a result, the material density increases and is distributed according to the interference pattern. Lastly, the hologram is cured under incoherent illumination to fully polymerize the rest of the monomers.

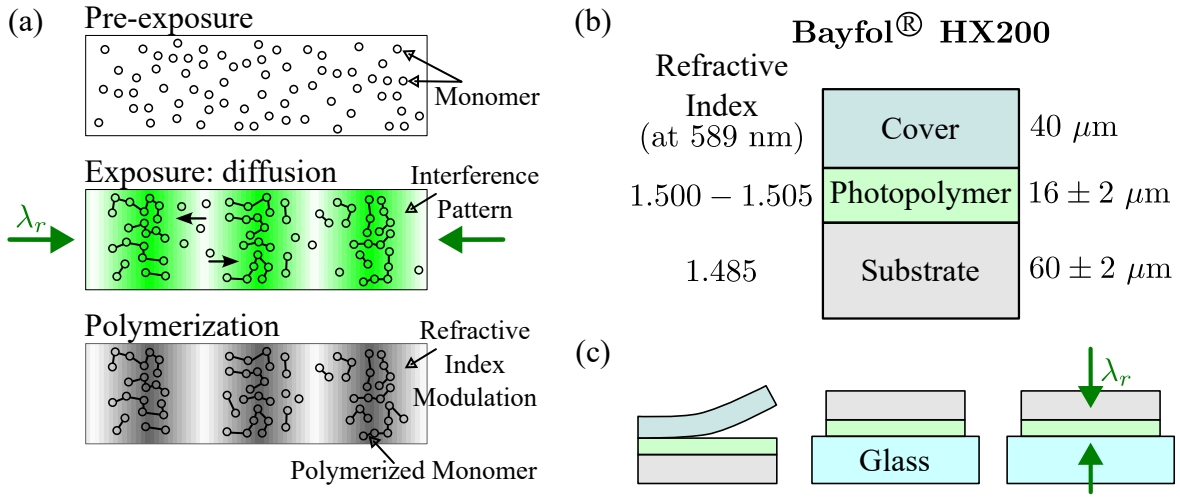

Figure 4.11: (a) Illustration of the physical process of hologram formation in a photopolymer [171]. (b) Bayfol HX200 photopolymer used in our study. (c) Preparation process.

Figure 4.11 shows the type of photopolymer we used from Covestro: Bayfol® HX200 [186, 187]. HX200 can be used across the RGB range. The photopolymer layer is sandwiched between a transparent substrate and a protective cover. During the preparation process, we remove the protective cover from the film and then laminate it onto a solid glass substrate (such as a microscope slide) before proceeding with the recording.

We mainly use Bayfol photopolymers. They are easy to handle and do not require any chemical processing. However, the recording time per μhologram can be up to 1 second, with a typical sensitivity of 10 $\mathrm{mJ/cm^2}$.

Silver Halides

Silver halides were the first recording materials used in holography [188]. They are emulsions of various silver halide crystals embedded in a gelatin layer. Silver compounds are sensitive to light and are converted into silver atoms in regions of high intensity. These silver atoms absorb light. Silver halides allow for the formation of both amplitude and phase holograms. The absorption modulation is transformed into a refractive index modulation by bleaching the emulsion, which removes the silver crystals [171].

We also use silver halide materials from Ultimate Holography [189], which are much faster to record, with a recording time per μhologram of up to 10–100 ms and a typical sensitivity ranging from 0.1 to 1 $\mathrm{mJ/cm^2}$. Silver halide materials require chemical processing, such as developing and bleaching.

4.3.2 Exposure and Refractive Index Modulation

In Equation (4.1), the refractive index $n(\mathbf{r})$ of the hologram is expressed. The crossmodulation term related to the formation of Δn depends on the intensity of the object and reference beams, as well as on the sensitivity of the recording medium.

The term *intensity* refers to the radiant flux per unit solid angle (in units of W/sr). However, in holography, we are concerned by the amount of flux per unit area falling on the surface of the hologram. The appropriate radiometric quantity is the *irradiance* E, measured in $\mathrm{W/cm^2}$. The amount of energy received by the hologram per unit area is defined as the *exposure* H, with units of $\mathrm{mJ/cm^2}$. It is simply the product of the irradiance and the exposure time: $H = E \times t$.

In holographic recording, one should also be aware of certain technical complexities. The object and reference beams must have the same polarization and similar intensities to ensure a high fringe contrast. In our case, we work with transverse electric polarization σ, which is tangential to the boundary of the holographic film.

Other technical subtleties include Fresnel reflections during recording, mechanical stability, and shrinkage/swelling of the hologram thickness. We should note that shrinkage and swelling [178] which refer to the decrease or increase in the hologram thickness, are not considered here. These effects, which slightly modify the magnitude and the direction of the grating vector $\mathbf{K}$, can result in a small shift in the reconstructed wavelength and slant angle. In applications where precise control of the grating response is required, such changes can be significant. In this study however, this aspect is not treated as it does not impact the objectives of my research.

In Figure 4.12, I present some results on the relationship between reflection efficiency and exposure. The reflection efficiency is directly related to the modulation Δn. (a) shows

transmission measurements of different gratings recorded with varying exposure levels. Based on these experimental results, a PSM fitting is applied to the spectral response, from which Δn is extracted. This is plotted in (b) as a function of exposure. A similar procedure is applied for different wavelengths (green at 0.532 μm and red at 0.640 μm) and for different materials, typically the Covestro photopolymer HX200 and the silver halide from Ultimate Holography.

Figure 4.12(c) provides a summary of the modulation Δn as a function of exposure. Silver halide exhibit higher sensitivity compared to photopolymer, requiring only low exposure levels, typically in the range of 0.1–1 mJ/cm^2. Typical irradiance levels are around 1–5 mW/cm^2. The RI modulation Δn can reach values as high as 0.05, compared to about 0.03 for photopolymers. At the red wavelength 0.640 μm (red markers), the silver halide is less sensitive than at the green wavelength. For the photopolymer, the typical exposure requirement is around 10 mJ/cm^2, with an irradiance level of approximately 10 mW/cm^2.

It should be noted that the reported exposure and irradiance values refer to either the object or the reference beam individually and not to the sum of both.

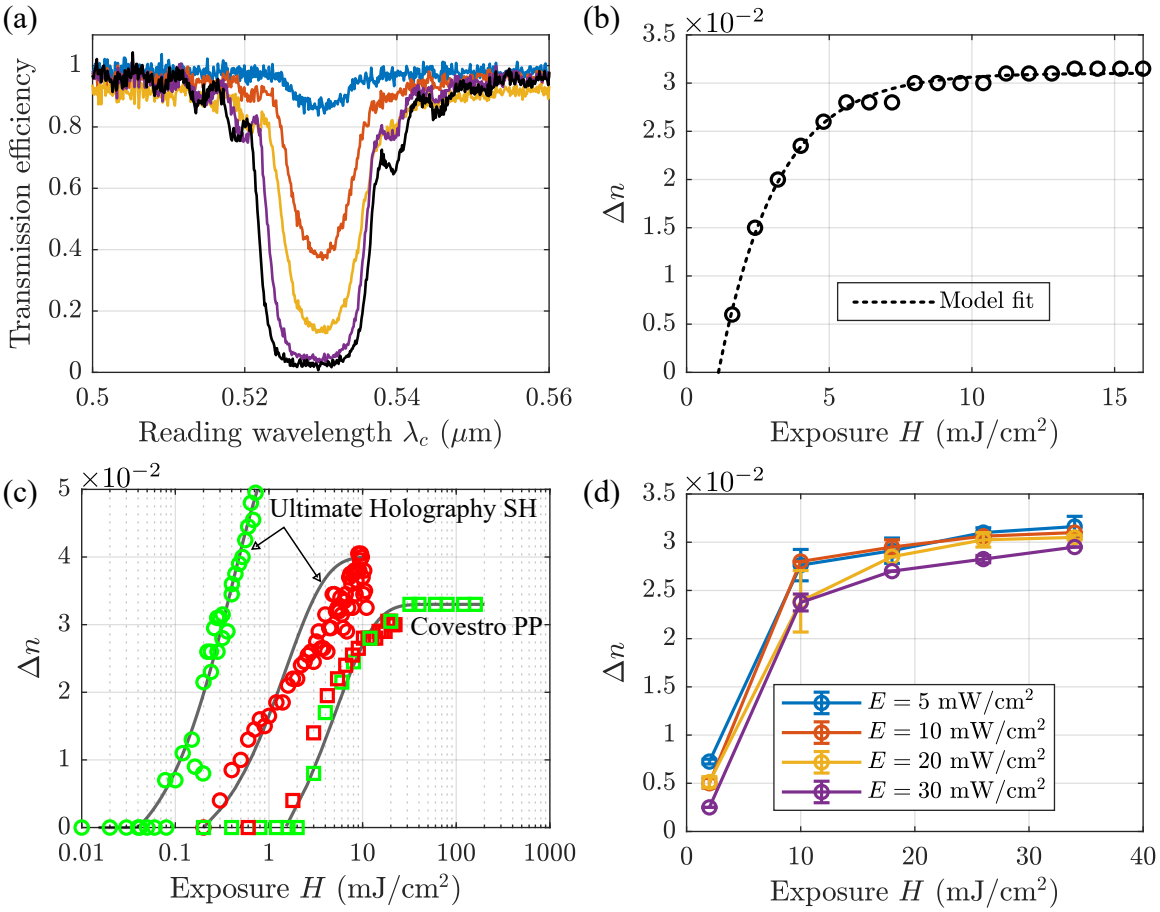

Figure 4.12: (a) Transmission measurements obtained using a spectrometer for different exposure values H (for unslanted hologram in photopolymer at 0.532 μm). (b) The spectral results are fitted, and the corresponding values of Δn are extracted and plotted as a function of H. (c) Summary of the modulation Δn as a function of H for different materials and wavelengths (green: 0.532 μm; red: 0.640 μm). (d) Reciprocity failure: Δn as a function of H for different irradiance levels.

Exposure $H = E \times t$ is generally expected to follow a reciprocity principle: high irradiance E with short exposure time t, or low irradiance with a longer exposure time, resulting in the same

exposure value, should yield similar Δn results. However, this reciprocity can fail at extreme values [178]. Therefore, the value of H must always be reported alongside the corresponding E or t. Figure 4.12(d) shows some reciprocity failure results for different irradiance levels at a wavelength of 0.532 μm for the photopolymer. Error bars are included. Ideally, the curves should overlap and be independent of irradiance.

The takeaway from this section: the recording time for a hologram is around 1 s for the photopolymer, while the silver halide is approximately ten times faster. The achievable RI modulation for the photopolymer is about 0.03. Since the total recording time increases with the number of μholograms or holographic pixels, silver halide can be used to reduce this time. The trade-off between resolution and recording time will be discussed in the hologram copying Section 4.5.3.

4.3.3 Mechanical Stability

The recording process of holographic pixels requires the sample holder to move for each μhologram. This movement induces vibrations. A "waiting time" is necessary to allow the system to stabilize before recording the next μhologram. Indeed, mechanical vibrations cause fringe movement and erasing of the grating.

In the following figure 4.13, I present results related to the waiting time. On the left, the modulation Δn is plotted as a function of the repetition number. The same hologram is repeated at different spatial locations. As the waiting time increases from 0.5 s to 2 s, the results stabilize around $\Delta n = 0.03$. On the right, the same results are plotted as a function of the waiting time. The repeated holograms are illustrated by error bars. As the waiting time increases, the variations are reduced and the results become more stable.

Note that these results were obtained during the first year of my work. However, over time, I observed in my holographic display that the number of dead holographic pixels increased. At some point, I started using a waiting time of 4 s to ensure a better stability. This significantly increased the total recording time as the number of pixels increase. Toward the end of my PhD, replacing the piezoelectric actuator motor with a new one allows to reduce the required waiting time to just 0.5 s.

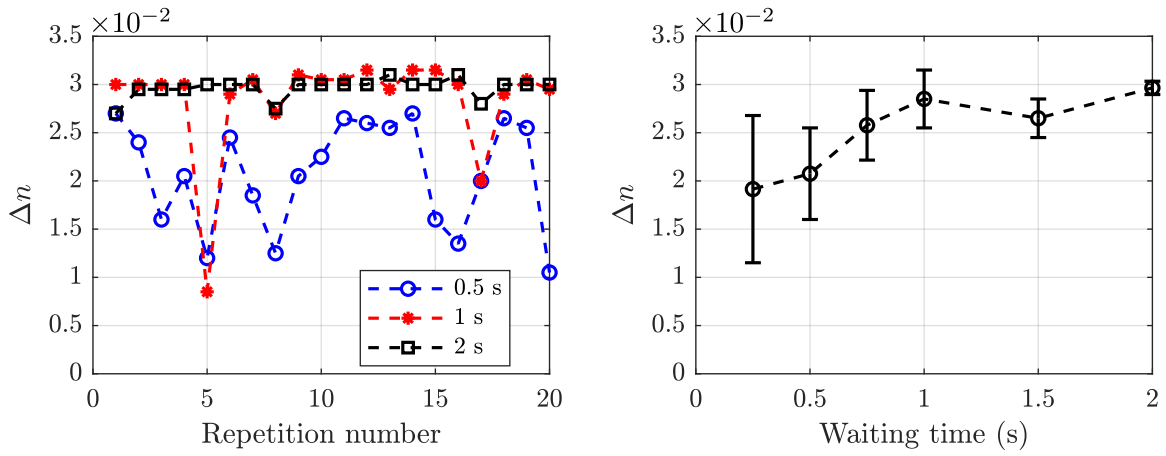

Figure 4.13: Importance of mechanical stability (vibration-free conditions) in holographic recording. The plots show the waiting time required between each μhologram recording to obtain stable Δn.

4.4 Holographic Printer

4.4.1 Objective

Directional displays offer numerous advantages, ranging from improved efficiency to enhanced visual comfort. Figure 4.14(a) illustrates an example of an unfolded near-eye display (NED) architecture, where the directivity of the display enables a uniform and unique EyeBox (EB) across the entire field of view (FoV). For clarity, a simple lens is shown as the combiner. In a more precise implementation, a volume hologram is used as a reflective combiner [105]. The display, located at point F, is positioned at the focal length of the lens. The lens at point C collimates the light field in the direction of the eye, whose pupil is at point E. The directivity of the pixels is designed to target the point V, as illustrated in the figure by the emissions from pixels P1 and P2. The image of the virtual point V through the lens is located in point E. Consequently, after refraction, the fields from the pixels converge at point E. This configuration allows the creation of a real exit pupil (STOP) using only a single lens as a combiner. The location of the exit pupil corresponds to the intersection of the parallel rays from the top and bottom edges of the display [3].

Figure 4.14(b) shows a schematic summary of the objective of this chapter: recording holographic pixels, each targeting a specific focal distance (FV). This means that each μhologram should encode a reflection function, as illustrated. An offset angle for illumination ϕ_{ref} is also desired to avoid specular reflection. In this schematic, only the central direction of the reflected light is shown.

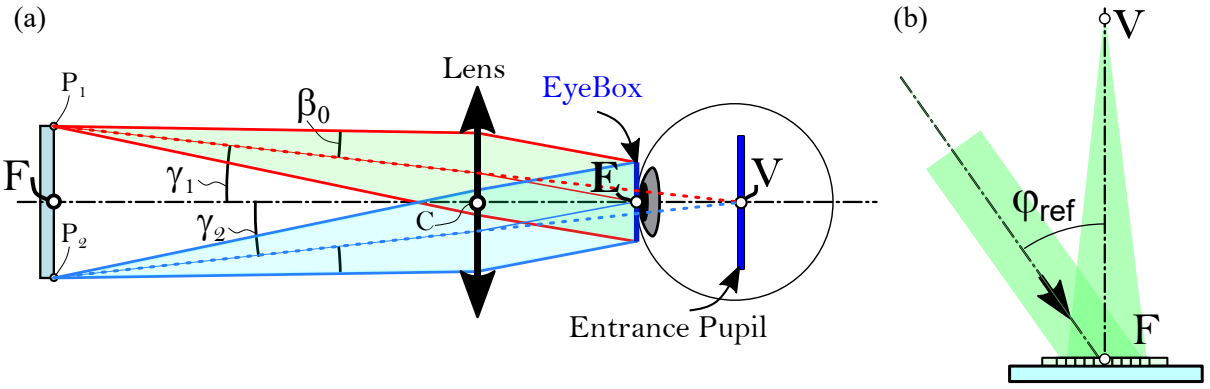

Figure 4.14: (a) Example use case of a directional display with a simple lens combiner, where the emission target specific focus distance (FV), enabling real exit pupil as an EyeBox. (b) Schematic of the holographic pixelization objective: by illuminating the μholograms, they reflect or focus light at a distance (FV). This schematic does not show the divergence of signal of each pixel, only their central direction.

4.4.2 Holographic Printers

Using holographic printers to synthesize 3D holographic images point by point dates back to the 1990s. For example, Yamaguchi [190] (Figure 4.15(a)) proposed a digital holographic printer to produce holographic stereograms. These holograms record 3D objects based on both horizontal and vertical parallax. The hologram is divided into a matrix of small holographic elements called *hogels*. Just as 3D printing revolutionized mechanical fabrication, holographic

printing could revolutionize the production of optical elements such as HOEs (Holographic Optical Elements) [191]. Figure 4.15(b) shows a holographic printer from Byoungho Lee's lab in Korea [192], used for recording HOEs. The holographic elements are recorded by interfering a reference beam with a structured wavefront beam generated using a spatial light modulator (SLM). Figure 4.15(c) presents a holographic printer developed by Meta [163], where SLMs are used in both the reference and object arms. Figure 4.15(d) shows an artistic 3D image created with a holographic stereogram. The printer *CHIMERA*, developed by the Gentet brothers [193], produces full-parallax, full-color images with 250 μm hogel size.

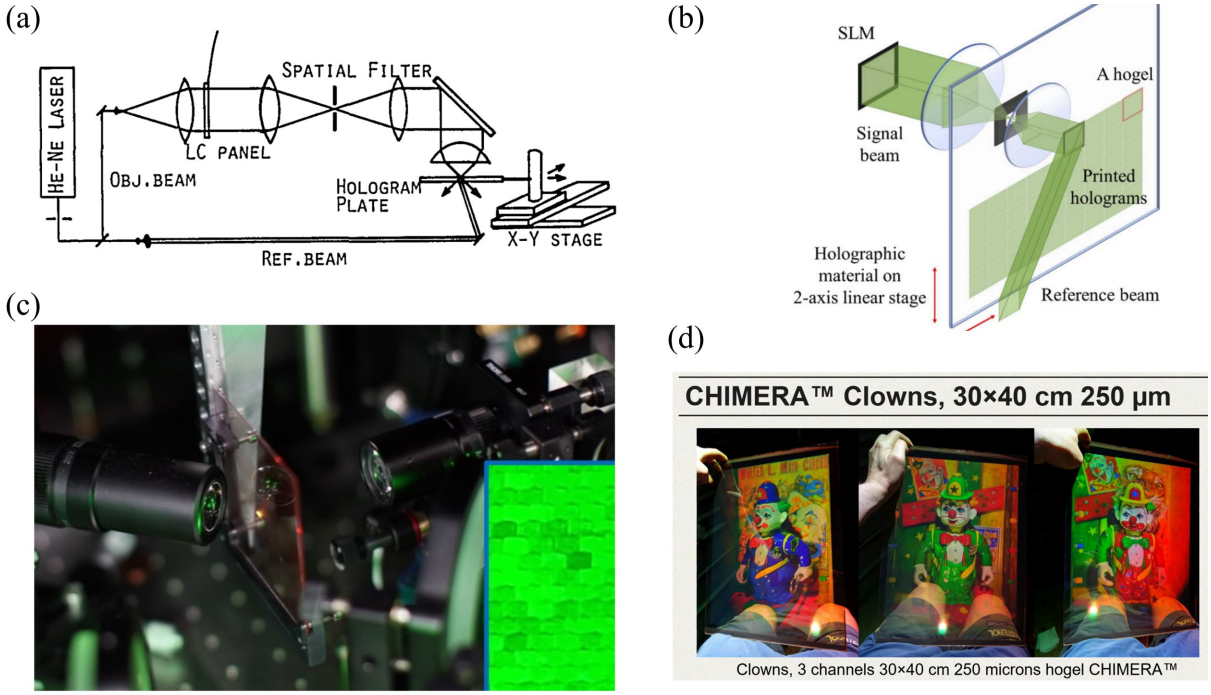

Figure 4.15: (a) Schematic of the digital holographic printer by Yamaguchi [190]. (b) Schematic of a holographic printer for recording HOEs developed by Byoungho Lee's lab in Korea [192]. (c) Photograph of the HOE printer developed by Meta [163]. (d) Ultra-realistic holographic stereogram printed by the CHIMERA holographic printer, developed by Gentet for artistic purposes [193, 194].

In our lab, we use a holographic printer [195] developed by C.Martinez for a retinal projection system based on holographic elements [109]. I used this printer in my research, adapting certain components to record the offset angle, improving the projection alignment for my case, and especially automating the recording process in LabView.

4.4.3 Setup Description

In Figure 4.16(a), we present our micro-hologram printer. A laser source in the visible spectrum is divided into the reference and object arms. Each arm includes two lenses: the first lens projects the point source from the fiber to the focal point $F2$ of the second lens. The second lens projects this point to infinity, ensuring collimation. A mask with a small aperture, positioned before the focal point of the second lens, is projected onto the holographic sample. This mask determines the shape and size of the holographic pixel.

The object fiber is actuated by a piezoelectric motor, and its movement in the (xy) plane shifts its image in the focal plane of the second lens. This shift allows the sample to be illuminated

with a beam tilted at various angles. It establishes a position–angle relationship that is essential for recording different reflection directions.

In our holographic setup, the encoded angle γ_{ij} and the fiber distance ϵ_{ij}, both measured with respect to the optical axis, are related through the magnification M of lens 2 and the focal length f_1 of lens 1, as expressed in the following geometric equation (refer to reference [195] for the derivation):

$$\gamma_{ij} = -\arctan\left(\frac{\epsilon_{ij}}{M \times f_1}\right) \tag{4.14}$$

In the reference arm, the fiber position is fixed along the optical axis. A reference angle ϕ_{ref} is set to separate the specular reflection from the reconstructed object wave. This asymmetry between the object and reference arms necessitates the use of two different masks or distinct magnifications to ensure identical projection on the holographic sample.

The sample holder is actuated by a piezoelectric motor, allowing the recording of each pixel individually. Figure 4.16(b) illustrates the pixel recording process. Movement of the sample holder to the next pixel induces some vibrations, necessitating a waiting period to stabilize before opening the laser shutter. The size of the pixel $(\delta x, \delta y)$ in the x and y directions is determined by the size of the mask aperture and the magnification.

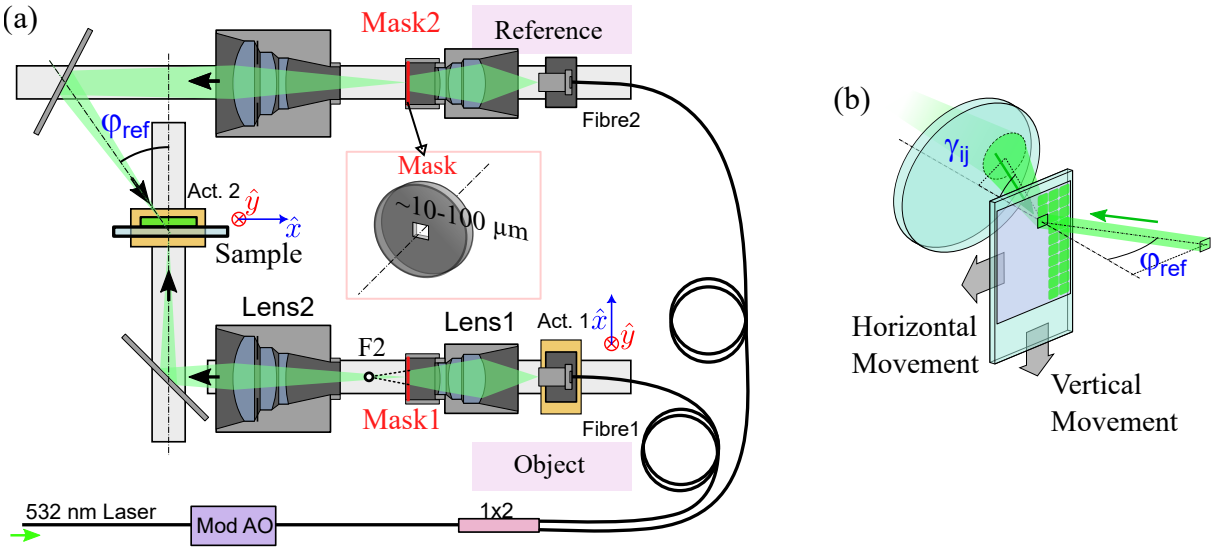

Figure 4.16: (a) Schematic of our micro-hologram printer [195]. (b) Schematic representation of the micro-holograms recording process.

We aim to create a pixelated holographic display as illustrated in the previous Figure 4.14(a), where the pixel directions γ_{ij} are designed to target the focus distance FV. Relative to the optical axis, the pixel distance FP_{ij} is related to FV and γ_{ij} through the following equation:

$$FP_{ij} = FV \times \tan(\gamma_{ij}) \tag{4.15}$$

The pixel distance FP_{ij} is related to the display size (N, M) via the equation:

$$FP_{ij} = \sqrt{\left(\left(\frac{N}{2} - i\right) \times \delta x\right)^2 + \left(\left(\frac{M}{2} - j\right) \times \delta y\right)^2} \tag{4.16}$$

The indices i and j denote the i-th row and the j-th column, respectively.

Equations (4.14) and (4.15) allow us to establish a relationship between the fiber positions and the holographic sample position through the following equation:

$$\epsilon_{ij} = -\frac{M \times f_1}{FV} \times FP_{ij} \tag{4.17}$$

In our display manufacturing process, all the μ-holograms H_{ij} are recorded. Then, the emissive points from the photonic chip (PIC) address these μ-holograms. The term "μ-hologram" or "holographic pixel" does not refer to the actual emissive pixel. A single μ-hologram can overlap several emissive pixels. The size of the holographic pixel I achieved is around 20 μm for $\phi_{\text{ref}} = 0°$. At higher values of ϕ_{ref}, alignment becomes more challenging. For $\phi_{\text{ref}} = 35°$, I achieved a size of 50 μm.

As an initial demonstration, I implement the recording of the holographic pixels to provide static image projection (without PIC). This image is loaded into the holographic printer. The matrix FP_{ij} is generated based on the image size and a corresponding matrix for fiber movement is created using Equation (4.17), which is defined by the focus distance FV.

4.4.4 Automation

The printing process is automated using LabView, as illustrated in the flow chart in Figure 4.17. After loading the image and entering the recording parameters (image dimensions, distance of focus, pixel size, magnification, and waiting time), two sets of matrices are generated: one for the sample holder and another for the object fiber. The process loops over each pixel until completion. The exposure time is set to 1 second, with an irradiance of approximately 10 mW/cm^2 for each of the object and reference beam.

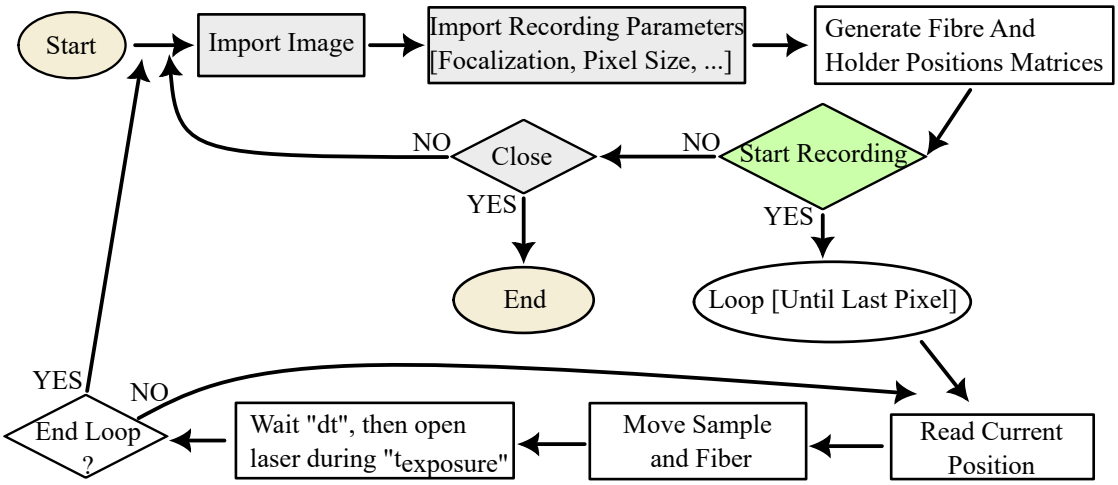

Figure 4.17: Flowchart of the printer automation for encoding a micro-holographic display.

4.5 Characterization and Results

4.5.1 Microscopic and Macroscopic Views

Fig. 4.18 shows close-up images of some pixelated samples. Fig. 4.18(a) presents an image to be printed, consisting of 20×20 pixels. Figures 4.18(b) and 4.18(c) are microscopic images of the results, with a pixel size of 50 μm. In this sample, each μhologram encodes a reflection angle, which will be characterized in the reconstruction section. The offset angle is $\phi_{\text{ref}} = 22°$. In Fig. 4.18(c), we can see a slight horizontal overlap. In fact, as ϕ_{ref} increases, the projected image of the square mask becomes rectangular. This projection obliquity factor could be corrected in the future by using an appropriate rectangular mask in the reference arm.

Fig. 4.18(d) shows an image of 160×120 pixels to be printed. Fig. 4.18(e) presents a photograph of the result, and Fig. 4.18(f) shows a close-up image of the holographic pixels. This is not a microscopic image but an imaging result obtained using a lens and a camera sensor. Some dead pixels can be observed, caused by the waiting time required for the stability of the translation stage. There is room for improving this stability to enable recording with high resolution at a reasonable frequency [194].

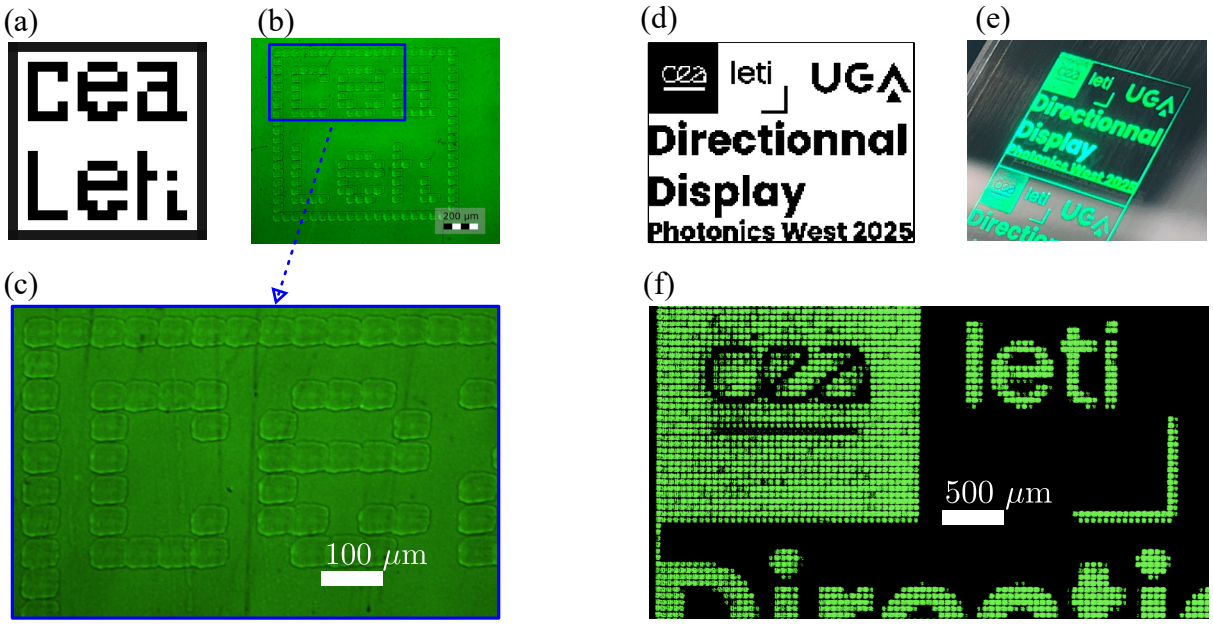

Figure 4.18: (a) Image to be encoded (20×20 pixels). (b) and (c) microscope images of the holographic printed image with a pixel size of 50 μm. (d) Example of an image to be encoded (160×120 pixels) and the corresponding results; photograph (e) and (f) an image using a lens and a camera sensor.

The main challenge during recording is managing the overlap between the object and reference beams. Moving the fiber away from the optical axis introduces optical aberrations, particularly coma. High-quality imaging optics are essential for minimizing these effects. The current achievable angle interval without significant degradation in imaging quality is approximately $-4°$ to $4°$. For a holographic display with a diagonal of 10 mm, this corresponds to a minimum field focus distance of about 7.15 cm, as calculated using Equation (4.15). This value is sufficient for our NED specifications, but, if necessary, it can be further reduced by decreasing the magnification M.

In the example presented before in Figure 4.14(a), the focal length of the free-space combiner is 5 cm. For an eye relief distance of 2.2 cm between the lens and the eye and a display size with a 1 cm diagonal, the required focus distance FV is 9 cm.

4.5.2 Reconstruction of the Encoded Focus

Figure 4.19 highlights the key result of this chapter. We present in Figure 4.19(a) a schematic of the reconstruction process: the holographic pixelated image is reconstructed using an incident collimated beam with an offset angle of $\phi_{\text{ref}} = 22°$. As already mentioned, we chose this angle to separate the holographic reflected field from the specular reflection.

To visualize the field profile, a camera sensor is positioned at different distances from the normal axis of the static display. We show in Figure 4.19(b) and (c), the field captured at distances of 7.5 cm, 9 cm, and 12 cm. Two cases are presented: (b) with a focus encoded at 9 cm, and (c) with a focus located at infinity. In case (b), the fields overlap to form a diffraction pattern. This confirms that the focus function FV has been achieved correctly. In the unfocused case (c), the field maintains a similar shape as a function of distance and slightly diverges due to diffraction.

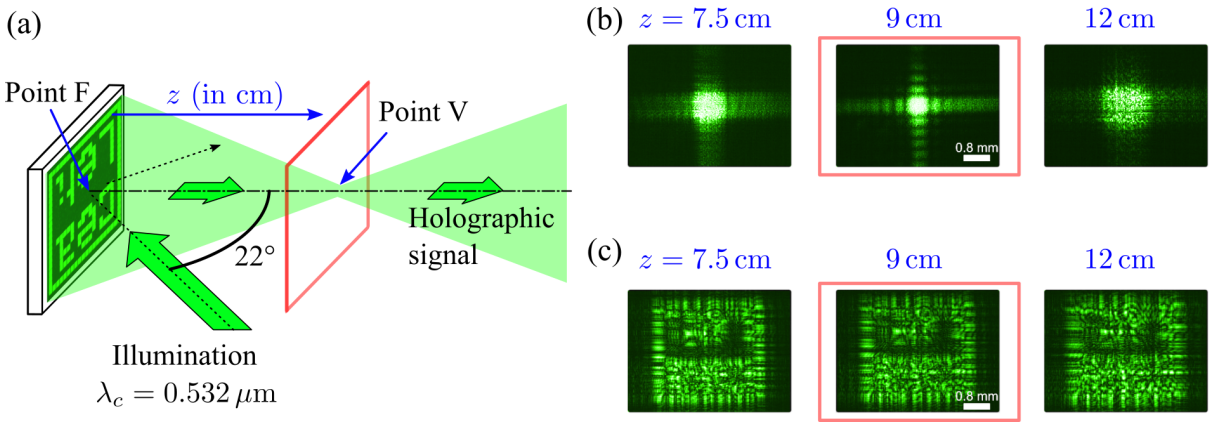

Figure 4.19: (a) Principle of the holographic display characterization using an offset reference angle of 22°. (b) and (c) field imaging results at three different distances: 7.5 cm, 9 cm, and 10 cm, for two sets of samples recorded with FV = 9 cm (b) and FV = ∞ (c). The pixel size is 155 μm.

The pixel size for the sample used in Figure 4.19 is 155 μm. The corresponding diffraction angle for a reconstruction wavelength of 0.532 μm is $\theta = 0.2°$. We calculate the size of the central lobe in the diffraction pattern at the focus distance reaches approximately a value of 0.62 mm. It is coherent with the observed pattern in the center of Figure 4.19(b). This pattern, measured at the pixel's signal convergence, corresponds to the superposition of the diffraction patterns generated by all the pixels. The focus spot of Figure 4.19(b) is diffraction-limited by the pixel size, as result of the collimated incident light. In practice, the divergence will be determined by the size of the emitters beneath the holographic layer. The *étendue* of the emission can be increased by encoding a diffuse function in the holographic pixel. We may recall that focusing the field of the display provides a unique and uniform EyeBox across the entire Field of View. In addition to enhancing visual comfort, this effect improves coupling efficiency, as the light from each pixel is better aligned with the acceptance cone of the combiner [101].

The following Figure 4.20 provides more results. Encoded FV at 5; 9; 10 and 20 cm. The encoded focus $FV = 100$ m can be considered as FV = ∞. For reconstruction, we add $z = 0$ cm;

in practice, it corresponds to the image of the pixelated hologram through a lens. Similarly to the previous results, we show the evolution of the field at different distances.

For FV = 5 cm, the field focuses at $z = 5$ cm. In my reconstruction setup, there is limited space for illuminating the hologram and placing the camera. The minimum distance was this in practice $z = 5.5$ cm. The diffraction lobes are not clear at this distance. For FV = 9 cm, the field focuses at $z = 9$ cm. Similarly for FV = 10 and 20 cm. All pixels focus exactly at the encoded focus. The profile of the diffraction is the superposition of the diffraction from all pixels.

The last row, with FV = 100 m, corresponds to a holographic display encoded with vertical emission and no directivity $\gamma_{ij} \approx 0°$.

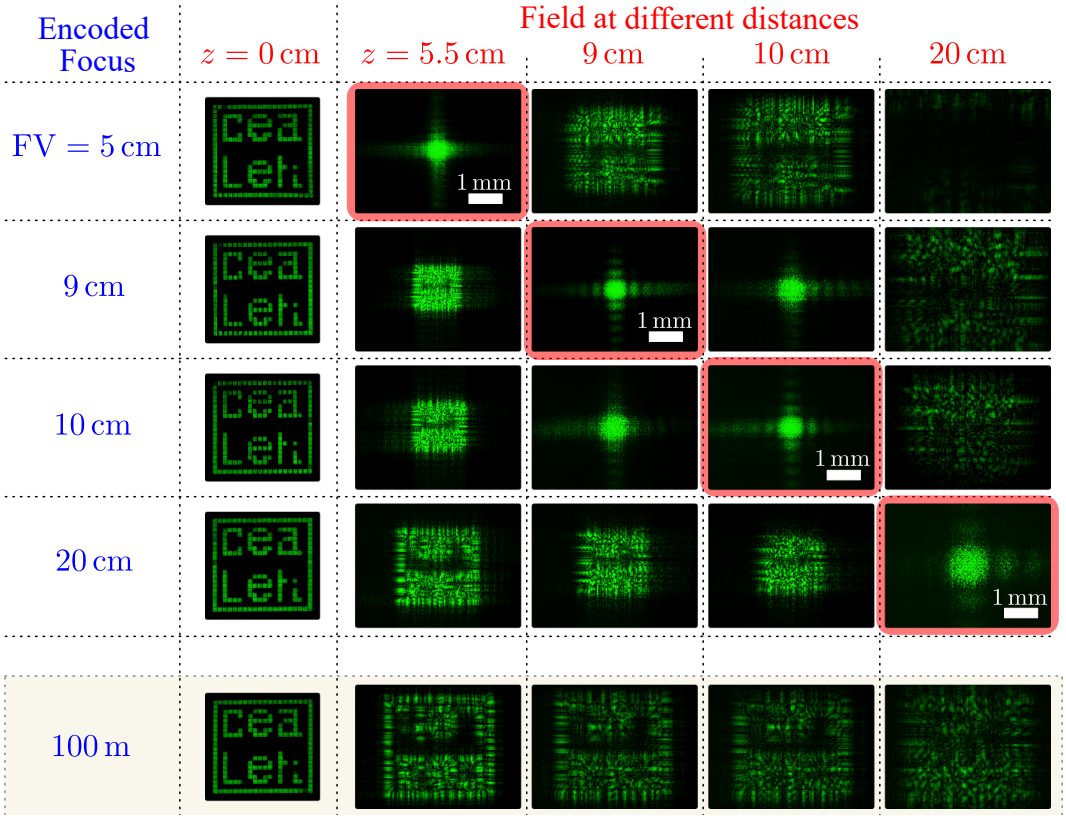

Figure 4.20: Encoded focus for different values of *FV* and the corresponding results of the field profile captured at different distances. The offset reference angle is 22° and the pixel size is 155 μm.

4.5.3 Replication and Perspectives

Holographic pixelization is time-consuming for large resolution. Photopolymers are less sensitive than silver halide. If we consider 1 s for each pixel for the photopolymer and 0.2 s for the silver halide, recording time can be reduced by a factor of 5. However, this is not sufficient; we also need to consider the waiting time between each recording. If we consider the photopolymer with 1 s exposure time and 0.5 s waiting time, recording a VGA (640×480) resolution would take 128 hours. For silver halide, 60 hours are expected.

Since silver halide has a low sensitivity of $\approx 0.5\,\text{mJ/cm}^2$, using a high irradiance of $50\,\text{mW/cm}^2$ gives a recording time of 10 ms. This can significantly reduce the overall recording time; however, the bottleneck is the waiting time for vibration, which must be minimized by using a high quality translation stage. Gentet reports in [194], using the silver halide Ultimate

U04 [189], a recording frequency of 50 Hz for holographic elements of size 250 μm. This value includes both the exposure and the waiting time. A frequency of 50 Hz corresponds to 20 ms. For VGA resolution, this results in a total recording time of about 1h42min, which is much more attractive. For UXGA resolution (1600 × 1200), he reported a total recording time of 11 hours.

Hologram copying (replication) is a possible solution for mass production. In a first step, we record the directivity matrix pixel by pixel in a master hologram. In a second step, the master is replicated as a holographic stamp. In a similar manner to the nanoimprint process, which is more mechanical and applied, for example, to surface relief gratings (SRG), our replication method is optical. The master is illuminated, and with the same reference beam, the resulting interference pattern is recorded. For the copy, it is possible to use the same material or a different material than that of the master.

Figure 4.21(a) shows an example of contact copying. After recording the master pixel by pixel, a photopolymer film is laminated onto the master. Upon illumination with the reference beam, the reflection angles interfere with the reference and are transferred to the copy. The copy is then removed and laminated onto a second glass substrate.

Figure 4.21(b) shows a close up of the lamination between the copy and the master during recording. The reflected field R interferes with the incident reference and register in the copy.

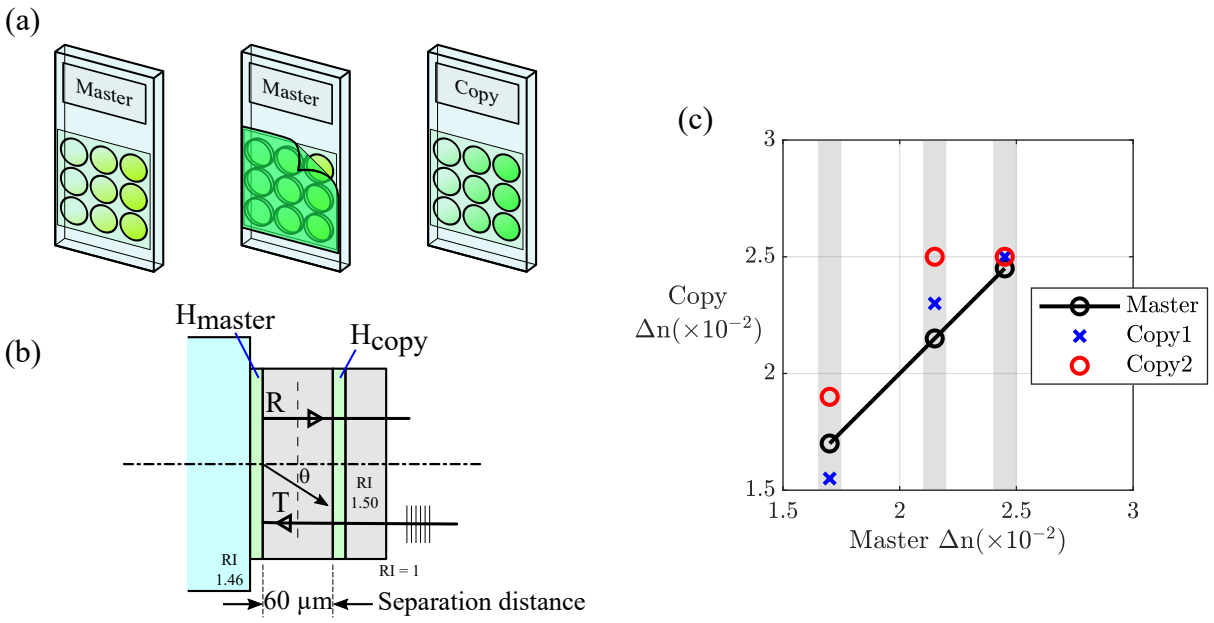

Figure 4.21: (a) Holographic pixel copying by contact onto a photopolymer film. (b) The reflected angles interfere with the incident reference. (c) Reflection efficiency of the copies and the master for two different exposure times.

In general, for a hologram in which the feature size is a, the distance between the copy and the master must be smaller than the Fresnel length $\ell_{FR} = \frac{a^2}{\lambda}$. This helps to avoid diffraction effects. However, the feature size of a hologram can be as small as 0.2 μm, which makes it complicated to achieve contact below ℓ_{FR}. In our case, we do not copy a complex hologram profile. We want to avoid diffraction effects at the scale of the pixel. Since the pixel size on the copy depends on the separation distance, it can become larger, and cross-talk between pixels may occur. If we consider a holographic pixel size of 20 μm, the separation should be lower than $\ell_{FR} = 752$ μm at $\lambda = 0.532$ μm. In our case, the separation is 60 μm, so diffraction effects

on the pixel size can be neglected.

Another aspect, more important than diffraction, that impacts pixel cross-talk, is the reflection angle. If we consider a reflection angle of 4° with a separation of 60 μm, the reflected pixel can overlap a neighboring one over a distance of 4.2 μm. This overlap increases as the reflection angle increases and decreases as the separation becomes smaller.

Figure 4.21(c) shows some experimental results of the copying efficiency. The master contains three holograms with different efficiencies at different positions. After laminating the photopolymer film, we record a copy with fixed exposure. Then we delaminate and laminate another film and record with a different exposure time. We show that the reflection efficiency of the copies is independent of that of the master. However, the reflection efficiency of the master should be high enough in order to achieve a similar irradiance level between the reflected beam and the incident beam.

We should note that the actual protocol involves contact copying of the photopolymer laminated on the silver halide. This contact does not have a separation distance, in contrast to the 60 μm gap present in photopolymer-on-photopolymer copying.

Contact copying is simple and straightforward. I have only tested this process. However, to overcome the limitation of pixel cross-talk, we can opt for other methods, such as imaging the master pixel onto the copy and interfering it with a reference beam. Here are some references related to hologram copying [196–201].

Some considerations for replicating efficient copies that can be taken into account: the reflected and incident waves must have similar irradiance levels. This helps produce copies with high fringe visibility and thus high efficiency. If direct contact is not possible, index matching must be used to reduce Fresnel reflections [161]. The illumination should be uniform to ensure consistent reflection from all pixels. For that, the beam expansion of the reference must be uniform; otherwise, a scanned laser beam combined with a moving stage can be used [197].

4.6 Conclusion

Pixelated holograms or holographic optical elements are used here to record reflection functions. These help tilt the emission axis and provide efficient coupling, as well as control over the EyeBox properties. This chapter discussed how such reflection functions are encoded.

First, I introduced some key physical elements related to reflection volume Bragg gratings (VBGs). We discussed both angular and spectral selectivity, since our μholograms are passive components that interact with the emission from the waveguides.

I presented several simulations where I compared the PSM model and Kogelnik's coupled-wave theory with numerical RCWA simulations. The PSM is more intuitive and provides excellent agreement with the experimental results. I chose this model particularly for RGB multiplexing (not discussed here). With the PSM (parallel stacked mirrors), we understand that the properties of reflection VBGs arise from reflection and interference processes.

Recording these pixelated holograms requires materials to capture the interference. I discussed the efficiency of the materials we use, namely the photopolymer and the silver halide.

A description of the holographic printer used for recording μholograms with reflection functions was provided. The automation process I developed allows recording of arbitrary reflection angles; however, in this chapter I focused on the recording of a focusing function. The fields reflected by all the μholograms superimpose at a given distance to form a unique diffraction pattern, as expected.

More work is needed to improve the capabilities of the printer by reducing the magnification M and enhancing the alignment process. Currently, the encoding interval angle is 8° ($\pm 4^\circ$). I achieved pixels of size $20\,\mu$m; however, for an offset angle of 35°, a pixel size of $50\,\mu$m was obtained.

Interference is highly sensitive to vibrations. The manufacturing process still has room for improvement, especially in the mechanical stability of the translation stage. This is important for reducing the recording time for a large number of pixels (VGA or more).

We also discussed the replication/hologram copying, which is important for mass production.

Another point, not covered in this chapter, is recording a divergence function for the emission. This was not discussed here and was left for future work. Controlling divergence is important to achieve both efficiency and high luminance.

In the following chapter, we will explore the implementation of the passive display using pixelated holograms in a near-eye display prototype. The goal is to assess its efficiency and provide useful comparisons to highlight the importance of directional displays

Chapter 5

Prototype: Passive Demonstration of Efficiency

Contents

5.1 Introduction and Motivation **145**
5.1.1 Motivation 145
5.1.2 Overall Goal and Results 145
5.1.3 Overview of the Building Blocks 146
5.2 Preliminary Physics: Radiometric/Photometric Notions **148**
5.2.1 Role of Radiometry and Photometry 148
5.2.2 The Fundamental Quantities 149
5.2.3 Intensity and Solid Angle 149
5.2.4 Radiance/Luminance and Étendue 150
5.3 Building Blocks **151**
5.3.1 Passive Display Module 151
5.3.2 LED Collimator 152
5.3.3 Holographic Combiner 152
5.3.4 Beam Splitter 153
5.4 Characterization and Performance **154**
5.4.1 VBG and LED Illumination 155
5.4.2 Holographic Lens Mirror (Combiner) 156
5.4.3 Diffuser 159
5.4.4 Luminance 162
5.4.5 EyeBox 165
5.5 Conclusion **170**

5.1 Introduction and Motivation

5.1.1 Motivation

The objective of this thesis is the development of an efficient microdisplay for near-eye display (NED) applications. Several elements impact the efficiency. The display component itself, characterized by its wall plug efficiency (WPE) and the efficiency of the display within the NED optical system. For the latter, key factors include the transmission of the optics, the coupling efficiency into the entrance pupil, the combiner used, and the efficiency of each subcomponent with respect to field of view (FoV), wavelength, and other system parameters. Efficiency is a key parameter as it affects battery weight, usage time, and thermal management.

If a display generates N photons per second (power). How many of these photons actually reach the retina?

We consider here a typical NED architecture (MagicLeap1), including: LCoS microdisplay, primary source LED, collimating lens, polarizer, PBS (polarizing beam splitter), relay optics, and a diffractive waveguide with exit pupil expansion (EPE). We estimate that only 1 photon of 10 000 reaches the retina. This corresponds to an overall efficiency of 0.01%. About 7% of the light is transmitted in the entrance pupil of the optical system. The losses in the EPE stage are around 0.6% [202, 203]. For more details, we refer to Chapter 1, Section 1.4.1.

EPE is important because it provides a large EyeBox (EB), ensuring comfortable image viewing for different eye pupil positions. It also enables NED to be widely used by people with varying interpupillary distances (IPD). An efficiency of 0.6% is very low, but it comes at the cost of comfort and compactness. To increase it, the EB can be reduced in size; however, to maintain comfortable viewing, an eye-tracking system is required to dynamically position the EB. The author in [204] proposes a Maxwellian-view [34] holographic NED, where eye tracking is used to form the EB by pupil switching.

The other 7% losses are due to the divergence cone of the emission that couples into the optics. We will focus here on this kind of coupling loss.

On a sunny day outdoors, the background luminance ("brightness") reduces the visibility of the virtual image. Therefore, a high luminance of the virtual image (in units of cd/m^2, or nit) is essential for NED applications.

Luminance is proportional to the luminous power and inversely proportional to the Étendue, which depends on the source size and the emission cone. For example, achieving 10 000 cd/m^2 with a 1 cm^2 source requires approximately 1.6 lumen for a 45° emission cone, but only 0.02 lumen for a 5° cone.

For the same luminous power, reducing the emission cone increases the luminance of the virtual image. In this chapter, our objective is to evaluate the importance of this effect. Theoretically, this is straightforward to understand. However, since we are visual beings, an experimental demonstration of this effect can help us better appreciate its impact and drive this research forward. For this reason, we developed a passive demonstration using a simple prototype.

5.1.2 Overall Goal and Results

In this section, I provide an overview of the goals and results of this chapter. Figure 5.1(a) shows an image of the prototype. The NED is monocular and monochromatic (green). The combiner is a simple holographic lens in free-space with a beam splitter. The resolution is low, at 33×33

pixels with a pixel size of 150 μm. The FoV is 6.2°. A smaller pixel size was not used, as the holographic lens exhibits strong aberrations, and the goal was simply to produce a visible virtual image.

The prototype produces a static image. Figure 5.1(b) shows the static display window, where a hologram is pixelated. Upon illumination, the holographic pixels act as "emissive" points. In the lower part, we added a diffuser to increase the divergence of the beam.

Figure 5.1(c) shows some visual rendering under outdoor and indoor conditions. In the directional (low-divergence) upper part of the display, where the word "CEA" appears, the image is brighter. The luminance is approximately 6 times higher than in the lower part, where the word "Leti" is displayed. The diffuser used is not Lambertian; with a Lambertian emitter, we would expect up to 100 times higher luminance.

In this chapter, I will present the characterization of the luminance efficiency, the building blocks, and other characteristics of the prototype.

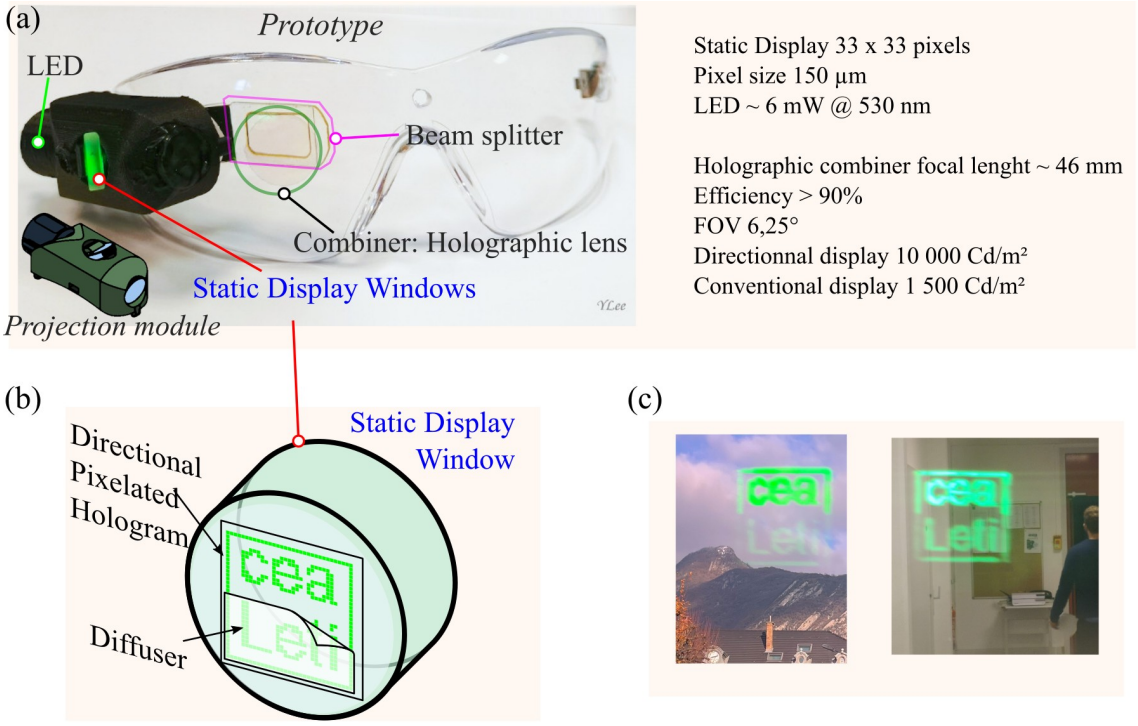

Figure 5.1: (a) Photograph of our monocular prototype. (b) Static windows using pixelated holograms; a diffuser is used to increase the divergence. (c) Visual results in outdoor and indoor conditions.

5.1.3 Overview of the Building Blocks

Figure 5.2(a) shows a schematic of an active prototype with a free-space combiner. This design is the basis of our development and requires a mature photonic integrated circuit (PIC), an active light extraction layer, and a distribution of μholograms (directional display). In the current stage of this research, we build a passive prototype based on the μholograms distribution. Figure 5.2(b) shows its building blocks.

The static display window is illuminated with a green LED source, which is collimated using a holographic off-axis lens (holographic collimator). LED source is not efficient, but, we are only interested in comparing what happens after illumination. Figure 5.2(c) shows a

schematic of the emission divergence. The upper part of the pixelated hologram exhibits a smaller divergence compared to the lower part. The offset angle of $\phi_{ref} = 35°$ is used to avoid specular reflection.

After the static display module, the following building block presented in Figure 5.2(b) is a simple beam splitter. A small portion of the emission is reflected toward the holographic combiner. The latter, which acts as a mirror lens function operating at the recording wavelength, collimates the display light toward the eye. The eye focuses and perceives a virtual image. The beam splitter used is a simple microscope slide cover glass, reflecting only 10% of the light, which is not efficient.

A more efficient configuration without a beam splitter is shown in (a), where the off-axis holographic lens directly collimates the emission toward the eye.This free-space configuration is similar to that of North Focal [102] or Intel Vaunt [103], where a Laser Beam Scanning (LBS) display engine is used. However, the beam splitter remains adequate for a simple demonstration.

Even if the glasses were curved, we successfully recorded a holographic lens on their surface. The building blocks have been selected for their simplicity and off-the-shelf availability. All components were independently developed in a short time. For example, the holographic lens (the combiner), which we recorded for the first time, is not fully optimized, but the main objective was to provide an acceptable visual image and to measure the drop in efficiency.

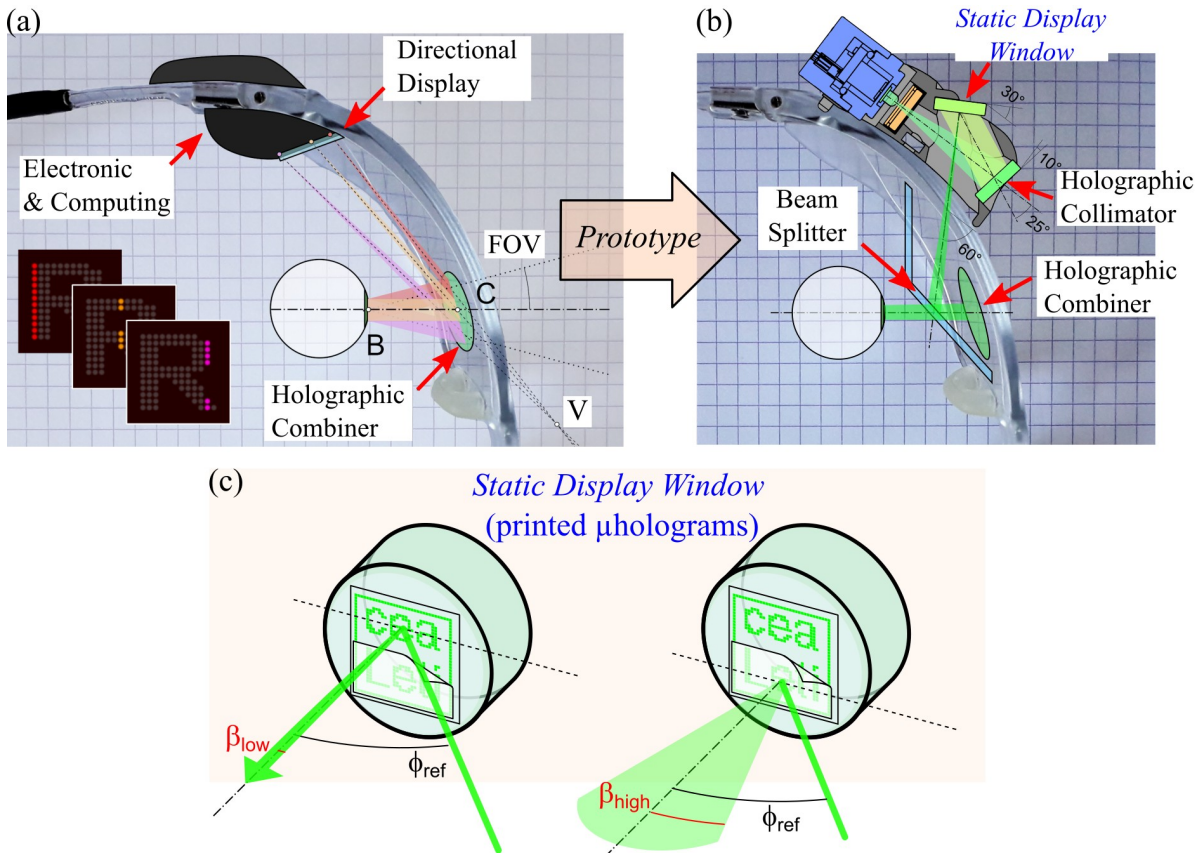

Figure 5.2: (a) Schematic of our future perspective: a directional scanning display (PIC and μholography) in a free-space configuration. (b) Our current NED prototype for comparison between directional and non-directional emission. (c) The static display window incorporating printed μholograms: the upper part is directional with a narrow emission cone, while the lower part is non-directional. The offset illumination is $\phi_{ref} = 35°$.

Prototype Framework and Contributions

This chapter highlights the importance of directional displays and emphasizes the relevance of pursuing our approach using PIC and holography. The prototype was proposed, initiated, and supervised by my supervisor C. Martinez. Other members were involved in building this prototype*. My main contributions are the recording of the static display window, participation in the design, performance analysis, and the synthesis and presentation of the team results.

5.2 Preliminary Physics: Radiometric/Photometric Notions

In the AR community, which brings together researchers and engineers from various fields, there is frequent misuse of certain optical terminology. The most common example is the term "waveguide" instead of "lightguide" when referring to a family of optical combiners. Another example is the use of "brightness" instead of "luminance" even though brightness refers to a subjective perception influenced by viewing conditions. Under indoor conditions, a virtual image may appear brighter than it does outdoors, even if its luminance remains the same. The goal of this section is to recall some rigorous definitions that will be used later.

5.2.1 Role of Radiometry and Photometry

Radiometry deals with the measurement of radiant energy across all wavelengths [205]. The key characteristics involved in radiometric measurements include [206]:

- **Geometric**: the spatial and angular distribution of radiation as it propagates.

- **Spectral**: the wavelength-dependent behavior of emission, transmission, or detection, described as a function of λ.

- **Energetic**: the amount of radiant energy emitted, transmitted, or received.

For example, a diffuser can alter the radiative characteristics of an incident beam. The rays become more divergent, and spectral effects may also occur due to diffraction and refraction.

Photometry is restricted to radiation in the visible region of the spectrum. It is spectrally weighted by the relative spectral sensitivity of the human eye.

The basic unit of power P or flux F (the rate of transfer of energy) in radiometry is the watt (W), while in photometry it is the lumen (lm). For example, 1 watt of radiation at a wavelength of 1.5μm corresponds to 0 lumen, since the human eye can not see infrared radiation.

The relative sensitivity function of the eye, $V(\lambda)$, reaches its maximum at 555 nm under photopic conditions [205]. Photometric quantities are weighted as follows: 1 lumen = $683 \times V(\lambda) \times 1$ W. For example: 1 W at $\lambda = 555$ nm (where $V(555\text{ nm}) = 1$) corresponds to 683 lumen. 1 W at $\lambda = 530$ nm, where $V(530\text{ nm}) = 0.862$, corresponds to 589 lumen under photopic conditions.

Photometry can be a bit confusing, as it uses its own specific terminology, which is conventionally applied (luminous power, illuminance, luminance, luminous intensity). However, the principles and equations are the same for radiometric quantities (power, irradiance, radiance, intensity); it is only a matter of spectral weighting.

*Acknowledgements: To C. Martinez, S. Meunier Della Gatta, Y. Lee, and K. Abdoul-Carime for their contribution.

5.2.2 The Fundamental Quantities

5.2.3 Intensity and Solid Angle

We consider a point source radiating in certain directions as presented in Figure 5.3(a). To calculate the flux at a given position in space that can be collected by an observer (the eye) or a detector with surface area S, we need to know how the radiation, or rays, are distributed in different directions.

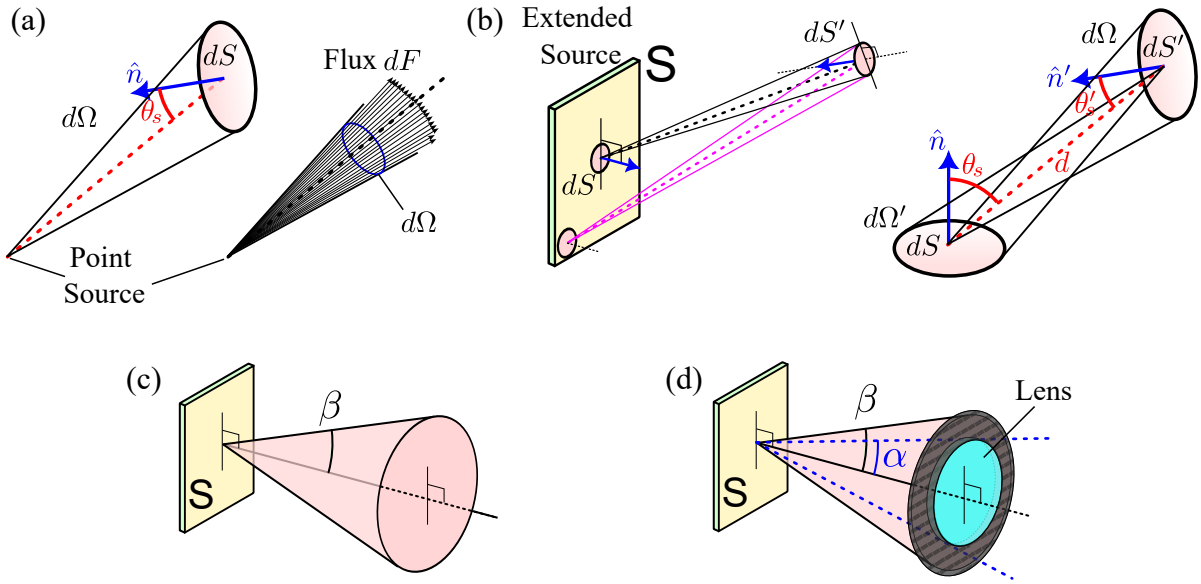

Figure 5.3: (a) Point source and definition of intensity: the flux emitted in a fixed angular direction is defined using the solid angle. (b) Extended source: the flux emitted in an angular direction from an element of the surface is defined using the étendue. (c) Étendue of the emitter: $G = n^2 \pi S \sin^2(\beta)$ if the emitter is spatially uniform and Lambertian in angle (constant luminance). (d) Étendue of the optical system defined by the cone angle α (if $\beta > \alpha$).

Geometric characteristics of radiation involve the use of the solid angle. This quantity is angular and does not depend on position. An element of solid angle $d\Omega$ subtended by a surface element dS in space is defined as follows:

$$d\Omega = \frac{dS \cdot \cos(\theta_s)}{d^2} \tag{5.1}$$

$dS \cdot \cos(\theta_s)$ is the apparent surface area with respect to the point source, θ_s is the angle between the surface normal $\hat{\mathbf{n}}$ and the direction of observation/detection.

The intensity is defined as the flux dF passing through this solid angle element:

$$I(\theta, \phi) = \frac{dF}{d\Omega(\theta, \phi)} \tag{5.2}$$

θ and ϕ describe the angular orientation. They can be considered as the angular coordinates of a unit vector in spherical coordinates.

The radiometric unit of intensity is the watt per steradian ($\mathrm{W \cdot sr^{-1}}$), while the photometric unit is the Candela (Cd).

The solid angle subtended by an aperture (lens, detection window) with respect to a point source is:

$$\Omega = 2\pi\,(1 - \cos(\alpha)) \tag{5.3}$$

α is the cone angle of the aperture with respect to the emission point. This formula, obtained by simple integration, is useful in practice since the detection aperture cannot be infinitesimally small ($d\Omega$). In my case, when measuring the intensity, I can choose $\alpha \approx 0.1°$–$0.4°$. In practice, Ω should be small enough, but too much reduction can decrease the detected flux and increase the noise. On the other side, one should also avoid diffraction effects.

5.2.4 Radiance/Luminance and Étendue

A point source is a theoretical concept, as energy or rays cannot be concentrated at a single point. In practice, sources are extended (Figure 5.3(b)). However, the hypothetical point source is useful and practical when the source is small or far away (for example, a star).

The differential element $d\Omega$ is a useful geometrical quantity for describing the propagation of rays from a point source. Information about the rays is conserved within this solid angle.

For an extended source, we need a similar type of geometrical quantity to describe the conservation of rays both angularly and spatially as illustrated in Figure 5.3(b). This geometrical quantity is the étendue, which is defined as:

$$d^2G = n^2 dS \cdot \cos(\theta_s)\, d\Omega = n^2 dS' \cdot \cos(\theta'_s)\, d\Omega' \tag{5.4}$$

Where n is the refractive index in the medium where étendue is calculated. This quantity is conserved after refraction (snell's law) or reflection.

The luminance of an extended source at the point (x, y) of its surface, in the direction (θ, ϕ), is the flux d^2F per unit element of étendue d^2G:

$$L(x, y, \theta, \phi) = \frac{d^2F}{d^2G(x, y, \theta, \phi)} \tag{5.5}$$

Luminance is a visual quantity; in radiometry, it is called radiance. The radiometric unit of radiance is the watt per square-meter per steradian ($\mathrm{W{\cdot}m^{-2}{\cdot}sr^{-1}}$), while the photometric unit of luminance is the candela per square-meter ($\mathrm{cd/m^2}$).

A common case is an emitter that is uniform and Lambertian, for which $L(x, y, \theta, \phi) = L_0$. Uniform means that the dependence on x and y is dropped, and Lambertian means equal luminance in all directions. In this case, the emitted flux or power can be obtained simply by integrating the element of étendue over the surface S and the emission cone β (Figure 5.3(c)).

$$G = n^2\,\pi\,S \cdot \sin^2(\beta) \tag{5.6}$$

For a typical Lambertian LED source, the emission cone is wide, with $\beta = 90°$. We consider an emitter with an area of 1 $\mathrm{cm^2}$ and an optical power of 1 mW. IT corresponds to a luminous power of $F = 0.59$ lumen at a wavelength of 530 nm. If the emission cone of the emitter is $\beta = 90°$, the luminance is $L_0 = F/G = 1\,874$ $\mathrm{cd/m^2}$. If $\beta = 15°$, then $L_0 = 27\,976$ $\mathrm{cd/m^2}$.

Typical values of luminance ($\mathrm{cd/m^2}$) are: 250 for a computer monitor, 150 for paper under office lighting, 5 000 for a blue sky, and 10 000 on a typical summer day. We note that: (1 nit = 1 $\mathrm{cd/m^2}$).

The eye is sensitive to luminance (illuminance on the retina is proportional to luminance). For this reason, the luminance of the virtual image must be at the same level as that of the outside scene.

If the optical system has an acceptance cone angle α smaller than the emission cone β, we use the étendue of the optical system by replacing β with α (Figure 5.3(d)). The flux collected by the optical system is simply the étendue of the optical system multiplied by the luminance of the object L_0 (assuming it is uniform and Lambertian within the acceptance cone α).

The efficiency of power coupling is in this case simply the ratio between the optical system étendue and the emitter étendue:

$$\eta = \frac{\sin^2(\alpha)}{\sin^2(\beta)} \tag{5.7}$$

Étendue is an important concept, especially its conservation within a lossless optical system (no absorption, no scattering, assuming zero Fresnel reflection). We can note that the conservation of étendue as a geometrical quantity is often confused with the conservation of luminance. For example, interference can change the distribution of ray density over a surface, so luminance is not always conserved. For more details about étendue and its conservation, see Koshel [207].

5.3 Building Blocks

In this section, I provide details on the building blocks of the prototype: the passive display module, the holographic LED collimator, the holographic combiner, and the beam splitter.

5.3.1 Passive Display Module

The display module is a static/passive display window. It contains holographic pixels that are recorded by the holographic printer (see previous chapter).

Figure 5.4(a) shows examples of the printed passive display. The pixel size is set to 150 μm. A smaller pixel size was not chosen because the recorded holographic lens (combiner) has a low modulation transfer function (MTF). This will be discussed in the characterization and performance section 5.4.2. The offset angle is fixed at $\phi_{\text{ref}} = 35°$.

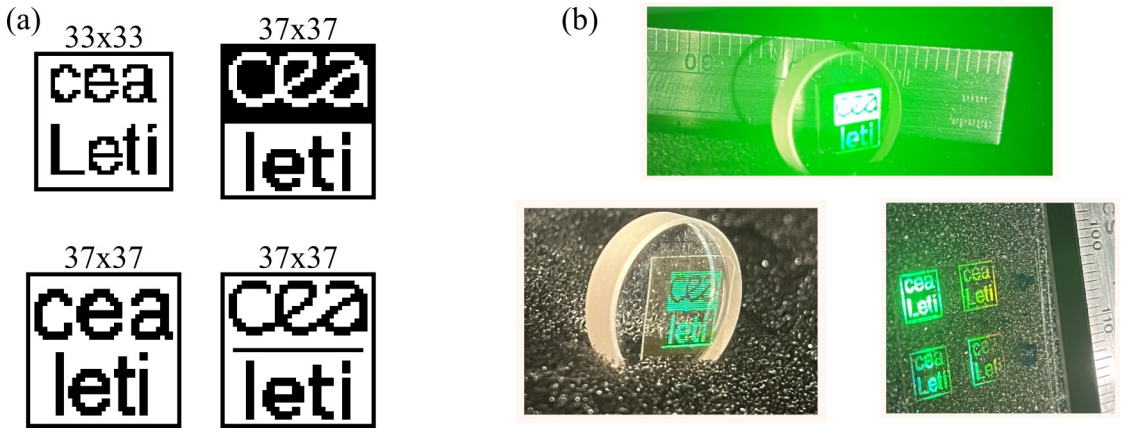

Figure 5.4: (a) Example images to be encoded as holographic pixels by the holographic printer. (b) Results of the holographic images used as passive display module.

Figure 5.4(b) shows photographs of the passive display module. The recorded holographic display is transferred from a microscope slide onto a rounded glass substrate. A photopolymer and a laser at 0.532 μm wavelength are used. Other wavelengths, such as 0.640 μm, have also been employed. Here, we focus on the results at the green wavelength 0.532 μm.

5.3.2 LED Collimator

The display is passive. The holographic pixels are illuminated by a green LED (Thorlabs LED528EHP) with a half-angle divergence of = 9° and a spectral FWHM of 35 nm. This LED is first collimated using a holographic collimator. The function of the collimator is illustrated in Figure 5.5(a). The LED is represented as a point. The direction of illumination and the point are separated to avoid obstruction of the illumination.

Figure 5.5(b) shows the recording process of this holographic collimator. We record the interference between a collimated reference beam and point source as an object. The reference is at 25° from the optical axis. The object is an image of an optical fiber. The substrate is tilted at 10°.

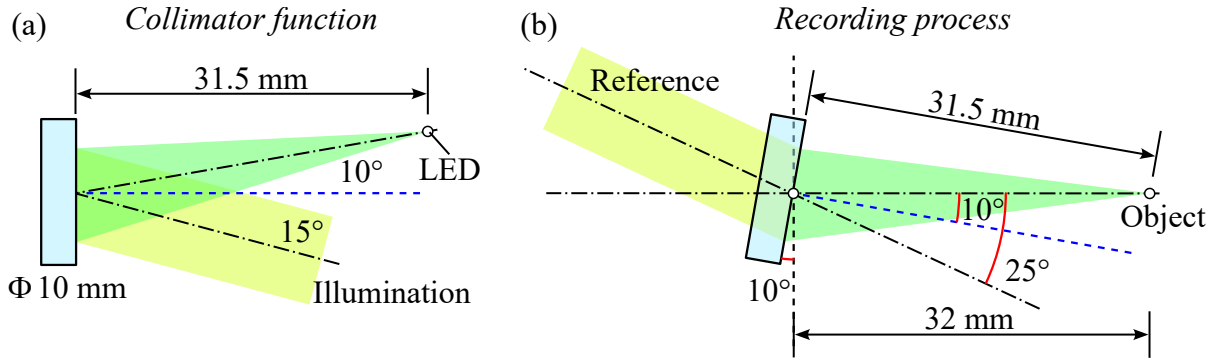

Figure 5.5: (a) LED collimator function recorded as a holographic function in reflection (Holographic Collimator). (b) The recording process.

We have to note that an LED source is spectrally broader than a laser source. Illumination of a volume Bragg grating with an LED will be discussed separately later, which will be helpful to understand the divergence β of the holographic pixel.

5.3.3 Holographic Combiner

The combiner is an element that combines the outside view with the overlaid virtual image. For the combiner, we chose to record a holographic lens function on a photopolymer. This mirror lens is spectrally selective at the recording wavelength. This means it is transparent over most of the visible spectrum. The combiner function is implemented simply by placing the lens in front of the eye. The display field is collimated toward the eye and combined with the transmitted rays from outside.

Figure 5.6(a) shows a photograph of the experimental setup. The photopolymer is cut into a circular shape and laminated onto the curved surface. We succeeded in laminating the film onto the curved surface without air bubbles. This was made possible by a heating process.

The glasses are positioned between a collimated reference beam and an object point source beam. The object is produced by imaging the optical fiber. The object and the reference must

have closely equal irradiance, which must also be uniform over the recording area. This is important to ensure an efficient reflection recording over the surface of the lens.

Figure 5.6(b) shows a schematic of the recording process. The distance between the object and the photopolymer determines the focal length. Figure 5.6(c) shows a close-up photograph of the glasses and the holographic lens. The lens is tilted at an angle of about 16–17°, which has some drawbacks.

Indeed, the tilt increases the aberrations of the lens, especially astigmatism. Astigmatism arises from the difference between the convergence of the sagittal rays (rays in the yz plane) and the tangential rays (rays in the xz plane). As shown in Figure 5.6(b), the rotational symmetry of the recording decreases with tilt. To correct this for the given tilt value, one could use a calculated cylindrical lens, or a lens with two different radii in the sagittal and tangential directions [208], or use an SLM to correct the wavefront directly. Since this is the first holographic lens we recorded, and given that the objective was not to improve the prototype but to have a functional model for comparing luminance, we did not address this aspect.

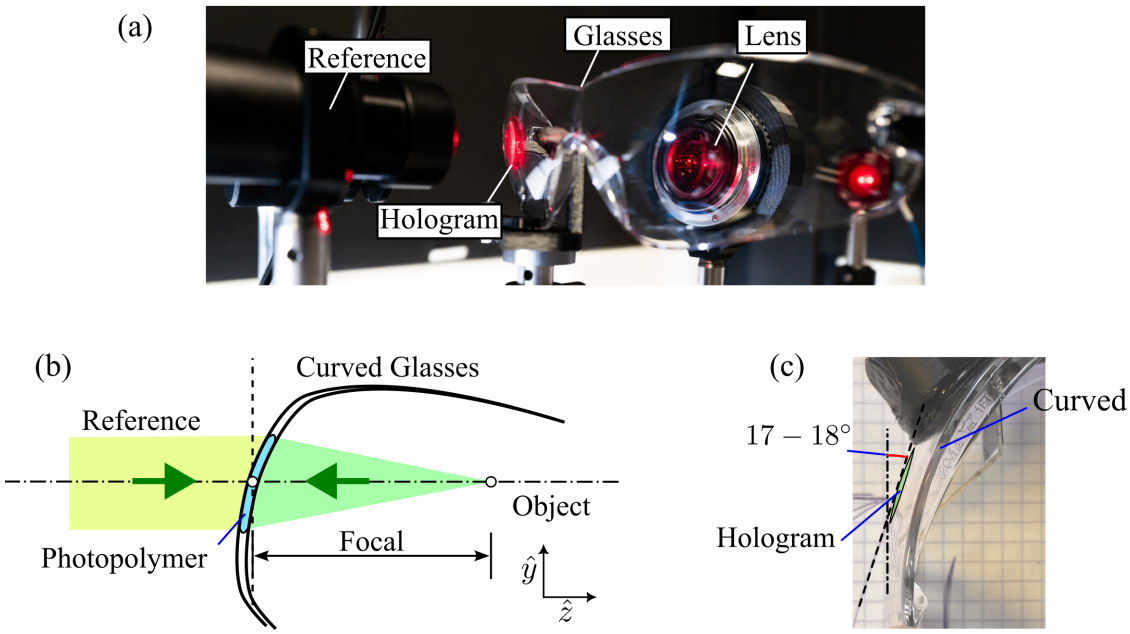

Figure 5.6: (a) Photograph of the recording setup for the holographic combiner (Photo credit: A.Aubert/CEA). (b) Schematic of the recording process. (c) Close-up photograph of the holographic film on the curved surface of the glasses.

5.3.4 Beam Splitter

A simple off the shelf beam splitter is a glass plate. We used a cover-slip (cover glass) as a beam splitter, with a thickness of around 130–170 μm. A glass plate consists of two parallel surfaces. Ideally, one surface should be anti-reflection coated to avoid secondary reflections.

In Figure 5.7(a), the beam splitter acts as a tilted mirror. The object is mirrored twice by the two parallel surfaces, with a shift in the y and z directions. The shift is directly related to the plate thickness and the angle θ.

One image is on the optical axis, and the other is slightly shifted. This is called a ghost image, as the holographic lens (combiner) sees two displays instead of one. We note that a

beam splitter is not efficient; only a fraction of the emission, around 10%, is reflected toward the combiner.

After collimation toward the eye, the viewer will perceive a doubling of the image: the intended image and the ghost image. The ghost image can be slightly off-axis and slightly out of focus. This means that the ghost image will be slightly aberrated. The extent of this aberration depends on the thickness of the plate.

Our pixel size is 150 μm. If we consider the same configuration as shown in (a) with $\theta = 45°$, the shift is 184 μm. In the prototype, the angle is about $\theta = 53°$, and the shift is 163 μm. Which is around a pixel size.

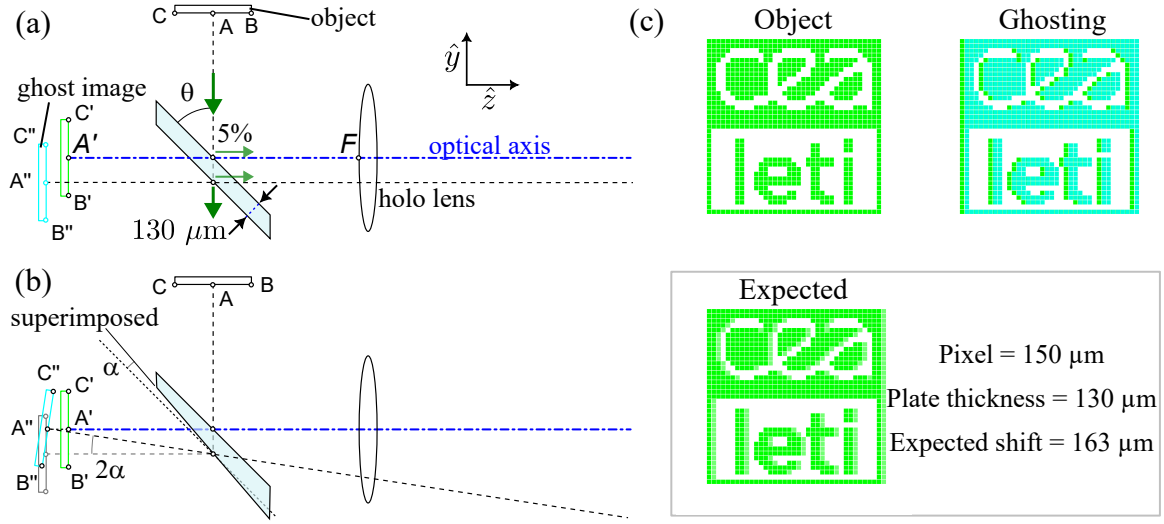

Figure 5.7: (a) Beam splitter showing reflections from the two surfaces and the resulting ghost image. (b) Wedge plate for correcting the ghost image, shown as a perspective approach. (c) Simulated expected visual result showing the ghost image shifted horizontally by 163 μm.

Figure 5.7(b) shows a perspective approach for correcting this shift by superimposing the ghost image. However, the ghost image remains slightly out of focus with respect to the focal plane. This is called a wedge plate. This configuration is only a perspective and has not been implemented.

Figure 5.7(c) shows a simulated ghost image. The object in green is superimposed on a blue ghost image. The latter is shifted horizontally by 163 μm. In the lower part of the figure, we show the expected visual rendering. Interestingly, the offset between the image and the ghost does not significantly impact the rendering, it mainly modifies the original font of the image.

5.4 Characterization and Performance

This section presents the characterization results. First, I explain the divergence results obtained when illuminating a volume Bragg grating (VBG) with an LED source. Then, I present the combiner results, followed by the characterization of the diffuser using a goniometer in reflection. The luminance results are provided with analysis and explanations. Finally, I present the results concerning the EyeBox (EB).

5.4.1 VBG and LED Illumination

In Figure 5.8(a) and (b), a mirror is illuminated with an LED source of divergence β. The mirror reflects light with the same divergence. In (c) and (d), the same LED source is used to illuminate a VBG. If the LED source is spectrally wide, the central reflection corresponds to the recording wavelength, determined by the spectral selectivity of the VBG. As the angle increases, other wavelengths (blue-shifted) satisfy the Bragg condition and are reflected. The reflected cone is therefore not uniform. The reflected divergence is lower than or equal to β. It equals β only when, at this angle, there is a wavelength within the source spectrum that satisfies the Bragg condition.

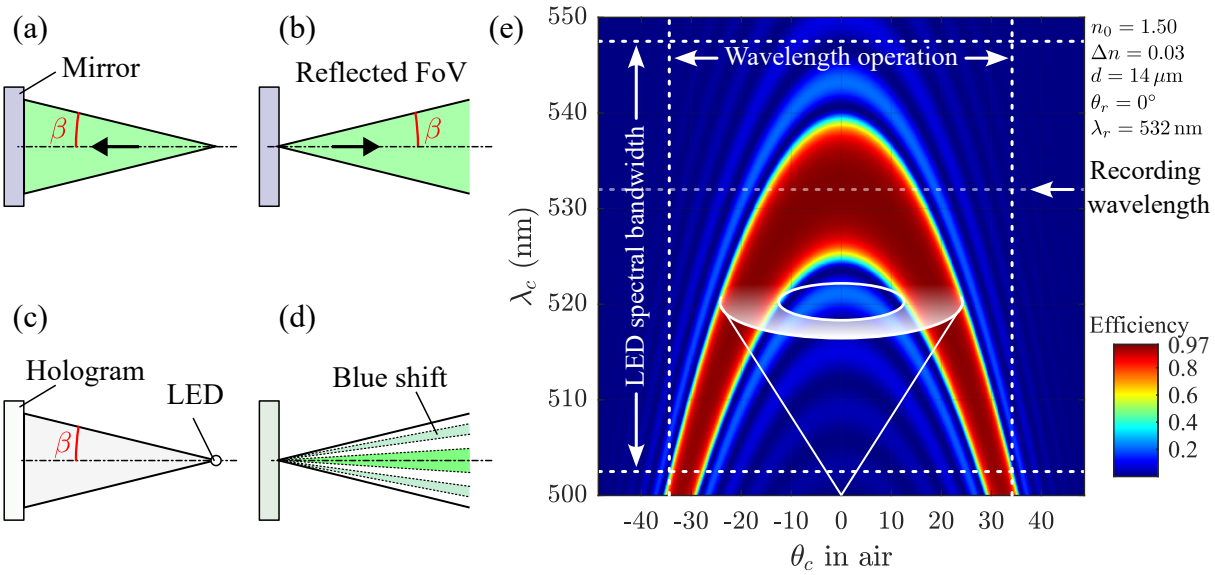

Figure 5.8: (a) Mirror with an incident divergence β. (b) The mirror conserves β. (c) Incident divergence β on an unslanted VBG in reflection. VBG acts as a "mirror", but It is wavelength dependent. (d) Depending on the spectral bandwidth of the LED and within β, the Bragg condition (angle–wavelength dependence) must be considered. In the maximum case, the reflected divergence is equal to β. (e) Spectral selectivity of an unslanted VBG: reading wavelength versus reading angle.

Figure 5.8(e) shows the selectivity of an unslanted VBG. The red zone corresponds to the maximum efficiency. The recording wavelength is 0.532 μm. A horizontal cut at this wavelength gives the angular selectivity. Higher wavelengths > 0.540 μm do not satisfy the Bragg condition, while lower wavelengths satisfy it but at angles different from the normal (0°).

This figure represents only the angle in one plane. In 3D, the angles that satisfy the Bragg condition are degenerate and form a cone, which I illustrate with the donut-shaped drawing.

Vertically, the spectral bandwidth of the green LED (Thorlabs LED528EHP) is shown. Depending on the incident angle and the LED divergence, the operating wavelength is restricted to the range between the horizontal dashed lines.

For a slanted VBG, the tip of the selectivity curve extends to higher wavelengths and shifts angularly relative to the grating normal.

The collimator is a slanted VBG. The slant varies with position, as it encodes a lens function. In Figure 5.9(a), a schematic of the collimator is shown. The LED source is spatially extended. Taking into account the diameter of the source and the focal length of the collimator, the expected divergence after collimation is about $2\beta \approx 4.5°$.

Figure 5.9(b) shows the selectivity of a slanted VBG. The plot corresponds to the central slant of the collimator (along the optical axis). A ray incident at 10° and at the recording wavelength is reflected at 15°.

Taking into account the extent of the source and the resulting incident 2β, we draw an interval around 10° together with the corresponding wavelength range. This interval lies within the LED spectral bandwidth. The collimator is expected to reflect only this portion.

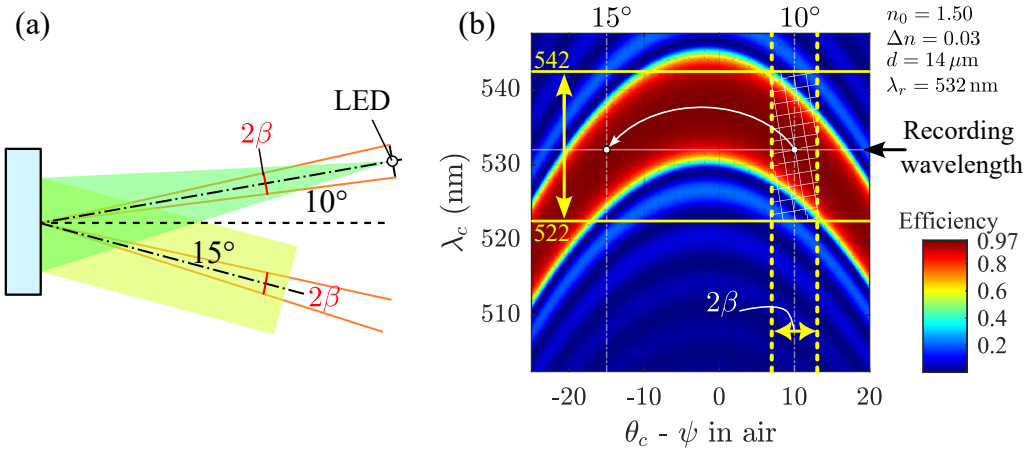

Figure 5.9: (a) The LED is an extended source. The collimator produces an illumination with divergence β. (b) Spectral selectivity of the central part of the collimator which is a slanted VBG.

5.4.2 Holographic Lens Mirror (Combiner)

In the recording process of a hologram, it is important to balance the irradiances of the object (E_o) and the reference (E_r) over the area of interest. The fringe visibility, $V = 2\sqrt{E_o E_r}/(E_o + E_r)$, describes the peak-to-valley modulation of the interference pattern. This is transferred directly into a modulation of the refractive index Δn. A higher Δn leads to a higher reflection efficiency. Ideally, $V = 1$ is desirable over the full area of interest.

For the holographic lens, the interference occurs between a collimated reference beam and the optical fiber acting as a point source. Both exhibit Gaussian distributions but with different waists. Figure 5.10(a) illustrates the irradiances of the reference and the object on the recording medium. The right y-axis shows an illustration of the expected efficiency. The hologram does not form in regions where the irradiance imbalance is significant. Note that the exposure time is also important: In regions where the object irradiance is lower, a longer exposure is needed. However, near $x = 0$ where the irradiance is the highest; overexposure can slightly reduce efficiency.

Exposure and fringe visibility are important when the objective is to achieve uniform efficiency. To overcome this challenge, pixelating the recording process can help to obtain uniform efficiency by balancing the irradiance at different positions. This was not the focus of this thesis.

Figure 5.10(b), (c), and (d) show the spatial efficiency of the three holographic lenses recorded with an exposure time from 4 s to 8 s. The average irradiance of the object and the reference beams is about 5 mW/cm^2. This average is measured over a circular area of approximately 1 cm^2 in diameter. The maximum efficiency η is depicted in each figure.

Increasing the exposure time increases the radius of the hologram. In (d), the highest efficiency takes an annular shape as the center is overexposed.

Outside the high-efficiency section of the lens, the efficiency varies between 0–20%. These variations correspond to holograms recorded between the incident reference and its Fresnel parasitic reflection (Lippmann hologram). Although their efficiency is low, it can be significant in contexts where the treatment of stray light is critical.

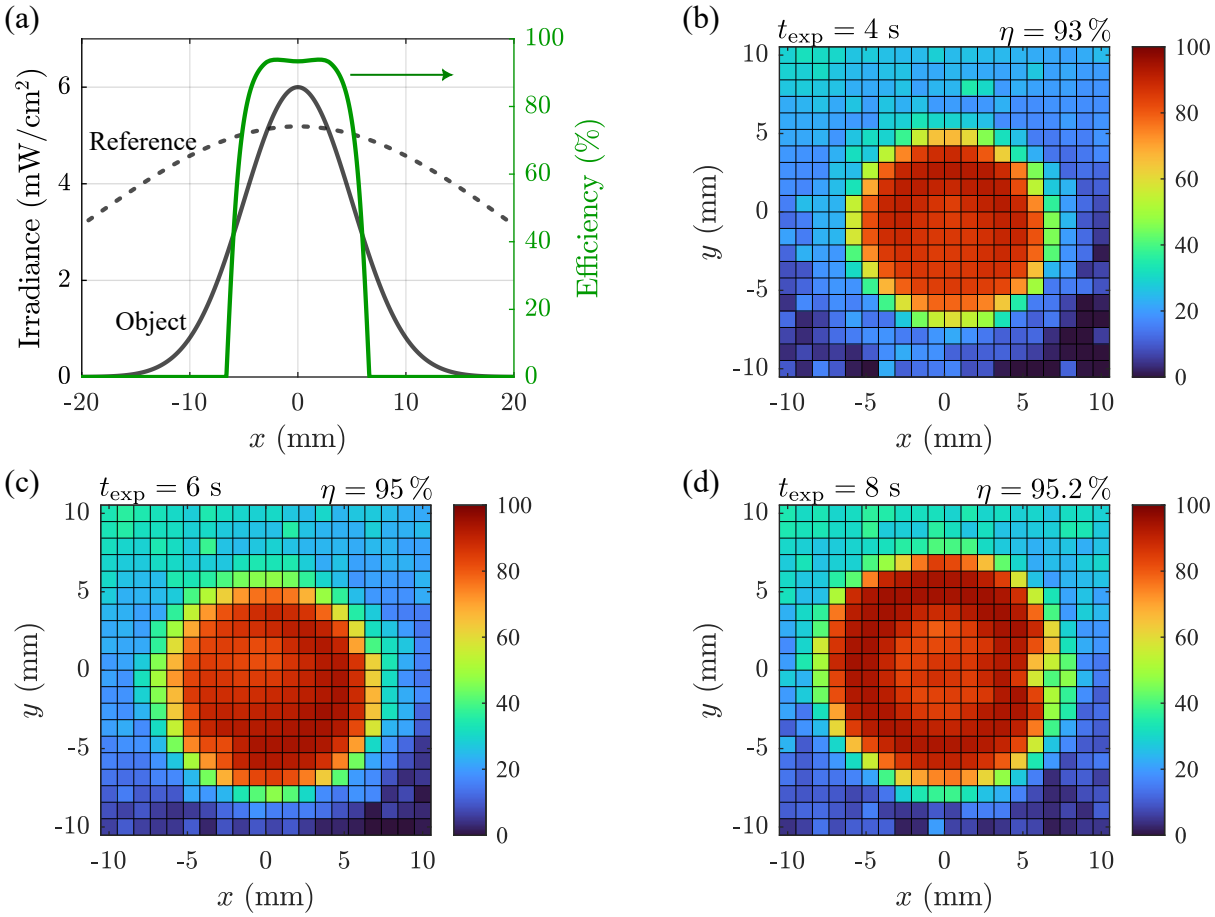

Figure 5.10: (a) Irradiance distribution difference between the reference and the object, and the impact on the effective recorded section. (b) Reflection efficiency map of our holographic lens for an exposure time of 4 s. (c) Results for exposure time of 6 s. (d) Results for exposure time of 8 s. The average irradiance is 5 mW/cm^2.

After recording, the holographic combiner was tested with the prototype. I conducted visual testing to ensure that the virtual image appeared at infinity. The theoretical focal length was $f = 50$ mm; however, a position error led to a final recorded focal length of $f = 46$ mm. The position of the virtual image was determined using a simple camera with auto/manual focus (iDS μEye XS). After calibrating the focus parameters with a scene of known position, the virtual image location was found. A focal length of $f = 46$ mm corresponds to an image distance of about ≥ 2 m.

As discussed in Section 5.3.4, a ghost image is expected due to the beam splitter thickness. In the following, I discuss only the imaging performance of the holographic combiner. First, let us recall the importance of the MTF. The MTF provides a quantitative measure of the smallest details the lens can resolve (here the pixel). It is usually expressed as a contrast value between 0 and 1 at a given spatial frequency (cycles/mm or line pairs/mm). The spatial frequency

corresponding to a display pixel size of 10 μm is $\frac{1}{2\times10\ \mu\text{m}}$ = 50 cycles/mm, which is the Nyquist frequency [209]. For a pixel size of 150 μm, the Nyquist frequency is 3.33 cycles/mm. The MTF contrast ranges between 0 and 1. A common resolution criterion is MTF contrast greater than > 30%, at the maximum frequency of interest [4, 209].

In Figure 5.11(a), I recall the recording process: the holographic film is tilted on the curved glass. The loss of rotational symmetry around the optical axis increases the off-axis aberrations.

In Figure 5.11(b), I show a simulated image using a holographic lens at 0° tilt. In this simulation, the beam splitter is not included. To the right, experimental virtual image I captured with the camera. The lower part of the image has a low luminance due to the use of a diffuser. Because the beam splitter ghost image is shifted horizontally, the resolution is better in the vertical direction than in the horizontal direction. Below in Figure 5.11(b), I present simulated images that include other tilt angles as well as the ghost image.

In Figure 5.11(c), the MTF results of the axial field simulated using Zemax OpticStudio® (hologram ray-tracing method can be found here [210, 211]). The modulation is plotted for different tilt angles: 0°, 10°, and 17°. The MTF of the solid and dashed lines correspond to the spatial frequencies in the tangential (vertical) and sagittal (horizontal) directions, respectively.

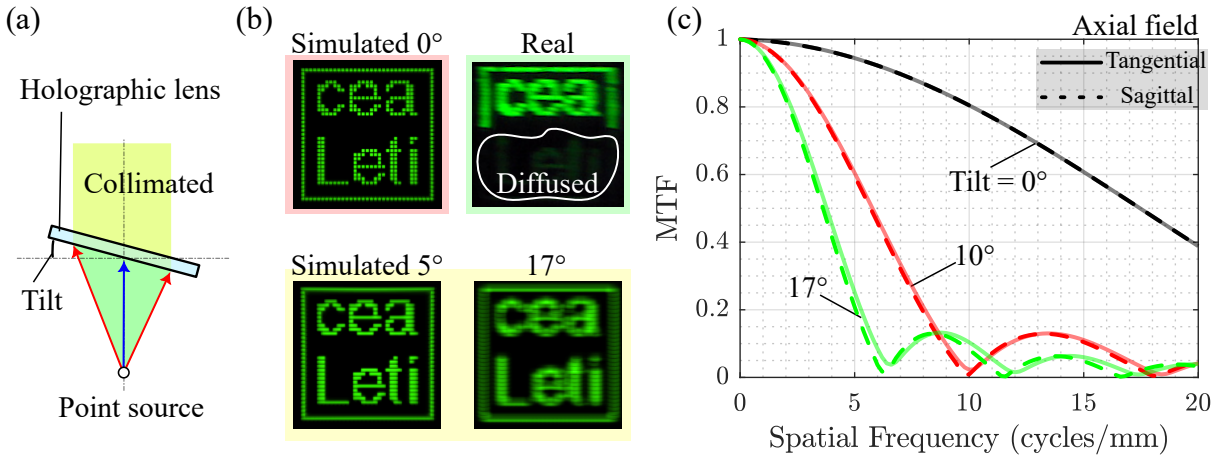

Figure 5.11: (a) Tilt of the holographic film caused by the curved glass during the recording process. (b) Simulated image at 0° tilt without considering the beam splitter. On the right, the real image of the prototype. Below, two simulations at 5° and 17° tilt with the consideration of the ghost image. (c) MTF simulation of the holographic lens.

The simulated holographic lens has a diameter of 20 mm and a focal length of 50 mm, corresponding to a fast lens ($f/2.5$). The MTF decreases with tilt; in our case, the tilt is about 17°. If we set the MTF criterion at a contrast of 0.4, the maximum resolution is about 4 cycles/mm (corresponding to a Nyquist pixel size of 125 μm). This value is only slightly above the required frequency of 3.33 cycles/mm to resolve our 150 μm pixels.

In this MTF simulation, I did not consider the ghost image from the beam splitter or the aberrations of the recording process. However, the curve remains consistent with the experimental results, since we observed a slightly blurred image for a pixel size of 150 μm. For future developments, it will be necessary to correct these aberrations, as the pixel size could be reduced to 20 μm or smaller. We also have to note that in this simulation only the axial field is presented. The off-axis field shows a lower MTF, and the sagittal and tangential curves do not overlap, which indicates the presence of astigmatism.

For the purpose of demonstrating a functional prototype with two images of different divergence, the aberrations caused by the holographic lens and the beam splitter are not critical. The image is visible and the letters are distinguishable, which is sufficient.

5.4.3 Diffuser

Diffuser Choice

The holographic pixels were illuminated with a full divergence of $2\beta \approx 4.5°$. This value accounts only for the extent of the LED source; however, mechanical errors in the positioning of the LED and in the focal plane of the collimator are possible. The measured full divergence after collimation was $2\beta \approx 8$–$9°$ in practice. Based on the LED spectral bandwidth, we will assume that the holographic pixels have a divergence of $\beta \approx 4$–$4.5°$.

We increase the divergence of the lower part of the pixels by introducing a diffuser. Initially, for comparison with micro-LED emission, we considered using a Lambertian diffuser. However, this would have reduced the luminance by a factor of 100. For a more reasonable comparison, we chose a diffuser with a narrower cone.

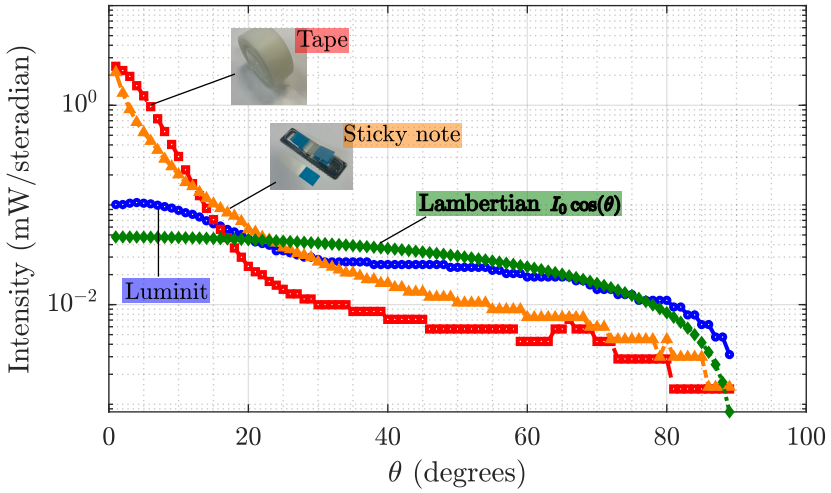

Figure 5.12: Experimentally measured intensity profiles of different diffusers

Figure 5.12 shows experimental results of the intensity distribution for several diffusers. The green curve corresponds to a theoretical Lambertian profile, while the blue curve represents a Luminit diffuser[†], this diffuser has a 40° as half-FWHM when its surface faces the light source. In my case, I used it in the opposite direction, resulting in a half-FWHM of around 20°.

I also show the diffusing profiles of simple office materials, such as adhesive tape and a sticky note. The sticky note and the tape exhibit a narrow diffusing profile. The **Sticky note** was the final choice used to increase the divergence of the pixel emission. It offers suitable diffuser characteristics and is convenient to use, as it comes with an adhesive layer. Note that all these diffusing profiles have been calibrated to provide the same total power, which is around 150 μW.

[†] https://luminitco.com/wp-content/uploads/2015/11/Luminit_Technical_datasheet.pdf

Further Characterization and Effect of Hologram Reflection

The characterization setup is a retro-goniometer, which can be used either in reflection or in transmission. The results shown in Figure 5.12 were measured in transmission. A collimated laser beam at 0.513 μm is used. The sample holder with the source rotates around the center of diffusion. A diaphragm aperture of diameter D and a focusing lens are placed in front of a power detector. The distance between the diaphragm and the center of the diffuser is denoted by r. The diaphragm subtends an angle $\delta_{\text{det}} = \arctan\left(\frac{D}{2r}\right)$ with respect to the diffuser.

Following the definition of intensity and solid angle, the total power P_{total} is obtained by integrating the detected power over the solid angle:

$$P_{\text{total}} = \int I(\theta, \phi) d\Omega = 2\pi \int_0^{\theta_{\max}} \frac{P_{\text{det}}(\theta)}{\Omega_{\text{det}}} \sin\theta \, d\theta \tag{5.8}$$

In practice, the angular scan is discrete, and the total power is expressed as a sum over the Q measurements:

$$P_{\text{total}} \approx \sum_{i=0}^{Q-1} \frac{P_{\text{det}}(i) \ \sin(i \times \Delta\theta) \, \Delta\theta}{1 - \cos(\delta_{\text{det}})} \tag{5.9}$$

Measuring the intensity profile and integrating according to formula (5.9) gives the transmitted power. The incident power is measured directly. This measurement gives the transmission value of the film. For example, for the sticky note we obtained a transmission of $T = 84.8\%$.

Further characterizations have been made on the sticky note diffuser in transmission and reflection modes. Figure 5.13(a) shows a schematic of direct transmission measurement without the diffuser. (b) shows a schematic of the measurement in transmission. (c) a schematic in reflection using a mirror. (d) a schematic of the measurement using a hologram. We note how a hologram and a mirror differ: with a mirror in (c) we measure the specular reflection.

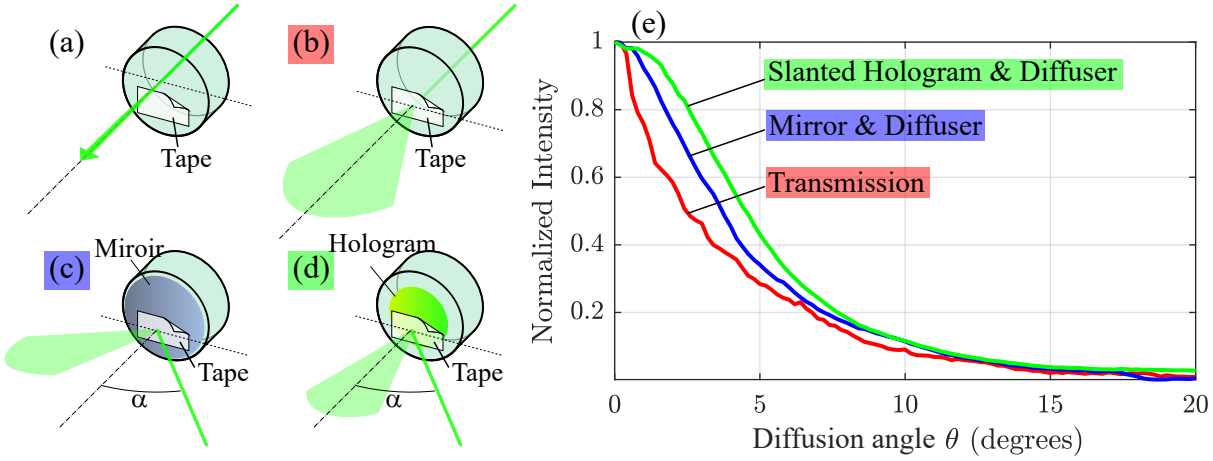

Figure 5.13: (a), (b), (c) and (d) are schematics of different measurement configurations. (e) Corresponding experimental diffusion profile of the sticky note.

Figure 5.13(e) shows the experimental intensity results. The angular width of the diffusion with a reflection hologram is slightly larger than with a mirror, and both are slightly larger than in transmission. For the mirror measurement, the incident angle is $\alpha = 0°$. For hologram

measurement, since the offset angle during recording at $\lambda = 0.532\ \mu$m is $\phi_{\text{ref}} = 35°$, the reconstruction angle used is $\alpha = 41°$, because the reconstruction wavelength is $\lambda = 0.513\ \mu$m.

Diffusing characteristics are angularly dependent. For example, Figure 5.14 shows the intensity results of the sticky note at different incident angles α. On the left, the raw results are plotted. On the right, the results are normalized and centered around 0°. As the incident angle increases, the width of the diffusion also increases.

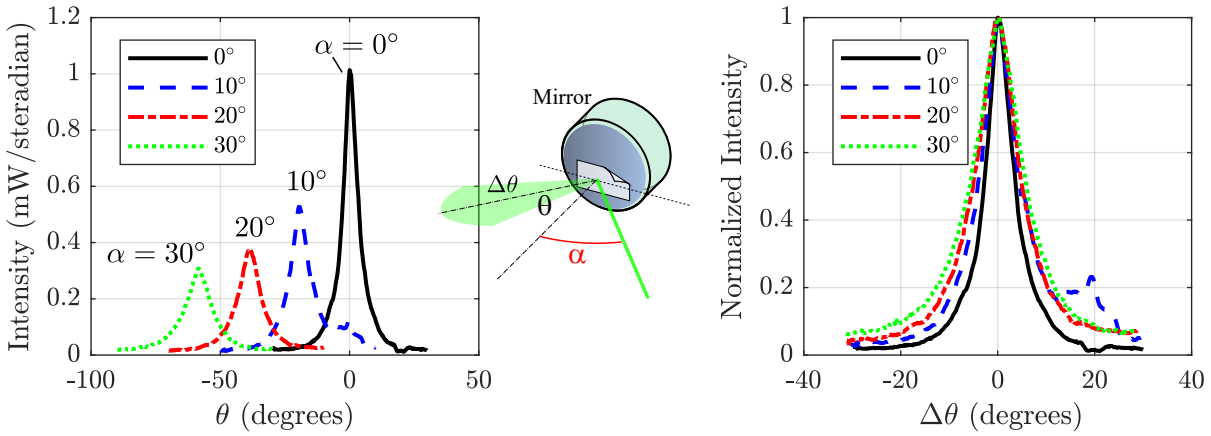

Figure 5.14: (a) Intensity profile as the incident angle increases. (b) The measurements are normalized and centered.

The measurements were performed with a monochromatic collimated beam. These results can be considered as the impulse response. If the incident beam has a full angular divergence of 2β, the diffusing angle can be estimated as the convolution of the impulse response with a window of width 2β.

2D analysis

Figure 5.15(a) shows the results of diffusion using a reflection hologram at a 41° incident angle.

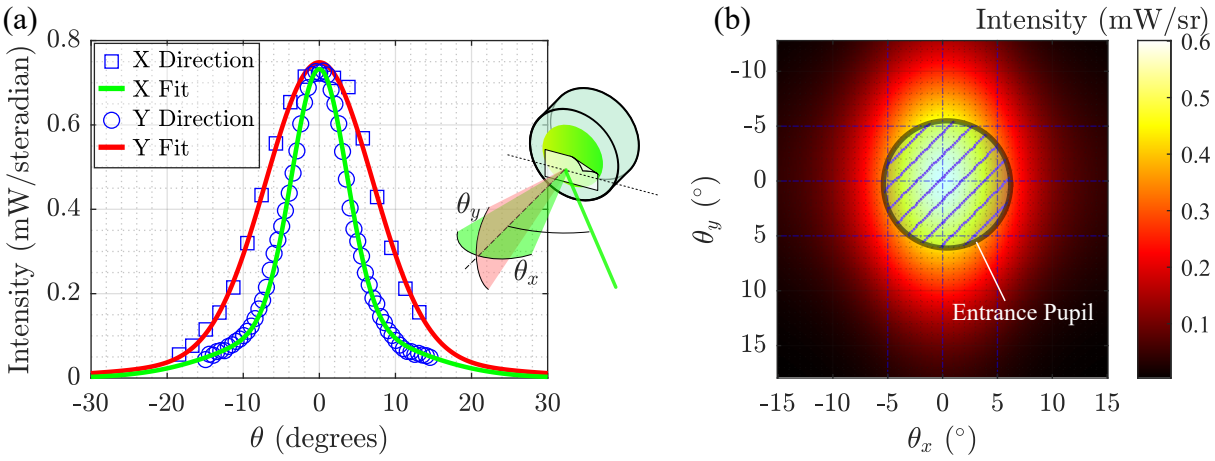

Figure 5.15: (a) Intensity profiles in both directions for the diffuser with the hologram. The incident angle is 41° at a wavelength of 0.513 μm. (b) The fitted results are used to plot the 2D intensity profile, assuming $I(\theta_x, \theta_y) = I(\theta_x) \cdot I(\theta_y)$.

The diffusion profile is not symmetric due to the large incident angle. The horizontal (X) data were measured by automatic acquisition, while the vertical (Y) data were obtained by manually varying the detector height. The results are fitted with two Gaussian functions: one to capture the narrow peak and another to model the broader background.

To produce a 2D profile of the diffusion, I assume that the 2D intensity can be written as the product of the horizontal and vertical contributions: $I(\theta_x, \theta_y) = I(\theta_x) \cdot I(\theta_y)$. This is plotted in Figure 5.15(b). The intensity profile is convolved with a window of width $2\beta = 9°$. The figure provides an estimate of the expected divergence profile from a holographic pixel with the diffuser. In our prototype, an aperture limits the captured flux and reduce the luminance, which will be discussed later.

5.4.4 Luminance

The goal is to compare the drop in luminance/efficiency when the pixels are diffused with the sticky note. Figure 5.16(a) shows the visual rendering under outdoor conditions. This provides a good fidelity representation of the visual rendering one can experience when looking through the prototype. To capture this photograph, I simply used my smartphone with the camera positioned at the eye location. The upper image appears brighter and is clearly visible compared to the diffused lower part. Figure 5.16(b) shows the visual results of an actual product, the Vuzix Z100, which uses a JBD monochrome micro-LED projector module as a light engine. Note how, relative to background luminance, the visual content appears either visible or washed out.

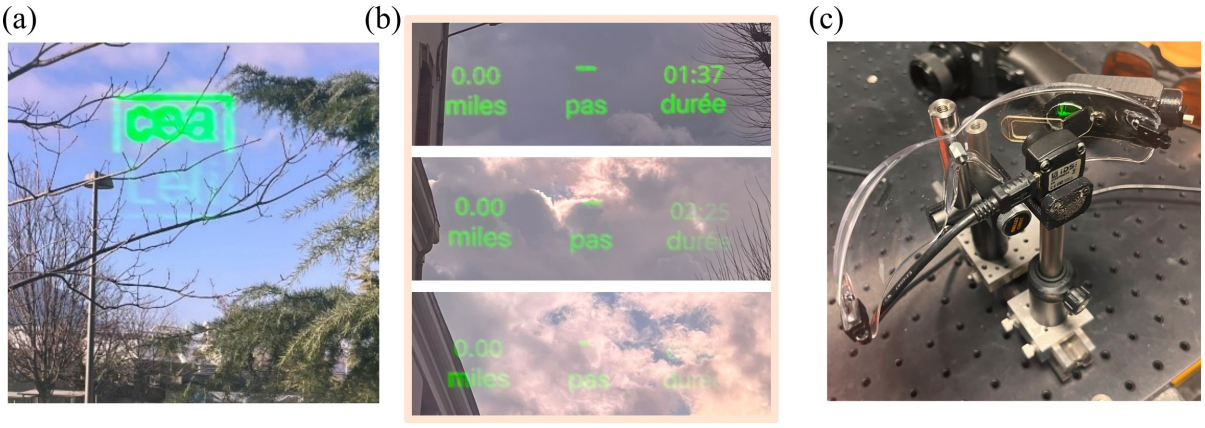

Figure 5.16: (a) Visual result of our virtual image with the sky as background. (b) Visual result of an actual product, the Vuzix Z100. The glasses are tinted, with a transmission of 24%. (c) Photographs of the experimental setup of our prototype and a camera.

We can define a relevant metric for the required luminance compared to the background. This quantity is the contrast ratio (CR) [212]:

$$CR = 1 + \frac{\text{Display Luminance}}{\text{Real World Apparent Luminance}} \tag{5.10}$$

A CR of 1.2 can be set as a minimum requirement for AR applications [25]. In Equation (5.10), the term "apparent" is important, since the transmission of the glasses can be low (tinted), thereby reducing the required display luminance.

Figure 5.16(c) shows a photograph of the experimental setup. The main tools for characterization are an iDS μEye XS camera and a luminance meter.

Figure 5.17(a) presents a schematic of the setup. A high-power Mightex LED at 0.530 μm is used to illuminate a 80° Luminit diffuser, producing a green background. The prototype is positioned in front of this background and the virtual image is overlaid with it. The background luminance is controlled by moving the high-power LED closer or farther away. The virtual image becomes washed out within the background as the luminance increases. A luminance meter was used to measure these values. We conducted this experiment with colleagues from the lab of different ages and sexes.

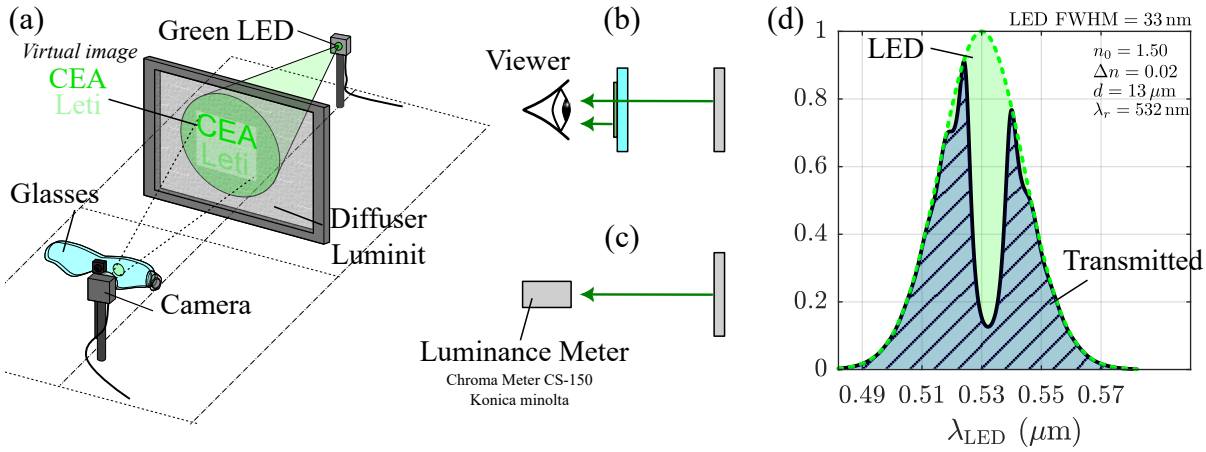

Figure 5.17: (a) Schematic setup for measuring luminance: a background scene with variable luminance helps wash out the virtual image. (b) Schematic of the viewing: the background luminance is reduced by the transmission of the glasses. (c) Schematic of the luminance meter used to measure the background luminance. (d) Spectral Gaussian profile of the LED; the hashed region indicates the transmitted spectral portion through the holographic lens.

Figure 5.17(b) shows a schematic of the eye with rays from both the combiner and the outside overlaid. The background luminance is reduced by the transmission of the glasses. In (c), the luminance meter directly measures the background value.

To calculate the transmission of the glasses, we should note that the background at 0.530 μm has a spectral Gaussian profile with a FWHM of 33 nm. The holographic combiner operates within this range. Figure 5.17(d) shows the background spectral profile. Since the hologram reflects a portion of this spectrum, the transmitted region is shown as the hatched area in the same figure. The integral of this portion is 71.5% relative to the LED profile. Without the holographic combiner and using a laser source at 0.513 μm, I separately measured the transmission of the optics (the glasses and the beam splitter). The transmission of the optics is 76%. The overall transmission for this experiment is thus $71.5\% \times 76\% \approx 54\%$.

The purpose of this setup is to evaluate the luminance difference between the upper and lower parts of the image. As the background luminance increases, the lower part washes out first. The criterion for measurement was defined as the point where the letters are no longer distinguishable. Since this depends on human perception, the results vary. Since the image is static, to reduce visual memory effects, the test has been performed in both directions: increasing luminance until washout, and decreasing luminance until the image reappeared.

Figure 5.18 shows the experimental luminance results in cd/m^2. The x-axis corresponds to the upper part of the image and the y-axis to the lower part. The values are scattered, and the circle marker indicates the mean value. For the background luminance threshold, the upper part reaches 10 614 cd/m^2, while the lower part reaches 1555 cd/m^2. Taking into account the transmission value of 54%, the estimated luminance of the two images is 5732 cd/m^2 and 840 cd/m^2, respectively. This corresponds to an efficiency ratio of 14.6%.

The dispersion observed in our experiments reflects both visual differences and the subjective nature of the washout criterion. Visual performance can vary between individuals [213, 214]. Despite this variability, the efficiency ratio obtained remains consistent with my other experimental results.

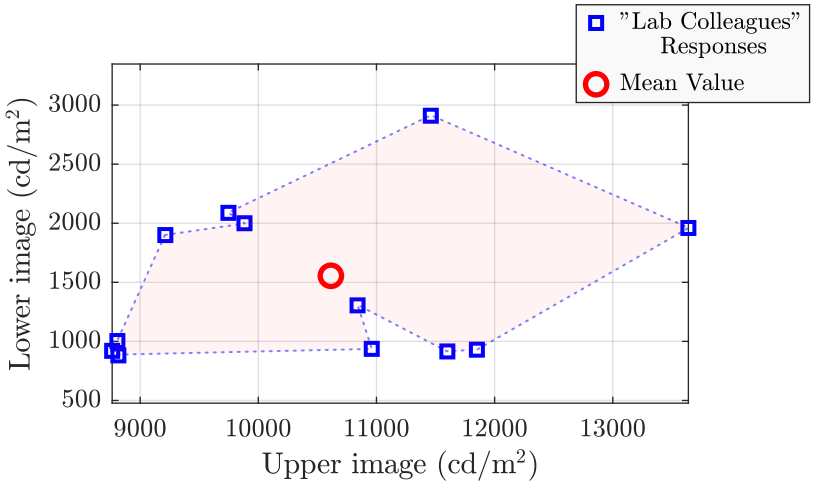

Figure 5.18: Background luminance required to wash out the upper image (x-axis) and the lower image (y-axis).

Based on the estimated entrance pupil of our prototype, I used the intensity profile after diffusion to calculate the efficiency ratio. This is another method to be compared to the previous one based on the luminance meter.

Figure 5.19(a) shows a photograph of the prototype components and indicates the distances in centimeters. Looking directly at μholograms through "A", one can see the static display. The upper image appears brighter and saturated. A dashed circle marks the mechanical aperture that limits the collected flux. The display is centered on C1, which is slightly offset from C2. Based on the position of this window, I estimate that the aperture subtends a half-angle of 5.8° with respect to the display.

The divergence of the holographic pixels in the upper part is $\beta \approx 4$–$4.5° < 5.8°$, which is below the entrance pupil. We therefore assume that the full flux is collected.

The intensity profile after diffusion by the sticky note is shown in Figure 5.19(b). Knowing the transmission of the sticky note ($T = 84.8\%$) and by integrating the intensity over the entrance window and multiplying by T^2 (since the diffuser is used in reflection), I obtain a coupling efficiency of 19.3%. This is of the same order as the previous result of 14.6%.

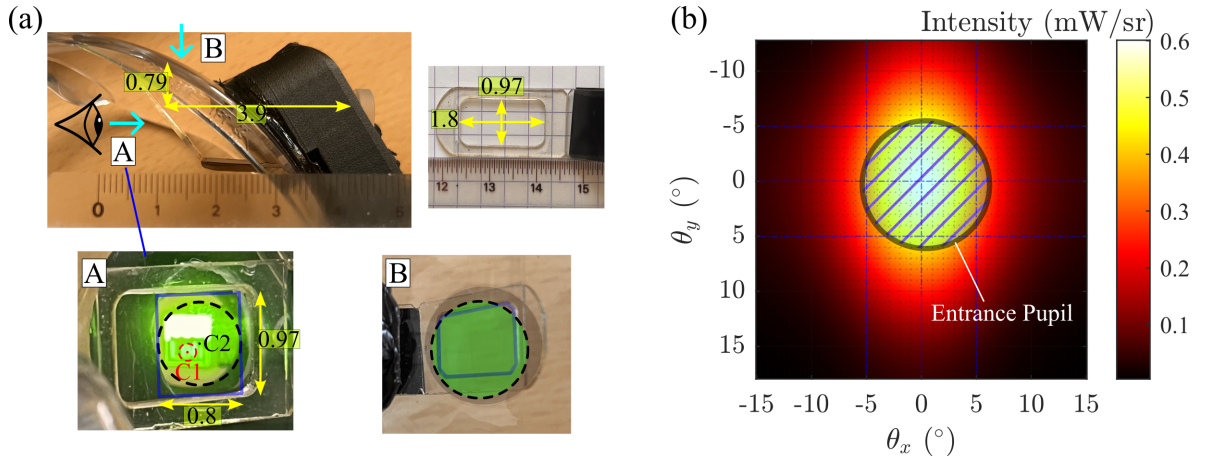

Figure 5.19: (a) Photograph of the prototype at different viewing angles for estimating the aperture that limits the captured flux. (b) Intensity profile of the diffused part after convolution with the emission divergence. The circle indicates the entrance pupil of our prototype.

5.4.5 EyeBox

This section discusses the measurement of the EyeBox (EB). The EB is the 3D spatial region [215] where the collimated fields of all pixels overlap. The eye pupil located in this region perceives the full virtual image (full FoV).

Generally, the distance between the lens and the eye is fixed at an Eye Relief (ER). The EB can be treated as surface normal to the optical axis at this ER. Eye movement, interpupillary distance, nose shape, the position of the glasses, and other variables require a larger Eyebox for visual comfort. A typical Eyebox size at $ER = 0$ mm is 20 mm horizontally and 15 mm vertically. For example, the Vuzix Z100 has an exit pupil of 20×15.7 mm^2.

For simplicity, I will use the horizontal value and express EyeBox size in millimeters.

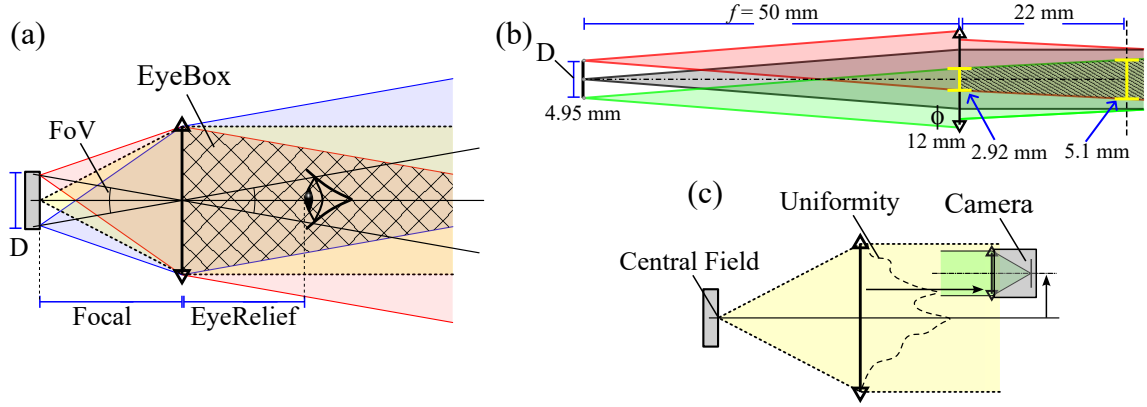

Figure 5.20: EB depends on the combiner type and the divergence of the emission. (a) EB if the lens is the aperture stop. (b) EB when the pixel divergence is low compared to the entrance pupil of the lens. (c) Schematic process for measuring the EB using the μEye XS camera.

Figure 5.20(a) shows a schematic of the EB with a simple magnifier configuration [3]. The lens is the aperture stop. The EB is reduced as the ER increases. We can write the equation of the EB as follows:

$$EB = EB_0 - 2ER \cdot \tan\left(\frac{\text{FoV}}{2}\right) \tag{5.11}$$

EB_0 is the diameter of the exit pupil (in this case, the lens). The FoV is simply related to the display diagonal D and the focal length f by $2\tan\left(\frac{\text{FoV}}{2}\right) = \frac{D}{f}$.

This configuration is the most common; for example, the EB of a diffractive lightguide combiner, such as the Vuzix Z100, follows this configuration.

In Figure 5.20(b), where the pixel divergence β is low (the lens is not the aperture stop), the EB can be expressed as follows:

$$EB = 2f\tan(\beta) \pm \frac{D}{f}(f - ER), \tag{5.12}$$

with "+" for $ER < f$ and "−" for $ER > f$.

From the previous chapter, we showed that by controlling the tilt of the emission, it is possible to form a real exit pupil with a single lens. However, in this prototype, the pixels are not tilted to target a specific distance (FV), since the goal is only to measure the efficiency drop due to divergence.

The schematic of Figure 5.20(b) is scaled. The emission divergence is $\beta \approx 4.5°$. For the upper image, we expect to be in this configuration. For $f = 46$ mm, $D = 4.95$ mm, $\beta = 4.5°$, and at $ER = 22$ mm, we obtain $EB = 4.66$ mm. For $ER = 17$ mm, we obtain $EB = 4.12$ mm.

The fields of the lower image, which is diffused, are expected to correspond to configuration (a). For a lens diameter of $EB_0 = 12$ mm, at $ER = 22$ mm we obtain $EB = 9.63$ mm. For $ER = 17$ mm we obtain $EB = 10.17$ mm. We must recall that EB is taken as the horizontal dimension of the EyeBox.

The EB of the low-luminance image is expected to be larger than that of the high-luminance image. Note that, by taking the surface of the EB ratio between the two: for example, at $ER = 17$ mm, we obtain $4.12^2/10.17^2 = 16.4\%$. This corresponds to the expected drop in efficiency and is consistent with the previous values. Therefore, the lower image is expected to have $\approx 1/6$ of the luminance of the upper image.

These values are only estimations. The EB uniformity decreases from the center due to emission non-uniformity, field stops and vignetting. Figure 5.20(c) shows a schematic of the measurement process. The camera is used here to observe the pixel in the center. By ensuring that the pixel level remains the same while translating horizontally (this is achieved by adjusting the integration time), we can evaluate the uniformity of the central field. This method can also be applied to other pixels (at the edges) to determine the EB. We should note that the pupil of the camera must be small compared to the size of the EB. For the μEye XS camera, I estimate the pupil size to be around 1.32 mm (for $f/2.8$ and $f = 3.7$ mm).

Figure 5.21(a) shows images from our prototype at different horizontal positions of the camera, where the image appears and disappears. Figure 5.21(b) shows images from the commercial product Vuzix Z100, which I tested using the same measurement protocol.

For the prototype, the upper image is fully visible approximately between 3 and 8 mm, giving a rough estimate of the horizontal EB of about 5 mm. Note that the camera is placed at an eye relief of $ER \approx 17$ mm from the holographic lens. The beam splitter limits the access of the camera to lower ER values.

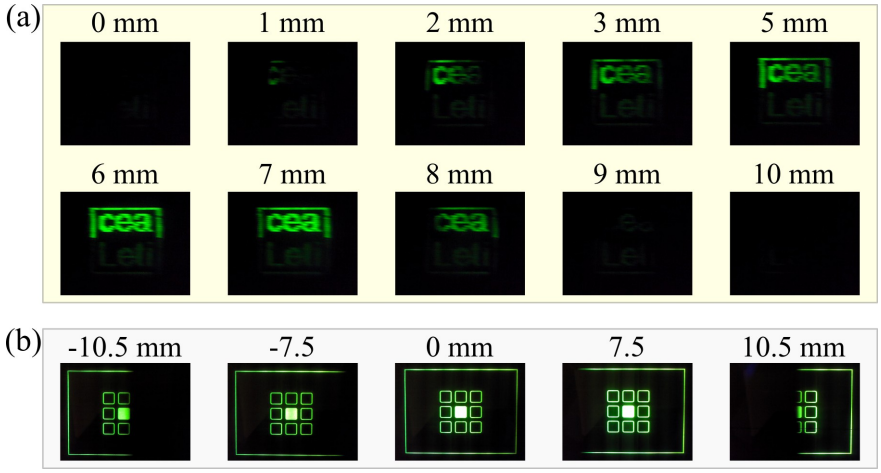

Figure 5.21: Images perceived by the camera during horizontal translation (in mm). (a) Our prototype. (b) Vuzix Z100.

For the Vuzix case, the full image is visible between −7.5 and +7.5 mm, corresponding to an EB of 15 mm at $ER = 10$ mm. This is consistent with the exit pupil size of $EB_0 = 20$ mm. The Vuzix FoV is about 30°, while our prototype FoV is approximately 6.2°.

The irradiance E (W·m^{-2}) on a camera pixel is proportional to the radiance L (W·m^{-2}·sr^{-1}): $E = L\,\mathrm{d}\Omega$. Energetic units are used instead of visual units (illuminance and luminance), since the spectral response of a camera differs from that of the human eye.

The camera integration time t_{in} is used to control the number of collected photons N. The pixel level (0–255), below saturation, is directly related to the collected flux or power (N/t_{in}). Since the radiance is proportional to the power, it is therefore inversely proportional to the integration time, i.e. $L \propto 1/t_{\text{in}}$.

In Figure 5.22(a), I present the result of calibration to verify this linear behavior of the camera sensor. The figure shows $1/t_{\text{in}}$ as a function of the power. An LED source of variable power is used and measured with a photodetector. Luminit diffuser placed in front of the LED is imaged. For a region of interest (ROI) or a pixel, as the power increases, the integration time is decreased to maintain the same pixel level (set here at 150).

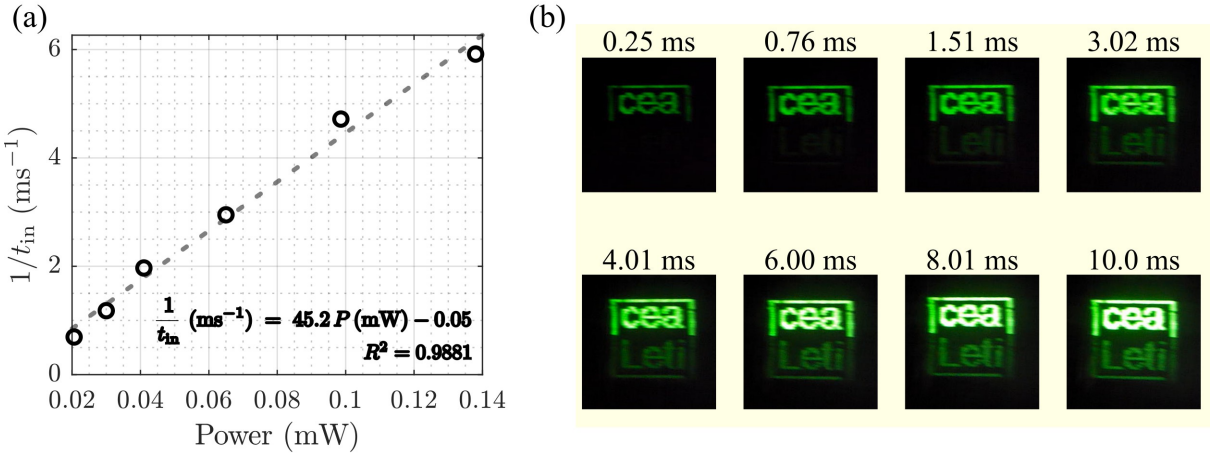

Figure 5.22: (a) The inverse of the integration time is proportional to the collected power. (b) The virtual image as seen by the camera at different integration times.

The proportionality $L \propto 1/t_{in}$ is used both to measure the uniformity of the EB and to provide a relative measure of the luminance difference between the upper image and the diffused one.

Figure 5.22(b) shows several images taken with the camera with increasing integration times. As t_{in} increases, the lower image becomes visible while the upper image saturates.

Figure 5.23(a) shows $1/t_{in}$ as a function of the camera position. Two plots are displayed, corresponding to the regions of interest indicated by crosses on the virtual image. This figure illustrates the axial field uniformity in the upper and lower parts of the image. The upper part has higher luminance because the required integration time is shorter ($1/t_{in}$ is larger). By integrating the two curves over the camera position, we obtain values of 11.5 and 1.82 ms^{-1}·mm, respectively. The corresponding luminance ratio is 15.9%. This result is consistent with my previous methods. The upper part of the static display is more than six times brighter than the lower part.

Figure 5.23(b) shows the normalized plot. The axial field for the lower image is wider. The EB is larger compared to the upper image. Let us define the EB as the width corresponding to a 25% decrease in uniformity. The lower image has $EB_0 = 8.26$ mm, while the upper one has $EB_0 = 4.03$ mm. This EB corresponds only to the pixels indicated by the crosses. This measurement is at $ER = 17$ mm.

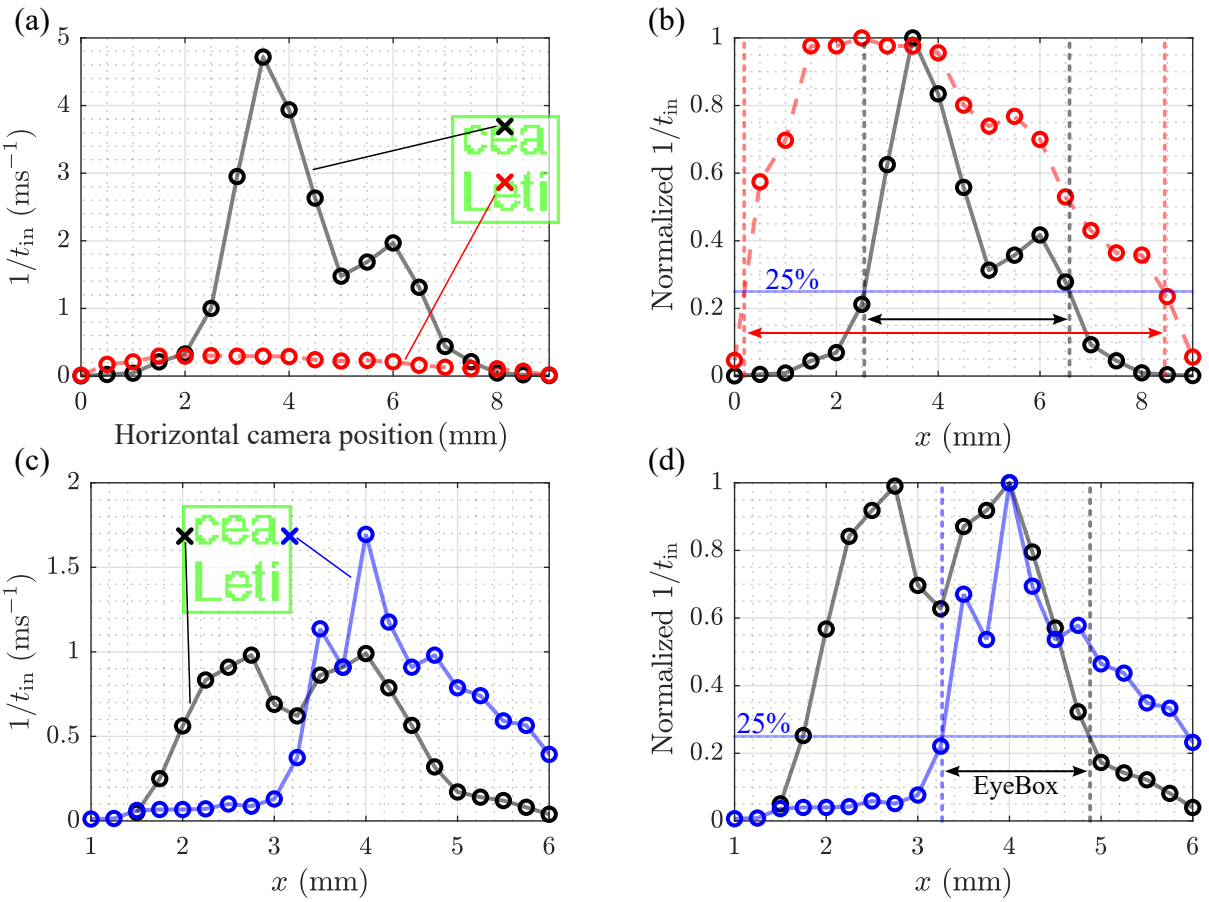

Figure 5.23: EyeBox measurement and uniformity using the integration time as the camera position is translated. (a) EB of the axial field shown by the crosses. (b) Normalized results of (a) with the 25% uniformity criterion. (c) EB measurement using the fields from pixels at the edges. (d) Normalized results of (c).

Figure 5.23(c) shows $1/t_{in}$ for two pixels located at the edges, and Figure 5.23(d) shows the normalized results. Defining the EB at a 25% uniformity drop gives EB = 1.62 mm at ER = 17 mm. This value is lower than the expected one (4.12 mm). This is because we did not account for the emission uniformity and we did not apply the same 25% criterion. For the emission divergence, if we use $\beta = 4°$ (instead of 4.5°), we obtain EB = 3.3 mm at ER = 17 mm.

In this section, I detailed my results regarding the characterization of the prototype. I used several methods to measure the drop in efficiency or luminance, as the entrance pupil limits the captured flux. These methods and the associated metrics are based on my understanding of the bibliography and were developed specifically for this prototype. There is room for improvement in both the prototype and the characterization methods.

Uncertainty values are not the main focus here, since the primary goal is to provide reasonable measured results. This aspect can be improved in future work. The table 5.1 summarizes the prototype characteristics.

Table 5.1: Summary of the luminance, efficiency, FoV, and EB of the passive prototype

Luminance (cd/m^2)	**Upper image**	**Lower image**	
	5732	840	
Efficiency Drop (%) / Methods	Luminance meter	Entrance pupil	Camera
	14.6%	19.3%	15.9%
FoV (°) full	6.2		
EyeBox horizontal	**Upper image**	**Lower image**	
Central field	4 mm	8.3 mm	
Full FoV at 25%	1.62 mm	≈ 4 mm	

5.5 Conclusion

In this chapter, I described a passive prototype we built to assess the impact of pixel directivity and divergence on the luminance of a near-eye display (NED). High luminance is particularly important for NEDs, especially in AR, where outdoor brightness can wash out the virtual information.

I provided a description of each building block. The display is a pixelated holographic image illuminated with collimated green light. Half of the display is covered with a diffuser to increase the divergence. The entrance pupil limits the captured power. As a result, the virtual image is divided into a high-luminance part of 5732 cd/m^2 and a low-luminance part of 840 cd/m^2. The efficiency drop of $\approx 15\%$ is analyzed with three different methods.

The diffuser characteristics are analyzed with a retro-goniometer.

The holographic combiner, which we recorded for the first time for this simple prototype, exhibits a low modulation transfer function (MTF) of 3–4 cycles/mm. The holographic pixels used are relatively large (150 μm). The image is visible. I provided some analysis of this low MTF and discussed possible improvements. Overall, the prototype is functional and the objective is achieved.

The beam splitter, a simple glass plate, causes ghost images. An analysis and possible improvements are provided.

The measurement of the EyeBox gives 4 mm for the brighter image and 8.3 mm for the dimmer image. These values correspond to the axial field at an eye relief of 17 mm.

We explored and validated the implementation of a passive demonstration highlighting the importance of directional displays. This emphasizes the relevance of pursuing our innovative approach using integrated photonic circuits and holography for local control of emission properties.

I presented this work at the beginning of 2025 at Photonics West in San Francisco, during the SPIE AR | VR | MR Student Optical Design Challenge. I was honored to receive the first-place award.

General Conclusion

This thesis aims to address efficiency in near-eye displays (NEDs) through a directional display concept based on photonic integrated circuit (PIC) and holography.

Conventional NEDs can exhibit an optical efficiency of 40 dB (0.01%). Only one photon out of 10 000 emitted at the display surface reaches the retina. Improving this low efficiency helps provide a high luminance virtual image, which is essential for outdoor use of smart eyewear. This, while maintaining low power consumption, reducing battery size, and minimizing heat generation.

In our concept, we can achieve an efficiency improvement by a factor of 100 (20 dB). This improvement is obtained through étendue matching, enabled by the directional emission properties of our display (divergence and direction) combined with efficient EyeBox formation using a free-space combiner.

An important element in our display architecture is the active extraction component. Light must be extracted locally and actively from the PIC into free space. Our patented approach, based on evanescent coupling and total internal reflection, satisfies the extraction requirements, especially the extraction rate over short distances and the directionality of the extraction with no diffraction orders. The analysis and comparison were summarized using a radiation decay constant α_r. I showed that our approach exhibits exponential behavior due to the evanescent part of the mode, where $\alpha_r \propto \exp(-2\gamma s)$. In this equation, s is the separation or the gap between the waveguide and the high-index layer used to outcouple the mode. γ is the transverse component of the wave vector, where $1/\gamma$ is a characteristic length of the evanescent part of the mode.

On the other hand, I compared this solution with a conventional approach based on activating a diffraction grating, where the decay constant has the form $\alpha_r \propto (n_g^2 - n_{LC}^2)^2$. This corresponds to a quadratic contrast dependence between the refractive index of the grating and that of the liquid crystal. Our solution provides an extraction length ten times greater, around 10 μm. Moreover, unlike in the binary grating, there are no diffraction orders.

I provided both simulation and analytical treatment. The analytical results were verified by FDTD simulations. This analytical study represents a comprehensive work that combines my understanding with a compilation of key literature.

I presented key theoretical elements comparing our component with an out-coupling grating in terms of extraction length, directionality, divergence, integration, RGB operation, polarization, and fabrication tolerance.

After introducing this new type of photonic component for the first time, we also demonstrate its experimental validation The demonstration was carried out using high refractive index resin by fabricating strips with sidewall angles of 45° and 54.74°. The process uses wet etching of silicon, which produces good quality surfaces. The NIL process was then used to replicate the structures using Inkron resin. The sample was bonded to a photonic chip, and light extraction was successfully validated after fiber coupling.

This static demonstration opens the perspective for a dynamic implementation of this new extraction component using liquid crystals. I provide a comprehensive overview of ferroelectric liquid crystals (FLCs), which we chose due to their high operating speed (<100 μs).

I discussed the holographic recording of pixelated hologram using a holographic printer. I automated the recording for reflection function. The interval angles is 8° (±4°). I achieved a holographic element of size 20 μm. For an offset angle of 35°, a size of 50 μm was obtained.

We built a passive prototype to visually assess the impact of a directional solution. In this prototype, the passive display is divided into a narrow emission cone and a wide one. I measured the impact on luminance. The efficient narrow cone couples light more effectively into the optical system, providing a brightness increase of about 6–7 times. The building blocks are described, including the holographic lens. Additional analyzes and measurements are also provided, such as the EyeBox evaluation.

Perspectives:

System part: There is a trade-off between divergence (through the waveguide width) and waveguide density. The geometry of the waveguide can also affect the loss of propagation. For future PIC designs, this must be taken into account when designing the waveguides layout.

Addressing color requires a clear design and an understanding of the related trade-offs. One approach is to use a single waveguide per color, which introduces dispersion in the effective index and leads to different efficiencies and extraction angles. The extraction angle can be compensated by the hologram by multiplexing the different reflection angles. Another option is to use three separate waveguides for RGB, which relaxes design constraints but increases the overall footprint.

A specific bibliographic review and analysis must be conducted on laser diodes and SLEDs, their suppliers, efficiencies, sizes, heat generation, and how to couple them with the PIC.

Further activities in the system concern the analysis of the compactness of the microdisplay, expressed in cm^3 (c.c), and compare it with the requirements for NEDs and other existing solutions. In this analysis, the electronics surrounding the active area must also be taken into account.

Extraction part: I give specific perspectives regarding the extraction element in Chapter 3. I can add here, as a perspective, the visual representation of the prismatic function with respect to TIR and transmission. For future work, the holographic function must be added to this representation in order to include the angular selectivity of the hologram model.

Holographic part: An important perspective is to improve the recording setup to increase the recorded angle γ.

Implementing the divergence function inside our pixelated hologram is not discussed in this manuscript. I have discussed in this thesis how divergence is related to the extraction process and the waveguide. The smallest achievable divergence can be expected to be around 15° (FWHM), due to diffraction limitations. Reducing the divergence using the hologram can be quite complex and would require incorporating micro-lens arrays functions. Increasing the divergence, on the other hand, is possible through a diffusing process by recording specific speckle sizes within the hologram. This point must be clearly addressed in future work with experimental results.

I hope this work will prove valuable for future theses or other projects building upon these ideas.

References

[1] Bernard C. Kress. *Optical Architectures for Augmented-, Virtual-, and Mixed-Reality Headsets*. SPIE, Jan. 2020. DOI: 10.1117/3.2559304.

[2] Kodai Matsuhashi, Toshiki Kanamoto, and Atsushi Kurokawa. "Thermal Model and Countermeasures for Future Smart Glasses". en. In: *Sensors* 20.5 (Jan. 2020). Publisher: Multidisciplinary Digital Publishing Institute, p. 1446. DOI: 10.3390/s20051446.

[3] Jim Melzer and Kirk Moffitt. *Head-Mounted Displays: Designing for the User*. Feb. 2011.

[4] Bernard Kress and Thad Starner. "A review of head-mounted displays (HMD) technologies and applications for consumer electronics". In: *Photonic Applications for Aerospace, Commercial, and Harsh Environments IV*. Vol. 8720. SPIE, May 2013, pp. 62–74. DOI: 10.1117/12.2015654.

[5] Bernard C. Kress and Ishan Chatterjee. "Waveguide combiners for mixed reality headsets: a nanophotonics design perspective". en. In: *Nanophotonics* 10.1 (Jan. 2021). Publisher: De Gruyter, pp. 41–74. DOI: 10.1515/nanoph-2020-0410.

[6] En-Lin Hsiang et al. "AR/VR light engines: perspectives and challenges". EN. In: *Advances in Optics and Photonics* 14.4 (Dec. 2022). Publisher: Optica Publishing Group, pp. 783–861. DOI: 10.1364/AOP.468066.

[7] Amal Ghosh et al. "Developing the World's Brightest WUXGA OLED Microdisplay". en. In: *Information Display* 38.2 (2022), pp. 19–23. DOI: 10.1002/msid.1286.

[8] Charles Wheatstone. "Contributions to the Physiology of Vision.–Part the First. On Some Remarkable, and Hitherto Unobserved, Phenomena of Binocular Vision". In: *Philosophical Transactions of the Royal Society of London* 128 (1838). Publisher: The Royal Society, pp. 371–394. DOI: https://www.jstor.org/stable/108203.

[9] W. Le Conte Stevens. "The Stereoscope: Its History". English. In: *The Popular Science Monthly Volume 21* (1882), pp. 37–53.

[10] Ivan E. Sutherland. "A head-mounted three dimensional display". In: *Proceedings of the December 9-11, 1968, fall joint computer conference, part I*. AFIPS '68 (Fall, part I). New York, NY, USA: Association for Computing Machinery, 1968, pp. 757–764. DOI: 10.1145/1476589.1476686.

[11] Hubert W. Upton. "Wearable Eyeglass Speechreading Aid". In: *American Annals of the Deaf* 113.2 (1968). Publisher: Gallaudet University Press, pp. 222–229.

[12] Paul Milgram et al. "Augmented reality: a class of displays on the reality-virtuality continuum". In: *Telemanipulator and Telepresence Technologies*. Vol. 2351. SPIE, Dec. 1995, pp. 282–292. DOI: 10.1117/12.197321.

[13] Deering M. F. “The Limits of Human Vision”. In: vol. 2. 1998.

[14] Karen Bredenkamp. “Head and Face Wearables”. In: *Product Fit and Sizing*. Num Pages: 71. CRC Press, 2024.

[15] Thomas M. Schnieders, Karen Bredenkamp, and Sebastian La Rosa. “Nose Shape Categorization and Its Impact on Design in Head Mounted Displays”. en. In: *Proceedings of the 22nd Congress of the International Ergonomics Association, Volume 3*. Ed. by Sangeun Jin et al. Singapore: Springer Nature, 2025, pp. 226–230. DOI: 10.1007/978-981-96-9330-6_33.

[16] Bernard C. Kress. “Digital optical elements and technologies (EDO19): applications to AR/VR/MR”. In: *Digital Optical Technologies 2019*. Vol. 11062. SPIE, July 2019, pp. 343–355. DOI: 10.1117/12.2544404.

[17] Vasudevan Lakshminarayanan. “Visual Acuity”. en. In: *Handbook of Visual Display Technology*. Springer, Berlin, Heidelberg, 2015, pp. 1–6. DOI: 10.1007/978-3-642-35947-7_6-2.

[18] Christine Garhart and Vasudevan Lakshminarayanan. “Anatomy of the Eye”. en. In: *Handbook of Visual Display Technology*. Springer, Berlin, Heidelberg, 2012, pp. 73–83. DOI: 10.1007/978-3-540-79567-4_4.

[19] Robert Earl Patterson. “Binocular Vision and Depth Perception”. en. In: *Handbook of Visual Display Technology*. Springer, Berlin, Heidelberg, 2012, pp. 121–127. DOI: 10.1007/978-3-540-79567-4_9.

[20] Vasudevan Lakshminarayanan. “Flicker Sensitivity”. en. In: *Handbook of Visual Display Technology*. Springer, Berlin, Heidelberg, 2015, pp. 1–10. DOI: 10.1007/978-3-642-35947-7_7-2.

[21] Robert Patterson. “Review Paper: Human factors of stereo displays: An update”. en. In: *Journal of the Society for Information Display* 17.12 (2009), pp. 987–996. DOI: 10.1889/JSID17.12.987.

[22] Minqi Wang and Emily A. Cooper. “Perceptual Guidelines for Optimizing Field of View in Stereoscopic Augmented Reality Displays”. In: *ACM Trans. Appl. Percept.* 19.4 (Nov. 2022), 19:1–19:23. DOI: 10.1145/3554921.

[23] Maliha Ashraf, Alexandre Chapiro, and Rafał K. Mantiuk. “Resolution limit of the eye — how many pixels can we see?” en. In: *Nature Communications* 16.1 (Oct. 2025). Publisher: Nature Publishing Group, p. 9086. DOI: 10.1038/s41467-025-64679-2.

[24] Brian Wheelwright et al. “Field of view: not just a number”. In: *Digital Optics for Immersive Displays*. Vol. 10676. SPIE, May 2018, p. 1067604. DOI: 10.1117/12.2307303.

[25] Aaron Bauer and Jannick P. Rolland. “The Optics of Augmented Reality Displays”. en. In: *Springer Handbook of Augmented Reality*. Ed. by Andrew Yeh Ching Nee and Soh Khim Ong. Cham: Springer International Publishing, 2023, pp. 187–209. DOI: 10.1007/978-3-030-67822-7_8.

[26] Parth Arora et al. *Positioning Monocular Optical See Through Head Worn Displays in Glasses for Everyday Wear*. 2025. URL: https://arxiv.org/abs/2505.09047.

[27] Martin S. Banks, Joohwan Kim, and Takashi Shibata. "Insight into Vergence-Accommodation Mismatch". In: *Proceedings of SPIE* 8735 (May 2013), pp. 10.1117/12.2019866. DOI: 10.1117/12.2019866.

[28] Kirk Moffitt and Michael P. Browne. "Visibility of color symbology in head-up and head-mounted displays in daylight environments". In: *Optical Engineering* 58.5 (Mar. 2019). Publisher: SPIE, p. 051809. DOI: 10.1117/1.OE.58.5.051809.

[29] Zhangyi Zhong. "17-2: Invited Paper: Laser Safety Considerations in Laser Beam Scanning Light Field Displays". en. In: *SID Symposium Digest of Technical Papers* 50.1 (2019). _eprint: https://sid.onlinelibrary.wiley.com/doi/pdf/10.1002/sdtp.12896, pp. 225–227. DOI: 10.1002/sdtp.12896.

[30] Walter H. Ehrenstein, Birgit E. Arnold-Schulz-Gahmen, and Wolfgang Jaschinski. "Eye preference within the context of binocular functions". en. In: *Graefe's Archive for Clinical and Experimental Ophthalmology* 243.9 (Sept. 2005), pp. 926–932. DOI: 10.1007/s00417-005-1128-7.

[31] Yves Galifret. "Visual persistence and cinema?" fr. In: *Comptes Rendus. Biologies* 329.5-6 (2006), pp. 369–385. DOI: 10.1016/j.crvi.2006.03.008.

[32] "Near-to-Eye Systems". en. In: *Introduction to Microdisplays*. Chapter 11. John Wiley & Sons, Ltd, 2006, pp. 337–363. DOI: 10.1002/9780470057056.ch11.

[33] Gerald Westheimer. "The maxwellian view". In: *Vision Research* 6.11 (Dec. 1966), pp. 669–682. DOI: 10.1016/0042-6989(66)90078-2.

[34] Junguo Lin et al. "Retinal projection head-mounted display". en. In: *Frontiers of Optoelectronics* 10.1 (Mar. 2017), pp. 1–8. DOI: 10.1007/s12200-016-0662-8.

[35] Yuqiang Ding et al. "Waveguide-based augmented reality displays: perspectives and challenges". In: *eLight* 3.1 (Dec. 2023), p. 24. DOI: 10.1186/s43593-023-00057-z.

[36] Jannick P. Rolland and Jeremy Goodsell. "Waveguide-based augmented reality displays: a highlight". en. In: *Light: Science & Applications* 13.1 (Jan. 2024). Publisher: Nature Publishing Group, p. 22. DOI: 10.1038/s41377-023-01371-4.

[37] Zeyang Liu et al. "Metasurface-enabled augmented reality display: a review". In: *Advanced Photonics* 5.3 (May 2023). Publisher: SPIE, p. 034001. DOI: 10.1117/1.AP.5.3.034001.

[38] Yizhou Qian et al. "Power consumption of light engines for emerging augmented reality glasses: perspectives and challenges". In: *Advanced Photonics* 7.3 (Mar. 2025). Publisher: SPIE, p. 034001. DOI: 10.1117/1.AP.7.3.034001.

[39] Jianghao Xiong et al. "Augmented reality and virtual reality displays: emerging technologies and future perspectives". en. In: *Light: Science & Applications* 10.1 (Oct. 2021). Number: 1 Publisher: Nature Publishing Group, p. 216. DOI: 10.1038/s41377-021-00658-8.

[40] Ryan T. Ley et al. "Revealing the importance of light extraction efficiency in InGaN/GaN microLEDs via chemical treatment and dielectric passivation". In: *Applied Physics Letters* 116.25 (June 2020), p. 251104. DOI: 10.1063/5.0011651.

[41] Jinpeng Huang et al. "GaN-based resonant cavity micro-LEDs for AR application". In: *Applied Physics Letters* 121.20 (Nov. 2022), p. 201104. DOI: 10.1063/5.0117568.

[42] Fabian Rol et al. “Study of Far-Field Electroluminescence Emission to Enhance Micro-LED Performance”. en. In: *Journal of the Society for Information Display* (). DOI: 10.1002/jsid.2114.

[43] Larry J. Hornbeck. “Digital Light Processing for high-brightness high-resolution applications”. In: *Projection Displays III*. Vol. 3013. SPIE, May 1997, pp. 27–40. DOI: 10.1117/12.273880.

[44] François Templier. “GaN-based emissive microdisplays: A very promising technology for compact, ultra-high brightness display systems”. en. In: *Journal of the Society for Information Display* 24.11 (2016), pp. 669–675. DOI: 10.1002/jsid.516.

[45] Chien-Chung Lin et al. “The micro-LED roadmap: status quo and prospects”. en. In: *Journal of Physics: Photonics* 5.4 (Oct. 2023). Publisher: IOP Publishing, p. 042502. DOI: 10.1088/2515-7647/acf972.

[46] Yifan Wu et al. “Full-Color Realization of Micro-LED Displays”. en. In: *Nanomaterials* 10.12 (Dec. 2020). Publisher: Multidisciplinary Digital Publishing Institute, p. 2482. DOI: 10.3390/nano10122482.

[47] Peng Chen and Qiming Li. “55-4: Invited Paper: Monolithic MicroLED Display for AR Applications”. en. In: *SID Symposium Digest of Technical Papers* 54.1 (2023). _eprint: https://sid.onlinelibrary.wiley.com/doi/pdf/10.1002/sdtp.16683, pp. 1874–1877. DOI: 10.1002/sdtp.16683.

[48] Guijun Li et al. “Color-conversion displays: current status and future outlook”. en. In: *Light: Science & Applications* 13.1 (Nov. 2024). Publisher: Nature Publishing Group, p. 301. DOI: 10.1038/s41377-024-01618-8.

[49] Tae Soo Kim et al. “Future trends of display technology: micro-LEDs toward transparent, free-form, and near-eye displays”. en. In: *Light: Science & Applications* 14.1 (Sept. 2025). Publisher: Nature Publishing Group, p. 335. DOI: 10.1038/s41377-025-02027-1.

[50] François Olivier et al. “Influence of size-reduction on the performances of GaN-based micro-LEDs for display application”. In: *Journal of Luminescence*. E-MRS 2016, Symposium M: Silicon compatible materials and integrated devices for photonics and optical sensing 191 (Nov. 2017), pp. 112–116. DOI: 10.1016/j.jlumin.2016.09.052.

[51] Kaili Fan et al. “Analysis of size-dependent optoelectronic properties of red AlGaInP micro-LEDs”. EN. In: *Optics Express* 31.22 (Oct. 2023). Publisher: Optica Publishing Group, pp. 36293–36303. DOI: 10.1364/OE.503024.

[52] Jordan M. Smith et al. “Comparison of size-dependent characteristics of blue and green {InGaN} microLEDs down to 1~µm in diameter”. In: *Applied Physics Letters* 116.7 (Feb. 2020), p. 071102. DOI: 10.1063/1.5144819.

[53] David Armitage, Ian Underwood, and Shin Tson Wu. *Introduction to Microdisplays*. English. John Wiley & Sons Inc., 2006.

[54] Daniel Krüerke et al. “Liquid Crystal Over Silicon (LCOS) Microdisplays and their Applications”. In: Jan. 2002, pp. 148–155.

[55] Yuge Huang et al. “Liquid-Crystal-on-Silicon for Augmented Reality Displays”. en. In: *Applied Sciences* 8.12 (Dec. 2018). Publisher: Multidisciplinary Digital Publishing Institute, p. 2366. DOI: 10.3390/app8122366.

[56] Edward Tang. “The smallest LCoS engine: introducing the AG-30L2”. In: *SPIE AR, VR, MR Industry Talks 2023*. Vol. 12450. SPIE, Mar. 2023, 124500O. DOI: 10.1117/12.2667981.

[57] Yuet-Wing Li et al. “Front-lit LCOS for AR displays”. In: *Journal of Optical Microsystems* 3.4 (Sept. 2023). Publisher: SPIE, p. 041205. DOI: 10.1117/1.JOM.3.4.041205.

[58] Yuet-Wing Li et al. “13-1: Invited Paper: Front-lit LCOS for AR Displays”. en. In: *SID Symposium Digest of Technical Papers* 54.1 (2023), pp. 154–157. DOI: 10.1002/sdtp.16512.

[59] Yuet-Wing Li et al. “40-1: Invited Paper: Ultra high brightness Front-lit LCOS for AR applications”. en. In: *SID Symposium Digest of Technical Papers* 56.S1 (2025). _eprint: https://sid.onlinelibrary.wiley.com/doi/pdf/10.1002/sdtp.18801, pp. 338–340. DOI: 10.1002/sdtp.18801.

[60] Joyce K. S. Poon et al. “Silicon photonics for the visible and near-infrared spectrum”. EN. In: *Advances in Optics and Photonics* 16.1 (Mar. 2024). Publisher: Optica Publishing Group, pp. 1–59. DOI: 10.1364/AOP.501846.

[61] Zhujun Shi et al. “Flat-panel laser displays through large-scale photonic integrated circuits”. en. In: *Nature* 644.8077 (Aug. 2025). Publisher: Nature Publishing Group, pp. 652–659. DOI: 10.1038/s41586-025-09107-7.

[62] Thomas Charisoulis et al. “FLCoS: a promising path towards small form-factor, high performance color-sequential micro-displays”. In: *Emerging Liquid Crystal Technologies XX*. Vol. 13387. SPIE, Mar. 2025, pp. 14–23. DOI: 10.1117/12.3041412.

[63] Yoshitomo Isomae et al. “Superior spatial resolution of surface-stabilized ferroelectric liquid crystals compared to nematic liquid crystals for wide-field-of-view holographic displays”. en. In: *Japanese Journal of Applied Physics* 59.4 (Mar. 2020). Publisher: IOP Publishing, p. 040901. DOI: 10.35848/1347-4065/ab7a49.

[64] Fengling Peng et al. “High-efficient and compact LCoS (liquid crystal on silicon) for AR glasses”. In: *Liquid Crystals XXIX*. Vol. 13587. SPIE, Sept. 2025, pp. 118–123. DOI: 10.1117/12.3066381.

[65] Edward Tang. “Spotlight display technology: world’s first adaptive LED illumination LCoS architecture”. In: *SPIE AR, VR, MR Invited Talks 2024*. Vol. 12914. SPIE, Apr. 2024, p. 129140M. DOI: 10.1117/12.3024888.

[66] Kishore V. Chellappan, Erdem Erden, and Hakan Urey. “Laser-based displays: a review”. EN. In: *Applied Optics* 49.25 (Sept. 2010). Publisher: Optica Publishing Group, F79–F98. DOI: 10.1364/AO.49.000F79.

[67] Sven T. S. Holmström, Utku Baran, and Hakan Urey. “MEMS Laser Scanners: A Review”. In: *Journal of Microelectromechanical Systems* 23.2 (Apr. 2014), pp. 259–275. DOI: 10.1109/JMEMS.2013.2295470.

[68] Franz Fidler et al. “Laser beam scanning in XR: benefits and challenges”. In: *Optical Architectures for Displays and Sensing in Augmented, Virtual, and Mixed Reality (AR, VR, MR) II*. Vol. 11765. SPIE, Mar. 2021, p. 1176502. DOI: 10.1117/12.2576490.

[69] Stepan Essaian and John Khaydarov. “State of the art of compact green lasers for mobile projectors”. en. In: *Optical Review* 19.6 (Nov. 2012), pp. 400–404. DOI: 10.1007/s10043-012-0065-z.

[70] Stefan Morgott et al. “Laser-based projection displays for all-day-use consumer AR glasses”. In: *Optical Architectures for Displays and Sensing in Augmented, Virtual, and Mixed Reality (AR, VR, MR) IV*. Vol. 12449. SPIE, Mar. 2023, pp. 98–103. DOI: 10.1117/12.2657215.

[71] Jörg Reitterer et al. “Ultra-compact micro-electro-mechanical laser beam scanner for augmented reality applications”. In: *Optical Architectures for Displays and Sensing in Augmented, Virtual, and Mixed Reality (AR, VR, MR) II*. Vol. 11765. SPIE, Mar. 2021, pp. 33–43. DOI: 10.1117/12.2576704.

[72] Brian Wheelwright et al. “Advances in MEMS-based laser scanning displays for AR glasses”. In: *Optical Architectures for Displays and Sensing in Augmented, Virtual, and Mixed Reality (AR, VR, MR) VI*. Vol. PC13414. SPIE, Mar. 2025, PC134140B. DOI: 10.1117/12.3042320.

[73] Oleg Petrak et al. “Laser beam scanning based AR-display applying resonant 2D MEMS mirrors”. In: *Optical Architectures for Displays and Sensing in Augmented, Virtual, and Mixed Reality (AR, VR, MR) II*. Vol. 11765. SPIE, Mar. 2021, pp. 15–32. DOI: 10.1117/12.2579695.

[74] Ulrich Hofmann. “MEMS and Laser based microdisplay light engine for AR”. In: *SPIE AR, VR, MR Invited Talks 2024*. Vol. 12914. SPIE, Mar. 2024, p. 129140X. DOI: 10.1117/12.3024902.

[75] Hakan Urey, David W. Wine, and John R. Lewis. “Scanner design and resolution tradeoffs for miniature scanning displays”. In: *Flat Panel Display Technology and Display Metrology*. Vol. 3636. SPIE, Apr. 1999, pp. 60–68. DOI: 10.1117/12.344656.

[76] Karl Guttag. “Analyzing Optics’ Pivotal Role in Augmented and Mixed Reality Displays”. en. In: *Information Display* 39.2 (2023), pp. 20–26. DOI: 10.1002/msid.1379.

[77] Stijn Roelandt et al. “Human speckle perception threshold for still images from a laser projection system”. EN. In: *Optics Express* 22.20 (Oct. 2014). Publisher: Optica Publishing Group, pp. 23965–23979. DOI: 10.1364/OE.22.023965.

[78] Joseph W. Goodman. *Speckle Phenomena in Optics: Theory and Applications, Second Edition*. SPIE. 2020.

[79] Yuhei Kuratomi et al. “Speckle reduction mechanism in laser rear projection displays using a small moving diffuser”. EN. In: *JOSA A* 27.8 (Aug. 2010). Publisher: Optica Publishing Group, pp. 1812–1817. DOI: 10.1364/JOSAA.27.001812.

[80] Trinh-Thi-Kim Tran et al. “Speckle reduction in laser projection displays through angle and wavelength diversity”. EN. In: *Applied Optics, Vol. 55, Issue 6, pp. 1267-1274* (Feb. 2016). Publisher: Optica Publishing Group. DOI: 10.1364/AO.55.001267.

[81] Anna Kafar et al. “Design and optimization of InGaN superluminescent diodes”. en. In: *physica status solidi (a)* 212.5 (2015), pp. 997–1004. DOI: 10.1002/pssa.201431741.

[82] Anna Kafar et al. “Review—Review on Optimization and Current Status of (Al,In)GaN Superluminescent Diodes”. en. In: *ECS Journal of Solid State Science and Technology* 9.1 (Nov. 2019). Publisher: IOP Publishing, p. 015010. DOI: 10.1149/2.0282001JSS.

[83] M. Malinverni et al. “InAlN cladding implementation in green superluminescent diodes and lasers”. In: *Applied Physics Letters* 122.20 (May 2023), p. 201104. DOI: 10.1063/5.0151764.

[84] M. Malinverni et al. “The crucial role of InAlN for blue and green LDs and SLEDs with low power consumption”. In: *Gallium Nitride Materials and Devices XIX*. Vol. 12886. SPIE, Mar. 2024, pp. 47–50. DOI: 10.1117/12.3000476.

[85] M. Malinverni et al. “Extending the emission wavelength of SLEDs to the pure-green spectral region”. In: *Gallium Nitride Materials and Devices XX*. Vol. 13366. SPIE, Mar. 2025, pp. 44–48. DOI: 10.1117/12.3041920.

[86] Adarsh S. Prasad et al. “Evaluating an AR display employing laser beam scanner with waveguide combiner against the IEC 60825-1:2014 standard”. In: *Optical Architectures for Displays and Sensing in Augmented, Virtual, and Mixed Reality (AR, VR, MR) IV*. Vol. 12449. SPIE, Mar. 2023, pp. 72–79. DOI: 10.1117/12.2655110.

[87] Qian Zhang et al. “Polarization recycling method for light-pipe-based optical engine”. EN. In: *Applied Optics, Vol. 52, Issue 36, pp. 8827-8833* (Dec. 2013). Publisher: Optica Publishing Group. DOI: 10.1364/AO.52.008827.

[88] Brian Lemoff. “Ultra-Dense Micro-Led Array with Partially Overlapping Microlenses”. en. Oct. 2024.

[89] Mohamed S. Abdelkhalik et al. “Enhanced and directional electroluminescence from MicroLEDs using metallic or dielectric metasurfaces”. en. In: *Communications Engineering* 4.1 (Apr. 2025). Publisher: Nature Publishing Group, p. 63. DOI: 10.1038/s44172-025-00401-w.

[90] Luce Alexander, Alaee Rasoul, and Abass Aimi. “Ultra-directional and high-efficiency µLEDs via gradient index filled micro-Horn collimators”. In: *Preprint arXiv* (Dec. 2024).

[91] Robert D. TeKolste and Victor K. Liu. “Outcoupling grating for augmented reality system”. en. US20180113313A1. Apr. 2018.

[92] Chulwoo Oh. “Waveguide light multiplexer using crossed gratings”. en. US20180143509A1. May 2018.

[93] *Laser-Based AR on the Rise - Information Display - Wiley Online Library*. en. DOI: 10.1002/0050124.

[94] Steven A. Hickman et al. “Laser to photonic integrated circuit coupling to enable consumer AR display engines”. In: *Optical Architectures for Displays and Sensing in Augmented, Virtual, and Mixed Reality (AR, VR, MR) VI*. Vol. PC13414. SPIE, Mar. 2025, PC134140D. DOI: 10.1117/12.3041404.

[95] Aleksandrs Marinins et al. “Wafer-Scale Hybrid Integration of InP DFB Lasers on Si Photonics by Flip-Chip Bonding With sub-300 nm Alignment Precision”. In: *IEEE Journal of Selected Topics in Quantum Electronics* 29.3: Photon. Elec. Co-Inte. and Adv. Trans. Print. (May 2023), pp. 1–11. DOI: 10.1109/JSTQE.2022.3223641.

[96] K. M. Davis et al. “Writing waveguides in glass with a femtosecond laser”. EN. In: *Optics Letters* 21.21 (Nov. 1996). Publisher: Optica Publishing Group, pp. 1729–1731. DOI: 10.1364/OL.21.001729.

[97] Francesco Ceccarelli and Roberto Osellame. “Photonic integrated circuits through femtosecond laser waveguide writing in glass”. en. In: *Photoniques* 125 (2024). Publisher: EDP Sciences, pp. 39–44. DOI: 10.1051/photon/202412539.

[98] David Coenen et al. “Thermal Characterisation of Hybrid, Flip-Chip InP-Si DFB Lasers”. en. In: *Micromachines* 14.2 (Feb. 2023). Publisher: Multidisciplinary Digital Publishing Institute, p. 381. DOI: 10.3390/mi14020381.

[99] Kyllian Millard. “Conception d’éléments de routage en optique guidée pour l’intégration d’un système de projection rétinienne”. fr. PhD thesis. Université Grenoble Alpes, Nov. 2023.

[100] Haoyang Sun et al. “Silicon Photonic Phase Shifters and Their Applications: A Review”. en. In: *Micromachines* 13.9 (Sept. 2022). Publisher: Multidisciplinary Digital Publishing Institute, p. 1509. DOI: 10.3390/mi13091509.

[101] Salaheddine Toubi, Elise Ghibaudo, and Christophe Martinez. “Directional display for AR applications based on holography and photonic integrated circuits”. In: *Optics, Photonics, and Digital Technologies for Imaging Applications VIII*. Vol. 12998. SPIE, June 2024, pp. 269–277. DOI: 10.1117/12.3014264.

[102] Stefan Alexander et al. “Systems, devices, and methods for eyebox expansion in wearable heads-up displays”. en. US10031338B2. July 2018.

[103] Eric Tremblay, Mickael Guillaumee, and Christophe Moser. “Method and apparatus for head worn display with multiple exit pupils”. en. US9846307B2. Dec. 2017.

[104] Eric Marcellin-Dibon and Cédric SIOURAKAN. “Systems and methods for optically displaying at a set of spectacles”. US20230168515A1. June 2023.

[105] Christophe Martinez. “Device for projecting an image formed by a screen”. US20240219725A1. July 2024.

[106] Kyllian Millard et al. “Multilayer photonic-integrated circuit design for dense random waveguide distribution addressing, application to near-eye display”. In: *Optical Architectures for Displays and Sensing in Augmented, Virtual, and Mixed Reality (AR, VR, MR) IV*. Vol. 12449. SPIE, Mar. 2023, pp. 144–151. DOI: 10.1117/12.2649858.

[107] Kyllian MILLARD and Christophe Martinez. “Multilevel retro-coupling device”. US20240201441A1. June 2024.

[108] Jeff Chiles et al. “Design, fabrication, and metrology of 10 × 100 multi-planar integrated photonic routing manifolds for neural networks”. In: *APL Photonics* 3.10 (July 2018), p. 106101. DOI: 10.1063/1.5039641.

[109] Christophe Martinez et al. “See-through holographic retinal projection display concept”. EN. In: *Optica* 5.10 (Oct. 2018). Publisher: Optica Publishing Group, pp. 1200–1209. DOI: 10.1364/OPTICA.5.001200.

[110] Christophe Martinez et al. “Evaluation of a pixelated holographic display concept for a near-eye display: recent results and technological developments”. In: *Advances in Display Technologies XIII*. Vol. 12443. SPIE, Mar. 2023, pp. 54–60. DOI: 10.1117/12.2650111.

[111] Christophe Martinez2. “Device for projecting an image formed by a screen”. US20240219726A1. July 2024.

[112] R. Ulrich. “Theory of the Prism–Film Coupler by Plane-Wave Analysis”. EN. In: *JOSA* 60.10 (Oct. 1970). Publisher: Optica Publishing Group, pp. 1337–1350. DOI: 10.1364/JOSA.60.001337.

[113] Donald L. Lee. *Electromagnetic principles of integrated optics*. eng. Wiley, 1986.

[114] Dietrich Marcuse, ed. *Theory of Dielectric Optical Waveguides (Second Edition)*. https://doi.org/10.1016/B978-0-12-470951-5.X5001-X. Academic Press, Jan. 1991.

[115] A. Yariv and M. Nakamura. "Periodic structures for integrated optics". In: *IEEE Journal of Quantum Electronics* 13.4 (Apr. 1977), pp. 233–253. DOI: 10.1109/JQE.1977.1069323.

[116] Jean-Emmanuel Broquin and Lionel Bastard. "Ion-exchanged glass amplifiers and DFB matrices". In: *Applications of Photonic Technology 6*. Vol. 5260. SPIE, Dec. 2003, pp. 246–256. DOI: 10.1117/12.543407.

[117] D. Marcuse. "Directional couplers made of nonidentical asymmetric slabs. Part II: Grating-assisted couplers". In: *Journal of Lightwave Technology* 5.2 (Feb. 1987), pp. 268–273. DOI: 10.1109/JLT.1987.1075493.

[118] Christophe Martinez et al. "Advanced spectral filtering functionalities in ion-exchanged waveguides with artificial cladding gratings". In: *Optics Communications* 233.1 (Mar. 2004), pp. 97–106. DOI: 10.1016/j.optcom.2004.01.031.

[119] Hiroshi Nishihara, Masamitsu Haruna, and Toshiaka Suhara. *Optical Integrated Circuits*. New York: McGraw-Hill Professional, Dec. 1988.

[120] Daivid Fowler et al. "Fiber grating coupler development for Si-photonics process design kits at CEA-LETI". In: *Smart Photonic and Optoelectronic Integrated Circuits XXI*. Vol. 10922. SPIE, Mar. 2019, pp. 19–25. DOI: 10.1117/12.2511845.

[121] Jia-ming Liu. *Photonic Devices*. Cambridge: Cambridge University Press, 2005. DOI: 10.1017/CBO9780511614255.

[122] Andrew Michaels and Eli Yablonovitch. "Inverse design of near unity efficiency perfectly vertical grating couplers". EN. In: *Optics Express* 26.4 (Feb. 2018). Publisher: Optica Publishing Group, pp. 4766–4779. DOI: 10.1364/OE.26.004766.

[123] Riccardo Marchetti et al. "Coupling strategies for silicon photonics integrated chips [Invited]". EN. In: *Photonics Research* 7.2 (Feb. 2019). Publisher: Optica Publishing Group, pp. 201–239. DOI: 10.1364/PRJ.7.000201.

[124] T. Tamir and S. T. Peng. "Analysis and design of grating couplers". en. In: *Applied physics* 14.3 (Nov. 1977), pp. 235–254. DOI: 10.1007/BF00882729.

[125] Scott M. Norton, Turan Erdogan, and G. Michael Morris. "Coupled-mode theory of resonant-grating filters". EN. In: *JOSA A* 14.3 (Mar. 1997). Publisher: Optica Publishing Group, pp. 629–639. DOI: 10.1364/JOSAA.14.000629.

[126] Karl Joachim Ebeling. *Integrated Optoelectronics*. en. Berlin, Heidelberg: Springer, 1993. DOI: 10.1007/978-3-642-78166-7.

[127] P. K. Tien and R. Ulrich. "Theory of Prism–Film Coupler and Thin-Film Light Guides". EN. In: *JOSA* 60.10 (Oct. 1970). Publisher: Optica Publishing Group, pp. 1325–1337. DOI: 10.1364/JOSA.60.001325.

[128] E. Gros and L. Dupont. "Ferroelectric liquid crystal optical waveguide switches using the double-refraction effect". In: *IEEE Photonics Technology Letters* 13.2 (Feb. 2001), pp. 115–117. DOI: 10.1109/68.910506.

[129] Noel A. Clark and Sven T. Lagerwall. “Submicrosecond bistable electro-optic switching in liquid crystals”. In: *Applied Physics Letters* 36.11 (June 1980), pp. 899–901. DOI: 10.1063/1.91359.

[130] Per Rudquist. “Smectic LCD Modes”. en. In: *Handbook of Visual Display Technology*. Springer, Berlin, Heidelberg, 2012, pp. 1445–1467. DOI: 10.1007/978-3-540-79567-4_89.

[131] Chris Mathew et al. “86-4: Optimizing Electrically Suppressed Helix Ferroelectric Liquid Crystals for Commercial Applications”. en. In: *SID Symposium Digest of Technical Papers* 56.1 (2025). _eprint: https://sid.onlinelibrary.wiley.com/doi/pdf/10.1002/sdtp.18392, pp. 1186–1189. DOI: 10.1002/sdtp.18392.

[132] Cliff Jones. “Bistable Liquid Crystal Displays”. en. In: *Handbook of Visual Display Technology*. Springer, Berlin, Heidelberg, 2012, pp. 1507–1543. DOI: 10.1007/978-3-540-79567-4_92.

[133] Carl V. Brown. “Physical Properties of Nematic Liquid Crystals”. en. In: *Handbook of Visual Display Technology*. Springer, Berlin, Heidelberg, 2012, pp. 1343–1361. DOI: 10.1007/978-3-540-79567-4_84.

[134] Jong-In Baek et al. “P-173: Fast Turn-Off Switching of a Liquid Crystal Cell by Optically Hidden Relaxation”. en. In: *SID Symposium Digest of Technical Papers* 39.1 (2008). _eprint: https://sid.onlinelibrary.wiley.com/doi/pdf/10.1889/1.3069542, pp. 1846–1849. DOI: 10.1889/1.3069542.

[135] Tae-Hoon Choi, Jung-Wook Kim, and Tae-Hoon Yoon. “Fast gray-to-gray switching of a hybrid-aligned liquid crystal cell”. In: *Emerging Liquid Crystal Technologies X*. Vol. 9384. SPIE, Mar. 2015, pp. 176–182. DOI: 10.1117/12.2076542.

[136] Melanie Klasen-Memmer and Harald Hirschmann. “Liquid Crystal Materials for Devices”. en. In: *Handbook of Visual Display Technology*. Springer, Berlin, Heidelberg, 2014, pp. 1–21. DOI: 10.1007/978-3-642-35947-7_83-2.

[137] Esther Nabadda et al. “Ferroelectric liquid-crystal modulator with large switching rotation angle for polarization-independent binary phase modulation”. In: *Optics and Lasers in Engineering* 159 (Dec. 2022), p. 107204. DOI: 10.1016/j.optlaseng.2022.107204.

[138] J. W. Goodby. “Introduction to Defect Textures in Liquid Crystals”. en. In: *Handbook of Visual Display Technology*. Springer, Berlin, Heidelberg, 2012, pp. 1289–1314. DOI: 10.1007/978-3-540-79567-4_82.

[139] Lesley Parry Jones. “Alignment Properties of Liquid Crystals”. en. In: *Handbook of Visual Display Technology*. Springer, Berlin, Heidelberg, 2012, pp. 1387–1402. DOI: 10.1007/978-3-540-79567-4_86.

[140] J.C. Jones. “On the biaxiality of smectic C and ferroelectric liquid crystals”. In: *Liquid Crystals* 42.5-6 (June 2015), pp. 732–759. DOI: 10.1080/02678292.2015.1028492.

[141] Michael J. O’Callaghan et al. “Bistable FLCOS devices for doubled-brightness microprojectors”. en. In: *Journal of the Society for Information Display* 17.4 (2009). _eprint: https://onlinelibrary.wiley.com/doi/pdf/10.1889/JSID17.4.369, pp. 369–375. DOI: 10.1889/JSID17.4.369.

[142] D.J. Channin. “Optical waveguide modulation using nematic liquid crystal”. In: *Applied Physics Letters* 22.8 (Apr. 1973), pp. 365–366. DOI: 10.1063/1.1654675.

[143] D. J. Channin. “Liquid-Crystal Optical Waveguides”. en. In: *Introduction to Liquid Crystals*. Ed. by E. B. Priestley, Peter J. Wojtowicz, and Ping Sheng. Boston, MA: Springer US, 1975, pp. 281–295. DOI: 10.1007/978-1-4684-2175-0_15.

[144] J.P. Sheridan, J.M. Schnur, and T.G. Giallorenzi. “Electro-optic switching in low-loss liquid-crystal waveguides”. In: *Applied Physics Letters* 22.11 (June 1973), pp. 560–561. DOI: 10.1063/1.1654508.

[145] Chenming Hu and J. R. Whinnery. “Losses of a nematic liquid-crystal optical waveguide*”. EN. In: *JOSA* 64.11 (Nov. 1974). Publisher: Optica Publishing Group, pp. 1424–1432. DOI: 10.1364/JOSA.64.001424.

[146] Wei Yu Lee et al. “SSFLC optical directional coupler switch with a short device length: a proposal”. In: *Journal of Lightwave Technology* 13.11 (Nov. 1995), pp. 2236–2243. DOI: 10.1109/50.482043.

[147] Milica Notaros. “Integrated Visible-Light Platforms, Devices, and Systems for Augmented Reality and Beyond”. en. Accepted: 2023-11-02T20:16:48Z. Thesis. Massachusetts Institute of Technology, Sept. 2023.

[148] Lukas Van Iseghem et al. “Low power optical phase shifter using liquid crystal actuation on a silicon photonics platform”. EN. In: *Optical Materials Express* 12.6 (June 2022). Publisher: Optica Publishing Group, pp. 2181–2198. DOI: 10.1364/OME.457589.

[149] Katsumi Nakatsuhara, Akifumi Kato, and Yoshiki Hayama. “Latching operation in a tunable wavelength filter using Si sampled grating waveguide with ferroelectric liquid crystal cladding”. EN. In: *Optics Express* 22.8 (Apr. 2014). Publisher: Optica Publishing Group, pp. 9597–9603. DOI: 10.1364/OE.22.009597.

[150] Shin-Tson Wu and Khoon-Cheng Lim. “Absorption and scattering measurements of nematic liquid crystals”. EN. In: *Applied Optics* 26.9 (May 1987). Publisher: Optica Publishing Group, pp. 1722–1727. DOI: 10.1364/AO.26.001722.

[151] Antonio d’Alessandro and Rita Asquini. “Light Propagation in Confined Nematic Liquid Crystals and Device Applications”. en. In: *Applied Sciences* 11.18 (Jan. 2021). Number: 18 Publisher: Multidisciplinary Digital Publishing Institute, p. 8713. DOI: 10.3390/app11188713.

[152] T. G. Giallorenzi, J. A. Weiss, and J. P. Sheridan. “Light scattering from smectic liquid-crystal waveguides”. In: *Journal of Applied Physics* 47.5 (May 1976), pp. 1820–1826. DOI: 10.1063/1.322898.

[153] Salaheddine Toubi et al. “Study and validation of switchable grating using liquid crystal for active waveguide addressing”. In: *Emerging Liquid Crystal Technologies XVIII*. Vol. 12442. SPIE, Mar. 2023, pp. 58–66. DOI: 10.1117/12.2649749.

[154] Matthias Colard et al. “Study of a liquid crystal impregnated diffraction grating for active waveguide addressing”. In: *Emerging Liquid Crystal Technologies XVII*. Vol. 12023. SPIE, Mar. 2022, p. 1202302. DOI: 10.1117/12.2607475.

[155] lain W. Stewart. *The Static and Dynamic Continuum Theory of Liquid Crystals: A Mathematical Introduction*. 1st ed. CRC Press., 2004.

[156] Qian Wang et al. “Interactive finite-difference method for calculating the distribution of the liquid crystal director”. In: *Optical Engineering* 40.11 (Nov. 2001). Publisher: SPIE, pp. 2552–2557. DOI: 10.1117/1.1411974.

[157] Krzysztof P. Rola. “Anisotropic etching of silicon in KOH + Triton X-100 for 45° micromirror applications”. en. In: *Microsystem Technologies* 23.5 (May 2017), pp. 1463–1473. DOI: 10.1007/s00542-016-3103-0.

[158] A Brockmeier et al. “Surface tension and its role for vertical wet etching of silicon”. en. In: *Journal of Micromechanics and Microengineering* 22.12 (Nov. 2012). Publisher: IOP Publishing, p. 125012. DOI: 10.1088/0960-1317/22/12/125012.

[159] Krzysztof P. Rola et al. “Silicon 45° micromirrors fabricated by etching in alkaline solutions with organic additives”. en. In: *Microsystem Technologies* 20.2 (Feb. 2014), pp. 221–226. DOI: 10.1007/s00542-013-1859-z.

[160] Prem Pal et al. “High speed silicon wet anisotropic etching for applications in bulk micromachining: a review”. In: *Micro and Nano Systems Letters* 9.1 (Feb. 2021), p. 4. DOI: 10.1186/s40486-021-00129-0.

[161] P. Hariharan. *Optical Holography: Principles, Techniques and Applications*. 2nd ed. Cambridge Studies in Modern Optics. Cambridge: Cambridge University Press, 1996. DOI: 10.1017/CBO9781139174039.

[162] D. H. Close. “Holographic Optical Elements”. In: *Optical Engineering* 14.5 (Oct. 1975). Publisher: SPIE, pp. 408–419. DOI: 10.1117/12.7971806.

[163] Changwon Jang et al. “Design and fabrication of freeform holographic optical elements”. In: *ACM Trans. Graph.* 39.6 (Nov. 2020), 184:1–184:15. DOI: 10.1145/3414685.3417762.

[164] Johannes Hofmann et al. “Angle-compensated holographic wave front printing for the fabrication of holographic optical elements operating in the infrared”. In: *Optical Engineering* 59.10 (Dec. 2019). Publisher: SPIE, p. 102405. DOI: 10.1117/1.OE.59.10.102405.

[165] Paul Umbanhowar. “Patterns in the sand”. en. In: *Nature* 389.6651 (Oct. 1997). Publisher: Nature Publishing Group, pp. 541–542. DOI: 10.1038/39174.

[166] Boris Ya. Zel’dovich, Alexander V. Mamaev, and Vladimir V. Shkunov. *Speckle-Wave Interactions in Application to Holography and Nonlinear Optics*. CRC Press. 1995.

[167] Boris Ya Zel’dovich, V. V. Shkunov, and T. V. Yakovleva. “Holograms of speckle fields”. en. In: *Soviet Physics Uspekhi* 29.7 (July 1986). Publisher: IOP Publishing, p. 678. DOI: 10.1070/PU1986v029n07ABEH003464.

[168] W.R. Klein and B.D. Cook. “Unified Approach to Ultrasonic Light Diffraction”. In: *IEEE Transactions on Sonics and Ultrasonics* 14.3 (July 1967), pp. 123–134. DOI: 10.1109/T-SU.1967.29423.

[169] M. G. Moharam and L. Young. “Criterion for Bragg and Raman-Nath diffraction regimes”. EN. In: *Applied Optics* 17.11 (June 1978). Publisher: Optica Publishing Group, pp. 1757–1759. DOI: 10.1364/AO.17.001757.

[170] Chi Sun et al. “Investigation of -1st-order diffraction in conditions between thin and thick holograms”. EN. In: *Optics Express* 32.18 (Aug. 2024). Publisher: Optica Publishing Group, pp. 31130–31141. DOI: 10.1364/OE.528063.

[171] Pierre-Alexandre Blanche. *Field Guide to Holography*. SPIE. 2014.

[172] Martin Fally. *Diffraction theories for off-Bragg replay: J.T. Sheridan's seminal work and consequences*. URL: https://arxiv.org/abs/2411.13495.

[173] Naoya Uchida. “Calculation of diffraction efficiency in hologram gratings attenuated along the direction perpendicular to the grating vector”. EN. In: *JOSA* 63.3 (Mar. 1973). Publisher: Optica Publishing Group, pp. 280–287. DOI: 10.1364/JOSA.63.000280.

[174] Bernard C Kress. *Field Guide to Digital Micro-Optics*. SPIE. 2014.

[175] Herwig Kogelnik. “Coupled Wave Theory for Thick Hologram Gratings”. In: *Bell System Technical Journal* 48.9 (1969), pp. 2909–2947. DOI: 10.1002/j.1538-7305.1969.tb01198.x.

[176] D. Brotherton-Ratcliffe. “A treatment of the general volume holographic grating as an array of parallel stacked mirrors”. In: *Journal of Modern Optics* 59.13 (July 2012), pp. 1113–1132. DOI: 10.1080/09500340.2012.695405.

[177] David Brotherton-Ratcliffe et al. “Comparative study of the accuracy of the PSM and Kogelnik models of diffraction in reflection and transmission holographic gratings”. EN. In: *Optics Express* 22.26 (Dec. 2014). Publisher: Optica Publishing Group, pp. 32384–32405. DOI: 10.1364/OE.22.032384.

[178] Hans Bjelkhagen Brotherton-Ratcliffe David. *Ultra-Realistic Imaging: Advanced Techniques in Analogue and Digital Colour Holography*. Boca Raton: CRC Press, Mar. 2013. DOI: 10.1201/b14060.

[179] Pierre-Alexandre Blanche. “Chapter 1 - Introduction to Holographic Principles”. In: *Optical Holography*. Ed. by Pierre-Alexandre Blanche. Elsevier, Jan. 2020, pp. 1–39. DOI: 10.1016/B978-0-12-815467-0.00001-3.

[180] Zhenyu Li et al. “Volume holographic spectral imaging”. In: *Spectral Imaging: Instrumentation, Applications, and Analysis III*. Vol. 5694. SPIE, Mar. 2005, pp. 33–40. DOI: 10.1117/12.611350.

[181] Pengyu Liu et al. “Expanding field-of-view of near-to-eye display by hybrid angular and wavelength multiplexing”. EN. In: *Optics Express* 33.1 (Jan. 2025). Publisher: Optica Publishing Group, pp. 1466–1477. DOI: 10.1364/OE.546186.

[182] Wen-Kai Lin et al. “Crosstalk noise reduction of angle-multiplexed volume-holographic gratings for see-through lightguide display”. EN. In: *Optics Express* 33.10 (May 2025). Publisher: Optica Publishing Group, pp. 20951–20963. DOI: 10.1364/OE.562149.

[183] Takeru Utsugi et al. “[Paper] Volume Holographic Waveguide Using Multiplex Recording for Head-Mounted Display”. In: *ITE Transactions on Media Technology and Applications* 8.4 (2020), pp. 238–244. DOI: 10.3169/mta.8.238.

[184] Hiroshi Mukawa et al. “A full-color eyewear display using planar waveguides with reflection volume holograms”. en. In: *Journal of the Society for Information Display* 17.3 (2009). _eprint: https://sid.onlinelibrary.wiley.com/doi/pdf/10.1889/JSID17.3.185, pp. 185–193. DOI: 10.1889/JSID17.3.185.

[185] Michael R Gleeson and John T Sheridan. “A review of the modelling of free-radical photopolymerization in the formation of holographic gratings”. en. In: *Journal of Optics A: Pure and Applied Optics* 11.2 (Jan. 2009), p. 024008. DOI: 10.1088/1464-4258/11/2/024008.

[186] Friedrich-Karl Bruder, Thomas Fäcke, and Thomas Rölle. “The Chemistry and Physics of Bayfol® HX Film Holographic Photopolymer”. en. In: *Polymers* 9.10 (Oct. 2017). Number: 10 Publisher: Multidisciplinary Digital Publishing Institute, p. 472. DOI: 10.3390/polym9100472.

[187] Friedrich-Karl Bruder et al. “A standardized NIR sensitized Bayfol HX film”. In: *Photosensitive Materials and their Applications III*. Vol. 13015. SPIE, June 2024, pp. 23–34. DOI: 10.1117/12.3016779.

[188] Hans I. Bjelkhagen. “Introduction”. en. In: *Silver-Halide Recording Materials: for Holography and Their Processing*. Ed. by Hans I. Bjelkhagen. Berlin, Heidelberg: Springer, 1995, pp. 1–12. DOI: 10.1007/978-3-540-70756-1_1.

[189] Philippe Gentet, Yves Gentet, and Seung-Hyun Lee. “Ultimate 04 the new reference for ultra-realistic color holography”. In: *2017 International Conference on Emerging Trends & Innovation in ICT (ICEI)*. Feb. 2017, pp. 162–166. DOI: 10.1109/ETIICT.2017.7977030.

[190] Masahiro Yamaguchi, Nagaaki Ohyama, and Toshio Honda. “Holographic three-dimensional printer: new method”. EN. In: *Applied Optics* 31.2 (Jan. 1992). Publisher: Optica Publishing Group, pp. 217–222. DOI: 10.1364/AO.31.000217.

[191] Hiroshi Yoshikawa and Takeshi Yamaguchi. “Review of Holographic Printers for Computer-Generated Holograms”. In: *IEEE Transactions on Industrial Informatics* 12.4 (Aug. 2016), pp. 1584–1589. DOI: 10.1109/TII.2015.2475722.

[192] Jinsoo Jeong et al. “Holographically customized optical combiner for eye-box extended near-eye display”. EN. In: *Optics Express* 27.26 (Dec. 2019). Publisher: Optica Publishing Group, pp. 38006–38018. DOI: 10.1364/OE.382190.

[193] Philippe Gentet, Yves Gentet, and Seunghyun Lee. “An in-house-designed scanner for CHIMERA holograms”. In: *Practical Holography XXXVII: Displays, Materials, and Applications*. Vol. 12445. SPIE, Mar. 2023, pp. 79–83. DOI: 10.1117/12.2648520.

[194] Yves Gentet and Philippe Gentet. “CHIMERA, a new holoprinter technology combining low-power continuous lasers and fast printing”. EN. In: *Applied Optics* 58.34 (Dec. 2019). Publisher: Optica Publishing Group, G226–G230. DOI: 10.1364/AO.58.00G226.

[195] Christophe Martinez et al. “Sparse holographic imaging for an integrated augmented reality near-eye display”. EN. In: *Applied Optics* 62.8 (Mar. 2023). Publisher: Optica Publishing Group, pp. 1928–1938. DOI: 10.1364/AO.478849.

[196] Benjamin Chrysler and Raymond K. Kostuk. “Fabrication and replication of volume holographic optical elements”. en. US20210232092A1. July 2021.

[197] Makoto Okui et al. “Copying of holograms by spot scanning approach”. EN. In: *Applied Optics* 57.15 (May 2018). Publisher: Optica Publishing Group, pp. 4117–4122. DOI: 10.1364/AO.57.004117.

[198] V. A. Vanin. “Hologram copying (review)”. en. In: *Soviet Journal of Quantum Electronics* 8.7 (July 1978). Publisher: IOP Publishing, p. 809. DOI: 10.1070/QE1978v008n07ABEH010419.

[199] D. B. Brumm. “Copying Holograms”. EN. In: *Applied Optics* 5.12 (Dec. 1966). Publisher: Optica Publishing Group, pp. 1946–1947. DOI: 10.1364/AO.5.001946.

[200] Peter Nicholson. “Apparatus and method for holographic contact copying”. US4416540A. Nov. 1983.

[201] M. J. Landry. “The Effect of Two Hologram-Copying Parameters on the Quality of Copies”. EN. In: *Applied Optics* 6.11 (Nov. 1967). Publisher: Optica Publishing Group, pp. 1947–1956. DOI: 10.1364/AO.6.001947.

[202] Christophe Martinez et al. “3-4: Holography and Photonic Integrated Circuit: an Alternative Technology for Power-Efficient Near-Eye Display Architecture”. en. In: *SID Symposium Digest of Technical Papers* 56.1 (2025), pp. 11–14. DOI: 10.1002/sdtp.18071.

[203] Nihar Mohanty et al. “The evolution of display materials and processes for full augmented reality”. In: *Optical Architectures for Displays and Sensing in Augmented, Virtual, and Mixed Reality (AR, VR, MR) VI*. Vol. PC13414. SPIE, Mar. 2025, PC1341409. DOI: 10.1117/12.3041338.

[204] Andreas Georgiou et al. “A holographic near-eye display with glass form factor and spectacle-free operation”. In: *Digital Optical Technologies 2023*. Vol. 12624. SPIE, Aug. 2023, pp. 10–18. DOI: 10.1117/12.2679479.

[205] J. Smith Warren. *Modern Optical Engineering*. 3rd. McGraw-Hill, 2000.

[206] Jean-Louis Meyzonnette. *Radiométrie et sources non cohérentes*. Frensh. 1995. URL: https://www.techniques-ingenieur.fr.

[207] R. John Koshel. *Illumination Engineering: Design with Nonimaging Optics*. Wiley-IEEE Press. 2013.

[208] Seungjae Lee et al. “Analysis and Implementation of Hologram Lenses for See-Through Head-Mounted Display”. In: *IEEE Photonics Technology Letters* 29.1 (Jan. 2017), pp. 82–85. DOI: 10.1109/LPT.2016.2628906.

[209] Donald C. O’Shea and Julie L. Bentley. *Designing Optics Using Zemax OpticStudio®*. SPIE. 2024.

[210] Alessandra Croce, Michael Cheng, and Erin Elliott. *How to model holograms in OpticStudio*. en-US. URL: https://optics.ansys.com/hc/en-us/articles/42661708003347-How-to-model-holograms-in-OpticStudio.

[211] W. T. Welford. “A vector raytracing equation for hologram lenses of arbitrary shape”. In: *Optics Communications* 14.3 (July 1975), pp. 322–323. DOI: 10.1016/0030-4018(75)90327-2.

[212] Robert B. Wood and Michael J. Hayford. “Holographic And Classical Head Up Display Technology For Commercial And Fighter Aircraft”. In: *Holographic Optics: Design and Applications*. Vol. 0883. SPIE, Apr. 1988, pp. 36–52. DOI: 10.1117/12.944123.

[213] Michel Guillon et al. “The Effects of Age, Refractive Status, and Luminance on Pupil Size”. In: *Optometry and Vision Science* 93.9 (Sept. 2016), pp. 1093–1100. DOI: 10.1097/OPX.0000000000000893.

[214] Jie Chen et al. “Design of foveated contact lens display for augmented reality”. EN. In: *Optics Express* 27.26 (Dec. 2019). Publisher: Optica Publishing Group, pp. 38204–38219. DOI: 10.1364/OE.381200.

[215] Ozan Cakmakci, David M. Hoffman, and Nikhil Balram. “31-4: Invited Paper: 3D Eyebox in Augmented and Virtual Reality Optics”. en. In: *SID Symposium Digest of Technical Papers* 50.1 (2019). _eprint: https://onlinelibrary.wiley.com/doi/pdf/10.1002/sdtp.12950, pp. 438–441. DOI: 10.1002/sdtp.12950.

Appendix A

Asymetric coupling

Our extraction component originated as an idea based on the directional coupler. The mode in the waveguide is coupled into a different structure with distinct geometry and a different material (the liquid crystal). This configuration is considered an asymmetric coupling. Phase matching in this case needs to be achieved either by tuning the geometries or by adjusting the material. However, in our coupling mechanism, we moved from structures with two-mode coupling between two waveguides to the coupling between a guided mode and a radiation direction, since the second structure can be regarded as a lightguide rather than a conventional waveguide. The coupling condition in this case is simply $n_{\text{eff}} \geq n_{\text{LC}}$.

In this appendix, I present some theoretical elements and a simulation of *asymmetric* coupling in a directional coupler under both phase-matching (PM) and off-phase-matching conditions. I referred to this type of coupling as parallel. This can be regarded as supplementary material for Chapter 2.

The equations presented here can be found in K. J. Ebeling* and J. M. Liu†.

Let us consider a simple case involving the coupling between only two modes: a guided mode a with propagation constant β_a, and a guided mode b with propagation constant β_b, in waveguides a and b. This is illustrated in the following Figure A.1(a).

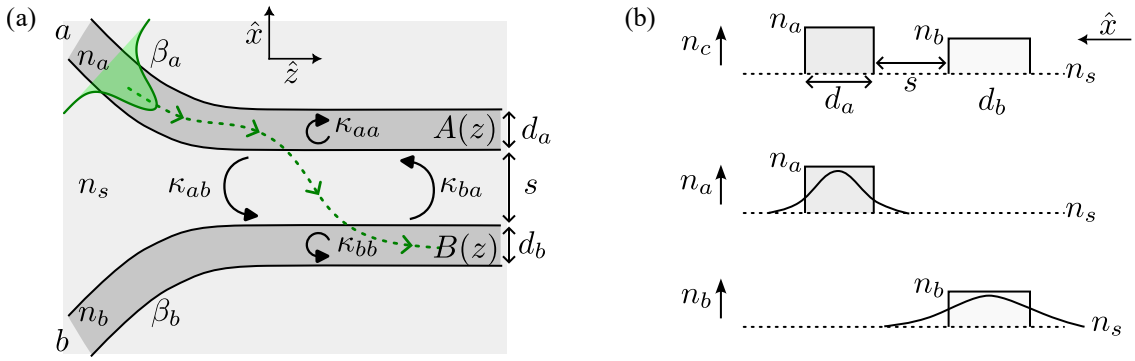

Figure A.1: (a) Schematic of the coupling between two modes and the associated coupling constants. (b) Refractive index profile in the coupling region and in the unperturbed waveguides (cf. K. J. Ebeling, Fig. 6.2, p. 145).

In the coupling region, we assume a weak perturbation; that is, the transverse fields $\mathbf{E}_a(x, y)$

*Karl Joachim Ebeling. *Integrated Optoelectronics*. Berlin, Heidelberg: Springer, 1993. link:doi.

†Jia-ming Liu. *Photonic Devices*. Cambridge: Cambridge University Press, 2005. link:doi.

and $\mathbf{E}_b(x, y)$ are not significantly affected. The variation occurs primarily along the propagation direction and is described by two amplitude coefficients, $A(z)$ and $B(z)$.

The total field in the coupling region can then be written as:

$$\mathbf{E}(x, y, z) = A(z)\,\hat{\mathbf{E}}_a(x, y)\,\exp\{i\beta_a z\} + B(z)\,\hat{\mathbf{E}}_b(x, y)\,\exp\{i\beta_b z\}\,, \tag{A.1}$$

Coupled-mode equations of the two-mode coupling can be written as:

$$\begin{aligned} \frac{dA}{dz} &= i\kappa_{aa}A + i\kappa_{ab}Be^{i(\beta_b-\beta_a)z}, \\ \frac{dB}{dz} &= i\kappa_{bb}B + i\kappa_{ba}Ae^{i(\beta_a-\beta_b)z}. \end{aligned} \tag{A.2}$$

As we can see, A is affected by itself through the coefficient κ_{aa}, and influenced by B through the coefficient κ_{ab}. The self-coupling terms describe the fact that, due to the evanescent field, the normal mode experience an index profile that differs from that of the original waveguide. This modifies the propagation constants of the modes by $\delta\beta$. We can express the coefficients κ_{aa} and κ_{bb} in the following intuitive form:

$$\kappa_{aa} = \delta\beta_a \quad \text{and} \quad \kappa_{bb} = \delta\beta_b. \tag{A.3}$$

The coefficients κ_{ab} and κ_{ba} are the coupling coefficients from mode a to mode b, and from mode b to mode a, respectively.

In the coupling region, waveguide b introduces a perturbation to waveguide a, which can be described by (see Figure A.2(b)):

$$\Delta\epsilon_a(x, y) = n_c^2(x, y) - n_a^2(x, y). \tag{A.4}$$

In a similar way, we have

$$\Delta\epsilon_b(x, y) = n_c^2(x, y) - n_b^2(x, y). \tag{A.5}$$

The change in propagation constant can be written as follow:

$$\delta\beta_a = \omega\epsilon_0 \int_{-\infty}^{\infty}\int_{-\infty}^{\infty} \Delta\epsilon_a(x, y)\left|\hat{\mathbf{E}}_a(x, y)\right|^2\,dx\,dy \tag{A.6}$$

The change depends on the self-overlap of the transverse field, but only within the region where the perturbation from waveguide b is present. Outside waveguide a, the field decays exponentially as $\exp(-\gamma_a x)$. Consequently, the variation $\delta\beta_a$ depends on the separation s and follows an exponential trend: $\delta\beta_a \propto \exp(-2\gamma_a s)$.

$$\kappa_{ab} = \omega\epsilon_0 \int_{-\infty}^{\infty}\int_{-\infty}^{\infty} \Delta\epsilon_b(x, y)\hat{\mathbf{E}}_a^*(x, y)\cdot\hat{\mathbf{E}}_b(x, y)\,dx\,dy \tag{A.7}$$

The coupling coefficient κ_{ab} depends on the overlap between the transverse fields of mode a and mode b. To couple from a to b, the perturbation considered is $\Delta\epsilon_b(x, y)$, induced by waveguide a. The integration is performed only over the region of waveguide a, where the field of mode b is evanescent.

As a result, κ_{ab} depends on the separation s between the waveguides and follows an exponential trend: $\kappa_{ab} \propto \exp(-\gamma_b s)$.

By exchanging the subscripts a and b, one obtains the coupling coefficient κ_{ba}, which describes the coupling from mode b to mode a, with the perturbation now induced by the waveguide a. A single coupling coefficient can also be defined as $\kappa = \kappa_{ab} = \kappa_{ba}^*$. This relation holds for symmetric waveguides or when the two modes are coupled within the same waveguide. However, this symmetry does not generally apply when waveguides a and b have different geometries or refractive indices. In such cases, the mode profiles and the spatial perturbations differ, and the coupling is no longer symmetric.

Here is an expression for the coupling constant κ for the fundamental modes in a symmetric waveguide under weak perturbation, (cf. K. J. Ebeling, Eq. 6.33, p. 149):

$$\kappa = 2\frac{\sqrt{n_1^2 - n_s^2}}{n_{\text{eff}}\, d_{\text{eff}}} \exp\left\{-|\gamma|\left(s + \frac{d}{2}\right)\right\} \tag{A.8}$$

Where $n_1 = n_a = n_b$, $d = d_a = d_b$, and $\gamma = k\sqrt{n_{\text{eff}}^2 - n_s^2}$, where n_s is the substrate refractive index. d_{eff} is the effective thickness of the mode.

For a constant perturbation, such as in a directional coupler, we can define the phase mismatch parameter δ using coupled-mode theory. The coupling between the two modes is most efficient when the interaction is phase-matched, i.e., when $\delta = 0$.

$$2\delta = \beta_b + \delta\beta_b - \beta_a - \delta\beta_a \approx \Delta n_{\text{eff}} k \tag{A.9}$$

Consider the initial condition where the power is in waveguide a before entering the coupling region: $A(z = 0) = A_0$ and $B(z = 0) = 0$.

The efficiency of the coupling can be written as:

$$\eta = \left|\frac{B(z)}{A(0)}\right|^2 = \frac{1}{1 + \left|\frac{\delta}{\kappa}\right|^2} \sin^2\left(\kappa.z\sqrt{1 + \left|\frac{\delta}{\kappa}\right|^2}\right) \tag{A.10}$$

For symmetric waveguides (i.e., waveguides a and b having the same geometry and materials), the phase-matching condition ($\delta = 0$) is always satisfied, regardless of the wavelength. The maximum coupling efficiency at the coupling length reaches 1. Only the coupling length itself depends on the wavelength.

However, for waveguides with different characteristics, the coupler is asymmetric, and the phase-matching condition is not automatically satisfied. The propagation constants, or equivalently the effective indices of the two waveguides, exhibit different dependencies on the wavelength. If the two waveguides have different core refractive indices, one may tune the geometry of one waveguide to match the effective indices and achieve phase matching.

Consider an example where the waveguide a has a core index $n_1 = 1.9$, a thickness $d_1 = 0.2$ μm, and surrounding indices $n_0 = n_2 = 1.5$. The second waveguide has a different core index of $n_1 = 1.8$. Neglecting the self-coupling coefficients κ_{12} and κ_{21}, we assume that the phase-matching condition is directly related to the difference in effective indices, as expressed in Equation (A.9).

In Figure A.2(a), this difference is plotted as a function of the thickness d_2 of waveguide b. At the wavelength of interest ($\lambda = 532$ nm), phase matching is achieved for $d_2 = 0.445$ μm.

In Figure A.2(b), the dispersion of the effective indices is plotted as a function of wavelength for the two waveguides. The curves intersect at the wavelength where phase matching occurs.

On the secondary y-axis (in red), the corresponding phase mismatch 2δ (in μm^{-1}) is also plotted. The point $\delta = 0$ indicates the phase-matching condition, which occurs at a wavelength of 532 nm.

For a fixed coupling length ℓ_c^{PM} (at 532 nm), the coupling efficiency reaches 1. Equation (A.10) can then be used to evaluate the drop in efficiency at other wavelengths for the same coupling length. Let us assume $\kappa(\lambda) = \kappa(532\text{ nm})$ is constant and fix $z = \ell_c^{\text{PM}}$. The resulting efficiency is plotted in Figure A.2(c) as the solid black curve, titled "Coupled-mode theory (PM)", where PM stands for phase-matched.

Since the assumption of a constant κ is a strong approximation, a 2D FDTD simulation was also performed. The corresponding result is plotted in blue with circle markers and labeled "FDTD (PM)". Similarly, another simulation was carried out with a change in the waveguide thickness from the phase-matched value $d_2^{\text{PM}} = 0.445\ \mu$m to a non-phase-matched value $d_2^{\text{NPM}} = 0.495\ \mu$m (a difference of 50 nm). The result is shown as a red curve labeled "FDTD (NPM)", where NPM stands for non-phase-matched.

In the FDTD-simulated case, the efficiency width at half-maximum in phase matching is around 95 nm. The approximated curve from the efficiency equation gives 113 nm. The approximation of a constant κ over the wavelength can still be used to gain some insight.

An error variation of 50 nm in the thickness causes a drop in efficiency around the wavelength of interest, from 100% to 70%, and results in a shift of the curve. In the simulated curves, the efficiency re-oscillates around 0.6–0.7 µm. In fact, the coupling efficiency given by Equation (A.10) can exhibit oscillations due to the sine factor, especially since both the phase mismatch $\delta(\lambda)$ and the coupling coefficient $\kappa(\lambda)$ are wavelength-dependent. The solid curve does not capture the re-oscillations due to the assumption of a constant κ.

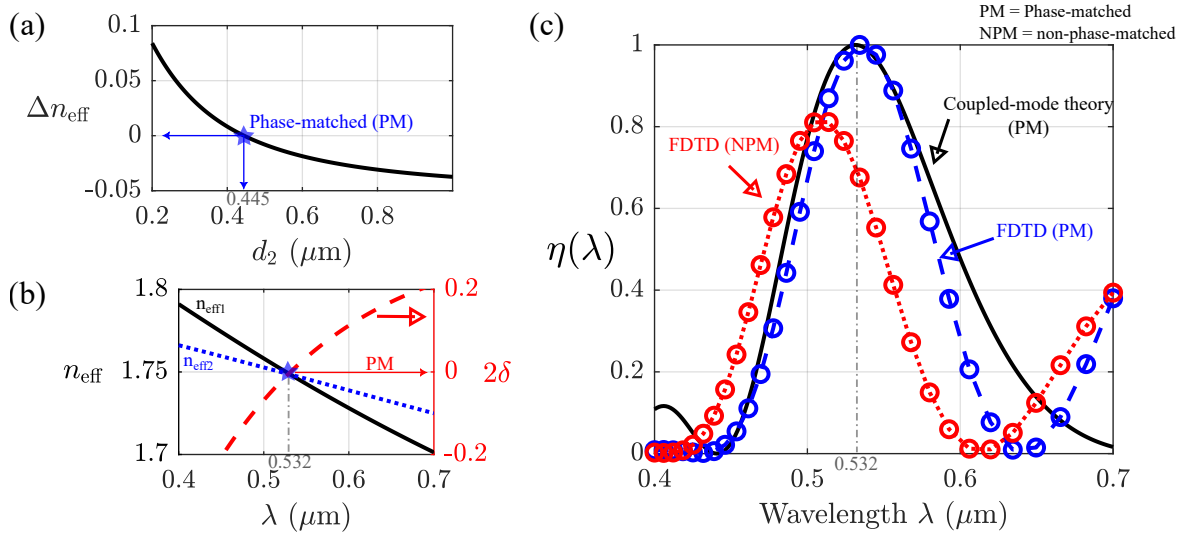

Figure A.2: (a) Difference between the effective indices of the two waveguides as the thickness d_2 of waveguide b varies. (b) Effective indices of the two waveguides as a function of wavelength. (c) Coupling efficiency as a function of wavelength for a phase-matched case; solid black is theory, blue is the FDTD simulation, and red corresponds to the non–phase-matched case obtained by varying the waveguide thickness away from the PM condition.

It might be interesting to study the dependence of κ on the wavelength. Figure A.3 shows, in the solid black curve, the theoretical coupling coefficient given by Equation (A.8) for a symmetric waveguide with $d = s = 0.2\ \mu$m and $n_a = n_b = 1.9$. The theoretical coupling

coefficient κ_{theo} increases with wavelength, which indicates that the evanescent field outside the waveguide becomes more extended.

The evanescence is related to the quantity $\gamma = k\sqrt{n_{\text{eff}}^2 - n_s^2}$, which depends on both the effective index $n_{\text{eff}}(\lambda)$ and the inverse of the wavelength $(1/\lambda)$. For this geometry and in the considered wavelength range, as the wavelength increases, n_{eff} decreases more rapidly than λ, leading to a smaller γ, and thus a deeper penetration of the evanescent field..

The dashed red and blue curves uses the expression $\kappa = (\beta_{\text{even}} - \beta_{\text{odd}})/2$, where β_{even} and β_{odd} are the propagation constants of the two fundamental supermodes[‡]. This value of κ, which we denote as κ_{num}, is more accurate. We compute it numerically.

In the symmetric case, κ_{theo} deviates from κ_{num} for wavelengths above 0.5 μm. As the wavelength increases, the evanescent field becomes more extended, leading to stronger coupling. However, κ_{theo} is only valid under weak coupling.

In the asymmetric case ($n_b = 1.8$, $d_b = 0.445$ μm), the theoretical expression for κ is not applicable at all, and only a supermode analysis can be used. The blue dashed curve shows the variation of the coupling coefficient as a function of the wavelength.

This structure is phase-matched at 532 nm; the coupling coefficient at this wavelength is $\kappa = 0.07$ μm^{-1}, which corresponds to a coupling length of $\ell_c^{\text{PM}} = \frac{\pi}{2\kappa} = 22.4$ μm.

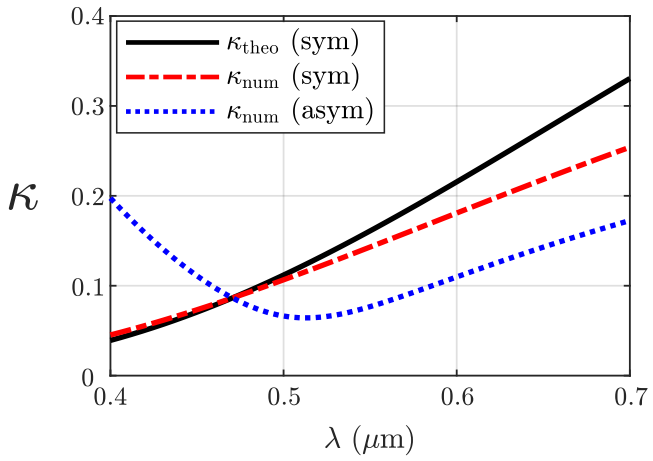

Figure A.3: The coupling constant κ as a function of wavelength.

[‡]In a two-waveguide structure, a new set of eigenmodes (normal modes) can be calculated. The incident mode can be expressed as a linear combination of these supermodes. It can be shown that $\kappa = (\beta_{\text{even}} - \beta_{\text{odd}})/2$. You can use https://www.computational-photonics.eu/oms.html to compute these even and odd eigenvalues.

Résumé en français

Résumé Chapitre 1

Le contexte est celui des dispositifs d'affichage proches de l'œil, ou *near-eye displays* (NEDs). La Fig. R.1(a) illustre un exemple d'application; une paire de lunettes informatives intégrant un écran. Le facteur de forme constitue l'un des défis technologiques dans la conception et la fabrication de ces dispositifs.

Dans des conditions d'application de la réalité augmentée, il est nécessaire que l'image projetée soit suffisamment visible dans des conditions extérieures lumineuses, sans que cela ne se fasse au détriment d'une forte consommation électrique ni de la taille de la batterie.

La Fig. R.1(b) illustre les pertes optiques d'une solution conventionnelle. On obtient environ 40 dB de pertes, ce qui signifie qu'un photon atteint la rétine pour 10 000 photons émis à la surface de l'écran.

Une solution conventionnelle utilise par example un écran miniaturisé (micro-écran) de taille inférieure à 1 cm^2, dérivé d'une technologie d'écran classique (écran domestique ou autre). Cependant, ses propriétés d'émission ne sont pas adaptées, car l'architecture des NEDs comporte un système optique entre l'œil et le micro-écran. Il faut donc raisonner à l'inverse : selon l'application visée (ici les NEDs), un nouveau type d'écran doit être développé.

Dans le chapitre 1, je revisite les source d'image classiques pour NEDs offrant une forte luminance : le *Laser Beam Scanning* (LBS), le *Liquid Crystal on Silicon* (LCoS) et les microLEDs inorganiques, ainsi que leurs principes de fonctionnement, limitations et avantages. Je présente également les solutions émergentes, notamment LCoS avec une illumination laser. J'analyse l'efficacité optique en me basant sur le schéma de raisonnement constitué des trois blocs présentés dans la Fig. R.1(c) : l'efficacité lumineuse à la surface (combien de lumens sont produits pour 1 W électrique), l'efficacité de couplage dans le système optique, et la taille de la boîte à œil. La boîte à œil, ou *EyeBox*, correspond à la taille de la fenêtre située au niveau de l'œil, pour observer l'image virtuelle : plus elle est grande, plus l'utilisation est confortable. Toutefois, une taille plus large disperse les rayons sur une plus grande surface, ce qui réduit la luminance, à puissance d'émission constante.

Les blocs 2 et 3 représentent les source de pertes les plus importantes. En effet, dans l'exemple des 40 dB de pertes, le micro-écran LCoS est illuminé par une LED lambertienne (divergence d'émission $\beta = 90°$). L'efficacité de couplage est de 11,5 dB, et pour la boîte à œil, l'efficacité de couplage dans l'œil est de 13,2 dB.

La solution proposée dans cette thèse est intitulée *écran directif*, comme montré dans la Fig. R.1(d). Chaque pixel possède une direction fixe γ et une divergence β. L'architecture de cette solution (Fig. R.1(e)) repose sur un circuit optique intégré (PIC) et des éléments holographiques. Une diode laser est couplée dans un guide d'onde puis divisée en une série de guides formant des lignes. L'affichage est séquentiel, avec l'activation colonne par colonne. Le

niveau d'intensité dans chaque ligne est modulé par un étage de modulation.

La lumière est extraite du guide d'onde vers l'espace libre grâce à un *composant d'extraction*, qui constitue l'un des sujets clés de cette thèse. Une fois extraite, la lumière est redirigée par un élément holographique dans une direction fixe.

La Fig. R.1(e) montre le schéma d'un élément holographique en réflexion. La pixelisation de l'hologramme en petits éléments de l'ordre de quelques dizaines de microns, ainsi que le codage d'une fonction optique définissant l'angle γ, constituent l'autre sujet central.

Le chapitre 1 donne davantage de détails sur l'architecture de cette solution ainsi que d'autres analyses (défis, pertes optiques, dimensionnements, etc.). Les pertes optiques sont estimées autour de 20 dB, soit une efficacité environ 100 fois supérieure à celle d'une approche conventionnelle. La directivité permet non seulement de coupler efficacement la lumière dans le système optique, mais également de contrôler la forme de la boîte à œil.

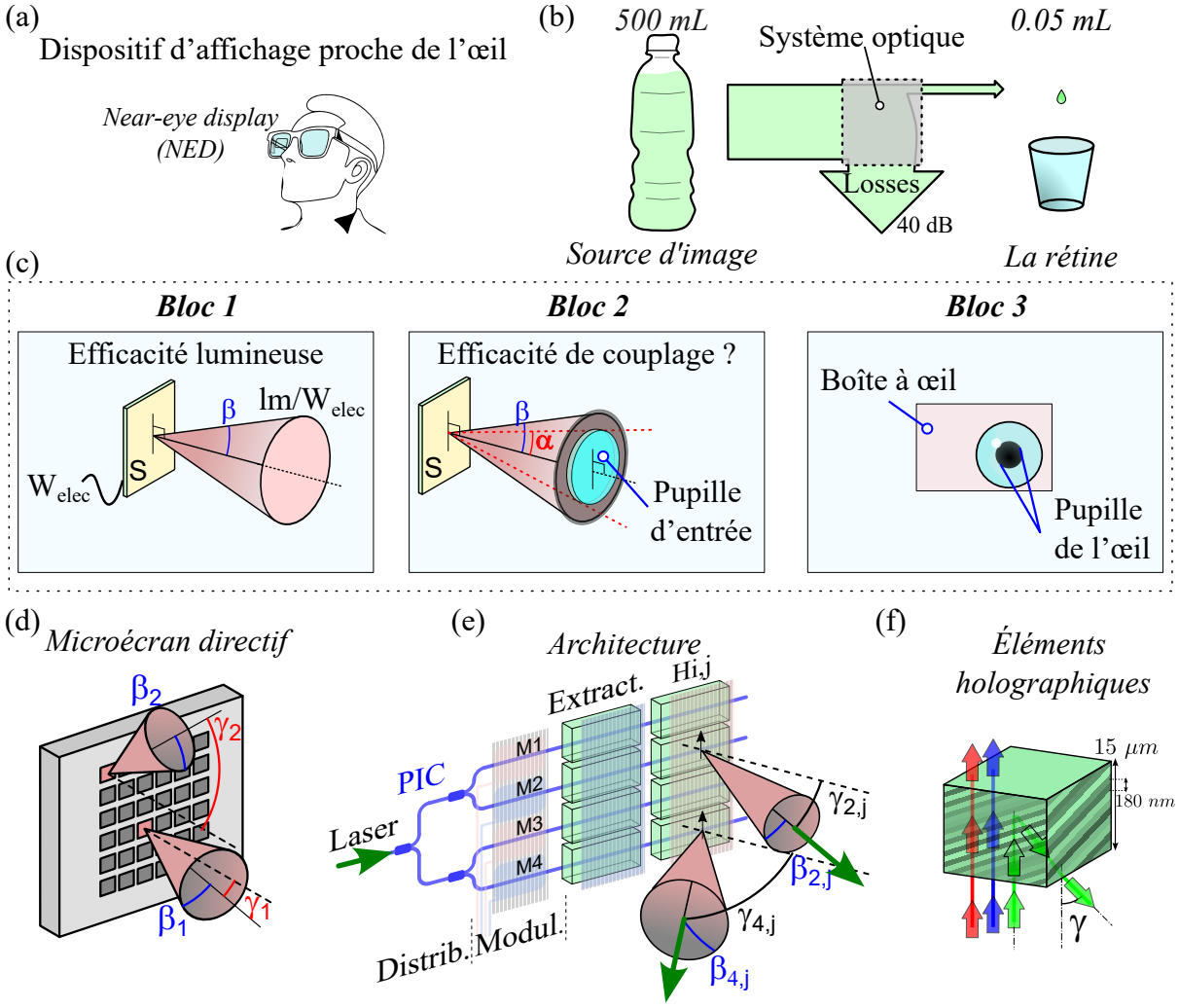

Figure R.1: (a) Contexte applicatif : les dispositifs d'affichage proches de l'œil (lunettes et casques). (b) Analogie illustrant les pertes optiques dans les solutions conventionnelles. (c) L'efficacité optique dans ce type d'application se décompose en trois blocs. (d) Notre solution d'écran directif, où chaque pixel est indépendant et possède une direction ainsi qu'une divergence bien définies. (e) Architecture de la solution basée sur un circuit photonique (PIC) et l'holographie. (f) Élément holographique utilisé pour redéfinir les propriétés d'émission, telles que la direction γ.

Résumé Chapitre 2

La lumière guidée dans notre circuit optique intégré doit être extraite vers l'espace libre à travers un composant d'extraction électriquement activable. Ceci est illustré en Fig. R.2(a). Un cahier des charges doit être respecté, notamment une taille de pixel de l'ordre de 10 μm, une extraction maximale de puissance, et la directivité (extarction uniquement vers le haut).

Un paramètre important, α_r (en μm^{-1}), que j'appelle taux de fuite ou *radiation decay constant*, est utilisé pour caractériser les performances. Le schéma (b) montre un bloc utilisé pour perturber la propagation et provoquer l'extraction. On y observe que, dans ce régime, l'*amplitude* du signal décroît selon $\exp(-\alpha_r z)$. La quantité $1/\alpha_r$ correspond à une longueur caractéristique d'extraction, associée à une extraction de *puissance* de 86.5% sur cette distance (soit $1 - e^{-2}$).

La première solution, abandonnée au profit de notre approche innovante, est celle d'un réseau de diffraction placé au-dessus du guide. La Fig. R.2(c) illustre ce réseau périodique permettant de diffracter le signal guidé vers l'espace libre. On remarque la non-directivité de cette solution.

Dans cette solution, l'extraction est activée par la perturbation due au contraste d'indice de réfraction entre les rainures, d'indice n_r, et le superstrat en cristal liquide, d'indice n_{CL}. En effet, le taux de fuite α_r est proportionnel à l'écart quadratique entre ces valeurs d'indice :

$$\alpha_r \propto (n_r^2 - n_{\text{CL}}^2)^2 \tag{R.1}$$

De manière évidente, l'effet réseau est annulé lorsque $n_r = n_{\text{CL}}$.

Dans la Fig. R.2(c), une courbe montre α_r en fonction de la profondeur de gravure. Le contraste d'indice dans cet exemple est élevé et égal à 0,5. Le taux de fuite atteint une valeur de 0,01 μm^{-1}, soit une longueur caractéristique d'environ 100 μm. Cette distance est trop grande, et la solution n'est donc pas adaptée à notre cahier des charges.

Le schéma de la Fig. R.2(d) présente notre solution innovante, brevetée dans le cadre de cette thèse. Localement, l'indice n_3 est augmenté dans la zone (2), de telle sorte que $n_3 > n_{\text{eff}}$, où n_{eff} est l'indice effectif du mode. Un couplage évanescent a alors lieu dans cette couche à haut indice. Une structure prismatique dans la zone (3) permet, par réflexion totale interne, de dévier le signal vers l'espace libre.

Le couplage évanescent est caractérisé par la séparation s et par la partie évanescente du mode guidé, décrite à travers la composante transverse $\gamma = \frac{2\pi}{\lambda}\sqrt{n_{\text{eff}}^2 - n_2^2}$. La quantité $1/\gamma$ (en μm) correspond à une longueur caractéristique d'évanescence. Le taux de fuite α_r de cette solution suit une tendance de forme exponentielle :

$$\alpha_r \propto \exp(-2\gamma s) \tag{R.2}$$

Le processus d'activation est illustré dans la Fig. R.2(e) : l'indice est modifié localement par l'activation d'une électrode. La Fig. R.2(f) montre la décomposition de la structure : (A) le circuit optique intégré, (B) la puce contenant les structures prismatiques, et entre les deux, un cristal liquide (C) est encapsulé. Les prismes jouent également le rôle d'espaceur.

Dans la Fig. R.2(g), le taux de fuite est représenté en fonction de l'indice n_3. Le seuil de couplage correspond à l'indice effectif du mode. La valeur de α_r atteint des ordres de grandeur de 0,1 μm^{-1}, soit dix fois supérieure à la solution précédente. La longueur caractéristique d'extraction devient alors inférieure à 10 μm. La solution est donc adaptée à notre cahier des charges.

On trouve dans le chapitre 2 d'autres analyses, telles que la divergence d'extraction, le coefficient d'extinction de polarisation du signal extrait, la dépendance en longueur d'onde, etc. Par exemple, la divergence dans la direction de propagation est liée à $1/\alpha_r$, tandis que dans la direction perpendiculaire, elle dépend de la taille effective du mode d_{eff}. En effet, la divergence ou champ lointain est directement reliée au champ proche d'extraction, dont l'extension caractéristique est déterminée par $(d_{\text{eff}}, 1/\alpha_r)$.

Je veille, dans mes analyses, à fournir des équations théoriques implémentables sur Matlab ou d'autres outils, afin d'estimer facilement des ordres de grandeur de $\alpha_r(s, \lambda, n_3, d)$. Je compare les résultats théoriques et les simulations FDTD tout au long du chapitre.

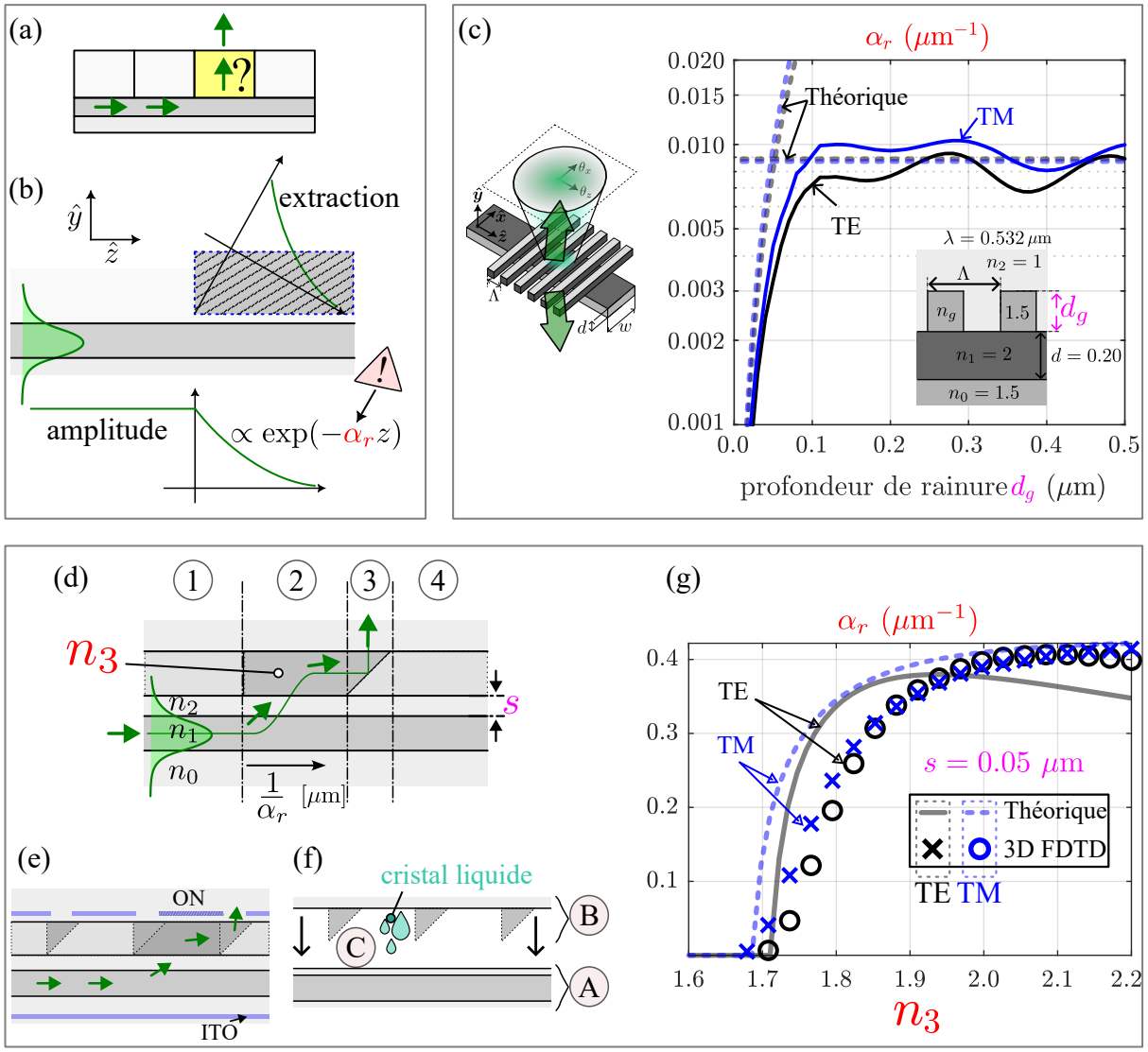

Figure R.2: (a) Schéma d'extraction localisée au niveau du pixel. (b) Introduction d'une perturbation constante pour extraire le mode guidé et définition du taux de fuite α_r. (c) Manque de directivité pour un réseau de diffraction, et courbes de α_r en fonction de la profondeur de gravure des rainures. (d) Principe de notre composant innovant : extraction par couplage évanescent suivie d'une réflexion totale interne vers l'espace libre. (e) Activation par électrodes. (f) Décomposition de la structure avec (A) la puce photonique, (B) la puce contenant les structures prismatiques, et (C) le cristal liquide. (g) Exemple de valeurs de α_r en fonction de n_3.

Résumé Chapitre 3

Dans le cahier des charges d'extraction, un besoin de commutation rapide de l'ordre de 100 μs a été identifié. Ce chapitre commence par une revue du principe des cristaux liquides ferroélectriques (FLC), qui répondent à cette exigence de vitesse.

Un matériau ferroélectrique est un diélectrique présentant une polarisation macroscopique en l'absence de toute influence extérieure. Un FLC est un cristal liquide dans la phase smectique C chirale. La chiralité brise la symétrie et entraîne l'apparition d'une polarisation spontanée hélicoïdale. Toutefois, pour obtenir une polarisation spontanée macroscopique, une cellule dite SSFLC (Fig. R.3(a)), pour *Surface-Stabilized Ferroelectric Liquid Crystal*, est utilisée : elle permet de bloquer l'hélicité et de conserver une polarisation spontanée macroscopique. L'épaisseur de la cellule doit rester faible (environ 2 μm).

Dans ce chapitre, j'analyse l'ensemble du composant avec le prisme. En effet, en se référant à la Fig. R.3(b), on observe que le couplage évanescent d'angle θ est incident sur le flanc incliné d'angle α. Deux conditions doivent être satisfaites : (1) une réflexion totale interne, et (2) une transmission vers le haut.

Pour un prisme d'indice de réfraction 1,8 entouré d'un milieu d'indice 1,46, les conditions (1) et (2) peuvent être représentées dans la zone en bleue de la Fig. R.3(c). Le centre de cette représentation polaire coïncide avec un rayon parallèle à l'axe $\hat{z}$. On y observe l'intensité du champ lointain issu du couplage évanescent. La condition d'extraction dans la zone bleue couvre suffisamment l'ensemble de la tache. Cette zone peut se décaler horizontalement si l'on oriente différemment les bandes prismatiques par rapport aux guides d'onde. Cela n'est pas illustré ici. Dans le manuscrit, je fais référence à cette rotation par l'angle ψ.

D'après mes simulations FDTD, il est possible d'atteindre une efficacité d'extraction dans l'air de 76 % pour une longueur totale $\ell_c \approx 5{,}5$ μm.

On procède à une démonstration passive (sans cristal liquide) en utilisant une résine à haut indice. La Fig. R.3(d) montre le schéma de la structure. En (1), la bande verte représente la structure en résine Inkron d'indice 1.808 @532 nm. Pour la fabrication, nous utilisons une réplication par *Nanoimprint Lithography* (NIL) avec un "master" souple. Le master rigide est réalisé par gravure humide du silicium, permettant d'obtenir deux angles possibles : $\alpha = 45°$ ou $54,74°$. La structure est d'abord répliquée depuis le silicium vers un moule souple. Ce dernier est ensuite utilisé pour reproduire la structure dans une résine à haut indice. La Fig. R.3(e) montre le résultat. La coupe MEB montre un léger effet de retrait estimé à 8 %, entraînant une réduction de l'angle de 45° à $42,5°$. L'épaisseur visée était de 2,5 μm ; après retrait, elle est de 2,3 μm.

En revenant à (d), la structure (1) est reportée sur un circuit photonique (2). Une colle UV d'indice 1.54 est déposée à l'intérieur pour remplacer l'air et permettre le collage des deux éléments.

La partie caractérisation consiste à coupler, depuis une fibre optique, de la lumière à 532 nm ou 660 nm dans le circuit photonique. Après couplage, la lumière est divisée en un ensemble de guides par une série d'arbres de division 1-vers-2. À l'extrémité des guides, des réseaux conventionnels d'extraction permettent d'extraire la totalité du signal. La bande passive à haut indice est reportée localement sur un ensemble de guides, en amont des réseaux.

La Fig. R.3(f) montre le résultat en imagerie. Le sens de propagation est de gauche à droite. Un zoom sur la bande met en évidence, horizontalement, les lignes correspondant aux guides d'onde, dont l'espacement n'est pas périodique. Verticalement, on distingue la bande d'environ

10 μm de largeur. L'extraction est localisée à l'extrémité de la bande et au niveau du croisement avec les guides d'onde.

Au bout des guides, entourés par le rectangle jaune, on observe l'extraction due aux réseaux de diffraction. La partie inférieure (ellipse blanche), correspondant aux guides recouverts par la bande, ne montre aucun signal extrait, indiquant que la lumière guidée est totalement couplée par couplage évanescent.

Pour évaluer la directivité de la bande par rapport aux réseaux, la Fig. R.3(g) montre l'extraction du côté opposé. On y observe une absence de lumière au niveau de la bande, tandis que les réseaux présentent un résultat similaire au précédent. Pour observer la direction opposée, un miroir a été placé derrière l'échantillon, car celui-ci est transparent.

Je mesure une divergence totale d'environ 20°. L'efficacité est estimée à 8 %. Cette valeur est faible car la largeur de la bande n'est pas optimisée. Dans ce chapitre 3, je présente les compromis à considérer pour extraire un maximum de signal (simulé à 76 %).

Ce chapitre offre de nombreuses perspectives intéressantes à poursuivre.

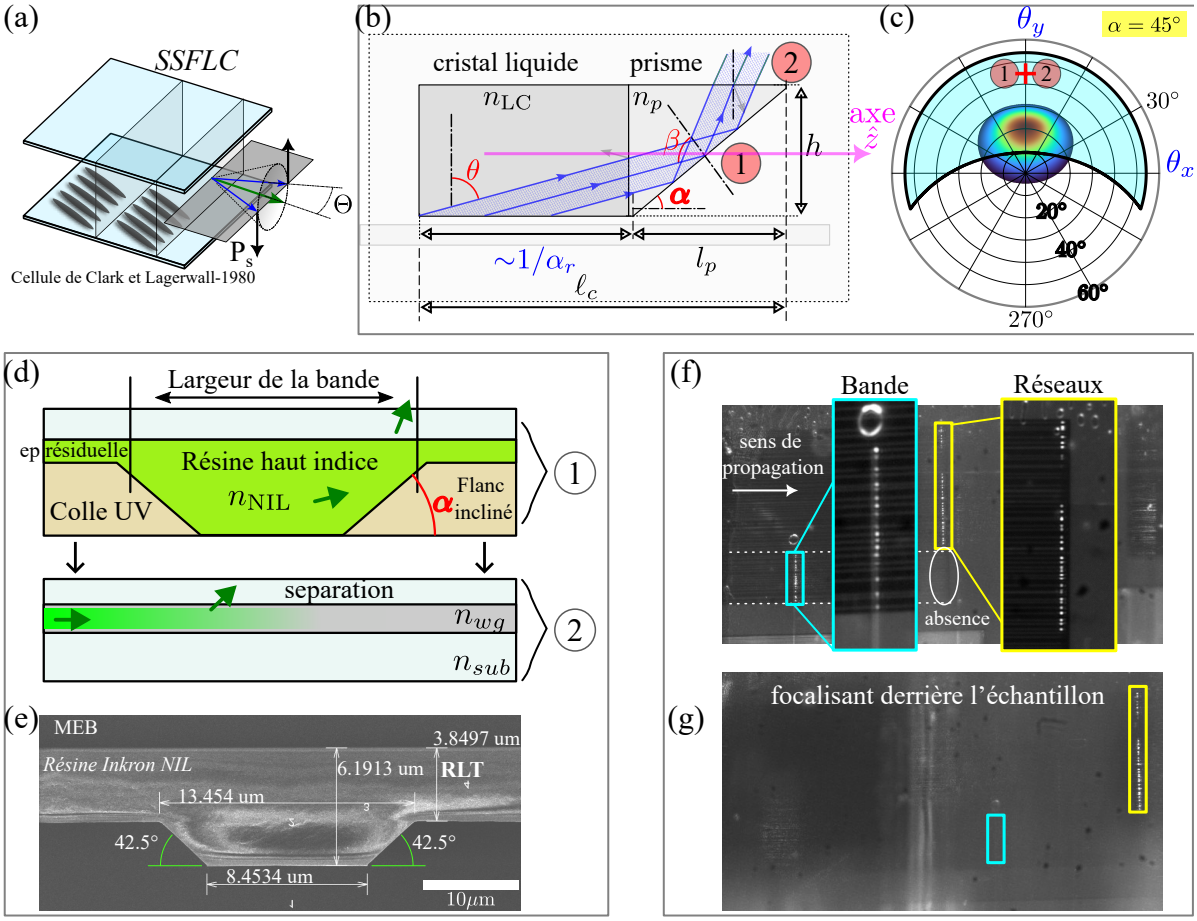

Figure R.3: (a) Géométrie avec phase SmC* pour obtenir un cristal liquide ferroélectrique. (b) Structure d'extraction avec les conditions (1) et (2) de réflexion et de transmission. (c) Visualisation en coordonnées polaires des deux conditions en bleu. La tache d'extraction (champ lointain) s'y trouve. (d) Structure avec une bande en résine à haut indice pour la démonstration passive. (e) Coupe MEB de la réplication NIL dans la résine Inkron d'indice 1,808@532 *n*m. (f) Caractérisation de l'extraction avec croisement de la bande avec les guides d'onde et les réseaux en extrémité. (g) Caractérisation dans la direction opposée montrant que le réseau n'est pas directif, contrairement à notre solution.

Résumé Chapitre 4

L'objectif de ce chapitre est de pixeliser des hologrammes en de petits éléments. La taille d'un élément holographique peut descendre à 20 μm. À l'intérieur de ces éléments, j'enregistre des composantes angulaires de réflexion suivant une distribution d'angles γ. Le chapitre commence par des notions théoriques permettant de comprendre la sélectivité angulaire et spectrale de cet élément, fonctionnant comme un réseau de Bragg en volume. L'épaisseur et la modulation d'indice sont directement liées à cette sélectivité.

Dans le chapitre, je compare les équations d'un modèle PSM (*parallel stacked mirror*) avec celles de Kogelnik ainsi qu'avec des simulations RCWA (*rigorous coupled wave analysis*). Le modèle géométrique PSM est élégant, simple à comprendre et fournit des résultats en accord avec la simulation.

La sélectivité angulaire du matériau photopolymère que nous utilisons est d'environ 27°, et la sélectivité spectrale d'environ 13 *n*m, pour une épaisseur effective de 14 μm et une modulation d'indice de 0,03. À la longueur d'onde de 532 *n*m, l'efficacité de réflexion atteint 98 %.

J'utilise une imprimante holographique pour la mise en œuvre de la pixelisation, dont le principe est illustré par le schéma de la Fig. R.4(a). L'angle de référence est fixé, tandis que l'angle objet est motorisé par le déplacement d'une fibre, ce qui introduit des angles d'incidence γ_{ij} différents. Une fois l'interférence enregistrée; environ 1 seconde pour le photopolymère, l'échantillon translate afin d'encoder l'angle suivant. J'ai automatisé la procédure sous LabView.

Les Fig. R.4(b) et (c) montrent des hologrammes imprimés par pixelisation. La résolution est de 20×20 pixels pour (b) et de 160×120 pixels pour (c). La taille de pixel est de 50 μm.

L'intervalle de codage angulaire de l'angle γ avec la configuration actuelle de l'imprimante est de 8° (±4°). Pour l'offset ϕ_{ref}, j'ai enregistré des éléments à 0°, 22° et également 35°. L'augmentation de ϕ_{ref} rend l'alignement de projection plus complexe. À $\phi_{\text{ref}} = 0°$, J'ai obtenu des pixels de 20 μm. Pour un offset de 35°, j'ai réussi à obtenir 50 μm.

L'enregistrement en haute résolution prend du temps. Je discute donc la réplication holographique afin de transférer l'ensemble des éléments vers un autre hologramme en une seule exposition. Néanmoins, pour enregistrer le « master », il est envisagé d'utiliser une emmulsion à base d'halogénures d'argent, dont la sensibilité est plus élevée, faisant passer le temps d'exposition par pixel d'environ 1 s à 20 ms. La réplication sera ensuite réalisée sur le photopolymère.

Un exemple de distribution angulaire que j'enregistre dans chaque élément holographique est illustré par le schéma de la Fig. R.4(d). Chaque élément encode un angle de réflexion γ qui vise le même point V. La référence d'illumination est $\phi_{\text{ref}} = 35°$, et la longueur d'onde d'enregistrement est 532 *n*m. L'intérêt d'une telle fonction est de pouvoir former une boîte à œil dont la position coïncide avec la pupille de l'œil (voir Chapitre 1, section 1.5.1).

La Fig. R.4(e) montre les résultats. Pour $FV = 9$ cm, je présente à $z = 0$ cm l'image de la distribution de pixels holographiques. Pour $z > 0$, le champ réfléchi est mesuré à différentes distances. À la distance correspondant à la focalisation encodée, l'ensemble des champs issus des éléments se focalise au même endroit, formant ainsi une tache de diffraction unique. La taille des pixels dans cet exemple est de 155 μm. Pour la longueur d'onde utilisée, la tache de diffraction mesurée coïncide avec la taille du pixel.

Pour $FV = 20$ cm, on mesure une focalisation qui coïncide avec cette même distance. Pour $FV = 100$ m, la focalisation correspond à une émission verticale sans directivité.

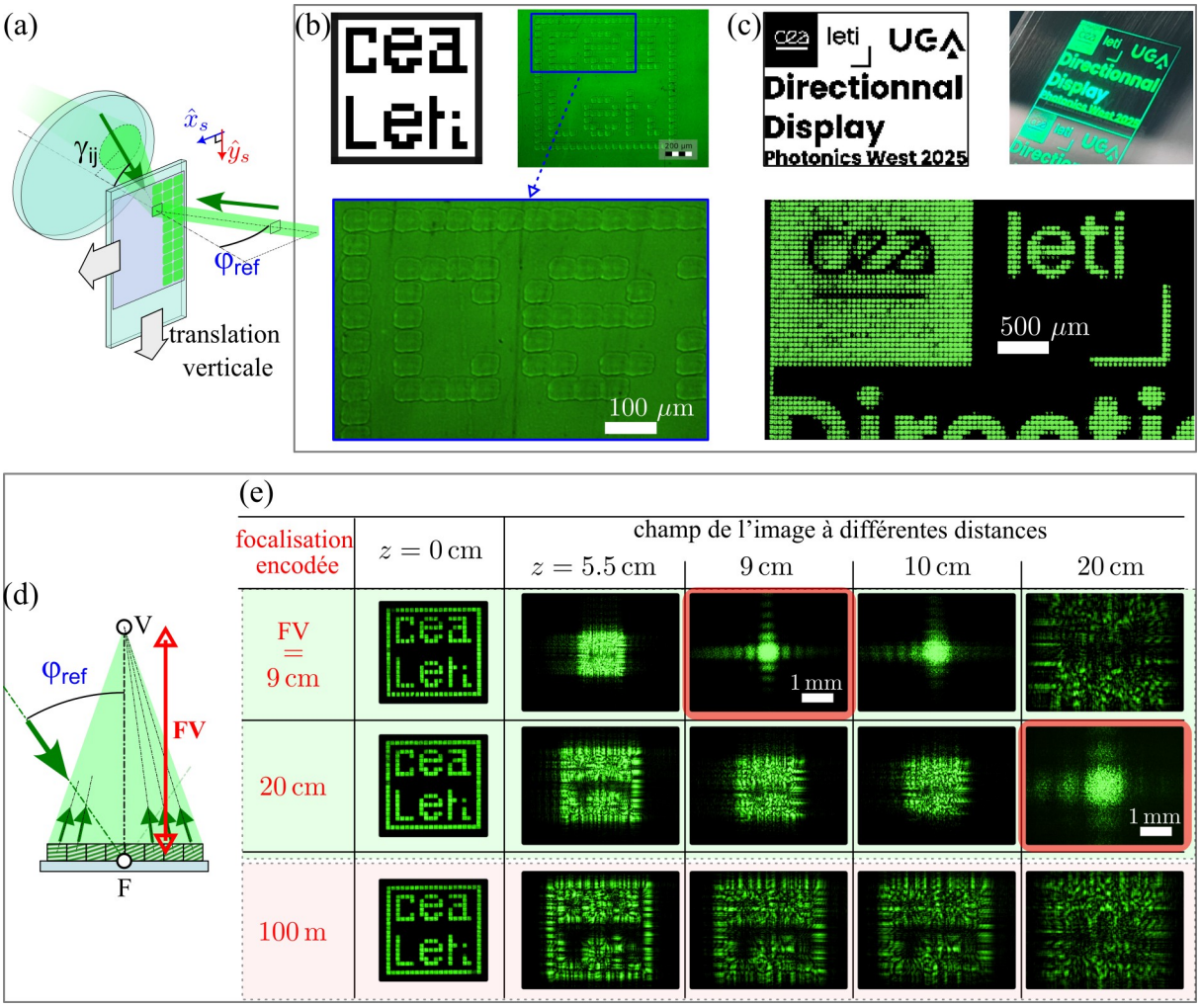

Figure R.4: (a) Principe d'enregistrement des éléments/pixels holographiques avec notre imprimante holographique, tout en codant des fonctions de réflexion γ_{ij} avec une référence ϕ_{ref}. (b) Résultat d'impression d'une image de 20×20 avec une taille de pixel de 50 μm. (c) Résultat pour une image de 160×120. (d) Schématisation d'une fonction optique où tous les pixels holographiques focalisent à la même distance FV. (e) Résultats de la focalisation encodée FV et champs mesurés par une caméra. La taille des pixels est de 155 μm et la longueur d'onde est 532 nm. La réference est $\phi_{\text{ref}} = 22°$.

Résumé Chapitre 5

Dans ce chapitre, je décris le prototype passif que nous avons développé. Ce prototype affiche une image enregistrée par pixelisation des hologrammes avec un offset de 35°. La Fig. R.5(a) montre ce prototype. Nous avons enregistré une lentille holographique, laminée sur la surface de cette lunette de protection. L'hologramme, intitulé écran statique, est schématisé sur la Fig. R.5(b). L'écran est divisé en deux : une partie directive et une partie diffusée afin d'augmenter la divergence. Dans le module de projection, l'écran est illuminé par une LED verte.

Le rendu visuel de l'image virtuelle est montré sur la Fig. R.5(c). L'image directive est plus brillante que l'image diffusée. Dans des conditions de luminance ambiante élevée, seule la partie directive reste visible.

Un protocole a été mis en place pour mesurer la luminance de l'image virtuelle. On se base sur le contraste entre l'image virtuelle et un arrière-plan de même couleur et de luminance variable. Nous avons demandé aux membres du laboratoire d'indiquer à quel moment l'image devenait imperceptible. La Fig. R.5(d) montre les résultats. En moyenne, la partie diffusée est estimée à une luminance de 1555 cd/m^2, tandis que la partie directive atteint 10614 cd/m^2.

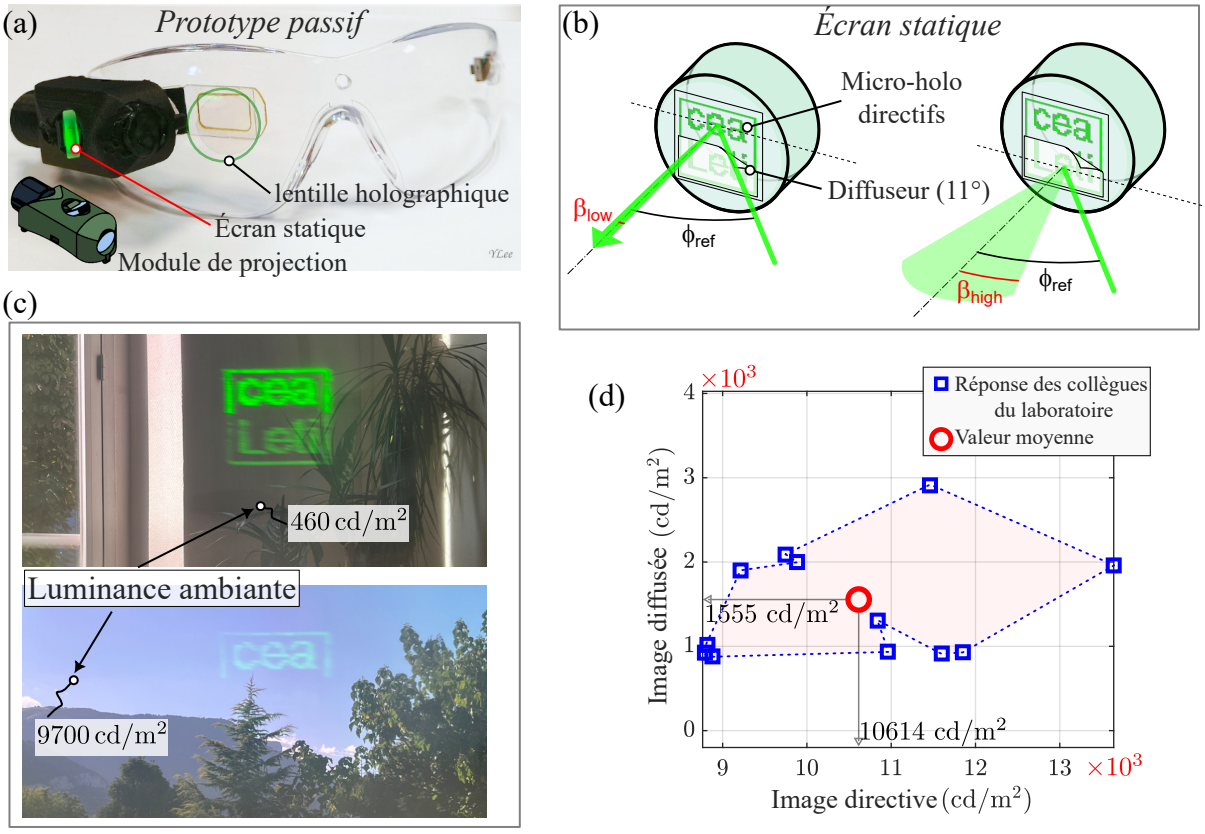

Figure R.5: (a) Un prototype NED passif développé dans cette thèse. (b) L'écran statique utilisé, composé de pixels holographiques. L'écran est divisé en deux parties : une directive et une diffusée. (c) Rendu visuel du prototype en conditions de luminance ambiante faible (en intérieur) et élevée (en extérieur). (d) Résultats de la mesure de luminance de l'image virtuelle, avec 1555 et 10614 cd/m^2 pour les parties diffusée et directive respectivement.

L'intérêt de ce prototype est de montrer l'importance d'une solution directive : pour une même consommation électrique, l'image est nettement plus brillante.

J'ai présenté ces résultats et le principe de notre NED directif lors du *Student Optical Design Challenge* à la conférence SPIE AR|VR|MR à San Francisco en 2025. J'ai eu l'honneur d'y recevoir le premier prix.